
Delocalization by disorder in GaAs/AlGaAs heterostructures

Inauguraldissertation

zur

Erlangung der Würde eines Doktors der Philosophie

vorgelegt der

der Universität Basel

von

Charulata Yashwantrao Barge

von India

Basel, 2012

Delocalization by disorder in GaAs/AlGaAs heterostructures

Inauguraldissertation

zur

Erlangung der Würde eines Doktors der Philosophie

vorgelegt der

der Universität Basel

von

Charulata Yashwantrao Barge

von India

Basel, 2012

Genehmigt von der Philosophisch-Naturwissenschaftlichen Fakultät
auf Antrag von
Prof. Dr. D. M. Zumbühl und Prof. Dr. C. Schönenberger

Basel, den 29. März 2011

Prof. Dr. M. Spiess
Dekan

Dedicated to

My grandmother,
Late Smt. Nirmala Ramchandra Barge

Abstract

An experimental study of quasiparticle and quasi-one dimensional properties of strongly correlated two-dimensional (2D) electron systems has been carried out. The samples were low disordered GaAs/AlGaAs heterostructures. Measurements were performed at low temperatures, down to 24 mK, in a dilution refrigerator (MCK 50-100 TOF) equipped with a superconducting magnet. The goal of our work was to study quasiparticle properties of 2DEG and to investigate the effect of local disorder on the conductance of the sample.

We have performed independent measurements of effective electron mass m^* , transport and quantum scattering time at three different temperatures and effective g-factor. We used Shubnikov de Haas effect, the oscillations in the longitudinal resistance in Hall effect to study the effective mass, scattering lifetimes and effective g factor. We found out that effective mass is unaffected and agrees well with the typical value of GaAs/AlGaAs system i.e. $0.067m_e$, where m_e is the electron mass. The quantum scattering time was studied at three different temperatures, base temperature (24mK), 200 mK and 400 mK as function of electron density. We found out that the quantum scattering time 24 mK is independent of electron density while at higher temperatures it decreases with decrease in density. The ratio of two lifetimes τ_t and τ_q is more than 10 for all temperatures. It means that remote Coulomb centers play a dominating role in the scattering mechanisms of our sample. More insight is needed to study the quantum scattering time at higher temperatures. The effective g-factor experiments were done with and without in-plane magnetic field. In both cases, the g-factor shows dependence on the magnetic field.

The main purpose of this thesis work is to investigate possible breakdown of the Anderson localization in presence of local disorder. To implement the local disorder and create delocalization we have used fine surface gates which tuned the potential barriers in the 2DEG. This was done in two different types of samples. In one sample the finger gates and top surface gate are isolated by an insulating layer of SiO_2 and in the other sample, the two gates are intercalated. The spacing in between the finger gates is determined by the mean free path of the system. The experiments are done in absence of magnetic field. We found out that the sample with SiO_2 shows the effect of disorder with decrease in the resistance. But due to charge trapped in the SiO_2 layer, the effect was not repeated. In the intercalated samples with two different finger gate spacings, the effect was not visible. The delocalization was not set in these sample even at high temperatures. More study is needed to prove this effect in GaAs/AlGaAs heterostructures. A low mobility wafer can be considered as the future candidate for this experiment.

Acknowledgment

First, I would like to to acknowledge my adviser, Prof. Dominik M Zumbuhl for his constant support and guidance during the course of my thesis. His wide knowledge and experience in the field and the way he was teaching me were always impressive. It was a great pleasure to work under his supervision.

I express my sincere gratitude to Prof. D.L. Maslov, Department of Physics, University of Florida, Gainesville, Florida, USA, for for the interesting topic, insightful ideas and inspiring discussions regarding the experiments and the theory.

I wish to thanks Prof. L.N. Pfeiffer, Department of Electrical Engineering, Princeton University, Princeton, NJ ,USA, for providing the excellent samples.

I would like to thank my co-referee Prof. Christian Schonberger, Nanoelectronics lab, Department of Physics, University of Basel, for taking his time and accepting to review the thesis.

My sincere thanks to the funding source, Swiss National Foundation, for support that made this project possible.

I wish to thank all my colleagues, especially Kai Schwarzwald, Florian Dettwiler who helped to set up the measurement system. I would like to thank Alexander Eichler for clean room training in the very beginning. I also owe a lot of thanks to the students that I worked with, Sandro Erni, Gregor Fessler, Raphael Wagner and Petar Jurcevik. Thanks for all the help. I want to thank members and former members Nanoelectronics group.

Special thanks to Dominik Sifrig, Patrik Stocklin, Sascha Martin and Michael Steinacher and members of mechanical and electrical workshops, for their technical support. Thanks to Barbara Kammermann and Astrid Kalt being always helpful in the administrative matters.

I wish to thank all my friends for making my stay enjoyable in the off-work times. I would like to thank the people who were always close to me though the geographical distance was quite considerable, my parents and my family members, back in India. It would have been difficult without you all.

At last, I am deeply indebted to my beloved husband, Dr. Mayank Prakash Agnihotri, for his support, encouragement and patience.

Contents

Abstract	ii
Acknowledgment	iv
1 Introduction	1
1.1 Outline of the thesis	3
2 Background of transport characteristics in 2DEG	4
2.1 Introduction	4
2.2 Semiconductor Heterointerfaces	4
2.3 Concepts in mesoscopic physics	6
2.3.1 Drude conductivity and Einstein relation	6
2.4 Mesoscopic time and length scales	8
2.4.1 Fermi wavelength (λ_F)	8
2.4.2 Mean free path ℓ	9
2.4.3 Phase coherence length ℓ_φ	9
2.4.4 Interaction parameter r_s	10
2.4.5 Magnetic Length	10
2.4.6 Transport regimes	10
2.5 Density of states	12
2.6 Density and mobility in the Drude model	13
2.7 Quantum Hall effect	13
2.8 Shubnikov–de Haas oscillations	16
3 Dilution Refrigerator and Superconducting Magnet	18
3.1 Introduction	18
3.2 $^3\text{He}/^4\text{He}$ dilution refrigerators	19
3.2.1 Cooling Power of the cryostat	21
3.3 MCK 50-100 TOF setup	23
3.4 Cold Finger extension	26
3.4.1 Socket and sample holder	26
3.5 Superconducting magnet	27
4 Characterization of 3-axis magnet at 4.2 K	29
4.1 Introduction	29
4.2 Construction and Fabrication of the Coils	29
4.3 Results and Conclusion	30
4.3.1 Room Temperature measurement	30
4.3.2 4.2K measurement	31
4.3.3 Field measurement in z-direction at 4.2K	31

5	Devices - Materials and sample fabrication techniques	35
5.1	GaAs/AlGaAs heterostructures	35
5.2	Wafer materials	36
5.3	Sample design	39
5.4	Fabrication Processes	42
5.4.1	Cleaving and cleaning	42
5.4.2	Electron beam lithography(EBL)	44
5.4.3	Optical photolithography	44
5.5	Etching	45
5.5.1	Reactive Ion Etching (RIE)	45
5.5.2	Wet chemical etching	47
5.6	Thin film deposition	48
5.7	Fabrication steps	48
5.7.1	Mesa photolithography and etching	48
5.7.2	Ohmic contacts	50
5.7.3	Fine gates and Finger Gates	51
5.7.4	Top gate	52
5.7.5	Large gates	54
5.8	Wire Bonding	54
6	Quasi-particle properties of 2DEG	56
6.1	Introduction	56
6.2	Density and mobility of the heterostructure	56
6.3	Effective mass m^*	66
6.3.1	Introduction	66
6.3.2	Theory	66
6.3.3	Results and discussion	67
6.3.4	Conclusion	76
6.4	Transport and Quantum Scattering times	76
6.4.1	Introduction	76
6.4.2	Theory	78
6.4.3	Results and Discussion	78
6.4.4	Conclusion	89
6.5	Effective g^* factor	90
6.5.1	Introduction	90
6.5.2	Theory	91
6.5.3	Results and discussion	91
6.5.4	Conclusion	95
6.5.5	Determination of electron temperature from Arrhenius plot	97

7	Transport and Quantum Scattering times	99
7.1	Quantum Scattering Time	99
7.1.1	Experimental Setup	101
7.1.2	Results and Discussion	107
8	Delocalization by disorder in layered system	110
8.1	Introduction	110
8.2	Theory	110
8.3	Experiments	113
8.3.1	Experiments with finger gates sample with SiO_2	114
8.3.2	Experiments with intercalated finger gate samples	129
8.4	Conclusion and outlook	141
9	Electron Temperature measurement in a Quantum Dot	143
9.1	Introduction	143
9.2	Charge Tunneling in a quantum dot	143
9.3	Different Temperature regimes	144
9.4	Materials and methods	145
9.4.1	Quantum dot sample	145
9.4.2	Measurement set up	147
9.5	Electron Temperature measurement	148
9.5.1	Single dot characterization	148
9.5.2	Temperature measurement	149
9.5.3	Improvements in the set up and the device	152
9.6	Electron temperature measurement in small sized quantum dot	152
9.6.1	Wall–wall measurements	152
9.6.2	Determination of the Electron Temperature	152
10	Conductance Quantization in Quantum Wires	156
10.1	Introduction	156
10.2	Quantum Wire device	156
10.3	Measurement set up	158
	Appendix	i
1	Appendix	i
1.1	Fabrication processes	i
1.2	Mesa Photolithography	i
1.3	Mesa Etching	i
1.4	Ohmic Photolithography	ii
1.5	Ohmic Evaporation	ii

1.6 Ohmic Annealing	iii
1.7 Electron beam lithography	iii
1.8 Small Gates Evaporation	iv
1.9 Large Gates Photolithography	iv
1.10 Large Gates Evaporation	v
1.11 Low noise filters	vi
List of Figures	vii
List of Tables	xv
References	xvi
Curriculum vitae	xxi

1 Introduction

Recent progress in epitaxial growth and micro-fabrication techniques has enabled us to design novel stages for the study of basic electronic processes in condensed matters. The properties of two-dimensional electron gas (2DEG) formed at the GaAs/AlGaAs heterointerface offers a well-defined environment for transport studies.

1. The system is close to the free electron picture.

As far as low energy phenomena are concerned, the energy band of the system is isotropic in k -space and takes the form of $\epsilon(k) = \frac{\hbar^2 k^2}{2m^*}$; $m^* = 0.067m_e$ being the effective mass for the GaAs conduction band. In state of the art samples, the mean free path of electrons exceeds $10^{-4}m$ at low temperature. The achievement of high electron mobility owes much to the development of the molecular beam epitaxy (MBE) growth and the modulation doping technique.

2. The electron density can be tuned within a single sample.

The electron density is typically $n = 10^{14} - 10^{15}m^{-2}$, the Fermi wave length is $\lambda_F 10^{-7}m$ and the Fermi velocity is $v_F = 10^4 - 10^5m/s$. We can control the electron density of a sample by applying a gate voltage.

3. A tailored potential can be applied to the 2DEG by microfabrication. We can fabricate a microstructure on the surface of the GaAs/AlGaAs structure and create an artificial potential profile for the 2DEG. This can be used to create an artificial potential barriers for the transport of electrons.

The two-dimensional electron gas in a strong magnetic field, B , exhibits a number of interesting many-body effects including the quantum Hall effect (QHE) ([1],[2]). The unique feature of this system responsible for its unusual behavior is the quantization of the energy spectrum.

Along with the magnetization, the change in the density of states is reflected in many other observable quantities. The simplest one to measure is oscillatory behavior in a magnetic field, or the longitudinal resistivity, R_{xx} . This is known as Shubnikov-de Haas effect (SdH), a measure of a non-equilibrium property (conductivity) of the 2DEG. The system is probed under electric field perturbation and understood in terms of current transport. It is a common and widely used technique to determine the electron density. We studied the temperature dependence of the amplitude, A , of the weak-field (sinusoidal) SdH oscillations to obtain the effective electron mass. Along with effective mass, spin splitting and effective g -factor is also a property to be studied to know the system better. Effective g -factor is influenced by the total magnetic field applied to the system hence it

is studied to see the effect of not only the perpendicular field and but also with presence of in plane magnetic field.

In the two-dimensional electron gas (2DEG) various lifetimes are introduced by a finite amount of disorder. Electron transport in semiconductors is generally characterized by a transport lifetime τ_t , which is also referred as momentum relaxation and is related to the conductivity, through $\sigma = n_s e^2 \tau_t / m^*$. There is also a quantum lifetime which is single particle relaxation time, τ_q describing the decay time of one-particle excitations and characterizing the quantum-mechanical broadening of the single-particle electron state.

It is important to distinguish between the quantum lifetime τ_q which is given by the total scattering rate and the transport lifetime τ_t which is weighted by scattering angle. For GaAs/AlGaAs heterostructure where the dominant scattering mechanism is usually the long-range potential associated with donors which are set back from the 2D electron gas and that typically differ by a factor 10 or more. We have done experiments at different temperatures to determine both scattering times and ratio of the two lifetimes which will emphasize the dominant scattering mechanism.

In the presence of random potential electrons are almost free on the atomic scale, but they are localized on a larger scale owing to interference effects in the wave function. This kind of localization, where the wave function spreads over a distance greater than the distance between impurities, and which makes the conductivity at zero temperature vanish, is called Anderson localization.

Anderson (1958) was the first one who showed that an electron which starts at a particular site cannot completely diffuse away from that site if the disorder is greater than some critical value. Anderson thus introduced the concept of localized and extended states. The single-particle density of states (DOS) averaged over the surface no longer abruptly increases to its constant value for two dimensions of $g_v m / \pi \hbar^2$. Extended states have a finite zero-temperature conductivity due to electron diffusion. But if the Fermi level lies in a region of localized states, the conductivity at zero temperature would vanish, because localized electrons can only move by thermally activated tunneling to another site.

Recently, the interest has increased substantially in order to find theoretical evidence for the breaking of Anderson localization by internal correlations in disordered systems. The idea is to use correlations between random scattering sequences and break Anderson localization.

In our experiments on high mobility GaAs/AlGaAs heterostructure, we implemented local disorder in the form of random potential to see enhancement in conductivity in the system.

1.1 Outline of the thesis

In this thesis we report measurements of the quasiparticle properties of two dimensional electron systems. Effective mass m^* , *Landé* g-factor, transport and quantum scattering times in a low-disordered strongly correlated 2D electron system in GaAs/AlGaAs. We performed experiments to see breakdown of Anderson localization and to see enhancement of conductivity as a function of bulk disorder. The work presented in this thesis has been done with clean GaAs/AlGaAs 2DEG samples available from Prof. L.N.Pfeiffer (Princeton University, Princeton).

The third chapter of this thesis describes theory and background for 2DEG system. It includes introduction to concepts of mesoscopic systems and different characteristic length scales. Here the effect of magnetic field on the 2DEG and corresponding properties like effective mass and g-factor are described.

In the fourth chapter, elements of cryogenics are described, including the working of $^3\text{He}/^4\text{He}$ and the superconducting magnet. It includes description of cold finger that was built in our lab. The fifth chapter is about house built split pair magnet system (Thanks to Petar Jurcevic). This includes the summary of room temperature and 4.2K test results of the split pair magnet.

The device fabrication is described in chapter 6. It includes various fabrication techniques for defining our sample geometries. The measurements and results of transport characteristics e.g. effective mass(m^*), g-factor and transport and quantum scattering time are described in chapter 7.

Chapter 8 we present the experimental outcome of our experiments on delocalization by disorder in GaAs/AlGaAs system. The motivation and theory about the project by Prof. Maslov is described along with the results.

Apart from this, other experiments such as experiments to find our electron temperature using Coulomb diamond in lateral quantum dot and the conductance quantization in quantum wires is described in chapter 9.

2 Background of transport characteristics in 2DEG

2.1 Introduction

The electronic properties of the two-dimensional electron system (2DEG) realized, e.g. in semiconductor heterostructures, exhibit an extremely rich phenomenology especially at low density, where correlations play an important role. Many crucial aspects of these interesting systems like the fractional and integer quantum Hall effect and the high- T_c superconductivity falls in this regime.

For the comprehension of the characteristics of a two-dimensional electron gas (2DEG) and the mesoscopic transport measurements performed in this work, it is important to understand the basic principles of the system. In this chapter mainly the 2DEG-system and its properties are discussed.

2.2 Semiconductor Heterointerfaces

The two-dimensional electron gas (2DEG) in heterostructure is one of the most popular choice to study the single particle and many particle properties of semiconductor nanostructures [3].

Here, an n-doped semiconductor layer with a larger bandgap, e.g. $Al_xGa_{1-x}As$, is grown epitaxially on a semiconductor layer with a lower band gap, e.g. GaAs [4]. Due to the adjustment of the Fermi level, electrons are transferred from the n-doped layer into the other semiconductor with the lower band gap. The band bending due to the band offset of both materials takes care that these electrons are only found at the interface of both layers. The electrons are trapped in a potential well. The electrons can only move freely along the interface, therefore these structures are called two-dimensional electron gases. In order to suppress impurity scattering, the impurities are separated by a spacer layer from the two-dimensional electron gas (modulation doping).

The well known semiconductor interface is the p-n junction. In this type of interface, the p-doped region forms an interface with a n-doped region of the same semiconducting material. But in contrast to such a system, the structure used in this work contains two different semiconductor crystals, i.e. GaAs and AlGaAs, thus forming a heterointerface. Gallium (Ga) and Aluminium (Al) are elements from column III where Arsenide (As) is a column V element in the periodic table. III-V semiconductor compounds often form zinc-blende crystal structures. GaAs and AlGaAs have quite similar lattice constants allowing a very sharp interface

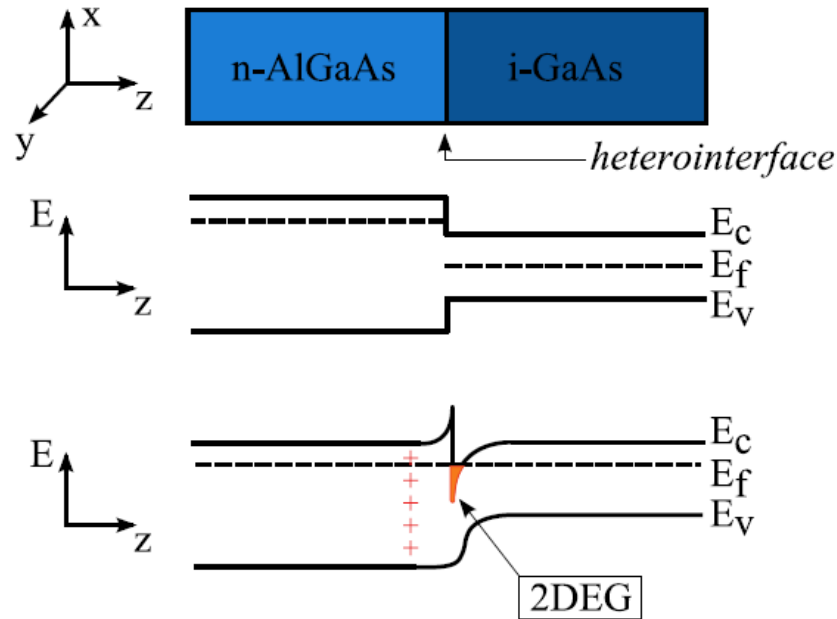


Figure 2.1: 2-dimensional electron gas is formed at the interface between intrinsic GaAs and n-doped AlGaAs. Silicon atoms act as a electron-dopant. After giving away an electron, the Si-atoms are positively charged.[5]

without disturbing lattice errors due to crystal strain. GaAs has a band-gap of 1.42 eV and AlAs has a larger gap of 2.16 eV. For $Al_xGa_{1-x}As$ alloy the band-gap is larger than 1.42 eV and smaller than 2.16 eV depending on the concentration x . The Fermi energy (E_F) in the widegap AlGaAs layer is higher than of the narrowgap GaAs. Bringing together the two crystals electrons start to spill over from the negatively doped n-AlGaAs leaving behind positively charged donors. The electrostatic potential will bend the bands as shown in Fig.2.1. At equilibrium the Fermi energy is constant everywhere. At the GaAs-AlGaAs interface the conduction band forms a triangular quantum well crossing the Fermi energy, thus forming a very thin conducting layer. Because the conducting electrons are constricted only perpendicular to the interface, a two-dimensional electron gas is formed.

2.3 Concepts in mesoscopic physics

2.3.1 Drude conductivity and Einstein relation

Paul Drude proposed the classical model for transport properties of electrons in metal [7]

When an electric field E is applied on a diffusive conductor, the average motion of electrons is given by linear differential equation:

$$\frac{dp}{dt} = eE - \frac{p}{\tau_t} \quad (2.1)$$

where p is the momentum of electron, e is the electronic charge, and τ_t is the mean free time between the two collisions. In above model the scattering assumes to follow a pure random process, which means the collision between the electrons is an uncorrelated and independent event. It is also assumed that the electrons ignore other interactions and hence follows the motion in a straight line. The probability of second collision in time dt is given by $\frac{dt}{\tau_t}$. The distance traveled by the electrons in between the two collision is termed as the mean free path is given by ℓ . The drift velocity of electron is given by v_d . If the electrons are accelerated for a time τ_t , the momentum relaxation time, then they are scattered and are assumed to lose their momentum. In equilibrium, the rate at which electrons receive momentum from the external field is exactly equal to the rate at which they loose momentum:

$$\left[\frac{dp}{dt} \right]_{scattering} = \left[\frac{dp}{dt} \right]_{field} \quad (2.2)$$

If $\frac{dp}{dt} = 0$ in 2.1 and the momentum is given by $p = m^*v_d$.

$$\frac{m^*v_d}{\tau_t} = eE \quad (2.3)$$

and hence the drift velocity is given by

$$v_d = \frac{e\tau_t}{m^*} E \quad (2.4)$$

The mobility μ is defined,

$$v_d = \mu E \Rightarrow \mu = \frac{e\tau_t}{m^*} \quad (2.5)$$

Since the current density is given by $j = nev_d = \sigma E$ (n is the electron density). One obtains the Drude conductivity,

$$\sigma = en\mu = \frac{ne^2\tau_t}{m^*} \quad (2.6)$$

For a degenerate Fermi-gas with wavefactor k and temperature T the Fermi energy E_F is greater or equal to kT , the Fermi sea is filled up to Fermi wave-vector k_F and Fermi energy E_F

$$k_F = \sqrt{\frac{4\pi n}{g_v g_s}}_{g_s=2, g_v=1} = \sqrt{2\pi n},$$

where g_s is the spin degeneracy (in GaAs, at $B = 0$, $g_s = 2$), and g_v the valley degeneracy (in GaAs, $g_v = 1$).

$$E_F = \frac{\hbar^2 k_F^2}{2m^*} = \frac{\pi \hbar^2}{m^*} n \quad (2.7)$$

The nonzero current is carried only by electrons around the Fermi energy. To understand the conduction properties, it is sufficient to consider electrons close to the Fermi surface, where electrons move with the Fermi velocity

$$v_F = \frac{\hbar k_F}{m^*} \quad (2.8)$$

Current is then carried by only a small fraction of electrons: $j = e(nv_d/v_F)v_F$. Scattering occurs with an average time τ_t , giving a mean free path

$$\ell = v_F \tau_t \quad (2.9)$$

Using Eq.2.7 and the above expression for ℓ , the conductivity can then be written in the following form:

$$\sigma = g_s g_v \frac{e^2 k_F \ell}{2h} = \frac{2e^2}{h} \frac{k_F \ell}{2} \quad (2.10)$$

The conductivity can be written as a ratio of mean free path ℓ and the Fermi wavelength by expression

$$\lambda_F = 2\pi/k_F \quad (2.11)$$

Since in metals, $k_F \ell \gg 1$ and $e^2/h \approx 25.812k\Omega$. By using the expression for the 2D density of states, one gets

$$\rho_{DOS} = \frac{g_s g_v m^*}{2\pi \hbar^2} = \frac{m^*}{\pi \hbar^2} \quad (2.12)$$

and the diffusion constant is

$$D = \frac{1}{2} v_F^2 \tau_m = \frac{1}{2} v_F \ell \quad (2.13)$$

One can use the Einstein relation to express the conductivity in terms of density of states and diffusion constant and can be written as;

$$\sigma = e^2 \rho_{DOS}(E) D \quad (2.14)$$

It is worth noting that in two dimensional unlike in three dimensional or one dimensional the resistivity ρ , a material parameter independent of sample shape and size, and the resistance R of a given sample have the same units (Ohms, Ω) and are related via a dimensionless quantity L/W , where L is the length and W is the width of a sample:

$$R = \rho \frac{L}{W} = \rho \square \frac{L}{W} \quad (2.15)$$

where the resistance or resistivity per square is $\rho \square = \rho$. The resistance of a sample can therefore be calculated by counting the number of squares that fit into the sample region since the resistance R of a square is independent of the size of the square in 2D.

2.4 Mesoscopic time and length scales

One can classify the mesoscopic systems by relating its size to specific characteristic length scales which determines the fashion in which the carriers propagate through the conductor and also the loss of phase memory in the phase coherence length. This section will introduce Fermi wavelength, mean free path, the elastic and inelastic mean free path which result from the scattering processes occurring in the sample. In case of a magnetic field applied the bending of the electron trajectories due to the Lorentz force defines the so-called magnetic length.

2.4.1 Fermi wavelength (λ_F)

At low temperatures $kT \ll E_F$, current is carried by electrons a few kT around Fermi energy E_F . The relevant length associated with these electrons is the Fermi wavelength.

$$\lambda_F = 2\pi/k_F = \sqrt{2\pi n} \quad (2.16)$$

which depends only on the carrier density n . Electrons below the Fermi energy have correspondingly longer wavelengths.

2.4.2 Mean free path ℓ

Mean free path ℓ is the distance traveled by an electron between two collisions. This is related to mobility and momentum relaxation.

$$l = v_F \tau_t = v_F \mu \frac{m^*}{e} \quad (2.17)$$

Elastic mean free path, ℓ_e The elastic mean free path ℓ_e is a measure for the distance between two elastic scattering events. These scattering events occur due to the fact that the conductor is not an ideal conductor but rather contains irregularities in the lattice, e.g. scattering due to impurities or dislocations. In case of elastic scattering the electron does not change energy. A typical example is the scattering of an electron at a charged impurity. Due to the large difference of the masses of the scattering partners effectively no energy is transferred from the electron during the scattering event, whereas its momentum can change largely. [8]

$$l_e = \tau_t v_F \quad (2.18)$$

where $v_F = \hbar k_F / m^*$ is the Fermi velocity, with k_F the Fermi wave number and m^* the effective electron mass.

Inelastic mean free path, ℓ_{in}

There are also non-stationary scattering events e.g. lattice vibrations. An electron moving within a crystal will be scattered by these lattice vibrations. While moving, electron can scatter due to lattice vibrations and loose energy. Unlike elastic scattering event, energy transfer is involved. Inelastic scattering length is the length between two inelastic scattering event.

2.4.3 Phase coherence length ℓ_φ

Phase coherence length ℓ_φ is a measure of the distance the electron travels before its phase is randomized. Many times the phase is modified by scattering event. By elastic scattering events, with a static scattering center, the phase of an electron is usually not randomized. The phase is shifted by exactly the same amount if the electron would travel the same path a second time. The phase shift an electron would acquire is different each time, since the scattering mechanism is statistically in space and time.

2.4.4 Interaction parameter r_s

The interaction strength is the ratio between average Coulomb energy and kinetic energy of electrons. This is a measure of distance between the electrons and related to strength of interaction between the electrons. It is defined as,

$$r_s = \frac{e^2}{4\pi\epsilon_0\epsilon r} \div E_F = \frac{e^2 m^*}{\epsilon\epsilon_0 h^2} \frac{1}{\sqrt{n}} \quad (2.19)$$

2.4.5 Magnetic Length

In a magnetic field electrons are deflected by the Lorentz force, which is perpendicular to the magnetic field B and the velocity of the electrons. Due to the magnetic field free electrons will travel along a circle. The radius of this circle, is called cyclotron radius r_c , can be calculated from the balance between the Lorentz force and the centrifugal force resulting in

$$r_c = \sqrt{\frac{\hbar}{eB}} \quad (2.20)$$

The magnetic length is defined as,

$$\ell_B = \frac{m^* v_F}{eB} \quad (2.21)$$

From the cyclotron radius we can further deduce the cyclotron frequency

$$\omega_c = \frac{v_F}{r_c} = \frac{eB}{m^*} \quad (2.22)$$

2.4.6 Transport regimes

By comparing the definitions given above with the dimension L of the sample and the Fermi wavelength λ_F different transport regimes can be classified.

Diffusive transport

If the elastic mean free path l_e is smaller than the dimensions L of the sample ($l_e < L$), many elastic scattering events occur. The carriers are traveling randomly, diffusively through the crystal (Fig. 2.2).

Diffusive transport- classical regime

If the phase coherence length l_φ is shorter than the elastic mean free path ($l_\varphi < l_e$),

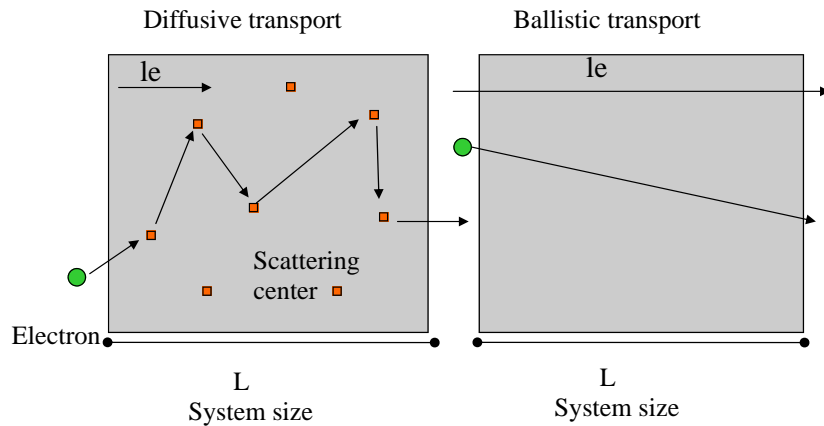


Figure 2.2: Illustration of the diffusive and ballistic transport regime.[8]

the transport can be classified as classical.

Diffusive transport- quantum regime

If phase coherence length is larger than elastic mean free path, $l_\varphi > l_e$, quantum effects due to the wave nature of the electrons can be expected. This diffusive transport regime is thus called quantum regime.

Ballistic transport

If elastic mean free path is larger than the dimensions of the sample, $l_e > L$, the electrons can travel without any scattering. This transport regime called ballistic (Fig. 2.2).

Ballistic transport- classical regime

If the sample dimension is larger than the Fermi wavelength $\lambda_F = 2\pi/k_F$ but smaller than the mean free path and the phase coherence length, $\lambda_F \ll L < l_\varphi, l_e$, the transport is termed as Ballistic classical transport.

Ballistic transport- quantum regime

If the sample dimension and Fermi wavelength are small than the phase coherence length and phase coherence length is smaller than the mean free path, $\lambda_F, L < l_\varphi < l_e$, this type of transport is called as ballistic transport in quantum regime.

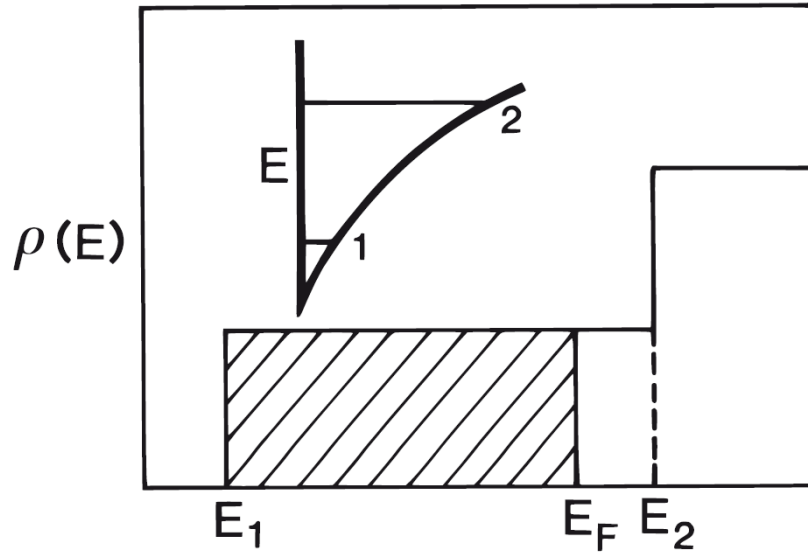


Figure 2.3: Density of states of a 2DEG with only one subband occupied ($E_F < E_2$). Inset: Energy levels in the 2DEG. [9]

2.5 Density of states

The energy dispersion relation for conduction electrons in a 2DEG, confined in z -direction, is given by,

$$E_n(k) = E_n + \frac{\hbar^2 k^2}{2m^*} \quad (2.23)$$

with the energy of the n th subband E_n and the effective mass m^* . If only one subband is populated, a 2DEG is formed. Otherwise, the electron gas is quasi two-dimensional. The density of states $N(E) = dn(E)/dE$ is the number of electronic states per energy and unit area. With $n(E) = m^*E/\pi\hbar^2$ the density of states for the first subband is given by,

$$N(E) = \frac{m^*}{\pi\hbar^2} \quad (2.24)$$

and is constant for all energies. If more than one subband is occupied, $N(E)$ is multiplied with a step function $\Theta(E - E_n)$ because every time $E_F \geq E_n$ a new subband is populated (Fig. 2.1). In the low temperature limit $kB_T \ll E_F$, all states are populated below the Fermi energy and the electron sheet density n_s is related to the Fermi energy via $n_s = m^*(E_F - E_n)/\pi\hbar^2$.

2.6 Density and mobility in the Drude model

To characterize the 2DEG in a Hall bar device, the Drude model serves as a simple model in transport experiments. If voltage is applied across the sample, the electrons receive momentum from the electric field E and acquire a drift velocity v_d . The electron mobility μ is now defined as,

$$\mu = \left| \frac{v_d}{E} \right| = \frac{e\tau_t}{m^*} \quad (2.25)$$

with τ_t as the momentum relaxation time or backscattering time or transport time. It depends on phonon scattering and at low temperature mainly on impurity scattering. e is the electron charge (> 0). In the Drude model, the force from an electric field and the Lorentz force from a magnetic field is in equilibrium with scattering forces,

$$\frac{mv_d}{\tau_t} = e(E + v_d \times B) \quad (2.26)$$

Using the current density $j = ev_d n_s$, the resistivity tensor ρ , and rearranging Eq. 2.26, the electron density and the mobility of the 2DEG are given by

$$n_s = \frac{1}{eR_H} \quad (2.27)$$

$$\mu = \frac{1}{en_s \rho_{xx}^{(0)}} \quad (2.28)$$

with the Hall coefficient $R_H = d\rho_{xy}/dBz$, the transversal or Hall resistivity $\rho_{xy} = R_{xy}$ and the zero field longitudinal resistivity $\rho_{xx}^{(0)} = R_{xx}(B = 0)W/L$. W is the width and L the length in the electric field direction of the Hall bar. In order to determine the electron density, the magnetic field has to be perpendicular to the xy -plane. At low temperatures, the mobility depends non-monotonically on the electron density and is limited by two opposing effects: increasing electron density (via gate voltage) lowers the longitudinal resistance due to enhanced screening of impurity potentials. On the other hand, it increases the confinement and therefore the surface roughness scattering at the interface.

2.7 Quantum Hall effect

The Hall resistance is linear in magnetic field. The classical Hall resistance can be understood by considering the asymmetric charge distribution resulting from the

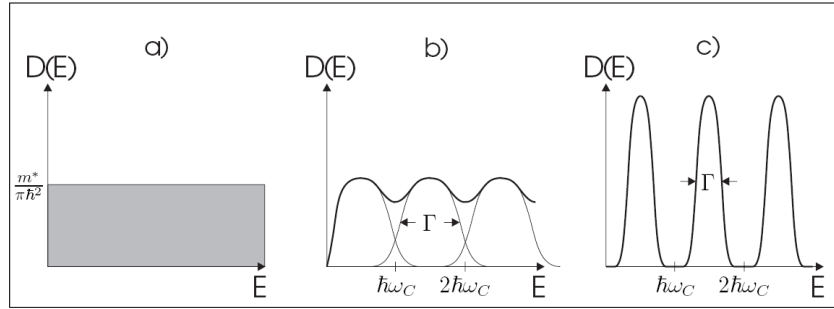


Figure 2.4: (a) Density of states of a 2DEG without external magnetic field. (b) Landau level quantization starts at low magnetic fields. (c) At high magnetic fields, the spacing is larger than the level broadening ($\hbar\omega_c > \Gamma$) and the density of states is zero between the Landau levels. [10]

Lorentz force. However, at high magnetic fields and low temperatures, the Hall resistance exhibits plateaus not predicted by the Drude model. This phenomenon is called quantum Hall effect (QHE) [1]. The step-like behavior of the Hall resistance has its origin in so called Landau levels and is a quantum mechanical effect. If now a magnetic field is applied perpendicular to the 2DEG, the energy dispersion is given by,

$$E_n(k) = \left(n + \frac{1}{2}\right)\hbar\omega_c, n = 1, 2, 3, \dots \quad (2.29)$$

With the cyclotron frequency, $\omega_c = eB/m^*$. The Landau level quantization results in the splitting of the density of states into a sum of peaks approximated by,

$$N(E, B) \approx \frac{2eB}{\hbar} \sum \delta(E - E_n) \quad (2.30)$$

If the magnetic field is increased from zero, the spacing $\hbar\omega_c$ between the peaks grows and the Landau level quantization starts. For sufficiently large magnetic fields, the density of states is zero between the levels. However, in an actual system the energy of the Landau levels is broadened due to scattering processes, at low temperature mainly impurity scattering (Fig. 2.4). Now, as either the magnetic field or the Fermi energy, by applying a voltage, is changed, the Landau levels cross the Fermi energy and new electronic states contribute to the resistance. On the other hand, if the Fermi energy lies between two Landau levels the Hall resistance is constant and gives rise to a quantum Hall plateau.

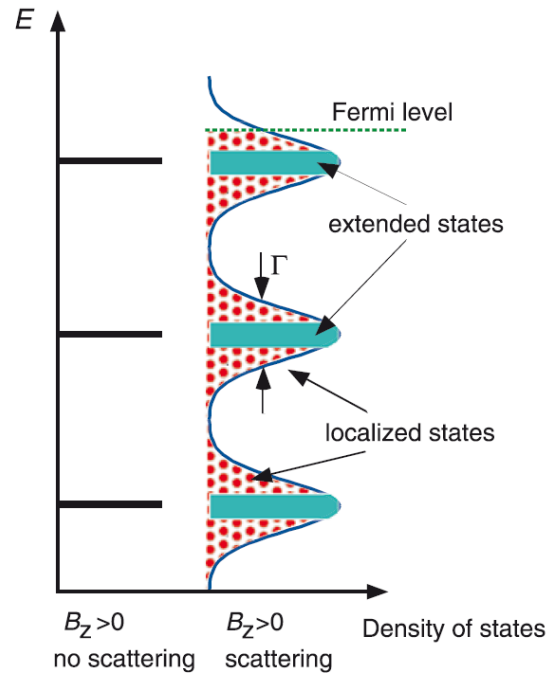


Figure 2.5: The Landau quantization without potential fluctuations in the bulk contains only extended states. When disorder potentials are present due to impurities, scattering in the bulk broadens the Landau levels and creates localized states. The extended states carry the current via edge states and the localized states stabilize the Fermi energy between the Landau levels.[11]

The density of states is zero between two Landau levels. Potential fluctuations from impurities in the interior of the sample due to disorder, localize the orbital motion of electrons at equipotential contours. Localized states are between the extended states of the Landau levels (Fig. 2.5). As consequence, the nonzero density of states stabilizes the Fermi energy between the Landau levels to form Hall plateaus. In the Landauer–Büttiker formalism, the edge states (extended states at the boundaries) are described as ballistic channels and the quantized Hall resistance is given by

$$R_{xy} = \frac{h}{2e^2} \frac{1}{\nu} \nu = 1, 2, 3, \dots \quad (2.31)$$

For a degenerated 2DEG with the filling factor ν that represents the number of edge states at the Fermi energy (number of bulk Landau levels below E_F). In strong magnetic fields the spin degeneracy is resolved as a result of Zeeman

splitting of the Landau levels that contributes to an additional energy term $sg^*\mu B$ in Eq. (2.29) (with the spin of the electron $s = \pm 1/2$, the Landé g -factor g^* and the Bohr magneton $\mu_B = e\hbar = 2me$). For spin-split Landau levels, we obtain $R_{xy} = h/e^2\nu$.

2.8 Shubnikov–de Haas oscillations

At sufficiently high magnetic fields, the longitudinal resistance of the 2DEG is not constant anymore but shows oscillatory behavior. These magneto-oscillations are known as Shubnikov–de Haas (SdH) oscillations and are connected to the QHE. The origin of both effects is the Landau level quantization due to the magnetic field dependence of the density of states. In a Born approximation the scattering rate τ_m^{-1} is proportional to the density of states. Using Eq. (2.25) and (2.28) we obtain the relation $\rho_{xx} \propto N(E_F)$. Therefore, oscillations in the density of states at the Fermi level are visible as magnetoresistance oscillations. Every time the Hall resistance remains constant, the resistance of the SdH oscillation is minimal. As discussed in the previous section, the Hall resistance does not change, if the density of states at the Fermi energy is zero. Curiously the longitudinal resistance is minimal even when no states at the Fermi energy seem to be present to carry the current. To have a closer look, we calculate the group velocity from the energy dispersion (2.29)

$$v_n(k) = \frac{1}{\hbar} \frac{\partial E_n(k)}{\partial k} = 0 \quad (2.32)$$

At a finite magnetic field, the unconfined electron waves in the 2DEG are executing circular orbits with cyclotron frequency $\omega = eB/m^*$ and radius $l_c = m^*v_F/eB$. In real samples, a 2DEG is not infinite but has a confining potential at the boundaries. Taking the boundary potential into account, the energy dispersion is not anymore independent of the wave vector and the Landau levels are bent upwards at the boundaries. Since the confining potential is approximately a square-well, the group velocity is only non-zero at the edge of the sample. If the Fermi energy is between the Landau levels, the states at the Fermi level consist only of edge states to carry the current. The edge states at opposite edges propagate in opposite directions and are spatially separated (Fig. 2.6). This separation of states suppresses the momentum relaxation (and therefore the longitudinal resistance) because the electrons cannot backscatter to the other edge due to their skipping orbital motion at the boundaries. The mobility in the quantized Hall regime is many orders of magnitude larger than at zero B-field. The density of states of a 2DEG with boundaries consists of localized and extended states. The localized

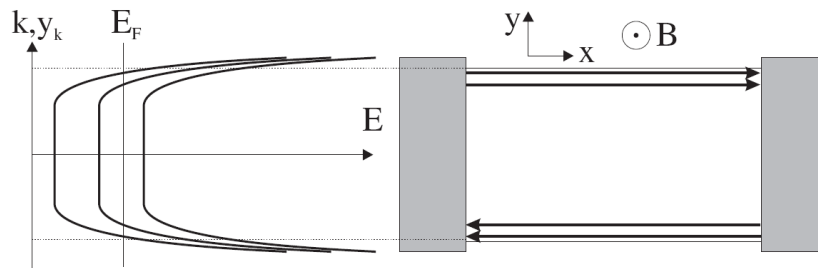


Figure 2.6: Landau level bending at the boundaries of a confined 2DEG. The resulting edge states at the Fermi energy transport the current spatially separated, giving rise to zero longitudinal resistance. [10]

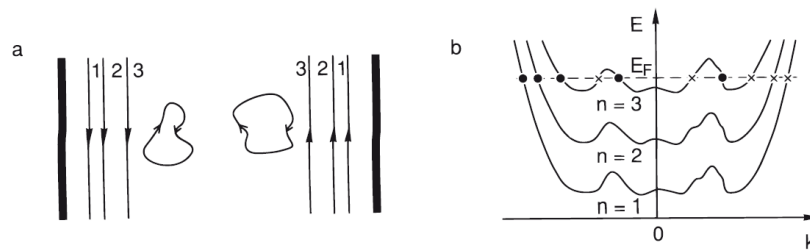


Figure 2.7: (a) Edge states near the sample boundaries and localized states in the bulk. (b) Regarding the Fermi velocity $v_F = 1/\hbar \delta E_n(k = k_F)/\delta k$ at the disorder potentials (black points and crosses), the cyclotron orbits circle along equipotential contours and are therefore localized. Localized states are the result of scattering on impurities due to local equipotentials. The scattering dependent broadening of the Landau levels stabilizes the Fermi energy between the Landau levels. [9]

states are in the bulk and the extended states form the edge channels at the boundaries of the sample (Fig. 2.7). The maximum of the SdH oscillations is explained by considering the extended states in the bulk. Every time the Fermi level crosses a Landau level, extended states are populated from the peaked density of states. But these extended states in the bulk are not spatially separated anymore giving rise to back-scattering. The criteria to see SdH oscillations are large magnetic fields (large level spacing) or a high mobility 2DEG (low Landau level broadening) at low temperature. Only then the electrons are localized sufficiently long before scattered (classically the electrons move in an orbit) giving almost zero longitudinal resistance (not exactly zero due to elastic scattering at impurities or due to the roughness at the boundaries).

3 Dilution Refrigerator and Superconducting Magnet

3.1 Introduction

Humankind has always been interested in achieving low temperatures - especially on a stable level - mostly to cool groceries and therefore prolong their storage lifetime. The first technical refrigerator was invented in the middle of the 18th century. Commercially available fridges were first constructed in the 1830s and technical improvements are made ever since, however most of them are still based on the same principle of a vapor compression cycle, which is more or less the inversion of a heat engine.

In science low temperatures are also of great importance and there is a multitude of applications, not only in physics but also in biology and medicine. In a scientific context the term low often has a different meaning. If a physicist is talking about cooling something down, he most probably refers to temperatures below 100 K. The whole field of physics that deals with experimental methods and material behavior at such low temperatures is called cryogenics. Permanent gases like nitrogen, oxygen, helium, neon and hydrogen have a boiling point below -180°C or 93.15 K. And exactly these gases or better their liquefaction play an important role in achieving such low temperatures. Just by dipping something into a cryogenic liquid, it already cools down to the temperature of the liquid, which is its boiling point under normal conditions. Sir James Dewar, the inventor of the dewar flask and the first to liquefy hydrogen, and Heike Kamerlingh-Onnes, the first to liquefy helium, are two of the main contributors to the progress in cryogenics. By a coincidence Kamerlingh-Onnes found also the superconductivity (of mercury, but for the first time ever) just by performing some electronic measurements in liquid helium [12].

What is temperature and why do physicists need low temperatures? Temperature is an intensive thermodynamic state function of a system which is closely related to energy. The temperature is basically the average of the kinetic energy of a system. This means it is the average over all microscopic motions, which include translational, rotational and vibrational energies of gas molecules but also lattice vibrations in solids. At absolute zero at 0 K (-273.17°C), which can not be achieved in practice, only the quantum mechanical zero-point energy is left, all other motions are frozen out. This concept of microscopic motion, but also the much simpler ideal gas law and considerations about the maximum efficiency of a heat engine led to this absolute temperature scale of Kelvin. For our experiments,

low temperatures are necessary to reduce noise as much as possible. No thermal motion of bulk atoms should disturb these measurements. For this purpose we use dilution refrigerators, which are able to achieve temperatures in the low millikelvin range. There are different methods, that enable scientists to cool down small samples below 300 mK. Dilution refrigerators (DR) which are discussed here have the advantage of a quite stable operation and a relatively easy way of controlling the temperature. The principle was first described by Heinz London in 1951 [13]. Since then, a lot of progress has been made on this field. An important contributor is Giorgio Frossati [19]. His research led to many improvements in the construction of DRs. In the next few section, we will discuss the basics about cryogenics and $^3\text{He}/^4\text{He}$ system.

3.2 $^3\text{He}/^4\text{He}$ dilution refrigerators

At the lowest possible temperatures, the helium remains in liquid state at atmospheric pressure. This unique feature plays key role in dilution refrigerators.[15] Helium has two isotopes ^3He and ^4He . They share quite few properties in common. The van der waals molecular forces are weak and hence to set the crystallization one has to apply a huge pressure ≈ 30 bar.

^4He under atmospheric pressure liquefies at $\Theta = 4.2\text{K}$. The density of liquid ^4He is $\rho(L^4\text{He}) = 125\text{kg}/\text{m}^3$. The vapor pressure drops exponentially as LHe gets colder, and reaches 1 mbar at $\Theta = 1.2\text{K}$. For $\Theta > 2.17\text{K}$, ^4He behaves just like any ordinary liquid. At some temperature the λ line is crossed, ^4He undergoes a phase transition. This transition is referred as He II. This phase transition is modeled as Bose–Einstein condensation. ^4He above the λ point is described as a gas. At $\Theta = 0$, on the other hand, all atoms of He II are in the ground state. At higher temperatures, the energy levels in a Bose–Einstein condensate (BEC) are occupied according to the Bose–Einstein distribution function.

The liquid ^4He behavior is explained as mixture of two states, a normal fluid and a superfluid [17]. The normal fluid behaves just like ^4He above the λ point with some entropy and viscosity, whereas the superfluid state has zero entropy and viscosity. As the temperature is lowered, the normal fluid fraction rapidly vanishes and an almost pure superfluid remains for $\Theta < 0.7\text{K}$. Due to zero viscosity in He II tends to creep over any wall of reasonable height, as long as its temperature stays below the λ point. The phase diagram of ^3He is shown in Fig. 3.1.

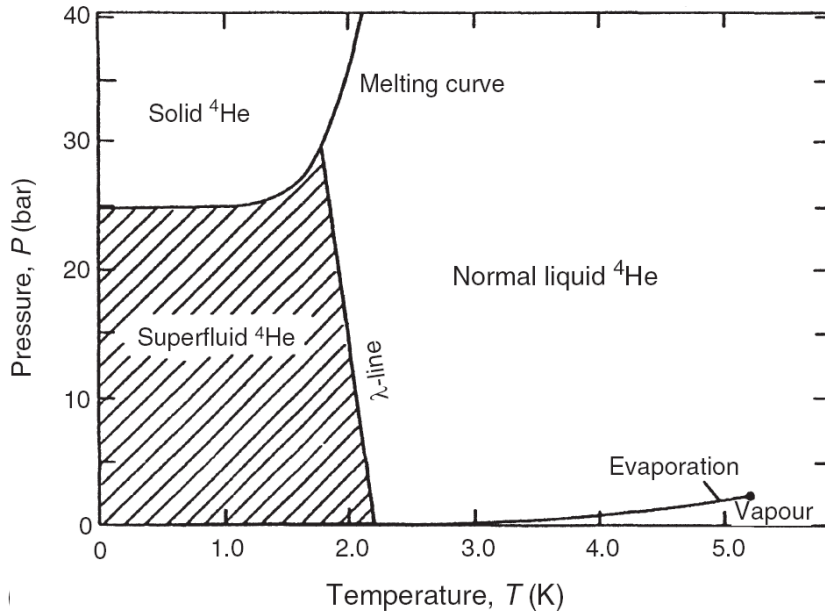


Figure 3.1: Phase diagram of ${}^4\text{He}$. [16]

$$f_{BE}(E, \Theta) = \frac{1}{e^{(E-\mu)/k_B\Theta} - 1} \quad (3.1)$$

The density of ${}^3\text{He}$ is $\rho({}^3\text{He}) = 59\text{kg}/\text{m}^3$. Under atmospheric pressure, it liquefies at $\Theta = 3.19\text{K}$. This boiling point is about 1K below that of ${}^4\text{He}$, since its mass is smaller, and thus the atoms have a longer average velocity at same temperature. The vapor pressure is also higher at identical temperatures. (Fig.3.2. It drops to 10^{-3} mbar at about $\Theta = 270\text{mK}$. ${}^3\text{He}$ atoms are fermions, and the liquid can be approximated by a Fermi gas, with many analogies to an electron gas. The effective mass by interaction at atmospheric pressure is $m^*({}^3\text{He in } {}^4\text{He}) \approx 3m({}^3\text{He})$.

Fig. 3.3 shows the phase diagram of this mixture. At temperatures over 860 mK, the mixture of liquid ${}^3\text{He}$ and liquid ${}^4\text{He}$ has no significant special properties. Below 860 mK, a phase separation into a ${}^3\text{He}$ poor phase (called dilute phase, D) and a ${}^3\text{He}$ rich phase, concentrated phase, C occurs. At this temperature, ${}^3\text{He}$ is a "normal" fluid, and ${}^4\text{He}$ is almost a superfluid. Since superfluid ${}^4\text{He}$ has zero viscosity, the ${}^3\text{He}$ atoms can move around without friction, once the ${}^3\text{He}$ - ${}^4\text{He}$ interaction is included in the effective mass. The ${}^4\text{He}$ atoms all are in the ground state and the diluted phase can be thought as a dilute Fermi gas with an effective mass given through the interactions between the ${}^3\text{He}$ and the ${}^4\text{He}$ atoms. The

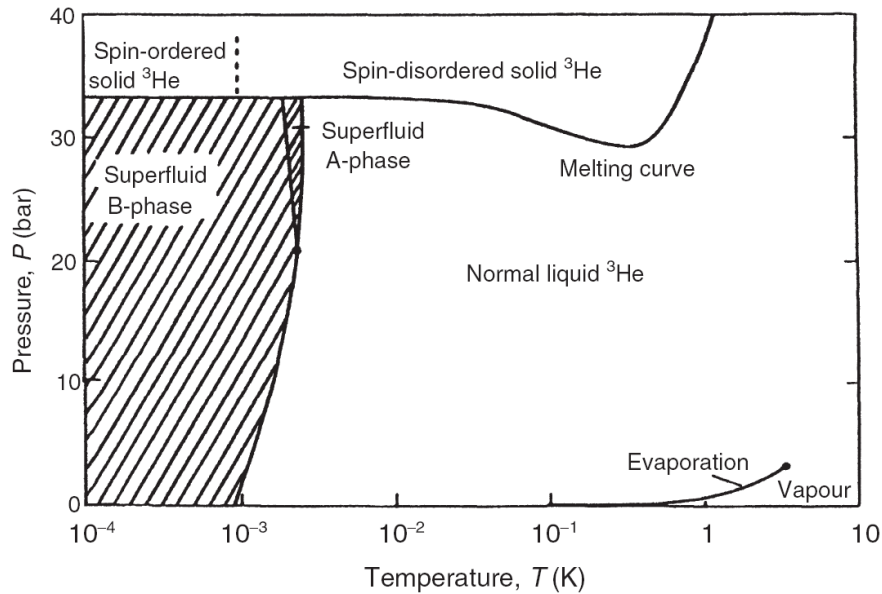


Figure 3.2: Phase diagram of ^3He . [16]

concentrated phase can be established as a Fermi gas as well. Hence ^3He atoms will go in the dilute phase till the chemical potentials of both phases are identical. The advantage of $^3\text{He}/^4\text{He}$ mixtures is the possibility to change the concentration and thus to tune the properties.

Using the ^3He and ^4He mixture properties, temperature below 1K is reached. The dilute phase can be regarded as the vapor of the concentrated phase. Because of the lower density, the concentrated (or "liquid") phase will float on the dilute (or "gas") phase. Now ^3He atoms are pumped out of the dilute phase, this causes ^3He atoms to "evaporate" from the concentrated in the dilute phase, pulling the latent heat out of the mixture. The helium mixture is situated in the mixing chamber. The dilute phase is connected to the still, at 600 mK. At this temperature ^3He can be distilled from the mixture. The distilled ^3He is brought in 1 K pot, where it is condensed and recycled. The whole system is isolated by a vacuum chamber and surrounded by a ^4He precooling bath.

3.2.1 Cooling Power of the cryostat

The cooling power \dot{Q} at the mixing chamber is strongly related to the number of ^3He atoms crossing the phase boundary or the rate \dot{n}_3 of the crossing. Every atom

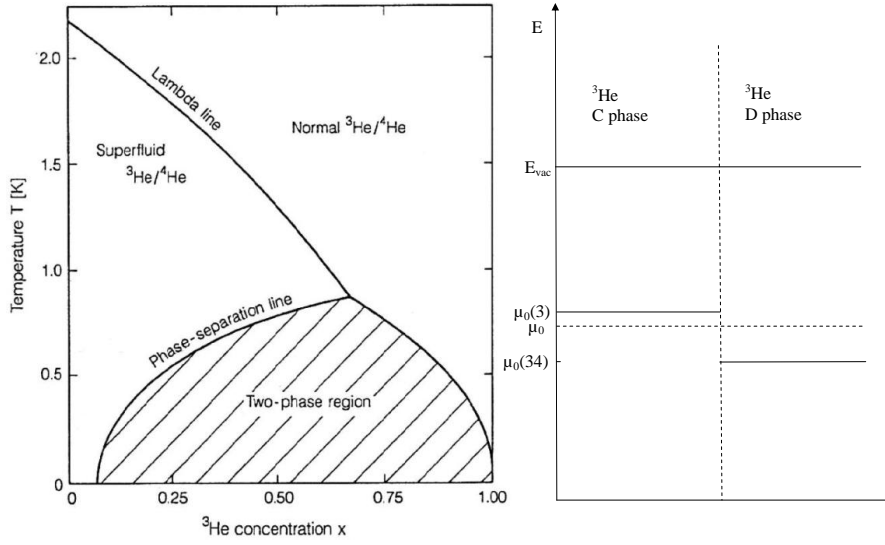


Figure 3.3: Left:Phase diagram of ${}^3\text{He}/{}^3\text{He}^4\text{He}$ mixture vs. ${}^3\text{He}$ concentration x and temperature Θ . The tricritical point is at $x=0.67$ and $\Theta = 860\text{mK}$. At lower temperatures, the mixture segregates into a ${}^3\text{He}$ – rich concentrated (C) phase and ${}^3\text{He}$ – poor dilute (D) phase. Right: Sketch of the chemical potential of the two phases at $\Theta = 0$ [15]

cools the system by the difference in enthalpy or the enthalpy of mixing ΔH

$$\dot{Q} = n\dot{n}_3\Delta H \quad (3.2)$$

$$\dot{Q} \propto T^2 \quad (3.3)$$

$$\text{Pobell} : \dot{Q} = 84\dot{n}_3T^2[18] \quad (3.4)$$

$$\text{Frossati} : \dot{Q} = 82\dot{n}_3T^2[19] \quad (3.5)$$

According to Eq. 3.3, the cooling power at 10 mK for example, is 100 times smaller than at 100 mK. The base temperature which can be reached with a certain fridge is the equilibrium at the point, where all the heat leaks can be compensated by the provided cooling power. So if the heating power in the still is increased in order to get a larger \dot{n}_3 , the cooling power increases. On the other hand this produces a heat load onto the MC.

3.3 MCK 50-100 TOF setup

For low temperature measurements, the dilution refrigerator (Leiden Cryogenics BV, Leiden, NL) was used. The main parts of this setup are an insert and a gas handling system, coupled to each other by flexible stainless-steel hoses and cables for the valves and gauges of the insert. The fridge is very convenient due to its fast operation time of few hours from room temperature to nearly base temperature. The mixture is circulated by a turbo-molecular drag-pump backed by a dry rotary pump so that the refrigerator is fully oil-free. A sorb pump is used for the final evacuation of the inner vacuum chamber (IVC).

The gas handling system (GHS) consists of a stainless steel cabinet made of hollow square tubes welded so as to make two leak-tight reservoirs. One is used for storing ^3He (20 liters), the other one is used for the ^4He -rich mixture (70 liters). A control panel attached to this GHS is used to monitor and control pressures in the DR unit. The MaxiGauge vacuum gauge controller (Pfeiffer Vacuum, Asslar, on the front of the cabinet, is used to monitor the Pirani pressure gauges (Pfeiffer Vacuum, Asslar, of the IVC and the still. Inside the cabinet there's a turbo pump (Varian Vacuum Technologies, Torino, I), two pumps for the ^3He circulation and the 1K pot.

Fig. 3.4 shows the picture of our setup including the dewar, insert and GHS.

The first step in operating the system is to fix the sample in the dilution refrigerator. Different parts of the refrigerator should be set up together and all the hoses and wires should be connected. Before cooling down the refrigerator, the inner vacuum chamber (IVC) should be pumped out, and tested for any possible leak using a mass spectrometer based leak detector. Before pre-pumping the tubes, one has to make sure that the nitrogen trap is not cold. Otherwise it may freeze out. After prepumping of the system with rotary pump i.e. when the pressure is lowered to 10^{-2} mbar, the DR unit and the tubes are pumped with turbo pump. The insert and tubes etc are usually pumped overnight before putting the insert in the dewar.

Dewar must be cold to liquid helium temperature at 4.2K. If the dewar is at room temperature, first it is cooled to liquid nitrogen temperature to 77 K for overnight. The next day the liquid nitrogen is extracted out and the dewar is filled up to the belly with liquid helium. The helium is transferred time to time to keep the helium level at a certain point, in our case, above the 1K pot when the insert is in the dewar.

Before inserting the DR unit in the dewar, it is important to make sure that the

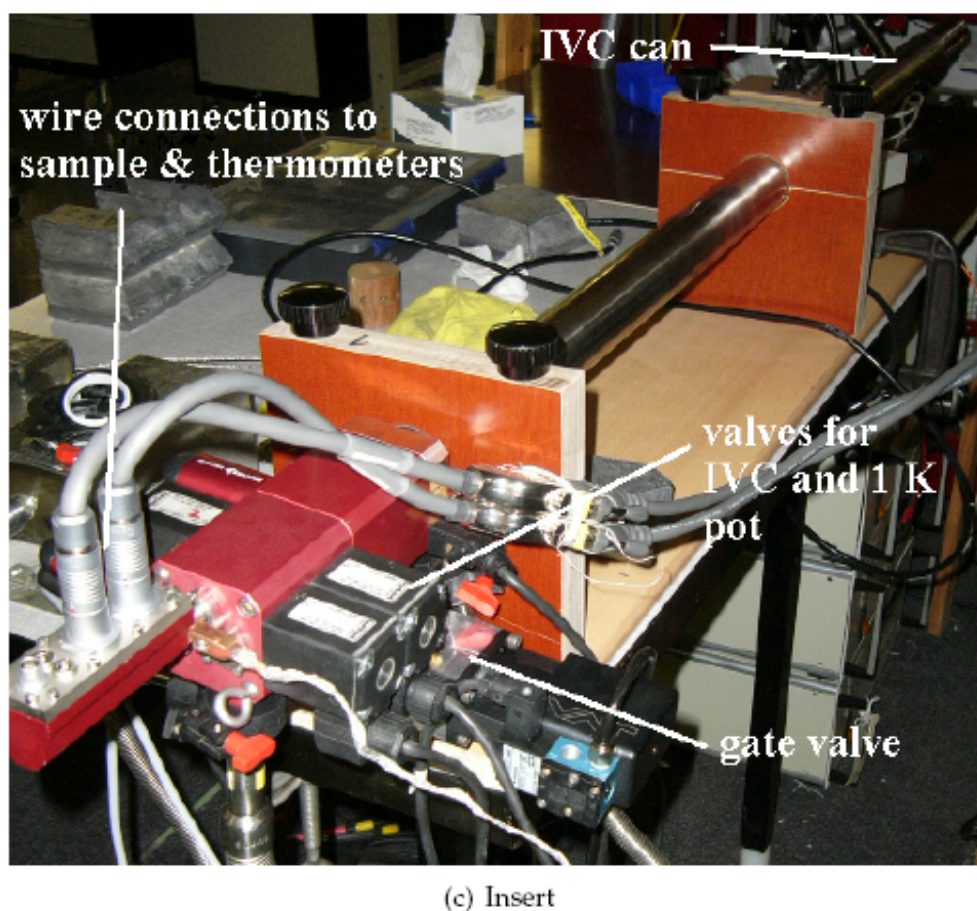
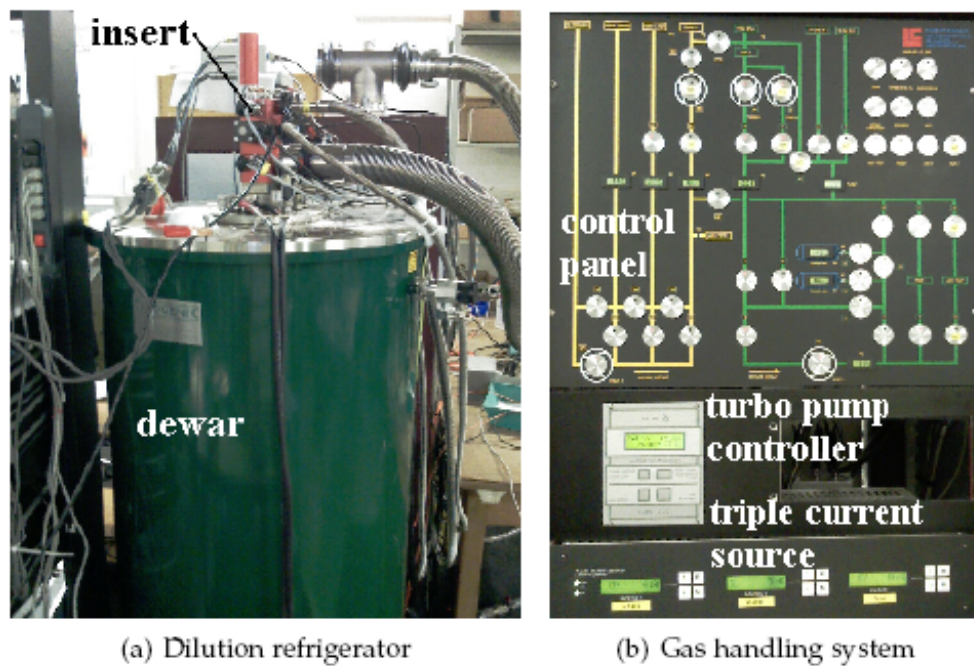


Figure 3.4: MCK 50 set up with dewar and gas handling system

1K pot is clean and not blocked. This can be done by pressurizing the 1K pot at room temperature and monitoring the pressure change from the 1K pot opening. Also a small amount of ^4He , $\approx 20\text{mbar}$ is introduced in the DR unit and the tubes at room temperature and then the DR unit is inserted slowly into the helium bath of the dewar. During this procedure, the increase in pressure at the 1K pot is monitored. 1K pot is not pumped now so the helium gas pressure inside the dewar should be noticed in the 1K pot pressure. The rate of increase is around 3-4 mbar/min.

Once all the parts of the insert are at 4.2K, the helium gas is pumped out to the gas handling system by means of a sorb pump at the insert and turbo pump at RT. We put around 40 mA on the sorb pump using triple current source (Leiden Cryogenics BV, Leiden, NL) at the RT set up. Once the insert is evacuated, ^3He and ^4He are introduced from the gas handling system to the DR unit via tubes.

As discussed in the earlier section, a liquid mixture of the two stable isotopes of helium, ^3He and ^4He exists homogeneously above a critical temperature 850 mK. When it is cooled below this critical temperature it separates into two phases with the lighter (concentrated phase) rich in ^3He floating on the top of the heavier (dilute phase) rich in ^4He . The phase separation occurs in the mixing chamber, and cooling is produced there by causing ^3He atoms from the upper concentrated phase to move across the phase boundary to the lower, dilute phase. The continuous dissolution of ^3He atoms from the concentrated to the dilute phase is obtained by circulating ^3He in the system by means of a pump at room temperature.

When the refrigerator starts working, the incoming gas from the gas handling system, ^3He and ^4He mixture is first precooled and liquefied in the condenser attached to the 1 K pot. In order to get the phase separation, the temperature must be reduced to below 0.86 K. This is achieved by reducing the vapor pressure of the liquid in the still using an external pumping system. The still is the first part of the refrigerator to cool down below 1.2 K. It cools the incoming ^3He before it enters the heat exchangers and mixing chamber. The ^3He should be extracted from the dilute phase and return into the concentrated phase keeping the system in an equilibrium. The ^3He is pumped away from the liquid surface in the still, which is typically maintained at a temperature around 0.6 to 0.7 K. A small amount of heat is then supplied to the still to promote the required flow. This is done using a heater attached to the still part and the triple current source at the room temperature set up. This current is around 8 mA. [20].

The concentration of the ^3He in the dilute phase in the still therefore becomes lower than it is in the mixing chamber, and consequently there is an osmotic pressure

difference which drives a flow of ^3He from the mixing chamber to the still. The ^3He leaving the mixing chamber is used to cool down the returning flow of the concentrated ^3He in a heat exchangers. The room temperature vacuum pumping system is used to remove the ^3He from the still, and compress it to a pressure of few hundred millibar. The gas is then passed through cold traps (77K) to remove impurities and returned to the DR unit, where it is pre-cooled in the main helium bath and condensed in the 1K pot.

3.4 Cold Finger extension

Our experiments are performed outside the mixing chamber. The cold finger of the mixing chamber is elongated by attaching an extension to it. This cold finger extension is designed in such a way that the sample will be in the center of both the solenoid and split pairs magnetic fields. This part connects the fork and cold finger of the MC by a screw thread. It is also made of ultra-pure silver. With the silver rod screwed to the fork, a better thermal conductivity and also a good stability can be achieved, although the mass is quite large. It is also easier to connect the rod to the cold finger extension by a simple slit and two brass bolts and nuts. As brass has a larger thermal expansion coefficient as copper it contracts more than the silver-plated copper of the cold finger and therefore it tightens upon cooling. The position of the sample can also be adjusted a little, because of the slits. The length of the existing part is designed to hold the sample in the lowest position possible in the existing IVC. In our set up the length of this extension is 20 cm. Fig. 3.5 shows the mixing chamber plug and the extension of the cold finger.

3.4.1 Socket and sample holder

We have used a 32– pin socket manufactured by Plastronics [22]. The body of the socket is made up of polyphenylene sulfid (PPS). Since most of the experiments are done in a magnetic field, the pins are chosen to be made up of non-magnetic material. Therefore the pins are of pure copper-berilium with the gold plating. A LED is mounted in the middle for experiments which needed LED illumination. The socket is milled to fit into the frame of sample holder.

The main idea of the socket holder was the possibility to adjust the angle of the sample. The basic design is a two armed fork which is holding the framed socket. The frame is attached at one axis and can be turned more or less freely. To adjust the angle, a thin plate was mounted between the fork and the frame, which allows to fix certain angles. For the fork and the frame ultra-pure silver was used. Because the socket is a polymer, which is also a bad thermal conductor. The silver

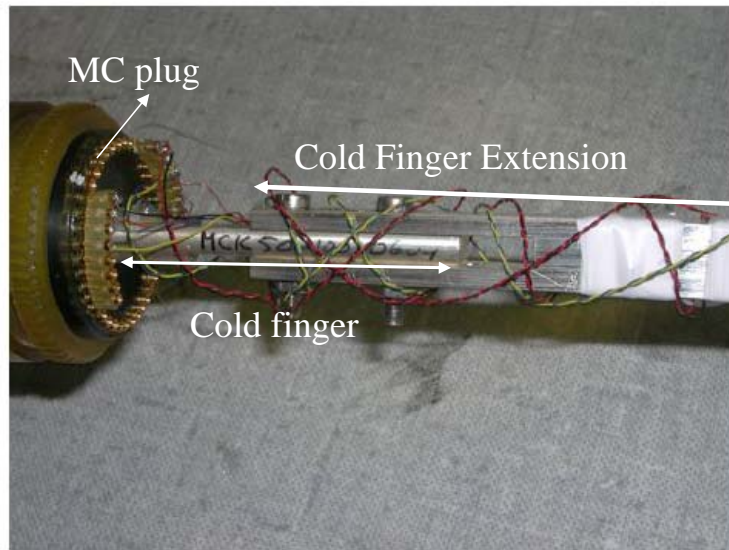


Figure 3.5: Mixing chamber plug, cold finger and cold finger extension

frame around it makes sure to cool it down fast from room temperature to around 1 K. But the remaining part of the sample cooling is mainly done through the copper wires connecting the sample. The plate to fix the angle is made of brass, which is also non magnetic and not as soft as silver and the thickness of only 1 mm . The socket is being held in the frame by the heads of the titanium screws. Fig. 3.6 shows the cold finger, socket and the sample holder with a chip inserted in.

3.5 Superconducting magnet

Our dewar is equipped with a superconducting solenoid magnet (Cryogenic Ltd, London, UK) with a maximum field of 9T. It is constructed to be physically and thermally stable under the large Lorentz force generated during operation. The superconducting a magnet has ability to operate in “persistence mode”. The superconducting circuit is closed to form a continuous loop, and the power supply can then be switched off, leaving the magnet at a fixed field. The field decays very slowly, at a rate depending on the inductance and other design parameters. Persistent mode operation is achieved using a superconducting switch, which is fitted to the magnet in parallel with the main windings.

The magnet will operate properly provided when all of the conductors remain in the superconducting state. The magnet is always maintained and operated at



Figure 3.6: Cold finger, socket and sample holder

4.2K. If any part of the windings goes normal or resistive, the current passing through it will cause ohmic heating. In this case all the stored energy in the magnet is dissipated rapidly, causing the liquid helium to boil off very quickly and often warming the magnet to a temperature significantly above 4.2 K. This is called a quench.

The maximum central field that can be reached is 9 T. The magnet has an inductance of 14.35H. The external diameter is 172 mm. There are certain limits to the ramp rates with which the magnet is ramped to a field. Upto 5.67 T, it can be ramped with a maximum current of 0.250A/s through the magnet. Upto 7.3, the ramp rate is 0.104A/s and for the maximum field it is reduced to 0.078A/s. These limits are to avoid excess heating in the leads and low boil off of the liquid helium.

4 Characterization of 3-axis magnet at 4.2 K

4.1 Introduction

Magnetic fields are needed to manipulate the spins. For many experiments it is enough to have a magnetic field along a fixed direction, but for others it is desirable to be capable to change and align the field in a certain direction. This can be achieved with three magnets each exciting a magnetic field x , y resp. z direction. By tuning each component separately the superposed field can be aligned in any desirable direction. The main aim of this project work¹ was to design and characterize such a 3-axis vector magnet for a cryogenic system with a dilution refrigerator setup.

A superconducting solenoid with a 89 mm bore from Cryogenic Ltd., is used to produce a magnetic field along the z -axis up to 9 T. Two additional homemade superconducting Helmholtz coil pairs generate the magnetic fields along x, y -axis. An important point is the design of the split coil pairs. The split coils have to fit into the 89 mm bore of the solenoid so the whole 3-axis vector magnet could be placed into the cryogenic system. Further the center of the generated field has to match the center of the inner vacuum chamber (IVC), where the sample is placed. This can only be achieved if the split coil pairs are arranged around the IVC. For various reasons, including available space, the coils are not flat but wrapped around a cylinder. The radius of curvature of the coils is 22 mm, slightly bigger than the radius of the IVC, which is 20 mm. All four coils fixed together form a cylinder wrapping around the IVC. Beside the construction and assembly of the magnetic system a further task was to test and characterize the split coil pairs.

4.2 Construction and Fabrication of the Coils

Niob/Titan superconducting wire is used [Supercon INC (type: SC-54S43)]. The bare wire diameter is 0.229 mm and with the formvar insulation 0.254 mm. This formvar insulation is a continuous formal film made of polyvinyl-enamel with a thickness of 0.025 ± 0.002 mm and a dielectric strength of $80kV/mm$. To remove the insulation, the wire is soaked in formic acid for about one minute and then rubbed it away with a Kleenex. The bared wire can be soldered with a common solder.

A non-magnetic material is needed for spool to avoid the influence of magnetic fields around. So brass is used as spool material. It is chosen in the way that

¹Magnet is built by Petar Jurcevic during his semester project in our lab [23]

four spools form a cylinder with a diameter $d = 44$ mm slightly bigger than the diameter of the IVC (inner vacuum chamber), which is 40 mm.

The cage consists of five discrete parts: the cage itself, where two coils can be mounted directly, two stiff bars, whereby the other coils can be mounted on the cage and a upper/lower flange to fix the cage into the solenoid. All parts are made of aluminum which is much stronger than brass. Although aluminum is paramagnetic with a magnetic susceptibility $\chi = 2.2 \times 10^{-5}$ [24], which is very small. Also aluminum has a slightly bigger thermal-expansion coefficient $\alpha_{293K} = 22.5 \times 10^{-6} K^{-1}$ [26] than brass $\alpha_{293K} = 17.5 \times 10^{-6} K^{-1}$. When the temperature decreases the aluminum shrinks faster than the brass, tightening around the pin, so that the spools are fixed more. The upper and the lower flange are each fixed with five stainless steel M5 screws to the cage. The flanges serve to mount the cage into the solenoid. With three further stainless steel M8 screws each flange is clamped to the solenoid. Stainless steel has also a lower thermal-expansion coefficient $\alpha_{293K} = 1.525 \times 10^{-6} K^{-1}$ [26] than Al, thus the screws are more tighten by decreasing temperature. But due to the fact that the thermal-expansion occurs in all space directions, one has to pay attention that the pre-drilled holes in the cage are deep enough otherwise the screw would be pushed away and high tensions would occur. Both flanges have additional bores so that evaporating helium can easily escape and that liquid helium can reach the inside of the cage and the IVC to cool it. The upper flange has in addition a funnel-like design to facilitate the insertion of the IVC.

The wires are wound using epoxy which kept the wire on the spool. It also acts as an additional insulation for the wires. The wire is thread through the spool and then the spool is mounted on the winding machine. Before winding, the inner side of the spool where the wire is in contact the brass is coated with epoxy. This coat should prevent a short between the wire and the spool. At the end the whole coil is coated again with epoxy to give it a protecting layer.

4.3 Results and Conclusion

4.3.1 Room Temperature measurement

Before mounting the split pairs at the magnet set up, they were tested for resistance, inductance, field at room temperature [23]. A short overview about these values for each coil is given in table 4.1.

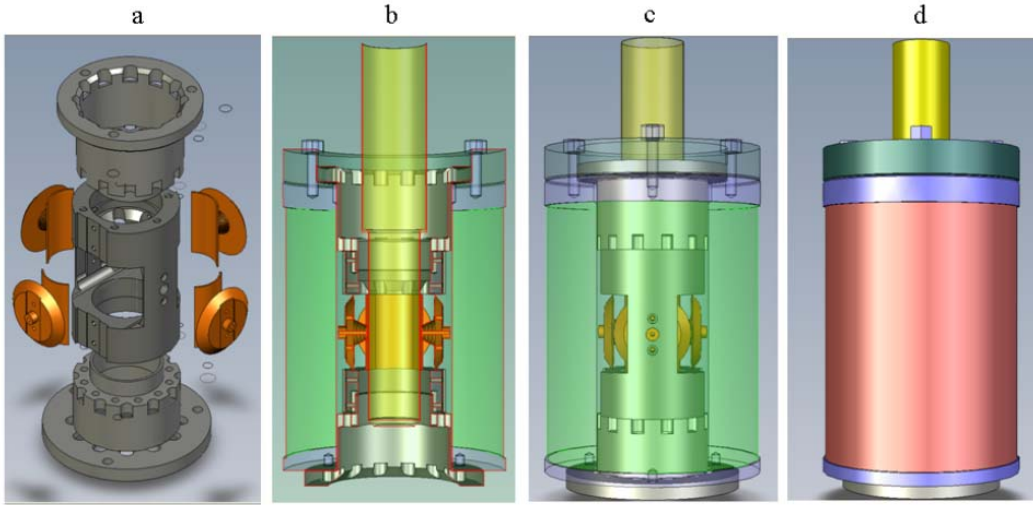


Figure 4.1: (a) the disassembled cage with the upper flange, the cage, the lower flange and the four spools. (b),(c),(d) assembled cage and mounted into the solenoid. yellow: IVC, green/red: solenoid. [23]

	Coil 1	Coil 2	Coil 3	Coil 4
Number of windings	2200	2200	2202	2200
Resistance R at DC	169.4 Ω	163.4 Ω	162.2 Ω	163.6 Ω
Inductance L at 1 kHz	62.1 mH	59.8 mH	60.6 mH	59.9mH
B_z at 100 mA	1.29 mT	1.26 mT	1.26 mT	1.25mT

Table 4.1: A short summary of the number of windings, resistance and inductance. [23]

4.3.2 4.2K measurement

4.3.3 Field measurement in z-direction at 4.2K

After testing the split pairs at room temperature, the split pairs are mounted on the cage and soldered to the copper wires to connect it to the magnet leads.

To measure maximum field at 4.2 K, we have used a dot mesa as a Hall bar. The sample is placed at the center of the solenoid perpendicular to solenoid field, parallel to split pairs, $\pm 0.5mm$ in X,Y Z- directions. The position can be confirmed by Hall resistance measurement. The solenoid is ramped to some field. The maximum of R_H gives the center of the field. Though the sample is not a conventional Hall bar, it is sufficient to calibrate the split pairs. The Hall resistance value of

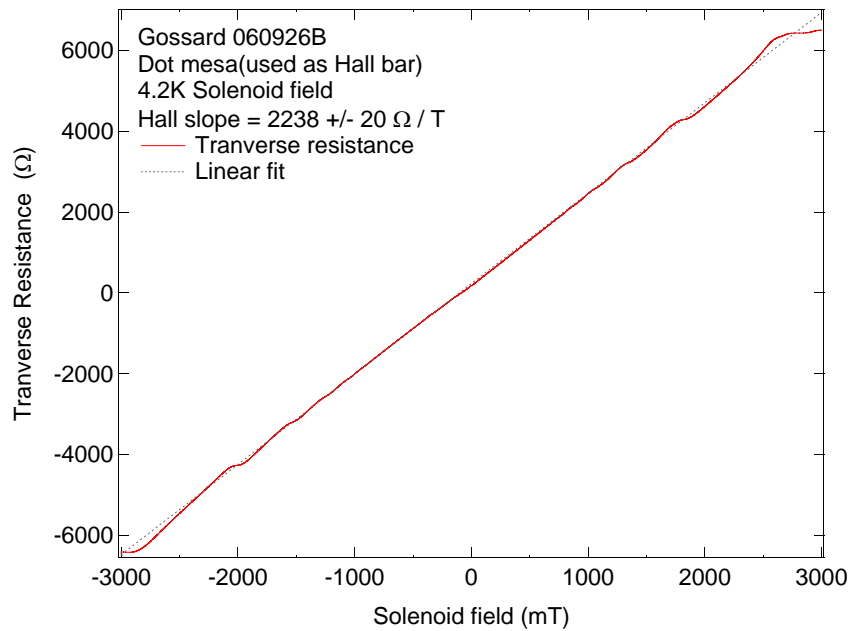


Figure 4.2: Hall resistance measurement on a dot mesa as a function of solenoid field. The same sample and calibration is used to determine the split pair fields.

the sample is first determined for solenoid field. Then sample direction is then changed and the sample is made perpendicular to split pair magnet and parallel to solenoid field.

To find the maximum of the split pair field with and without solenoid field, the current through the split pair is ramped till the quench point of the split pair. The quenching also depends on the ramp rate as the fast ramping heats the split pair and quenches the magnet earlier. The rate at which the split pairs are ramped is $0.253A/s$.

The inductance of the split pairs is measured. The value of inductance for coil 1–2 is 220 mH and for coil 3–4 pair is 202 mH. The maximum field of the split pairs is found for few different solenoid fields.

First the Hall slope or Hall resistance is determined for perpendicular magnetic field of solenoid, Fig. 4.2. Solenoid is ramped from $-3T$ to $+3T$. The split pairs are at zero. The Hall slope for this sample is $2238\Omega \pm 20\Omega$ per tesla. Now the sample is rotated in such a way that the split pair field is perpendicular. Now the current in the split pair e.g. in 3–4 is ramped and the transverse resistance of the sample is measured as a function of this current. Fig.4.3 shows the transverse

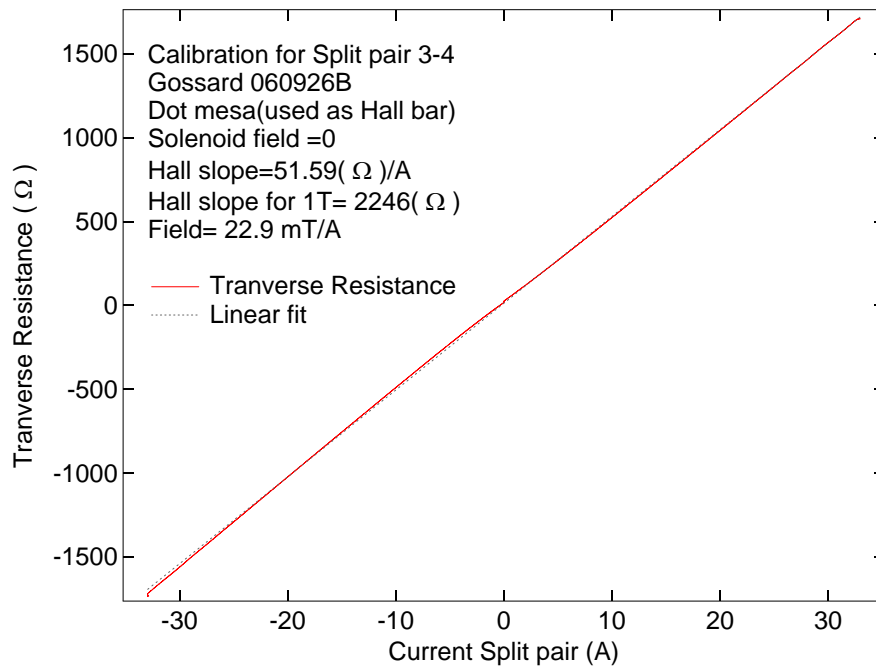


Figure 4.3: Transverse resistance as a function of current through split pair 3–4. The Hall slope from the linear fit is $51.59 \text{ } \Omega/\text{A}$

resistance as a function of current through split pair 3–4.

The slope of the transverse resistance from the linear fit is $51.59/\text{A}$. Comparing this value with the Hall slope of 2238Ω , we get the conversion factor for coil 3–4 to be $22.9 \text{ mT}/\text{A}$. The Hall voltage slope for coil pair 1 – 2 is $48.246\Omega/\text{A}$. From this slope, the conversion factor for 1–2 is $21.5 \text{ mT}/\text{A}$. Both the coils quench beyond 34 A. So the maximum field reached is around 750 mT. The detailed measurement is done with and without solenoid field.

The maximum field measured for both coils with and without solenoid field is done for both positive and negative directions. The quench points are noted for coils. This gives us a window of different field when all the magnets are being used. Fig. [4.4](#)

The solenoid field is kept constant. The split coil pairs data is checked ramping the coils in positive and negative directions for five different solenoid fields, 0T, 1T, 2T, 3T and 4T. The quench field point is lowered with the increase in solenoid field. Table [4.2](#) shows the values for different split pair fields for dif-

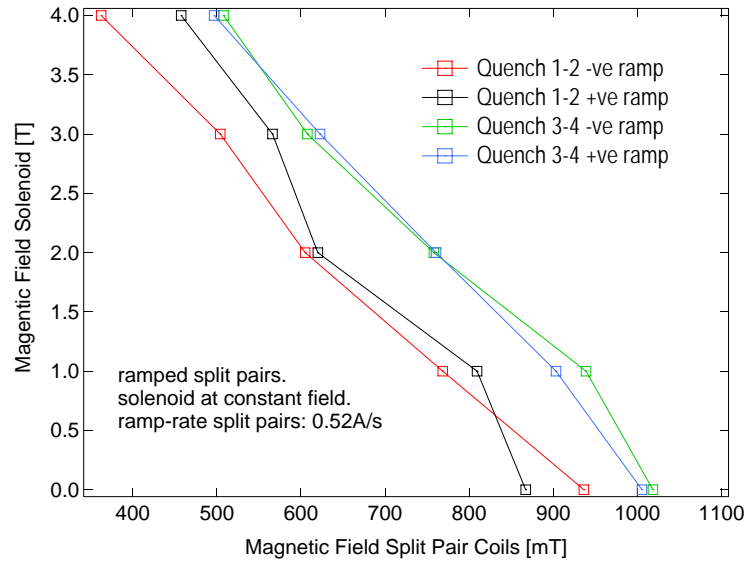


Figure 4.4: Maximum fields reached by split pairs 1–2 and 3–4 with solenoid field. The solenoid field is kept constant (positive) and the split pairs are ramped till the quenching points of the split pairs.

ferent fixed solenoid fields.

Solenoid(T)	Coil 1-2(mT)		Coil 3-4(mT)	
	-VE	+VE	-VE	+VE
0	936.325	1005.31	1018.36	867.095
1	768.625	903.176	938.9	809.26
2	605.01	760.509	757.99	620.06
3	503.96	622.651	607.537	566.095
4	362.49	496.7	507.92	457.52

Table 4.2: Short summary of the maximum fields of the split pair magnet in negative and positive directions at fixed solenoid field

The maximum field of the coils also depends on the ramp directions. Though we are limited to a certain value of the fields when we use both the magnets, these fields should be sufficient for many 2DEG phenomena since only weak field is needed in either direction.

5 Devices - Materials and sample fabrication techniques

5.1 GaAs/AlGaAs heterostructures

Fabrication of lateral structures like Hall bars, quantum wires and quantum dots starts with a semiconductor heterostructure as shown in Fig. 5.1. The stacked layers of GaAs and AlGaAs layers are grown by Molecular Beam Epitaxy (MBE). Dopants can be implanted during the growth process.

A 2-Dimensional Electron Gas (2DEG) forms by doping the n-AlGaAs layer with Si. The doping introduces free electrons that accumulate at the interface between the GaAs and the AlGaAs since there is a dip in the conduction band (see on right side of Fig. 5.1). Due to the confinement in the z -direction, the energy levels in this triangular potential are quantized. The 2DEG is separated from the n-AlGaAs donor layer by an undoped AlGaAs buffer layer. This separation greatly reduces the scattering with the Si donors resulting in extremely high mobilities of the electrons in the 2DEG. Usually, the heterostructure is engineered such that only the first subband is occupied. The gating effect on the 2DEG is typically realized by applying negative voltages to metal gates on top of the heterostructure.

The wafer material was deposited by molecular beam epitaxy (MBE) while spinning the substrate ¹. This allows very clean layers and interfaces in the wafer crystal.

For the experiments described in this thesis, we have used three different types of wafer materials. These wafer materials are described in detail in the following section.

¹The wafer was grown by L. N. Pfeiffer, Bell Laboratories, Lucent Technologies, Murray Hill, New Jersey 07974, USA, now at Princeton University, Princeton, New Jersey 08544

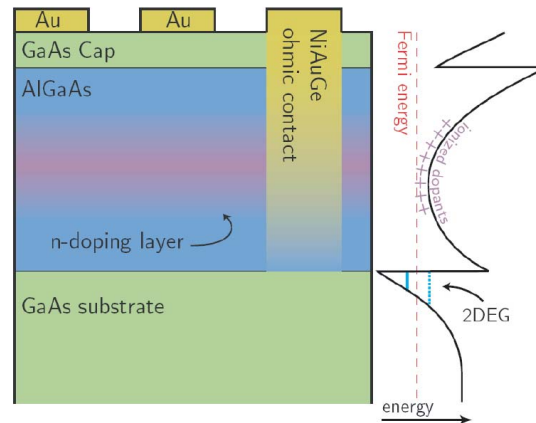


Figure 5.1: Growth profile and bandstructure of typical GaAs heterostructures.[28]

5.2 Wafer materials

(I) Pfeiffer 9.12.05.2 material

The sample consists of $GaAs/Al_{0.106}Ga_{0.894}As$ heterostructure. Si δ -doping (density $6.4 \times 10^{11}/cm^2$) was used to have additional electrons for the electron gas. A 80nm spacer layer of GaAlAs separates the Si atoms from the interface where the 2DEG is formed. The complete growth-profile is shown in. Before cutting the wafer for sample fabrication, density n and mobility μ was measured to be $n = 0.71 \times 10^{11}/cm^2$ and $\mu = 12.8 \times 10^6 cm^2/Vs$ after illumination with a GaAs LED ². Fig. 5.2 shows the growth profile for Pfeiffer 9.12.05.2. The 2DEG is 190 nm deep from the surface.

(II) Pfeiffer 7.28.08.02 and Pfeiffer 8.29.08.1 material

Pfeiffer 7.28.08.02 and Pfeiffer 8.29.08.1 are doped from two sides. Pfeiffer 7.28.08.02 consists of $GaAs/Al_{0.328}Ga_{0.672}As$ followed by Si δ -doping (density). Then $Al_{0.243}Ga_{0.757}As$ is added. The 2DEG is formed at the $GaAs/Al_{0.243}Ga_{0.757}As$ interface, at 398 nm. The quantum well is formed with second Si-doping as shown in Fig.5.3a. The density of Pfeiffer 7.28.08.02 sample is $n = 0.77 \times 10^{11}/cm^2$ and mobility $\mu = 4.9 \times 10^6 cm^2/Vs$ at 4K in dark ². At our lab, the density and mobility values at 4.2K in dark are $n = 0.76 \times 10^{11}/cm^2$ and $\mu = 4.5 \times 10^6 cm^2/Vs$ respectively after doing few fabrication processes. The two values agrees quite well.

²from measurements by Prof. L. N. Pfeiffer
2.

Sample:- Pfeiffer 9_12_05.2

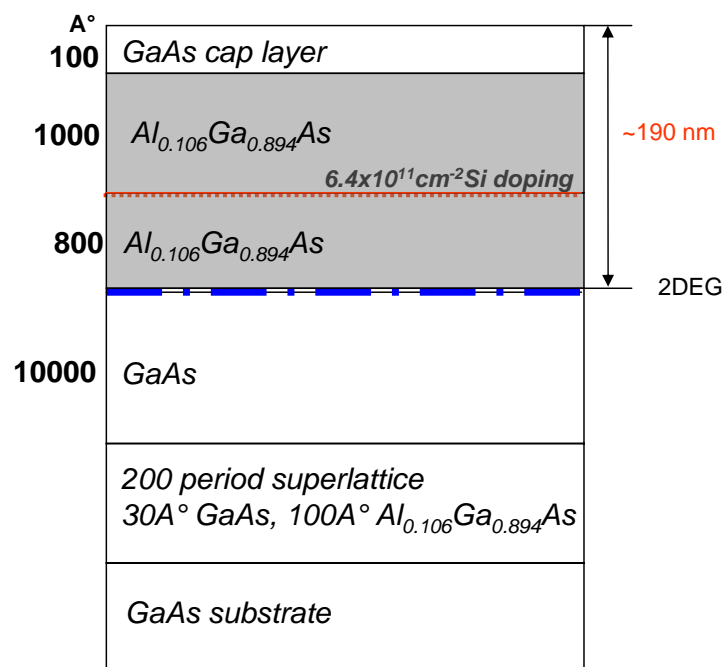


Figure 5.2: Complete growth-profile of the wafer Pfeiffer 9.12.05.2 used in this work. A spacing layer of 80nm separates the Si-atoms from the 2DEG plane. GaAs was used as a cap layer to protect the layers containing Al from fast oxidation.

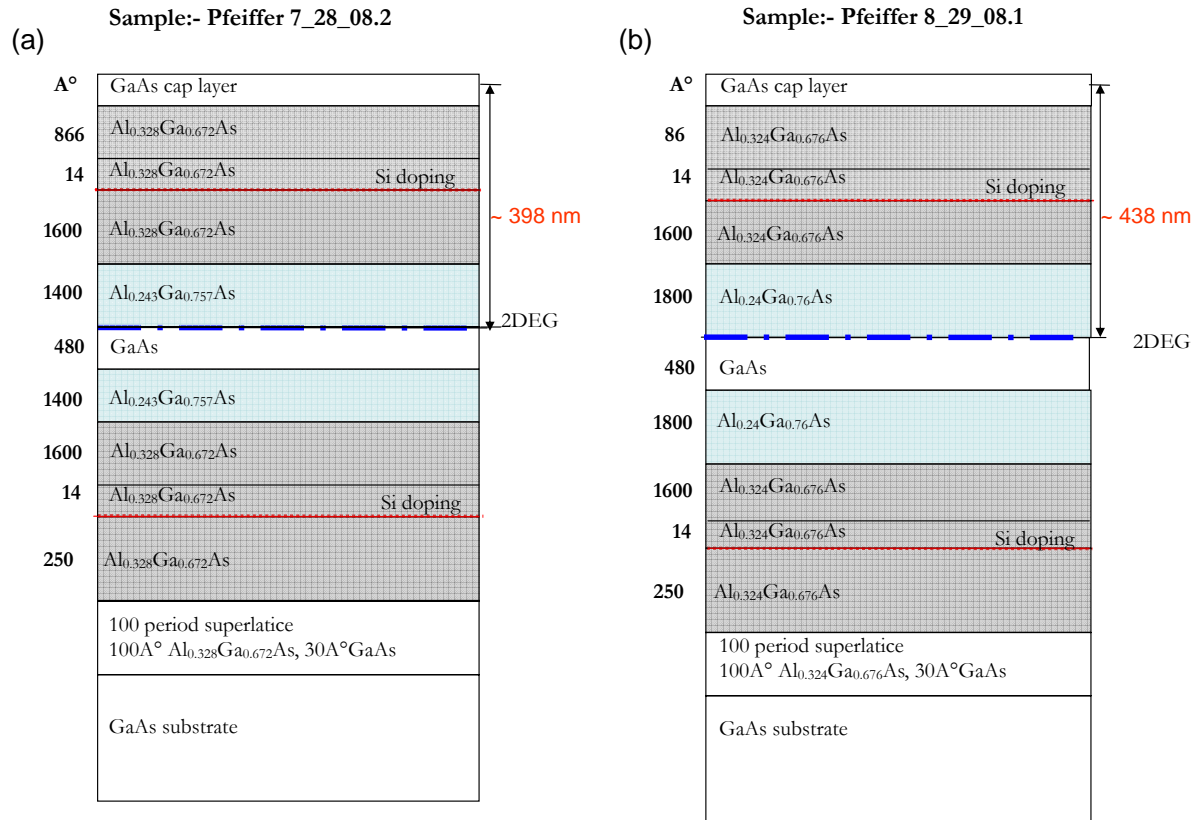


Figure 5.3: Complete growth-profile of the wafer (a) Pfeiffer 7.28.08.02 and (b) Pfeiffer 8.29.08.1 used in this thesis work. A spacing layer of 100 nm separates the Si-atoms from the 2DEG plane. GaAs was used as a cap layer to protect the layers containing Al from fast oxidation.

Fig. 5.3b shows growth profile for Pfeiffer 8.29.08.1. Pfeiffer 8.29.08.1 is grown in the same way as Pfeiffer 7.28.08.02. With $GaAs/Al_{0.324}Ga_{0.676}As$, the 2DEG is formed at 438 nm at the interface of $GaAs/Al_{0.24}Ga_{0.76}As$. The density of this wafer at 4K at dark is $n = 0.63 \times 10^{11}/cm^2$ and mobility is $\mu = 6.4 \times 10^6 cm^2/Vs$.² In our lab, after few lithographic steps, the density is $n = 0.75 \times 10^{11}/cm^2$ and $\mu = 5.4 \times 10^6 cm^2/Vs$ at 4K, in dark. The difference in two values can be due to the fabrication processes which increases the density and lowers the mobility.

Apart from these materials, we have also used one more type of materials. The quantum dot device fabricated from this wafer was used to measure the electron

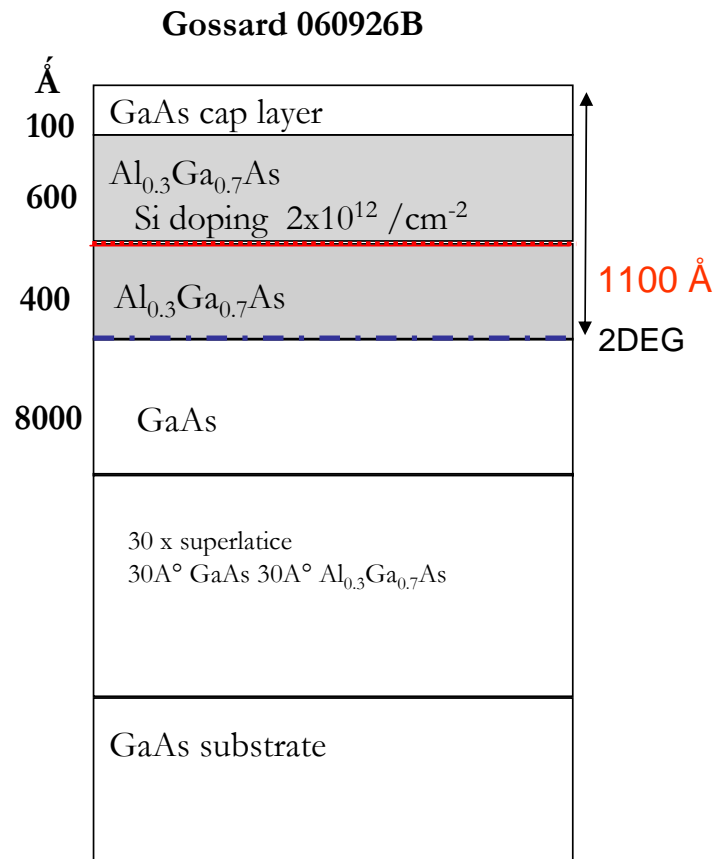


Figure 5.4: Complete growth-profile of the wafer Gossard 060926B used in this work.

temperature in the set up. The sample is grown by Prof. A.C. Gossard, UCSB, CA, USA.

Fig. 5.4 shows growth profile for sample Gossard 060926B With $\text{GaAs}/\text{Al}_{0.3}\text{Ga}_{0.7}\text{As}$, the 2DEG is formed at 110 nm at the interface of GaAs and $\text{Al}_{0.3}\text{Ga}_{0.7}\text{As}$. The density of this sample at 20K in dark is $n = 2.8 \times 10^{14} / \text{cm}^2$ and mobility is $\mu = 2.78 \times 10^5 \text{cm}^2 / \text{Vs}$.

5.3 Sample design

Clewin 3.2 is used for designing the sample geometry. We have used few different designs including Hall bar, double quantum dot, quantum wires, finger gated Hall bar etc. Here we will discuss the different designs in brief.

[I] Hall bar geometry

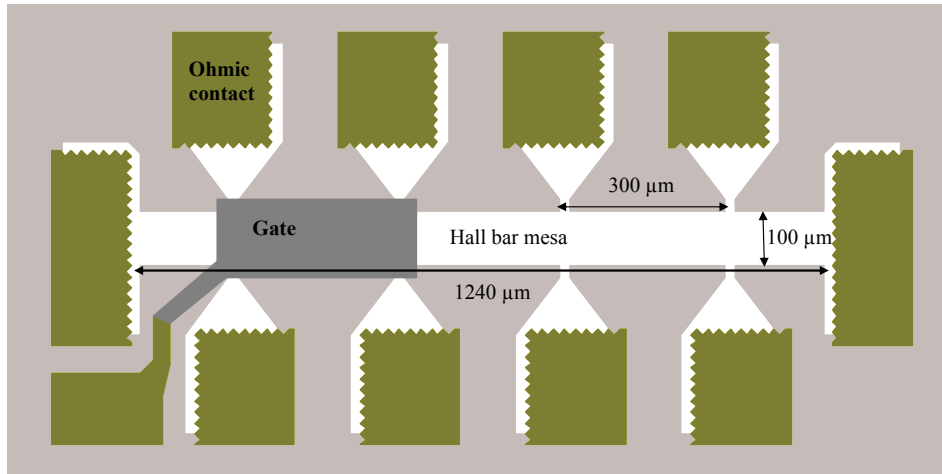


Figure 5.5: Hallbar design. The 2DEG is located at the white regions. The hallbar has a dimension of $1240 \times 100 \mu m^2$. The spacing between two adjacent ohmic contacts is $300 \mu m$. The width of Hall bar is $100 \mu m$. The measured ρ_{xx} between these two nearby contacts has to be divided by three to get ρ_{\square}

A Hall bar, as the name suggests is a device designed in such a way to see the magnetoresistance of the system. It has current and voltage probes to measure the longitudinal and transverse resistances.

Fig. 5.5 shows the geometry of the Hall bar which is used to characterize the wafer material and to measure the magnetoresistance data of the device. It consists of three different layers: Hall bar, ohmics and gates. The main Hall bar has a length of $1240 \mu m$ and a width of $100 \mu m$. Two adjacent ohmic contacts are $300 \mu m$ apart. From this it can easily be seen that there are three squares between two ohmic contacts to cover the Hall bar in between completely. This is important for later measurements of the 2DEG sheet resistance.

This is a very basic design of the Hall bar. It is modified according to the need of the experiment.

(II) Quantum dot design

We have fabricated few electron lateral quantum dots. These devices were mainly used in our set up to determine the electron temperature.

Fig. 5.6 shows the geometry of the quantum dot which is used to measure the

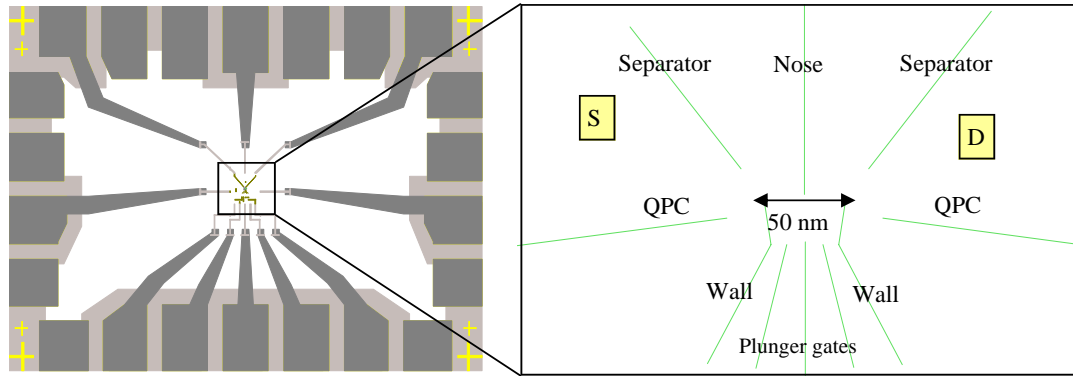


Figure 5.6: Quantum dot design. (a) Complete mesa dimension of $1520 \times 1140 \mu\text{m}^2$. The 2DEG is located at the white regions. (b) The yellow squares denote the source and drain. Quantum dot is formed by applying voltages to the fine gates.

electron temperature in the experimental set-up. It consists of four different parts, mesa, ohmics, ebeam gates and top gates. The mesa size is $1520 \times 1140 \mu\text{m}$. The quantum dot is defined in the middle of the mesa using electron beam lithography.

(III) Quantum wire design

The quantum wire conductance quantization was seen in our set up as a first step to characterize the quantum wires.

Fig. 5.7 shows the geometry of the quantum wire. It consists of four different parts, Hall bar mesa, ohmics, ebeam gates and top gates. The mesa size is $1210 \times 100 \mu\text{m}$. The width of Hall bar is $100 \mu\text{m}$. The spacing between the ohmic contacts is $300 \mu\text{m}$. The quantum wire gates are defined on the Hall bar mesa using electron beam lithography. We have designed wires of different lengths in the same sample, e.g. qpc with 0.5 nm , $5 \mu\text{m}$, $10 \mu\text{m}$ and $20 \mu\text{m}$ wires. We have two different widths of quantum wires designed $1.2 \mu\text{m}$ and $1.5 \mu\text{m}$, fabricated on different samples.

(IV) Finger gate design

The finger gate sample is used in the experiments of delocalization by disorder in layered system such as GaAs/AlGaAs. The finger gates are used to introduce the local potential barriers to the 2DEG.

Finger gates are fabricated on Hall bar mesa which has dimensions of $1210 \times 100 \mu\text{m}$. The spacing between adjacent finger gates is varied from $12 \mu\text{m} \pm 5 \mu\text{m}$, $23 \mu\text{m} \pm 5 \mu\text{m}$ and $46 \mu\text{m} \pm 5 \mu\text{m}$ in three different samples. The top gate geometries are discussed in detail in following section. Fig. 5.8 shows finger gate design for

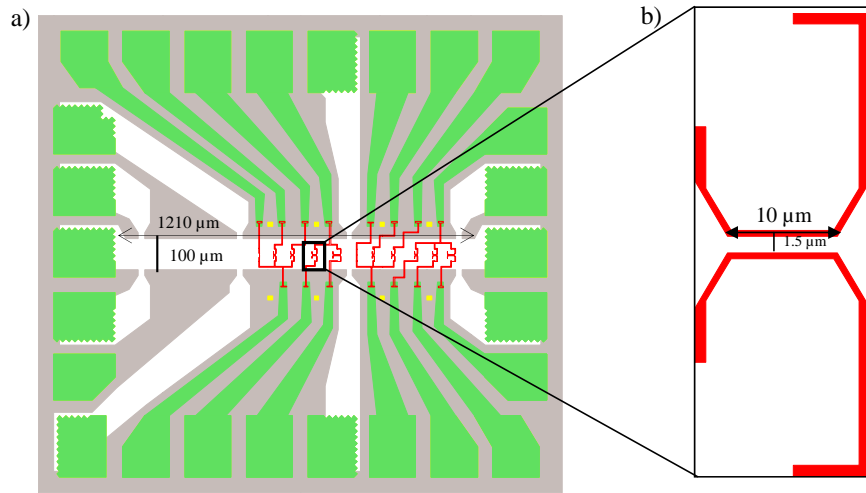


Figure 5.7: Quantum wire design. The Hall bar has a dimension of $1210 \times 100 \mu m^2$. (a) shows the complete device. The 2DEG is located at the white regions. (b) shows the $10 \mu m$ wide quantum wire gate.

average spacing of $23 \mu m$ without top gate. The length of individual finger gate is $115 \mu m$.

5.4 Fabrication Processes

Fabrication of micro- and nano- structures for mesoscopic transport experiments is a major technological challenge. Various processes are involved in the fabrication and every process is critical in its own terms.

During processing, its important to prevent the dust to hit the sample surface and destroy the process. Therefore processing is done in a clean room in which air is heavily filtered. Special care is taken to avoid the contamination by dust particles at every stage.

5.4.1 Cleaving and cleaning

The wafer material that we get is typically at least $3 \text{ cm} \times 3 \text{ cm}$ in dimension. We first need to cleave some part of it before starting the fabrication processes. GaAs samples are easy to cleave as GaAs is a crystal and the sample is cleaved along a crystal axis. To cleave a sample, we use fine tip diamond scribe and scratch at one edge of the wafer material depending on the sample size one plans to fabricate. Then from the same scribed side, force is applied to cleave the sample. The sample

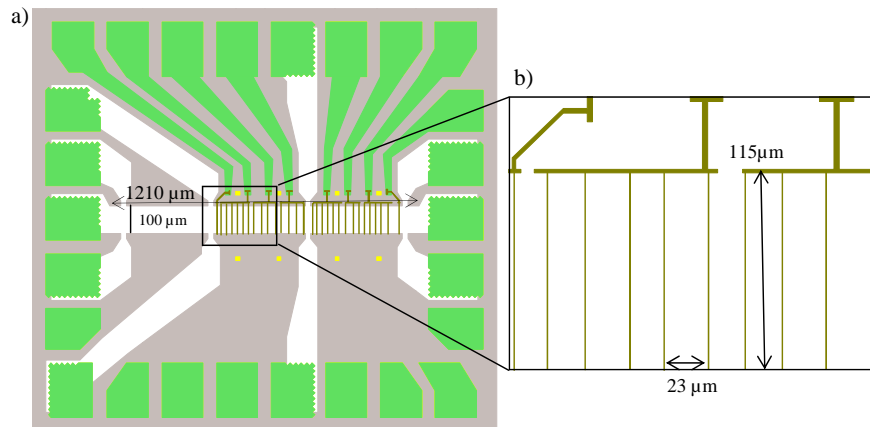


Figure 5.8: Finger gate design without top gate. The Hall bar has a dimension of $1210 \times 100 \mu m^2$. The average spacing between two adjacent finger gate $23 \mu m$. (a) shows the complete device. The 2DEG is located at the white regions. (b) shows detailed view of the finger gates.

is cut along the scratch due to crystal orientation. So it is important to scribe only once at a time so that the wafer is not full of scratches. In a way, cleaving the GaAs sample is easier compared with cleaving of Si wafer but at the same time delicate and critical.

For most of the wafers, gallium (Ga) glue is still sticking on the backside of the wafer. This glue is used to glue the substrate in MBE chamber. It is important to remove this glue as Ga can diffuse into. To remove this glue, first a protective layer is formed on the sample surface. In our case, we spun negative photoresist. Then the sample is dipped for a few seconds in 37% Hydrochloric acid (HCl). HCl reacts with the Ga glue and the Ga is removed. Sometimes a Q-tip is rubbed against the backside of the wafer to make sure that the Ga is completely removed. Then the sample is cleaned to remove the photoresist. And now it is ready for further fabrication steps.

The samples are cleaned with three different solvents, trichloroethylene (TCE), acetone and isopropanol in an ultra sound sonicator. This step is repeated before every lithography step. The sample after cleaning is blow dried using nitrogen gas to nullify the possibility of solvent residue on the sample.

5.4.2 Electron beam lithography(EBL)

The most important tool for fabrication of the devices presented in this thesis is Electron Beam Lithography (EBL). In essence it is the irradiation of a layer of an electron-sensitive polymer with a focused electron beam. The e-beam breaks the polymer chains in the resist and the exposed resist can then be selectively removed with a suitable solvent. The main advantages of EBL are high resolution and great flexibility. This general principle of EBL is depicted in Fig. 2.6. The first EBL machines were developed in the late 1960s. Shortly thereafter it was found that polymethyl methacrylate (PMMA) made an excellent e-beam resist [29]. The resist thickness that has to be used in the EBL process depends mainly on the thickness of the structure that is fabricated. The resist thickness is determined during spinning the resist on sample surface.

In general, resists with a lower molecular weight are more sensitive to exposure and dissolve faster in a developer. Therefore the contrast of a resist becomes higher as the molecular weight of the PMMA increases. To facilitate the spin coating of thin PMMA layers, the PMMA is diluted in solution, e.g. chlorobenzene or anisole.

In our lab we use Leo system for exposure and Raith for pattern generation. Typically we use an acceleration voltage of 20 keV. The higher voltage ensures to minimize the proximity effect due to backscattering of the electrons from the sample surface. The exposed/broken chain polymer can be easily dissolved in a 1:3 solution of methyl-isobutyl-ketone (MIBK) and isopropanol (IPA). In addition to this standard developer solution, we have added 1.3% by volume of the total solution methyl ethyl ketone (MEK). The addition of MEK improves the contrast of the structure. The developing process is stopped by rinsing the sample in pure IPA. The unexposed resist remains unaffected. After further processing (like metal deposition or wet etching of the surface) all remaining resist and any material on top of that resist is removed using acetone with mild sonication. After this process, called lift-off, we rinse in IPA and blow-dry the sample with nitrogen gas.

5.4.3 Optical photolithography

The photolithography is a method which brings a pattern into a deposited photoresistive layer through exposure of light. The light passes a mask with a certain pattern and then transforms this pattern into the photoresist. The resolution of the structure is around $1\mu m$ and depends on the wave length of the exposed light, the mask and the distance between mask and sample.

The thickness of the photoresist ma-N 415 (negative photoresist) at typical 4000 rpm is around $1.6\mu m$. The resist at the edges is thicker (edge beads) than on the

area of the sample, this unevenness may cause a bad resolution. If possible the edge beads are stripped away, before mounting the sample on the mask aligner. Stripping is possible in positive photoresist using a shadow mask to expose only the edges and then the sample is developed. The exposed part is removed and thus the edge bead. In negative photoresist case, one can strip the edges using a Q-tip. But this has to be very accurate. In this case, instead of removing the edge bead, we try to minimize them by spinning the resist at higher rpm. We use 600 rpm which gives the resist thickness of $1.3\mu m$. This reduces the edge bead height. Edge bead can be used as an indication of contact between the sample and the mask. Moving or growing of these Newtonian rings means there is still some space between the sample and the mask. After exposure, in case of negative photoresist, the exposed part stays as the crosslinked chains are formed because of UV light. The developer dissolves the unexposed polymer part. The sample is washed in DI water and then blow-dried with Nitrogen gas.

After deposition of the metal, the lift-off is done with NMP and then rinsed with DI water, followed by blow drying with N_2 . The procedure for optical lithography is shown in Fig. 5.9.

5.5 Etching

An important technique of transferring the resist pattern into the sample is etching. Patterned resists can be used as etch masks, provided the etchant is sufficiently selective. In this section we will describe reactive ion etching and wet chemical etching.

5.5.1 Reactive Ion Etching (RIE)

RIE etching is one method of dry etching. In RIE, the substrate is placed inside a reactor in which several gases are introduced. A plasma is struck in the gas mixture using an RF power source, breaking the gas molecules into ions. The Fig. 5.10 above shows a diagram of a common RIE setup. An RIE consists of two electrodes that create an electric field meant to accelerate ions toward the surface of the samples. The area labeled represents plasma that contains both positively and negatively charged ions in equal quantities. These ions are generated from the gas that is pumped into the chamber. The ions are accelerated towards, and react at, the surface of the material being etched, forming another gaseous material. This is known as the chemical part of reactive ion etching. There is also a physical part which is similar in nature to the sputtering deposition process. If the ions have high enough energy, they can knock atoms out of the material to be etched without

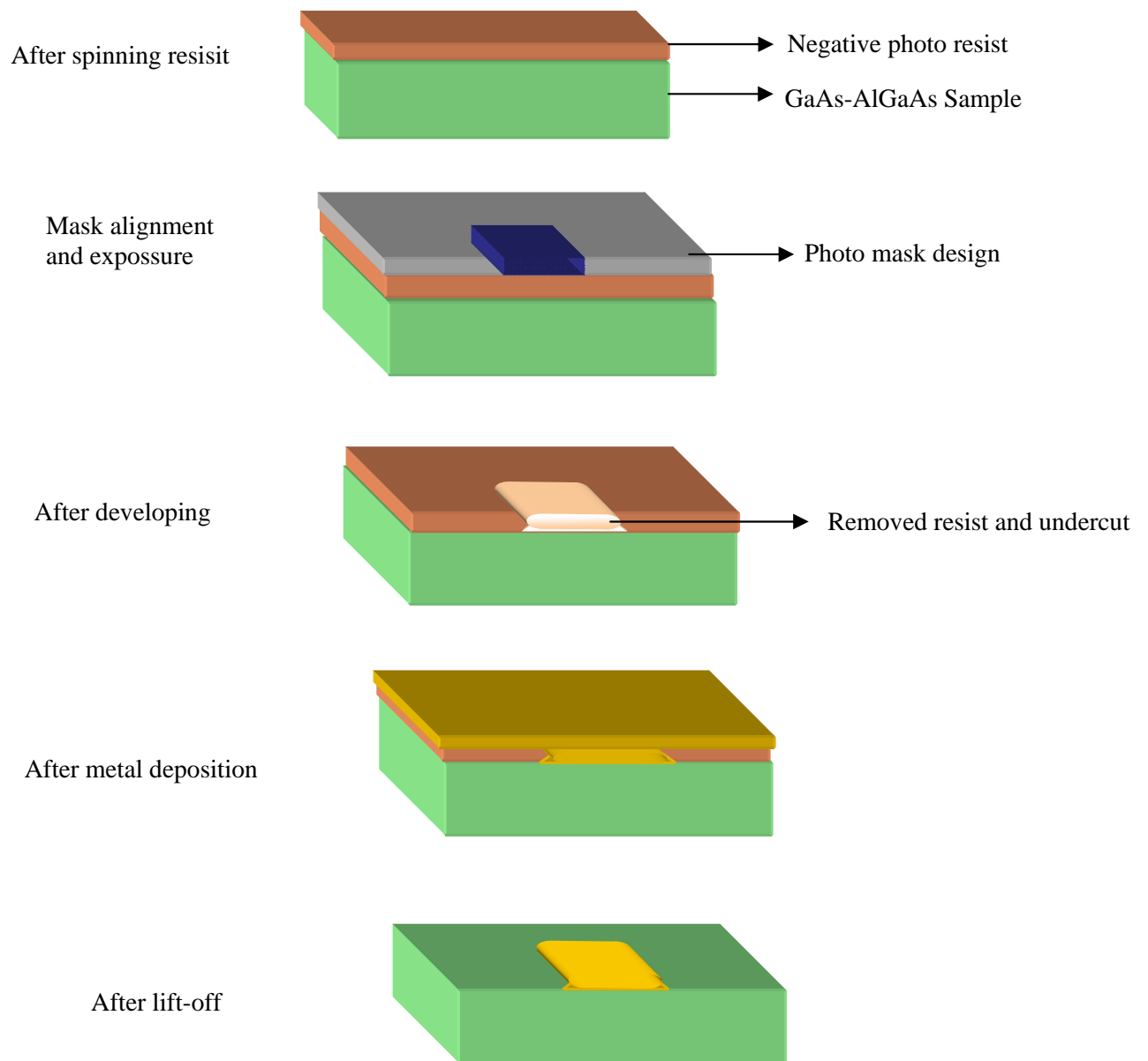


Figure 5.9: Optical Photolithography steps.

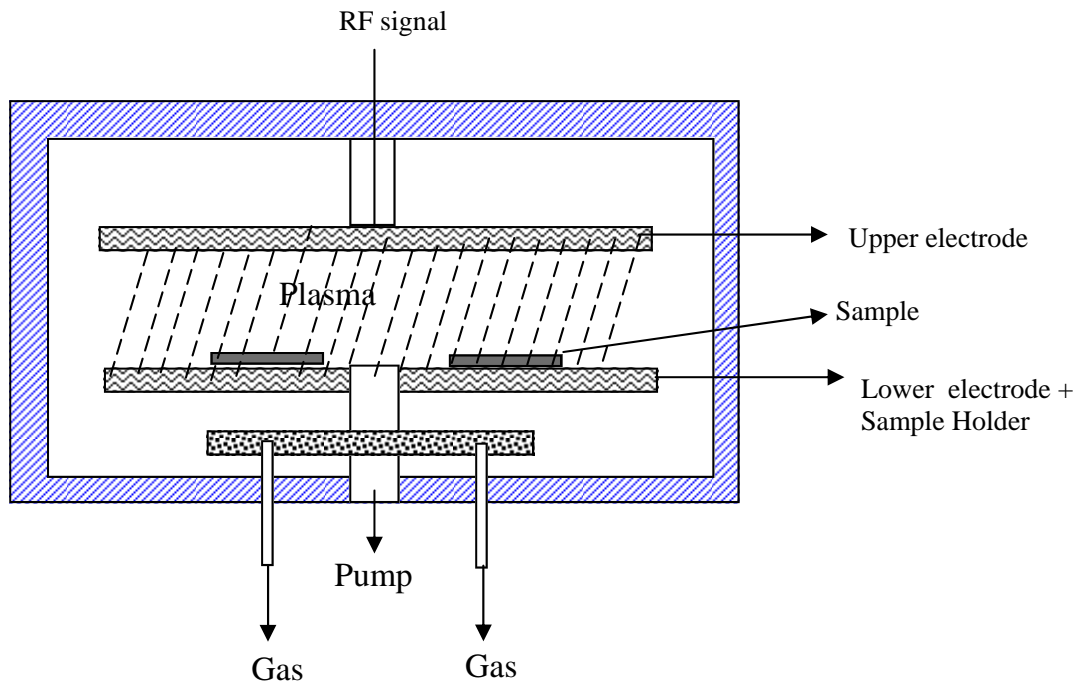


Figure 5.10: Reactive Ion Etching setup showing the RIE chamber [30]

a chemical reaction. It is a very complex task to develop dry etch processes that balance chemical and physical etching, since there are many parameters to adjust. By changing the balance it is possible to influence the anisotropy of the etching, since the chemical part is isotropic and the physical part highly anisotropic the combination can form sidewalls that have shapes from rounded to vertical.

In our devices, reactive ion etching with O_2 is done after ohmic photolithography, before depositing ohmic contact materials. After ebeam step for fine gates and finger gates, the sample is cleaned with RIE. The reactive oxygen plasma reacts with the resist residue in the developed region thus removing possible thin resist layer remained after developing. This makes better adhesion of the evaporated materials. It also improves the quality of ohmic contacts. The pressure in the RIE chamber is maintained below 10^{-6} .

5.5.2 Wet chemical etching

Wet chemical etching means immersing the sample in a suitable etchant solution. The etchants typically consists of mixture of an oxidizer (Hydrogen peroxide, H_2O_2) and an acid (Sulphuric acid, H_2SO_4) and water. H_2O_2 oxidizes the semiconductor, while the H_2SO_4 acid removes the freshly formed oxide. The oxidation

and etch rates depend on the etch composition, crystal direction as well as the temperature of the etchant solution.

5.6 Thin film deposition

The deposition of material films on the semiconductor surface is termed as thin film deposition. This is done by evaporation of the material in a vacuum chamber. The materials are molten in a crucible or boat made up of carbon and tungsten respectively. The material is molten either by heating the boat in case of thermal evaporation or by focusing an electron beam in case of electron beam evaporation. At sufficiently high temperature, the vapor pressure of the material is so high that a film is grown at the exposed surfaces with a rate of the order of nanometer per second. The film thickness is monitored by an oscillating quartz plate. As the material gets deposited on the quartz, its resonance frequency gets smaller. This effect can be calibrated, and the film thickness can be measured with high accuracy. For lift-off process, the film thickness should be smaller than the resist thickness.

5.7 Fabrication steps

The fabrication of devices used in this thesis required different steps. Each of these steps involves the writing of a specifically designed pattern using EBL and optical photolithography as described in the previous section. Fig. 5.11 describes briefly the different fabrication steps for finger gate sample.

5.7.1 Mesa photolithography and etching

The first step is the patterning a mesa by defining the pattern with negative photo resist (maN-415) and photolithography with i-line 415 nm. The typical exposure time is 14 seconds. The sample is then developed in developer (ma-D 377XP, metal ion free) and rinsed in water to stop developing process. The sample is checked under optical microscope to check whether it needs further developing.

Etching the heterostructure wafer is necessary to electrically isolate conducting regions of the device. This isolation is in principle achieved when all the Si donors in the n-AlGaAs layer are removed, since they provide the electrons to form the 2DEG. The mesa height or the amount of etching depends on samples. We had simulated our sample in Matlab before etching. This gives minimum mesa height to separate the devices. Depending on the simulation we etched our samples 20% more than simulated mesa height in order to make sure that the donor layers are

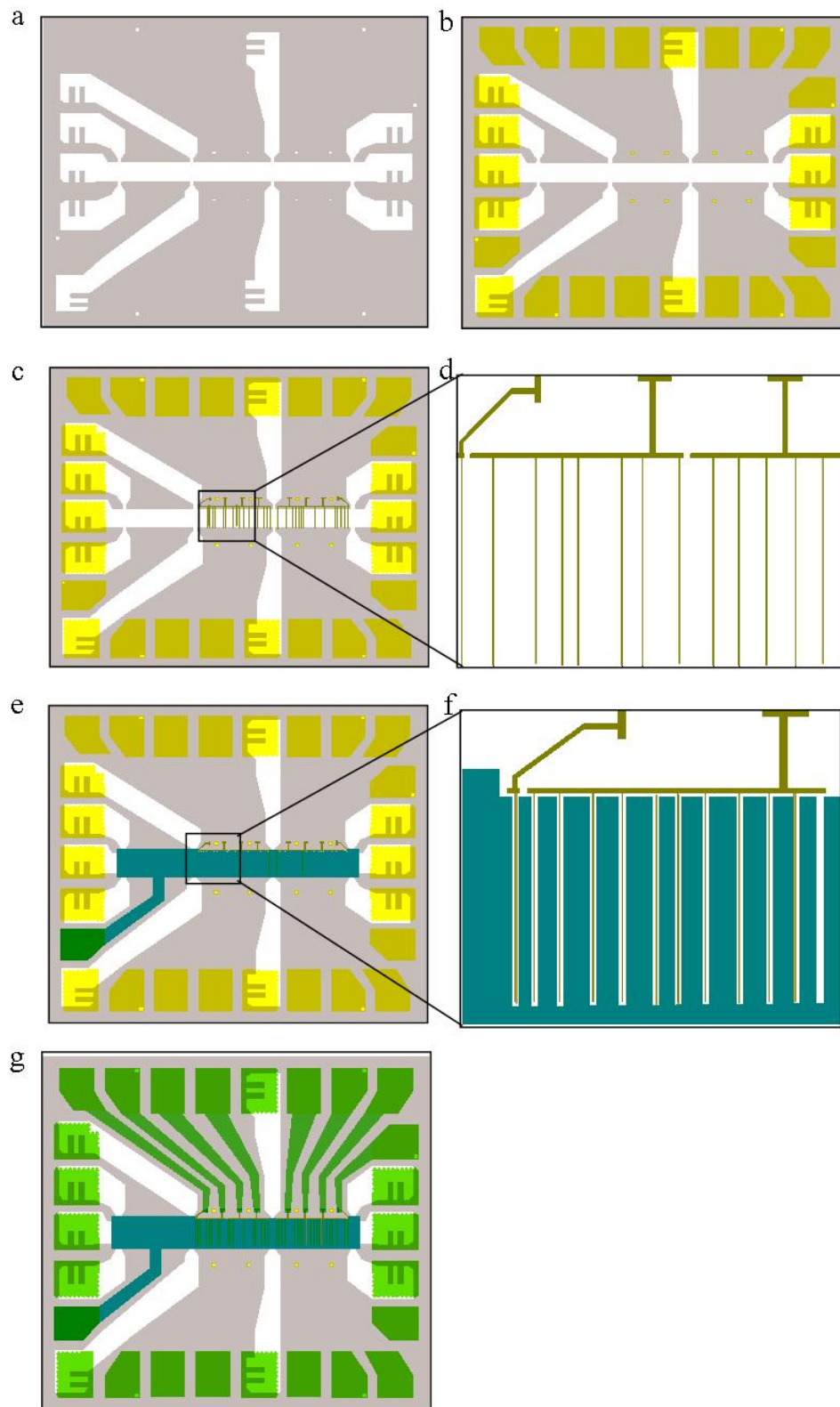


Figure 5.11: Sample fabrication steps. (a) Mesa:- After photolithography and etching, (b) Ohmic contact pads on the mesa, (c) Ebeam lithography step for finger gates, (d) Detailed view of finger gates after ebeam, (e) Ebeam exposure for top gate (f) Detailed view of top gate and finger gate, (g) Finished device with large gates

removed and devices are separated.

In practice we always etched below the doping layer. The etchant is $H_2SO_4 : H_2O_2 : H_2O$, a mixture of sulphuric acid, hydrogen peroxide and DI water, with a composition 2 : 16 : 480. This results in an etching rate of approximately 2 nm/s. The etching process is stopped by rinsing the sample in DI water. Finally the sample is blow dried. The Pfeiffer 7.28.08.02 and Pfeiffer 8.29.08.1 have 2DEGs well below the donor layer and practically it is not possible to etch 410 nm deep, we have etched these two wafers till donor layer $\approx 90nm$. This separates the two devices. For Gossard wafer, the mesa is etched till the 2DEG i.e. 110 nm deep.

5.7.2 Ohmic contacts

The purpose of the Ohmic contacts is to give a connection to the underlying 2-dimensional electron gas (2DEG). Good Ohmic contacts should have linear current-voltage (IV) dependence and a contact resistance as small as possible. An Ohmic contact is defined as a metal-semiconductor contact with a small resistance compared to the rest of the sample. Material is deposited on top of the sample and diffuses or alloys into the structure during an annealing step. Control over the process is only possible via temperature and annealing time.

Electrical contacts to the 2DEG are realized by thermal annealing of surface electrodes in the shape of bonding pads. These electrodes have an area of 150 by 200 μm^2 and are located at specific places near the edge of the mesa (Fig. 5.12a). To avoid edge currents around an contact, it is made sure that the edge of the ohmic contact intersects the mesa edge at several places. In our design we have used meanders at the edges of ohmic to ensure better contact.

Material deposition is done with ebeam evaporator. We deposit 375 nm of Au and Ge with a ratio $Ge : Au :: 125 : 250$. Ni with a thickness of 5 nm is deposited first as a sticking layer, followed by Ge and then Au. Then again 20 nm of Ni, followed by 50 nm of Au. The order of deposition can be summarized as $Ni : Ge : Au : NI : Au :: 5 : 125 : 250 : 20 : 50$. During evaporation, the sample holder is cooled with LN_2 . This cooling ensures better deposition of materials and also resist is not heated due to deposition of material vapors. The heating of resist may lead to glass transition if the resist and this transition will make it impossible to lift of the sample. The chamber pressure is maintained below 10^{-6} mbar. After evaporation the resist is removed in NMP and then the sample is rinsed in DI water. A typical ohmic contact before annealing is shown in Fig. 5.12a.

The melting temperature of the eutectic AuGe is $370^\circ C$. For the annealing we use

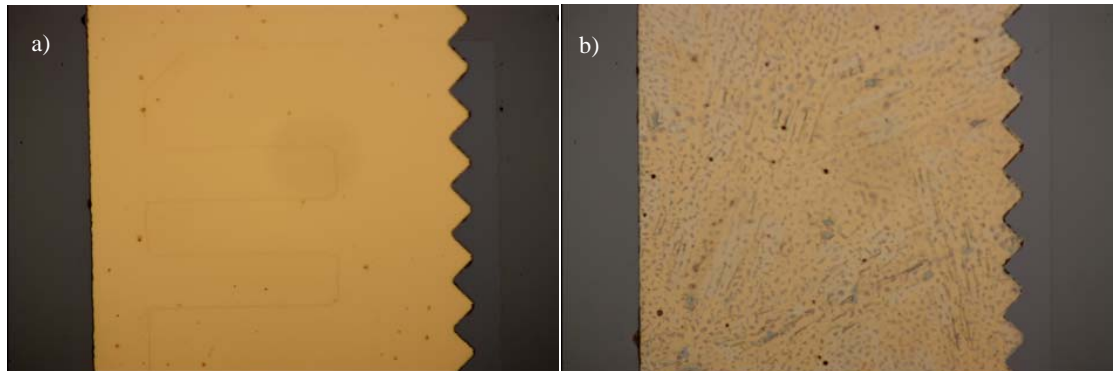


Figure 5.12: Ohmic contact (a) before annealing, (b) after annealing

a quartz plate oven at 480°C with a mixture of nitrogen and hydrogen, $\text{N}_2 + \text{H}_2$, known as forming gas, flow to prevent oxidation. During the annealing the electrodes melt and diffuse into the heterostructure wafer. The metal-rich phases penetrate into the wafer but do not actually reach the 2DEG. The Ge atoms form a highly doped region in between the diffused metal and the 2DEG, resulting in linear IV characteristics for the contact. At 4.2 K the contact resistance is well below 300Ω . A typical ohmic contact after annealing is shown in Fig. 5.12b.

5.7.3 Fine gates and Finger Gates

This step is the most critical step in the sample fabrication, since in this step the gates defining the quantum dot, quantum wire and the local disorder are made. For quantum dot design, the dot is aligned in the center of the mesa. For quantum wire and finger gates, the Hall bar is divided in three different sections. First region is only top gate region. This region is used to characterize the basic wafer properties such as density and mobility. The other two regions are called finger gate region I and finger gate region II. The average spacing between the finger gates is determined by mean free path parameters of the wafer. For our experiments, we designed three different average finger gate spacings, namely, $12\mu\text{m}$, $23\mu\text{m}$, $46\mu\text{m}$. The variation is $\pm 5\%$.

The structures are defined on the Hall bar as shown in Fig. 5.11c and Fig. 5.11d shows the detailed view of the sample for $12\mu\text{m}$ spacing. The pattern is written with a larger acceleration voltage for the electrons of 20 keV to reduce proximity effects. 5 nm Ti is deposited for 75 nm of Au as sticking layer. In this step the lift-off has to be done more carefully, typically the sample is left in warm (50°C) acetone

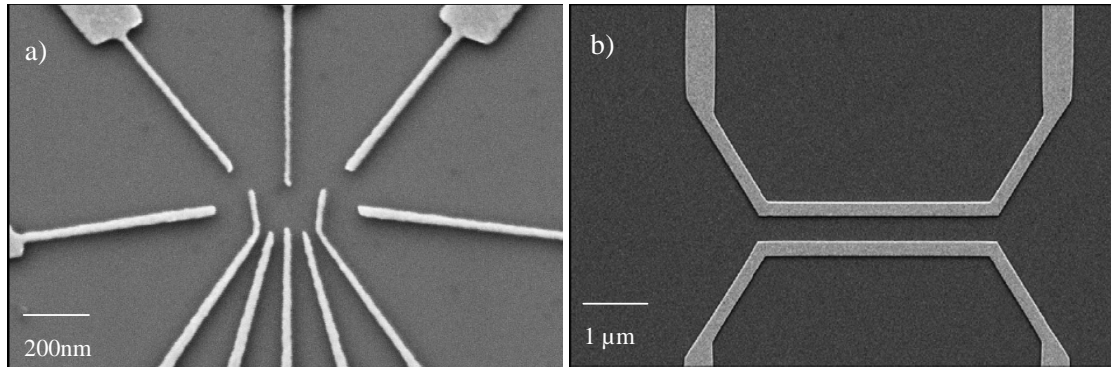


Figure 5.13: SEM micrograph (a) quantum dot gates (b) quantum wire gates

for several minutes. The sample in acetone is checked under optical microscope to make sure that the lift off is working. The sample is kept in ultrasound sonicator on low power for few seconds to make sure that the metal in-between the gates is lifted off. Fig.5.13 shows micrograph for quantum dot fine gates, quantum wire contact and finger gates.

5.7.4 Top gate

We have used two different designs for the top gate which is acting as a bulk disorder in our experiments. In the first generation of finger gate samples, we have used insulating layer of SiO_2 for separating the finger gates and top gate. The fabrication of this layer and the top gate is done in single optical lithography step. The thickness of SiO_2 layer deposited depends on the thickness of Ti-Au layer deposited for finger gates. In our sample we deposited ≈ 150 nm of SiO_2 for 80 nm thick finger gates of Ti-Au. Fig.5.14 shows the schematic of such a device.

For second generation of these samples, the design for top gate is changed. Now the top gate is not above the finger gate but the top gate is split between finger gates. This can be seen in fig.5.11 e and the detailed view in 5.11f. The fabrication of this gate is done in the step with finger gates. The thickness of this gate is 125nm with 5 nm of Ti as sticking layer and 120 nm of Au. Fig.5.15 shows the schematic for such a device. Fig. 5.16 shows SEM micrograph of such a device.

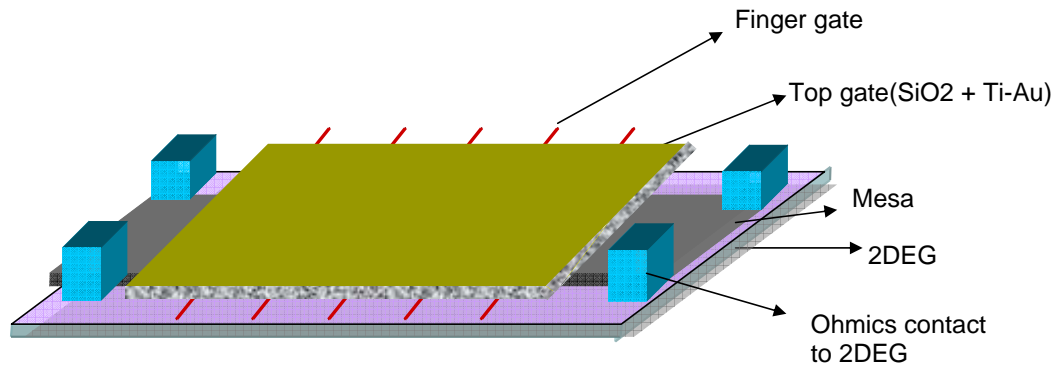


Figure 5.14: Finger gate with top gate + SiO_2 . + SiO_2 acts as a insulator between the finger gates and top gate

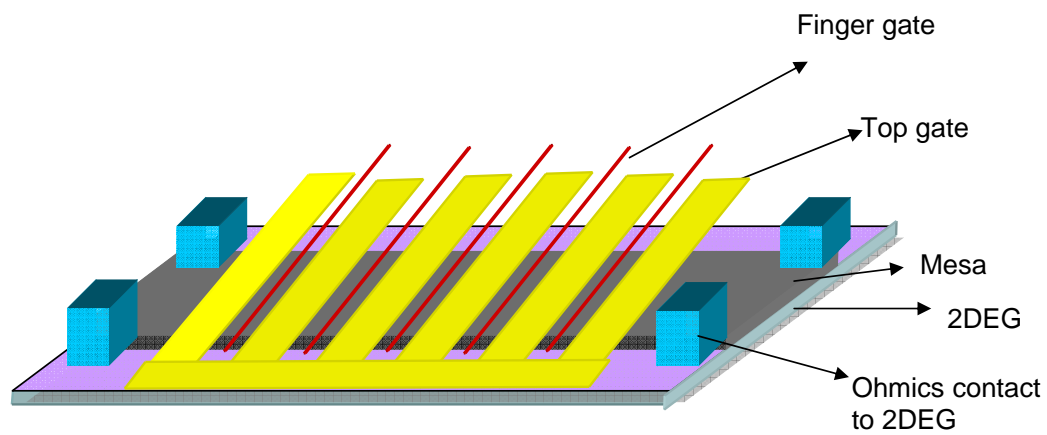


Figure 5.15: Finger gates sample design with intercalated top gate and finger gates. The distance between finger gate and portion of top gate is $1.3\mu m$

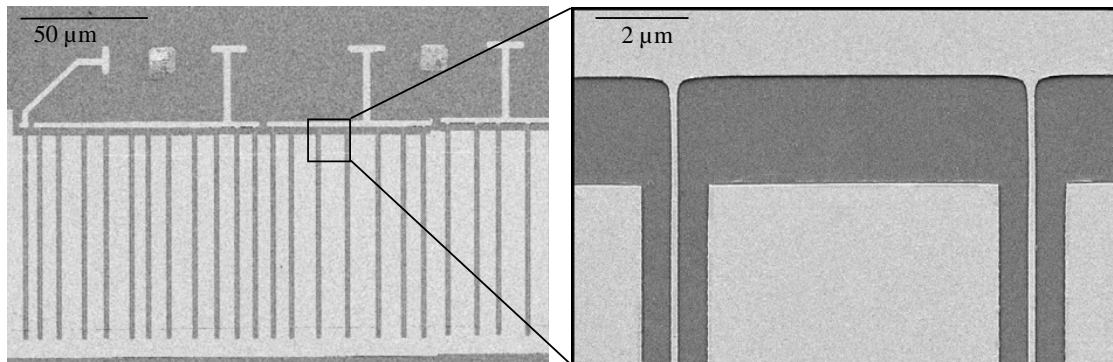


Figure 5.16: SEM micrograph of a finger gate sample

5.7.5 Large gates

The fabrication of the large gates is necessary to connect the fine gates to large bonding pads on the outside of the mesa (Fig. 5.11g). We deposit a thick layer (typically 170 nm) of Au with a Ti as sticking layer. After the processing is finished, the sample is glued onto a chip carrier with PMMA and bonding wires are attached to the bonding pads. the optical image of a finished finger gate sample can be seen in Fig.5.17

The samples are then bonded with Au-wire.

5.8 Wire Bonding

After successful fabrication steps, the sample is glue on a chip carrier with PMMA. The last step is to connect the wires to the ohmic contacts and gate electrodes. Here the wire is pressed against the bond pad and rubbed across it with an ultrasonic frequency. The friction force is sufficient to locally melt the materials and alloy is formed that holds the wire in place. After the second bond, the wire is pulled and breaks at the weakest point.

Very special care must be taken during bonding. First of all, the bonding machine, especially the sample chuck and the bonding tip, as well as the operator and the tools (e.g. tweezers) were grounded.

The sample is now ready to mount in the dip stick for 4.2K measurement or to mount in the cryostat for further measurements.

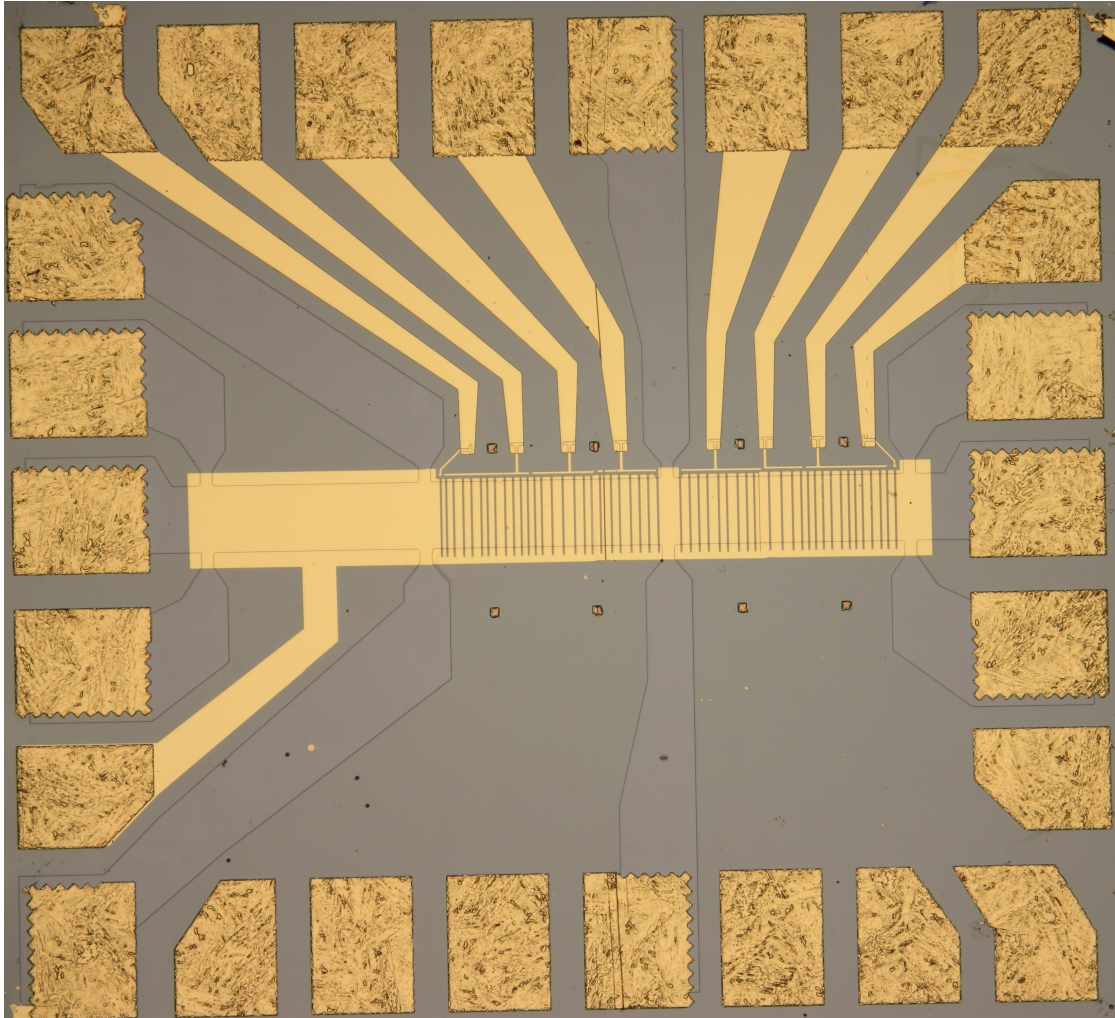


Figure 5.17: Finger Gate sample

6 Quasi–particle properties of 2DEG

6.1 Introduction

In a simple picture, the electrons are considered to be free and the system is considered to be non-interacting. The interaction between the electrons is neglected and every electron is characterized with its own charge, spin, momentum, mass and energy. The energy of the system is then sum of energy of individual particle. This is an ideal picture modeled as Fermi gas.[31]

Consider such a non–interacting system of electrons. If the Coulomb interaction is tuned between the electrons, the energy of the one electron level will be modified. This entity of interacting particles is called quasiparticle. For a quasiparticle the charge and spin will be the same as for elementary electron. The quasiparticle will be an Fermion. Since the interaction is tuned, the mass of the quasiparticle will not be the sum of mass of all the interacting particles. Due to Coulomb interaction, the mass will be modified as the effective mass of the electrons. Due to the electron–electron interactions, scattering mechanisms are also introduced in this picture. The scattering can be a long range scattering or short range scattering depending on the scattering center.

In this chapter, we have described the characterization of quasiparticle properties. This includes the effective mass (m^*), transport time (τ_t) and quantum scattering time (τ_q) and the Landé g –factor. In the first section we will see the basic properties of our heterostructure wafers. In the next section we will discuss the measurements and results of effective mass of electrons. The extraction of quantum scattering time is discussed, followed by extraction of g –factor.

6.2 Density and mobility of the heterostructure

The few basic properties of the wafer material includes the electron density or carrier concentration in the 2DEG and mobility, which is one of the parameters of the clean samples. There are various ways to find the density and mobility of the sample. One of the widely used method is low field Hall voltage measurement. The longitudinal and transverse voltages are measured while changing the magnetic field. The electron density is obtained from the Hall resistance (R_H) or the transverse resistance per unit magnetic field or Hall slope. The density in terms of the Hall slope is determined by

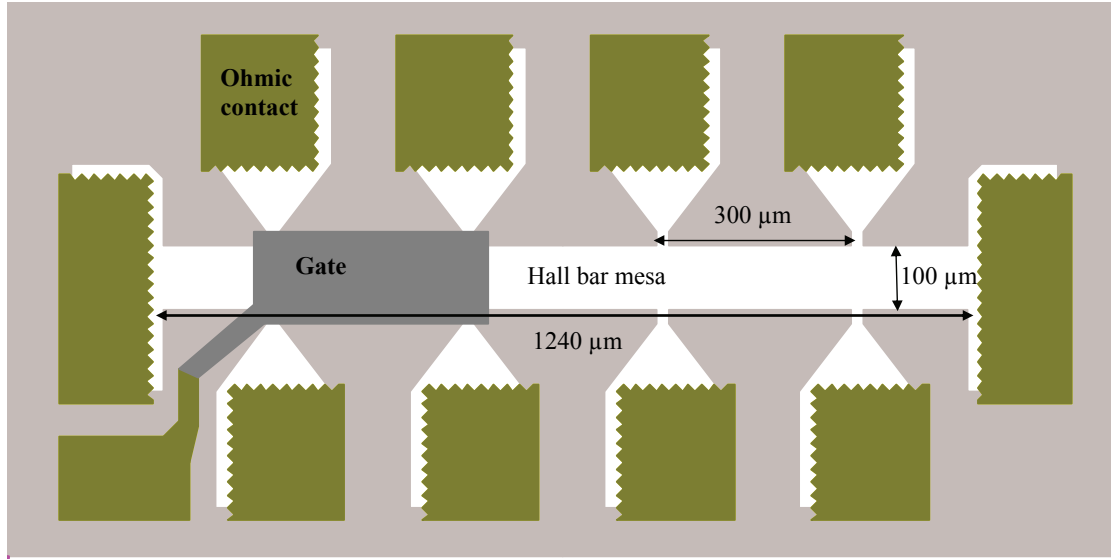


Figure 6.1: Hall bar geometry

$$n = \frac{1}{R_H e} \quad (6.1)$$

where n is the density, e is the electric charge.

The mobility μ is obtained from the density n and the resistivity per square ρ_{\square} in the sample. The mobility is given as,

$$\mu = \frac{1}{ne\rho_{\square}} \quad (6.2)$$

These equations are derived from the Drude model discussed in section 2.3.1

Typically a Hall bar geometry is used in our sample. The sample design is shown in Fig. 6.1. The distance between two adjacent ohmic probes is $300 \mu m$ and the width of the Hall bar is $100 \mu m$. To obtain the resistance per square we take 3 squares.

Fig. 6.2 shows such a low field magnetoresistance data used to determine the density and mobility of the Pfeiffer 7.28.08.2 sample. The current used is 9.1 nA with lock-in frequency 175 Hz and time constant of 300 ms with Q factor of 10 . The current is determined from few current tests and the optimum current is chosen where noise is less with high signal and is not heating the electrons.

In Fig. 6.2, the blue trace is longitudinal resistance (R_{xx}) on the left axis as a function of perpendicular magnetic field, the right axis shows the transverse resis-

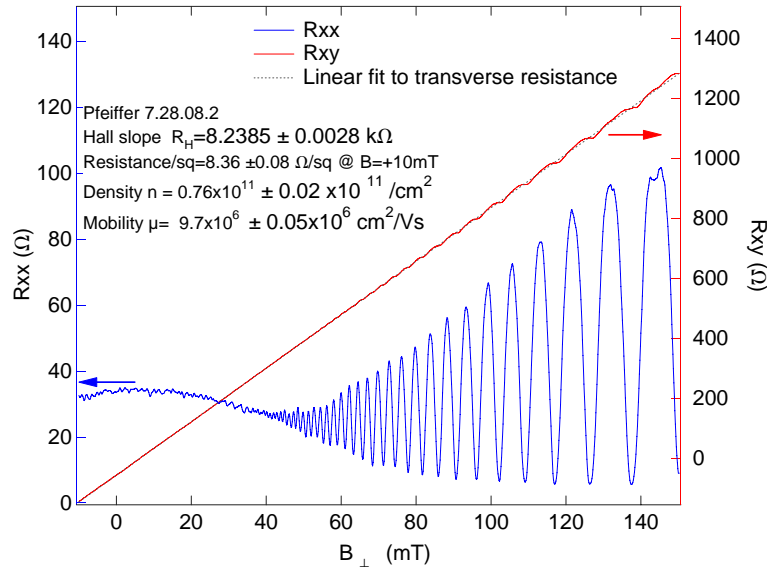


Figure 6.2: Low field magnetoresistance data used to determine the density (*left axis*) and mobility (*right axis*) of sample Pfeiffer 7.28.08.2. The Hall slope is $8.2385 \pm 0.0028 k\Omega/T$

tance, R_{xy} , black trace. The dashed gray line is the linear fit for the R_{xy} in the low field. The density and mobility of this sample measured using the Hall slope is $0.76 \times 10^{11} \pm 0.028 \times 10^{11}/cm^2$ with Hall slope R_H $8.2385 \pm 0.0028 k\Omega/T$ and $9.7 \times 10^6 \pm 0.05 \times 10^6 cm^2/Vs$ respectively with the 2DEG resistance at +10 mT, ρ_{\square} is $8.36 \pm 0.08 \Omega/\square$. It is observed that in GaAs/AlGaAs samples, the resistivity of sample is high at zero magnetic field due to localization effect compared to some small magnetic field.

We also did temperature variation measurement of the density and the mobility in Pfeiffer 7.28.08.2 from 4.2 K to the base temperature 24 mK on gated and not gated sample. Temperature variation of the wafer for both non-gated and gated sample can be seen in Fig. 6.3

Fig.6.3 shows the density and mobility as a function of temperature. We have tested two samples on same wafer Pfeiffer 7.28.08.02, one of the sample is gated Hall bar and other sample is not gated Hall bar. The graph shows the density for gated sample with red filled circles and the not gated sample density is shown by filled blue circle. The temperature varies from 5K to almost 20 mK. The density for not-gated and non gated samples is unaffected by the temperature variation. The density for gated Hall bar is $0.7 \times 10^{11}/cm^2$ and density for not gated sample

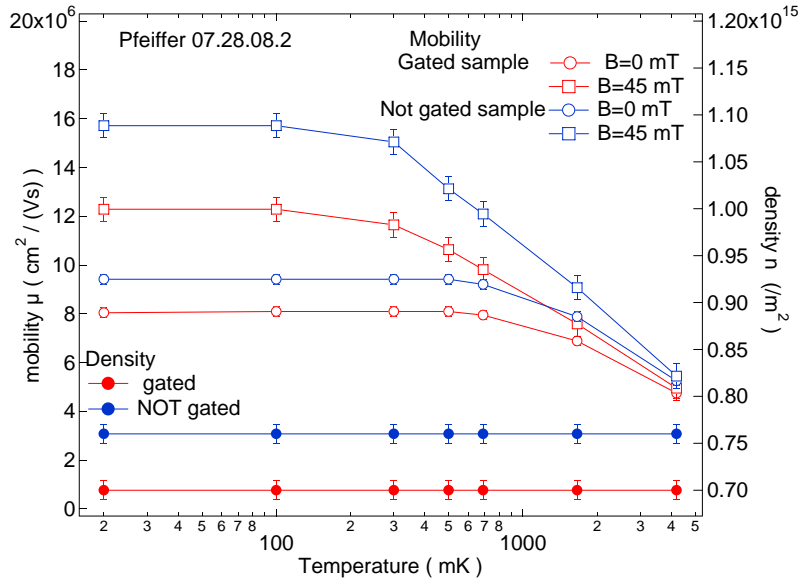


Figure 6.3: Variation of density (*right axis*) and mobility (*left axis*) in a gated and non gated sample as a function of temperature in Pfeiffer 7.28.08.2.

is $0.76 \times 10^{11} / \text{cm}^2$. The error bar in both data sets is obtained from Rxy linear fit error.

The mobility is obtained at in the absence and presence of small magnetic field. due to localization effect in high mobility samples, the resistance is higher at zero magnetic field. Hence mobility is determined at zero magnetic field and in presence of very small magnetic field of 45 mT. The gated sample mobility is shown by empty red squares at zero magnetic field and with empty red circles at 45 mT field. The non gated sample mobility is shown in blue squares for zero magnetic field and with blue circles for 45 mT magnetic field. The variation of mobility as a function of temperature can be seen till around 500 mK. For lower temperatures the mobility saturates. This can be seen for both gated and non gated samples, with or without perpendicular magnetic field. The mobility of the not-gated samples is higher than gated samples. At 5K, the mobility is $5 \times 10^6 \text{ cm}^2/\text{Vs}$ to $6 \times 10^6 \text{ cm}^2/\text{Vs}$ for all both samples with or without magnetic field. The difference starts to see as the temperature is lowered. For the non gated sample, the mobility is close to $16 \times 10^6 \text{ cm}^2/\text{Vs}$ at 45 mT magnetic field and $9.5 \times 10^6 \text{ cm}^2/\text{Vs}$ at zero magnetic field. for gated sample, the mobility at zero magnetic field goes from $5 \times 10^6 \text{ cm}^2/\text{Vs}$ to $8 \times 10^6 \text{ cm}^2/\text{Vs}$, and at 45 mT, the mobility goes from $5 \times 10^6 \text{ cm}^2/\text{Vs}$ to around $12 \times 10^6 \text{ cm}^2/\text{Vs}$. The strain induced by the top gate layer of Ti-Au on the GaAs

lattice, increases scattering and hence the mobility is lower in gated sample. The variation of mobility agrees well with [32].

In a similar manner the density and mobility for other wafers is obtained. For Pfeiffer 08.29.08.1, the density is found to be $0.71 \times 10^{11}/\text{cm}^2 \pm 0.02 \times 10^{11}$ with Hall slope of $8.815 \times 10^3 \pm 0.003 \times 10^3 \Omega/T$. The mobility is $10.8 \times 10^6 \text{cm}^2 \pm 0.3 \times 10^6 \text{cm}^2/Vs$ with resistance of 2DEG (R_{2DEG}) $8.16 \Omega/\square$. For Pfeiffer 9.12.05.2 sample we get density of $0.47 \times 10^{11} \pm 0.06 \times 10^{11}/\text{cm}^2$ and mobility of $2.2 \times 10^6 \pm 0.2 \times 10^6 \text{cm}^2/Vs$ with Hall slope of $13.2 \pm 1 \text{k}\Omega/T$ and Resistance of 2DEG $59.7 \Omega/\square \pm 0.3 \Omega/\square$ at zero magnetic field. This sample needs LED illumination to show the conductance. The LED is flashed for 1 min. with current through LED of 5 mA. Table 6.1 summarizes the density and mobility for wafers Pfeiffer 9.12.05.2, Pfeiffer 7.28.08.2 and Pfeiffer 08.29.08.1.

Sample	R_H $\text{k}\Omega/T$	R_{2DEG} Ω/\square	Density n $\times 10^{11}/\text{cm}^2$	Mobility μ $\times 10^6 \text{cm}^2/Vs$
Pfeiffer 9.12.05.2	13.2 ± 1	59.7	0.47 ± 0.06	2.2 ± 0.2
Pfeiffer 7.28.08.2	8.24 ± 0.003	8.36	0.76 ± 0.02	9.7 ± 0.05
Pfeiffer 08.29.08.1	8.815 ± 0.003	8.16	0.71 ± 0.02	10.8 ± 0.3

Table 6.1: Density , mobility derived from Hall resistance R_H for samples Pfeiffer 9.12.05.2 (after LED illumination, details in the text), Pfeiffer 7.28.08.2 and Pfeiffer 08.29.08.1 at 24 mK.

The negative magnetoresistance can be seen in the longitudinal resistance or Shubnikov de-Haas (SdH) oscillations in the low field regime, blue trace in Fig.6.2 . According to M.A. Paalanen et al [33] and theories predicted in [34],[35], this negative magnetoresistance is due to the electron interaction effect or the localization effect. In low mobility samples, this effect is seen in the limit $\omega_c \tau_t > 1$, where ω_c is cyclotron frequency and τ_t is transport scattering time. In high mobility samples, this limit is already reached at sufficiently low fields. This interaction is dominant in low field regime in low fields.

For gated samples, the density mobility parameters are also obtained as a function of gate voltage in presence of a small magnetic field. This is also based on Hall effect. This method also gives information about the depth of the carriers from the sample surface.

In this method, a fixed small perpendicular field is applied. The field is chosen

such that the system is still in classical Hall effect regime, before the onset of the Shubnikov de-Haas oscillations. The gate voltage is swept up to the depletion of the 2DEG. The magnetic field is now inverted, kept constant and the again the gate sweep is repeated till the depletion. The transverse (V_{xy}) and longitudinal voltages (V_{xx}) are probed in the Hall bar. The density is found from the difference in the transverse voltages and the mobility is determined from the longitudinal resistance. In principle, this can be done at either positive or negative magnetic field, but measuring V_{xy} and V_{xx} at $\pm B$ field nullifies the offset in the field. Usually the magnetic field is very small but still can make a difference in the density and mobility measurement.

If V_{xy} and $-V_{xy}$ are the Hall voltages for positive (+B) and negative fields (-B) and with an offset in the magnetic field (ΔB) and V_{xx} is the longitudinal voltage for both the fields with current I, the density and mobility are given as,

$$n = \frac{\frac{(B+\Delta B)-(-B+\Delta B)}{2} \frac{I_1+I_2}{2}}{e \frac{(V_{xy})-(-V_{xy})}{2}} \quad (6.3)$$

$$\mu = \frac{3 \times \frac{I_1+I_2}{2}}{n e \frac{(V_{xx}+V_{xx})}{2}} \quad (6.4)$$

Here e is the electric charge. In Eq. (6.4), 3 is the number of squares used to obtain the 2DEG resistance per square. Fig. 6.4 shows the corresponding traces for voltages, current, density and mobility.

With this method, density and mobility for Pfeiffer 8.29.08.01 sample we get is, $0.7 \times 10^{11}/cm^2$ and $11 \times 10^6 cm^2/Vs$ respectively. If the values from two different methods are compared, we see that the values for density and mobility agree with each other.

The density and mobility of Pfeiffer 07.28.09.02 is $0.7 \times 10^{11}/cm^2$ and $9.5 \times 10^6 cm^2/Vs$. The values from two different methods agrees very well with each other. The density and mobility variation for this sample is shown in Fig. 6.5

For Pfeiffer 9.12.05.2 sample, we can not determine the density and mobility with gate variation method. This sample needed the LED illumination to show conductance and with the top gate it did not work to illuminate the whole Hall bar since the LED light was not transmitted through the Ti-Au top gate.

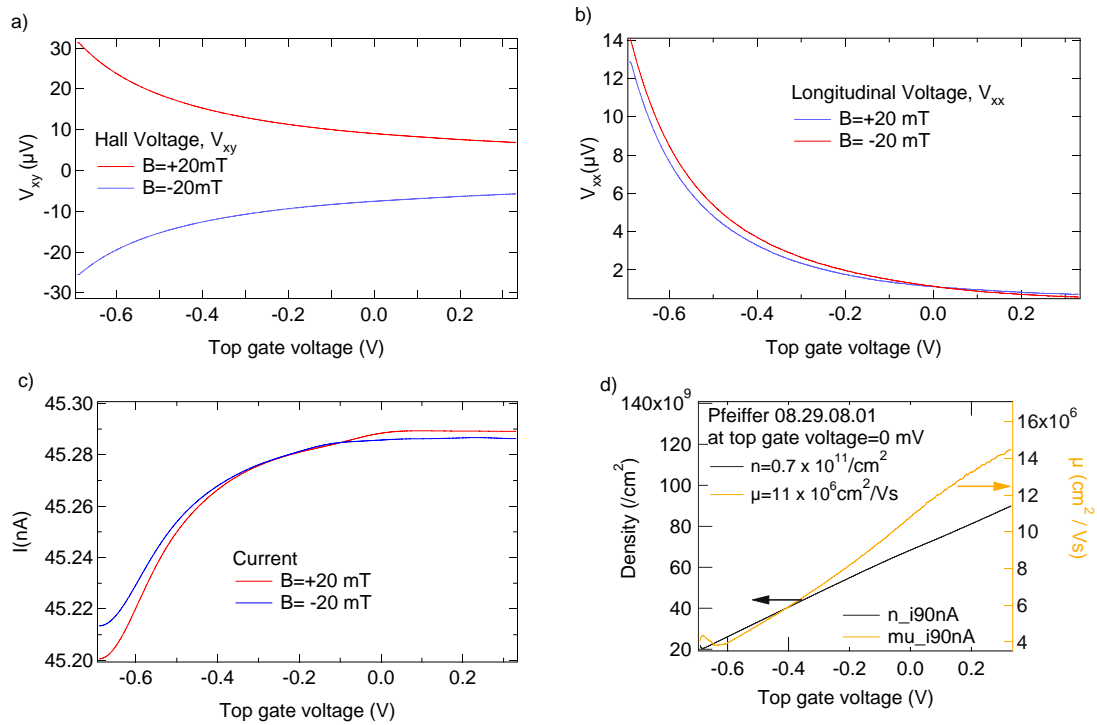


Figure 6.4: Variation of density (n) and mobility (μ) with gate voltage in sample from Pfeiffer 8.29.08.01. (a) shows the Hall voltage for both positive and negative fields. (b) show the longitudinal voltage and (c) shows current for bot positive and negative fields. From (d) we get the density and mobility at zero gate voltage. The data is taken at $B=\pm 20\text{mT}$ and base temperature 24mK

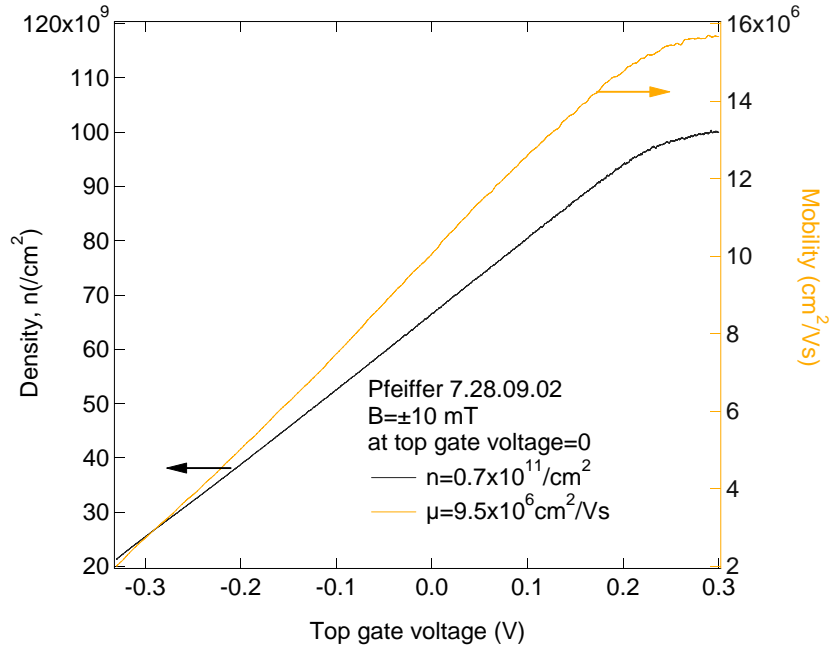


Figure 6.5: Variation of density (n) and mobility (μ) with gate voltage in Pfeiffer 7.28.09.02. The data is taken at $B=\pm 10$ mT and base temperature $T=24$ mK

The depth of the 2DEG can be determined from the gate voltage variation data of the density. Consider the system as a parallel plate capacitor with separation d , and a medium with permeability ϵ . The capacitance per unit area for such a capacitor is given as,

$$C = \frac{\epsilon\epsilon_0}{d} \quad (6.5)$$

The capacitance per unit area with charge Q and voltage V can be written as,

$$C = \frac{Q}{V} \quad (6.6)$$

The slope of density with respect to gate voltage is $\frac{dn}{dV}$, which simply means the variation of charge carriers in the capacitor with respect to the voltage applied. Thus the capacitance per unit area is

$$C = e \times \frac{dn}{dV} \quad (6.7)$$

The permittivity of GaAs is 12.9. So from Eq. (6.5) and Eq.(6.7) the separation d , or the depth of 2DEG is

$$d = \frac{\epsilon\epsilon_0}{e \times \frac{dn}{dv}} \quad (6.8)$$

Using Eq. 6.8, we get the depth of 2DEG in Pfeiffer 07.28.09.02 and Pfeiffer 08.29.08.01. For Pfeiffer 07.28.09.02, we get 2DEG depth around 380 nm and for Pfeiffer 08.29.08.01, the depth of 2DEG around 490 nm. The values are close to the values we get from growth profiles. (Fig. 5.3)

From the gate voltage variation of density and mobility, we can derive other parameters like mean free path, interaction strength etc. Table 6.2 shows the table for density and mobility for Pfeiffer 07.28.09.02 and other derived important parameters which include Fermi vector k_F , Fermi velocity, V_F , Fermi energy, E_F , mean free path, ℓ , Fermi wavelength λ_F and interaction strength r_s .

V	n	μ	k_f	V_F	E_F	ℓ	λ_F	r_s
mV	$E + 14/m^2$	$E + 2m^2/Vs$	E+7 m	E+5 m/s	meV	μm	nm	
-350	1.6	2.2	3.1	0.54	0.55	4.42	200.70	2.47
-300	2.5	3.1	4	0.7	0.88	8.05	159.18	1.96
-250	3.3	4.1	4.5	0.77	1.15	12.09	139.48	1.72
-200	4.0	5.1	5	0.86	1.43	16.77	124.87	1.54
-150	4.8	6.1	5.5	0.95	1.71	22.06	114.18	1.40
-100	5.6	7.2	5.9	1	1.99	27.94	105.95	1.30
-50	6.3	8.3	6.3	1.1	2.25	34.47	99.64	1.23
0	7	9.5	6.6	1.14	2.50	41.45	94.48	1.16
50	7.8	10	7	1.2	2.75	48.67	90.05	1.11
100	8.5	11	7.3	1.25	3.00	54.93	86.24	1.06
150	9.2	12	7.6	1.3	3.25	60.72	82.83	1.02
200	10	12.8	7.9	1.36	3.51	66.23	79.67	0.98
250	11	13.2	8.2	1.4	3.76	70.57	77.00	0.95
300	11.3	13.3	8.4	1.5	4.01	73.58	74.57	0.92

Table 6.2: Density , mobility and other parameters derived from gate voltage variation of density and mobility for sample Pfeiffer 07.28.09.02 at base temperature T=24 mK.

Similar table (table 6.3) we get for Pfeiffer 08.29.08.01 showing the density mobility along with Fermi vector k_F , Fermi velocity, V_F , Fermi energy, E_F , mean free path, ℓ , Fermi eavelength λ_F and interaction strength r_s .

The upper limit of the gate voltages depend on the leakage current through the sample.

V	n	μ	k_f	VF	E_F	ℓ	λ_F	r_s
mV	$E + 14/m^2$	$E + 2m^2/Vs$	E+7 m	E+5 m/s	meV	μm	nm	
-600	2.7	4.1	4.1	0.71	0.96	10.95	152.47	1.88
-550	3.1	4.5	4.4	0.75	1.1	13.11	143.12	1.76
-500	3.4	5.1	4.6	0.8	1.2	15.40	135.17	1.66
-450	3.8	5.6	4.9	0.84	1.4	17.83	128.48	1.58
-400	4.2	6.1	5.1	0.88	1.5	20.47	122.70	1.51
-350	4.5	6.6	5.3	0.92	1.6	23.29	117.64	1.45
-300	4.9	7.2	5.5	0.95	1.7	26.27	113.11	1.39
-250	5.3	7.8	5.8	0.98	1.8	29.47	109.22	1.34
-200	5.6	8.4	6	1	2	32.86	105.66	1.30
-150	6	9.1	6.1	1.05	2.1	36.45	102.48	1.26
-100	6.3	9.7	6.3	1.08	2.3	40.24	99.64	1.23
-50	6.7	10.4	6.5	1.1	2.4	44.24	97.10	1.19
0	7	11.1	6.6	1.14	2.5	48.45	94.80	1.17
50	7.3	11.8	6.8	1.17	2.6	52.52	92.72	1.14
100	7.6	12.4	6.	1.2	2.7	56.56	90.73	1.12
150	8	13	7.1	1.22	2.8	60.37	88.79	1.09
200	8.3	13.5	7.2	1.24	2.9	64.09	86.99	1.07
250	8.6	14	7.4	1.27	3.1	67.80	85.25	1.05
300	9	14.5	7.5	1.29	3.2	71.35	83.59	1.03

Table 6.3: Density , mobility and other parameters derived from gate voltage variation of density and mobility for sample Pfeiffer 08.29.08.01 at base temperature T=24 mK.

6.3 Effective mass m^*

6.3.1 Introduction

The electron is subject to internal forces from the lattice (ions and core electrons) and external forces such as electric fields. When an electron is moving inside a solid material, the force between other atoms will affect its movement. This can not be described by Newton's law. So the concept of effective mass is introduced. Electrons are accelerated by electric fields so there's a direct correspondence between voltage and electron mass-energy, or between the voltage and the resistance of a medium. The mass of electrons depends on their energy, so if their velocity changes while they accelerate or decelerate when propagating through, their effective mass also changes. The electrons are considered to be free having mass $m_e = 9.1 \times 10^{-31}$. The effective mass (m^*) is smaller than the electron mass in GaAs/AlGaAs.

The effective mass is important tool to understand magneto-transport properties and the band structure properties in semiconductor heterostructure.

Temperature dependence of SdH oscillations is used to determine the effective mass. In Si- MOSFET, Fang et al.[36], found apparent effective masses (m_{SdH}^*) which steeply decrease with decreasing magnetic field to values much smaller than the cyclotron effective mass (m_c^*). Galchenkov et al. [37] measured m_{SdH}^* of the 2DEG in an AlGaAs/GaAs heterostructure and also found a large difference between m_{SdH}^* and the commonly accepted value for m_c^* . Blom et al. [38] found a pronounced decrease of the apparent mass m_{SdH}^* , with decreasing magnetic field. The experimental results for m_{SdH}^*/m_c^* scale as a function of $k_B T/\hbar\omega_c$. Our results show weak dependence of m^* on the magnetic field but the average value of effective mass is $0.067m_e \pm 0.005m_e$

6.3.2 Theory

The Shubnikov-de Haas oscillations are small small and intermediate magnetic fields, i.e. for $\omega_c\tau \ll 1$, where ω_c is the cyclotron radius and τ is transport scattering time, also referred as τ_t elsewhere in the thesis . In this regime the density of states is weakly modified,. The oscillations in the density of states can be seen in the longitudinal resistivity. The analytical expression disused by Ando et. al [39] for $\rho_{xx}(B)$, in limit $\omega_c \ll 1$, valid in short range scattering regime, gives

$$\rho_{xx}(B) = \rho_{xx}(0)[1 - 4\cos(\frac{\pi\hbar m}{eB})D(m^*, \Theta)E(m^*, \tau_q)] \quad (6.9)$$

This is called Ando formula where the expression $D(m^*, \Theta)$ is known as Dingle term. It contains the temperature dependence term and depends on the effective mass. \hbar is the reduced Planck constant, τ_q is the quantum scattering time, and m^* is the electron effective mass. This equation is expected to be true for small magneto-oscillations before onset of quantum Hall states and zero longitudinal resistivity appear with increasing B. In addition, $\rho_{xx}(0)$ is the zero-field longitudinal resistivity $\rho_{xx}(B = 0)$ [40].

$$D(m^*, \Theta) = \frac{x}{\sinh x}, x = \frac{2\pi^2 k_B}{\hbar e B} m^* \Theta \quad (6.10)$$

At sufficiently high temperatures where $x > 1$ and small magnetic fields one can use $\ln(\sinh x) \approx x$,

$$\ln \frac{\Delta\rho_{xx}}{T} = C - \frac{2\pi^2 k_B}{\hbar e B} m^* T \quad (6.11)$$

The constant C is neglected further . This equation can be used obtain the effective mass.

6.3.3 Results and discussion

The effective mass extraction is done on two different samples, Pfeiffer 09.12.05.2 and Pfeiffer 07.28.09.02. The density and mobility of these samples is described in section 6.2.

All measurements were performed at cryogenic temperatures using a $^3\text{He}/^4\text{He}$ dilution refrigerator (Microkelvin MCK-50) obtaining a base temperature of 24 mK. The sample was glued on a chip-carrier with PMMA and bonded with Gold-wires. The sample was positioned in a high-field superconducting magnet solenoid (Cryogenics Ltd) which produces a maximum central field of 9T. In addition two perpendicular superconducting split-pair magnets producing a maximum operating field of 1T were mounted perpendicular to the solenoid field. This configuration allowed to apply a strong in-plane magnetic field and independently control the perpendicular field. Although the solenoid field have a large influence on the split-pair coils it was possible to have up to 0.5T while the solenoid field was about 4T. The temperature-control and control of the magnet power-supplies, special

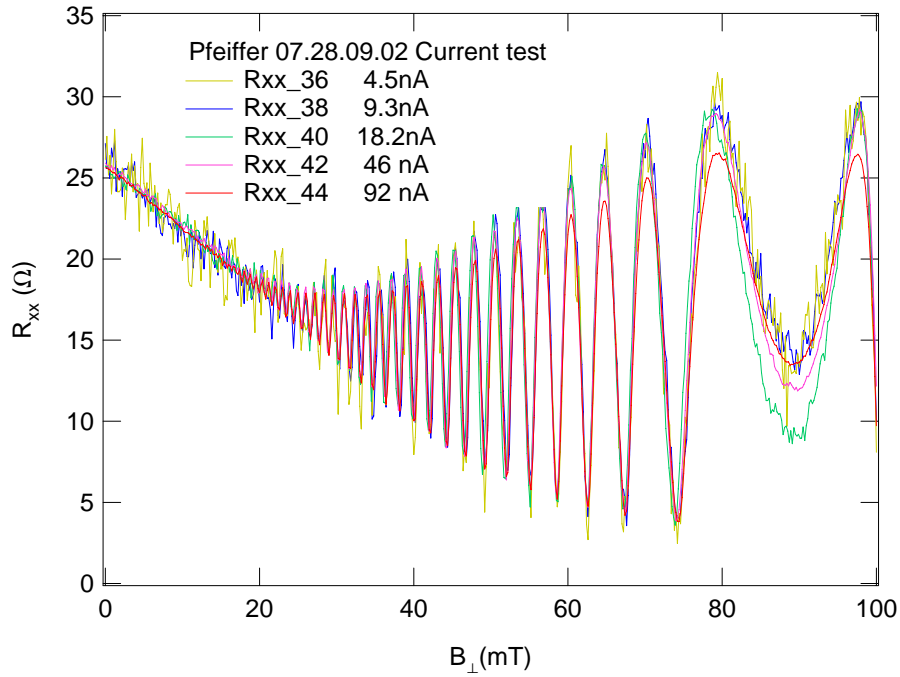


Figure 6.6: Low field magneto-resistance data for different currents in sample Pfeiffer 07.28.09.02 at base temperature $T=24$ mK

procedures were used in Igor Pro (Wavemetrics).

AC input bias current between 4.5 nA and 92 nA at a frequency of 176 Hz was applied. In order to find the maximum current which did not heat up the electrons significantly and the output signal is maximum, SdH oscillations were monitored while the current was increased until a reduction in SdH amplitude could be detected. Fig. 6.6 shows oscillations with different currents, 4.5 nA, 9.3 nA, 18.2 nA, 46 nA, 92 nA. . To eliminate wire and contact resistances a four-probe configuration was chosen to measure the transverse and longitudinal voltage drop using lock-in techniques.

In very high current, the amplitude of SdH oscillations is suppressed due to the heating of electrons while at smaller currents the noise is higher as can be seen from Fig. 6.6. Higher currents like 92 nA, red trace, shows the effect of heating which can be seen in decrease in SdH oscillation amplitude. For low currents like 4.5 nA, yellow curve shows the higher noise. Clearly the small currents show larger noise and higher currents show heating of electrons. Once the optimum current was determined (e.g. from Fig. 6.6, 9.3 nA is reasonably good in terms of signal

and noise) the other parameters like magnet sweep rate, time constant, the delay etc. were obtained in similar way, i.e. checking the amplitude of the magnetoresistance. For all magnetic field sweeps a ramp-rate $\Delta B/\Delta t \leq 1\text{mT}/s$ was used. For data acquiring and processing, the temperature-control and control of the magnet power-supplies, special procedures were used in Igor Pro (Wavemetrics).

The field sweep direction also plays a crucial role here. We had swept the the field in up i.e. in the increasing field direction and down i.e. decreasing field direction. During the up sweep, the electrons seem to be heating. This can be seen in the damping of the SdH oscillations. While in the sweep down, the amplitude of the SdH oscillations is higher than the sweep up direction. Fig.6.7 shows the sweep up and down directions for the magnet.

In Fig.6.7, upper panel shows the sweep up (red trace) and sweep down (blue direction) directions with the ramp rate 1 mT/sT. The amplitude of of the SdH oscillations is lower for magnet sweep up direction. When the magnet sweep up curve is shifted to coincide with the magnet sweep down direction (lower panel), the shift in the magnetic field is -20 mT. As the magnet sweep down direction shows the higher amplitude compared to magnet sweep down direction, all the measurements are done for magnet sweep down direction.

First we will discuss experiment performed with Pfeiffer 09.12.05.2.

The sample is illuminated to GaAs LED for 1 min at 4mA current through LED. With this illumination, we get density around $0.45 \times 10^{11}/\text{cm}^2$ and mobility around $2.2 \times 10^6 \text{cm}^2/\text{Vs}$. After finding the optimum current, magnet sweep rate, time constant etc, the SdH oscillations for different temperates are probed across the Hall bar. We use Piccowatt temperature controller to set the temperatures. The desired temperature value is provided by the *Igor* code to the resistance bridge. The resistance bridge is connected to the temperature controller. It works through feedback technique. The code is also monitoring the change in temperature and we wait around 30 min. to stabilize the temperature and then the magnetic field is varied to probe the SdH oscillations in the Hall bar. The accuracy of the temperature controller is within 1%. From base temperature, we changed 12 different temperatures to 300 mK.

At sufficiently high temperatures and low magnetic fields the effective electron mass m^* can be extracted from the temperature dependence of the SdH oscillations. The temperature dependence of the amplitude of the Shubnikov- de Haas oscillations is used to define an effective mass of the two-dimensional electron gas. The temperature variation is seen in the oscillation amplitude. Here few temper-

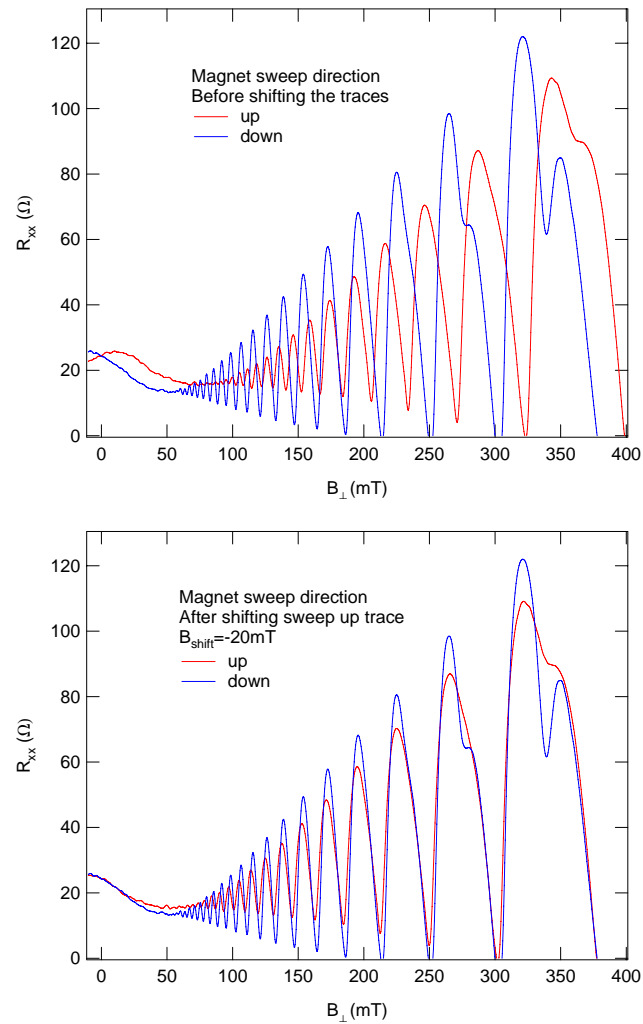


Figure 6.7: *Upper panel* Magnet sweep up and down direction before shifting the traces. *Lower panel* The up direction trace is shifted to coincide with the magnet down sweep. The field shift is around -20 mT. The data is taken with 1mT/s and at base temperature $T=24$ mK

ature dependence oscillations are shown in Fig. 6.8.

Fig.6.8 shows the SdH oscillation traces for few different temperatures. The upper panel shows complete field traces taken at various temperatures and the lower panel shows low field the zoom in. The temperature dependence can be clearly seen in the SdH oscillations. As the temperature goes up from the base temperature (24mK) to 300 mk, the SdH oscillations are damped.

There is always some offset in the magnetic field. The reason could be the time constant of the magnet, which depends on the inductance of the magnet. Though this field offset is few mT but this could change the effective mass values considerably. From Eq.6.11, the slope of $\ln \frac{\Delta \rho_{xx}}{T}$ and T gives the slope $\frac{2\pi^2 k_B}{\hbar e B} m^*$, which depends on the magnetic field, B. If value of B is $\pm 5\%$, the m^* can change by a significant number. So it is important to correct the field offset. This is done by sweeping the magnet upto some small negative field if the magnet is swept from a higher field in positive direction to low field and vice versa. The field offset is found from the polynomial fit at the peak in the SdH oscillation around zero field or the dip in the SdH field. This gives the offset and also the value of $\rho_{xx}(0)$. Fig.6.9 shows the R_{xx} and the polynomial fit.

Fig.6.9 shows the SdH oscillations around virtual zero field. We did a polynomial fit (black curve) to obtain the B offset and the $\rho_{xx}(0)$. This can be found from the fit parameters in the polynomial fit. The field offset is 11 mT and $\rho_{xx}(0)$ is 27.2 Ω . Here it shows for Pfeiffer 07.28.09.02 sample, but the same procedure is followed for other samples. In Pfeiffer 09.12.05.2 samples, we used dip in the R_{xx} data around zero field to obtain the field offset.

The upper panel in Fig. 6.10 shows $\ln(R_{xx}/T)$ shows the low field SdH oscillations at different temperatures. The B field offset is corrected. We define the *strength* of the feature in Rxx as $1/2(2P - V_1 - V_2)$ which is simply the mean amplitude ΔR_{xx} of one single SdH oscillation. Here P denotes the peak of the oscillation at the particular magnetic field, V_1 and V_2 denote the valleys in the SdH adjacent to the peak. This is found for SdH oscillation for every temperature at few magnetic fields in low field regime. This gives the term $\Delta R_{xx}/T$. Logarithm of $\Delta R_{xx}/T$ plotted as function of temperature T gives the slope $2\pi^2 k_B m^* / \hbar e B$ as shown in lower panel of Fig.6.10 . Since B values are known, the effective mass is extracted from the line as shown of Fig.6.10 for Pfeiffer 09.12.05.2. For too low temperatures the linear behavior is no more observable and the simplified form of the Dingle term is not valid any more. For higher fields, the spin effect starts to show and the Dingle term is no longer valid. In the low field, not enough data points are

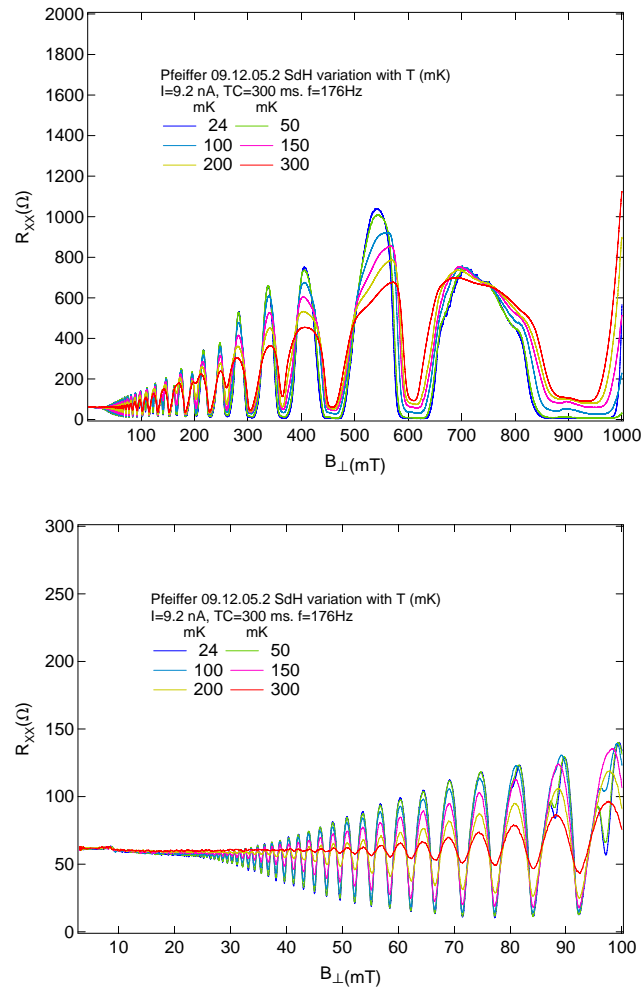


Figure 6.8: *Upper panel* Shubnikov de-Haas oscillations at different temperatures, complete field trace. *Lower panel* shows low field zoom in. These traces are for Pfeiffer 09.12.05.2

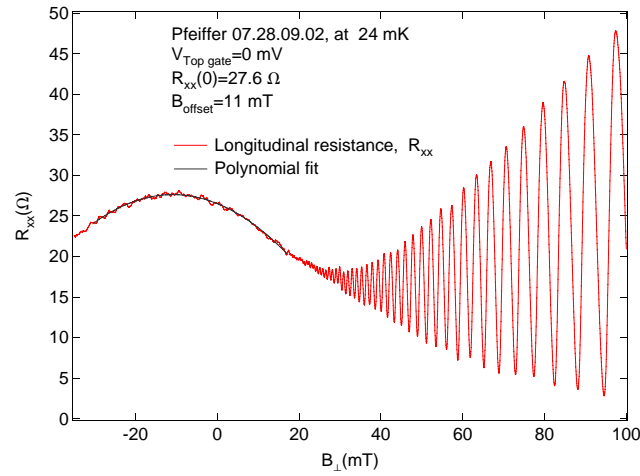


Figure 6.9: Polynomial fit around virtual zero magnetic field used to obtain the B_{offset} and $\rho_{xx}(0)$

found in SdH oscillations for high temperatures.

This was evaluated for four different single oscillations giving a mean effective mass $m^* = 0.065 \pm 0.004$ which is close to the expected value of $m_{GaAs}^* = 0.067$. However, there is a slight dependence on magnetic field visible in Fig. 6.10 lower panel.

The same experiment is performed on Pfeiffer 07.28.09.02.

LED illumination is not needed in this sample. In this sample the m^* is extracted for both not-gated and gated regions. The carrier concentration in the same sample for these two different regions is different. For not gated region, the density is $n = 0.76 \times 10^{11}/cm^2$ and for gated region it is $n = 0.67 \times 10^{11}/cm^2$. This is due to the strain on the sample because of top gate layer of Ti-Au. This difference is not very significant though.

In Fig. 6.11 upper panel shows the extraction of m^* in not gated section of the Hall bar and lower panel shows the extraction of m^* for gates section for few different magnetic fields. At lower temperature, the linear behavior deviates and Dingle term is not valid. For the fitting of data, low temperature points are neglected. The magnetic field offset is corrected using polynomial fit method as shown Fig. 6.9. In both regions, average m^* value is $(0.062 \pm 0.005)m_e$. These values are consistent with literature. In this sample also, slight field dependence is seen.

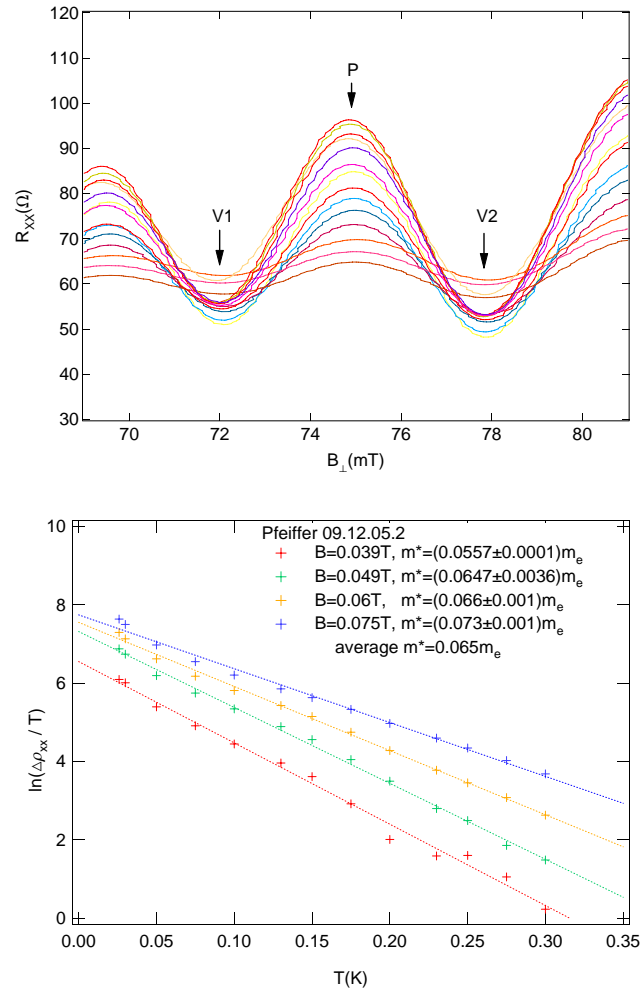


Figure 6.10: *Upper panel* Shows a low-field SdH oscillation which was used to extract the amplitude. *Lower panel* The effective mass m^* was obtained by fitting the linear regions in $\ln(\Delta R_{xx})$ vs T for Pfeiffer 09.12.05.2. The Dashed lines show the line fits.

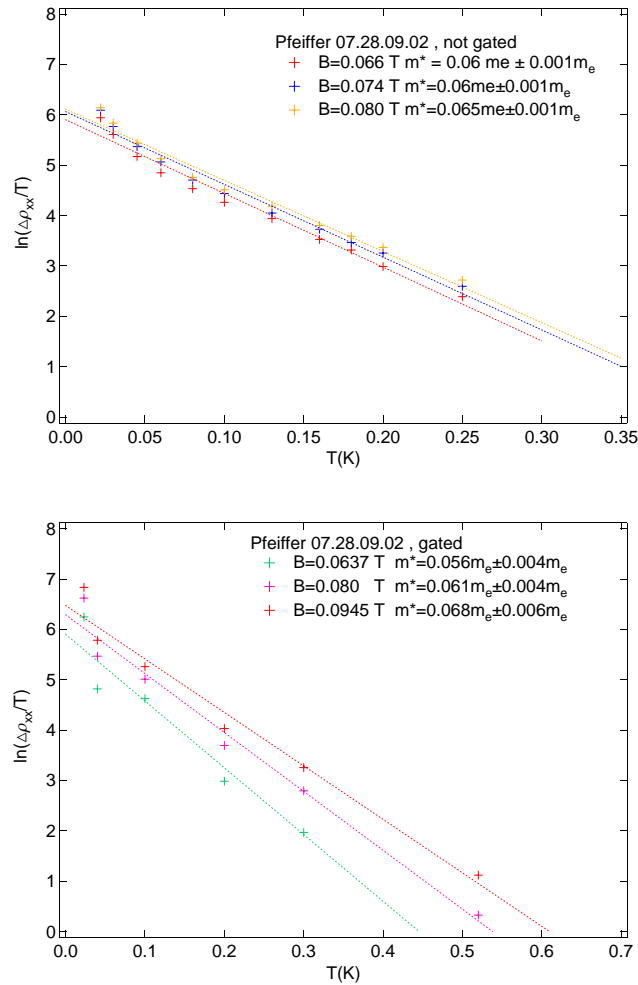


Figure 6.11: *Upper panel* shows $\ln(\Delta R_{xx})$ in the nongated region of the Hall bar. *Lower panel* shows $\ln(\Delta R_{xx})$ in gated region of the Hall bar. The effective mass m^* was obtained by fitting the linear regions in $\ln(\Delta R_{xx})$ vs T for Pfeiffer 07.28.09.02. The dashed lines show the line fits.

6.3.4 Conclusion

The temperature dependence of low field SdH oscillations was used to extract the effective mass m^* in two different samples, Pfeiffer 09.12.05.2 and Pfeiffer 07.28.09.02.

The effective mass in both the samples is around $(0.067 \pm 0.007)m_e$. This value does not depend on density or wafer materials.

6.4 Transport and Quantum Scattering times

6.4.1 Introduction

The electron-electron interaction leads to different scattering lifetimes. Different scattering mechanisms like alloy disorder scattering, surface roughness scattering and scattering due to remote Coulomb centers are involved. Here we will discuss the transport lifetime (τ_t) and quantum scattering lifetime (τ_q).

The transport time is a measure of an average time an electron moves without scattering, which is related to mobility through $\sigma = ne\mu = ne^2\tau_t/m^*$. The quantum scattering time is single particle relaxation time, which describes the decay time of one-particle excitations and characterizing the quantum-mechanical broadening of the single-particle electron state [[41] - [47]].

The quantum lifetime τ_q and the transport lifetime τ_t are given by [[43] - [44]]

$$\frac{1}{\tau_q} = \frac{m^*}{\pi\hbar^3} \int_{\pi}^0 d\theta |V(q)|^2 \quad (6.12)$$

$$\frac{1}{\tau_t} = \frac{m^*}{\pi\hbar^3} \int_{\pi}^0 d\theta |V(q)|^2 (1 - \cos\theta) \quad (6.13)$$

with $q = 2k_F \sin(\theta/2)$, and $k_F = \sqrt{2\pi n_s}$. $|V(q)|$ is the probability of scattering through an angle θ from a state \mathbf{k} to a state \mathbf{k}' on the Fermi circle. In transport scattering case, the small angle scattering events are negligible, which can be seen by $(1 - \cos\theta)$, whereas in case of quantum scattering time all the scattering events count together. The transport time is not sensitive to the small angle scattering but quantum scattering time is since all the scattering events contribute equally. Thus the ratio of the the two lifetimes, τ_t/τ_q gives information about angular dependence of scattering processes.

For a short-range scattering potential τ_t and τ_q are approximately equal [36]. In metal-oxide-semiconductor (MOS) structures, the two scattering times are the same [45]. In case for modulation-doped GaAs/AlGaAs heterostructure, where the dominant scattering mechanism is the long-range potential associated with ionized donors which are far from the 2DEG and which produce predominantly small-angle scattering, τ_q will be much smaller than τ_t . The ratio of the two time τ_t/τ_q is expected to vary with carrier density.

The ratio of τ_t/τ_q for a 2DEG has been investigated theoretically and experimentally by a number of researchers. Das Sharma and Stern [45] have calculated τ_t and τ_q due to remote ionized impurity scattering and predicted that their dependence on spacer layer thickness as well as the carrier density. Gold [46] has investigated the effects of interference-roughness scattering, alloy scattering, and remote ionized impurity scattering on the scattering times in the GaAs and $In_xGa_{1-x}As$ material systems. It is believed that in $GaAs/Al_xGa_{1-x}As$ modulation-doped heterostructure, at low temperatures, remote ionized impurity scattering is dominant scattering mechanism.

Experimentally, the ratio of transport and single particle scattering time or quantum scattering times has been investigated by Coleridge [47]. In their samples of different spacer thickness, they found that the the ration τ_t/τ_q is smaller than the theory. For Fang et al [36], the ratio τ_t/τ_q was 34.5 for spacer layer 200\AA . U. Bockelmann [48] studied these two characteristic times in multiple quantum well in narrow GaAs/AlGaAs samples. In their samples, scattering is dominated by remote-impurity and interface scattering.

In some earlier experiments, the single-particle lifetime τ_q in Si-MOSFET's was found [36] to be nearly equal to the transport lifetime τ_t while in AlGaAs/GaAs-heterostructure τ_t , turned out to be one or even two orders of magnitude larger than τ_q [[49], [50],[51]]. According to Das, Subramaniam, [52], the τ_q is independent of carrier concentration. The τ_t is increasing with increasing the carrier concentration.

While the τ_q for wafer with thicker spacer layer decreases with decreasing the carrier concentration. In other sample, with InAs self assembled quantum dot, the quantum lifetime is almost independent of carrier concentration [53]. In high mobility GaAs/AlGaAs, the quantum scattering time shows linear behavior density above $n = 10^{11}/\text{cm}^2$ at 15 mK. The quantum lifetime is 200-300 times shorter than the transport time.[54]

Quantum scattering time is studied to determine the single particle relaxation time. This helps to know the dominant scattering mechanism in the system.

6.4.2 Theory

The single particle scattering lifetime is related to the amplitude of the SdH oscillations and was calculated from Dingle plots. The expressions given by Ando [55] and Ishihara and Smrčka [56] for the magnetoconductivity. Coleridge, Stoner and Fletcher [57] modified the expression which made a distinction between the transport time and single-particle scattering time. The amplitude ΔR of the SdH oscillations is given by

$$\delta R = 4R_0 X(T) \exp(-\pi/\omega_c \tau_q), \quad (6.14)$$

where R_0 is the zero-field resistance, ω_c is the cyclotron frequency and $X(T)$ a thermal damping factor, given by

$$X(T) = (2\pi^2 kT/\hbar\omega_c) / \sinh(2\pi^2 kT/\hbar\omega_c) \quad (6.15)$$

In a Dingle plot, the logarithm of $\delta R/4R_0 X(T)$ is plotted against $1/B$, which is a straight line with an intercept of zero. A good Dingle plot is linear and has an intercept of zero. The slope of this straight line gives $1/\tau_q$.

6.4.3 Results and Discussion

The measurement setup for this experiment is current bias based Hall voltage measurement. The longitudinal voltage is measured to determine the τ_q across the top gate region in case of gated sample. The current for the measurement is determined by measuring SdH oscillation amplitude as described in previous section. The current is chosen such that the electrons are not heated by the current. This is determined from the maxima of the longitudinal oscillation amplitudes as a function of magnetic field for different currents. In the similar manner the sweep rate of the magnet is chosen.

In Pfeiffer 07.28.09.02, we have done the experiment for three different temperatures, base temperature i.e. 24 mK, 200 mK and 400mK. The current is different for each temperature. For 24 mK, the current is 9.2 nA (time constant, TC of 1s) , for 200 mK, it is 18.3 nA (TC 1s), and the current is 46 nA for 400 mK (TC=300 ms). The frequency was chosen to be 125 Hz. The time constant is determined by

doing few tests for different time constants.

PAR 124A acts as source, the AC voltage is read as current using a resistor of $1M\Omega$. Low noise BNC cables are used for entire measurement. The virtual ground to the sample is provided by Keithley IV convertor. The sample is mounted perpendicular to the solenoid field. Keithley 2440 Source-Measure Unit acts as current source for solenoid field. The V_{xx} and V_{xy} are probed along the sample using two slave lock-in amplifiers. These lock-in amplifiers are synchronized with the master lock-in amplifier PAR 124A which is source of the experiment.

The experiments were carried out on a Pfeiffer 07.28.09.02 with electron density of $0.7 \times 10^{11}/cm^2$ and mobility $9.5 \times 10^6 cm^2/V.s$ at zero top gate voltage at base temperature (24mK) of the cryostat. The electron density and mobility at different gate voltages is shown in table 6.2.

The amplitude of the longitudinal oscillations are used to extract the quantum scattering time of the sample. The quantum scattering time is measured for different densities which are tuned by varying the gate voltage in case of a gated sample. The density variation for three different gate voltages at 24 mK is shown in Fig. 7.3. The voltages shown here are $+50mV$, $0mV$, and $-150mV$. The green trace shows the SdH oscillations for top gate voltage $-150mV$, the middle red trace is for top gate voltage $+50mV$ and the blue trace in the lowermost panel is for 0 top gate voltage. The variation in density with different gate voltages can be seen in the SdH oscillations. For all the traces the magnet was swept from high field to low field. The effect of sweep directions is shown in Fig.6.7

Along with gate voltages, the effect of different temperatures is also seen in the oscillations. Fig6.13 shows the effect of temperature on the SdH oscillation at a zero gate voltage. The upper panel shows the complete field trace for SdH oscillations for three different temperatures 24mK, 200mK and 400 mK. The detailed low field view on the lower panel showing amplitude of SdH oscillations at fixed gate voltage, zero in this case, for different temperatures. The blue trace is SdH oscillation at base temperature, 24 mK, the green trace is for 200 mK and red trace is for 400 mK. The effect of different temperatures on the amplitude of SdH oscillations can be seen here. The different temperatures are controlled using AVS47 resistance bridge and picowatt temperature controller as described in previous section of effective m^* . The magnet is swept from high field to low field.

The experiment is done for three different mixing chamber temperatures, 24mK, 200 mK and 400 mK. The density in the 2DEG is tuned using top gate volt-

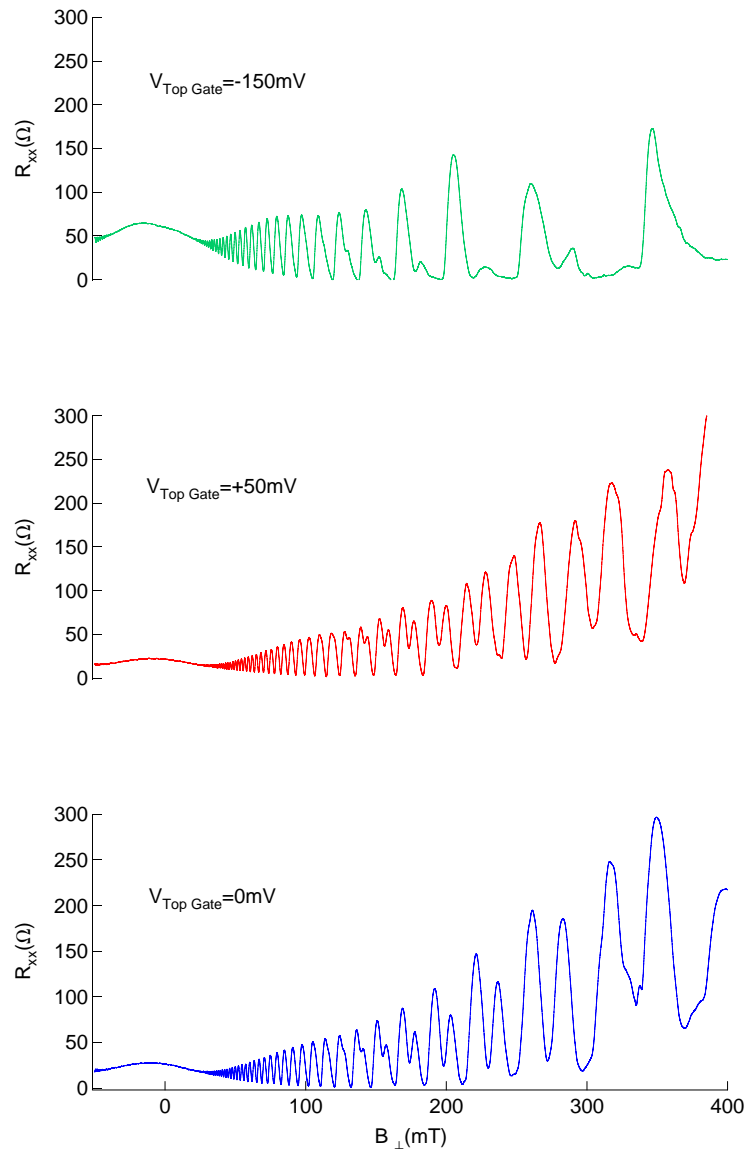


Figure 6.12: Longitudinal oscillations at three different top gate voltages, +50,0 and -150mV at base temperature 24 mK

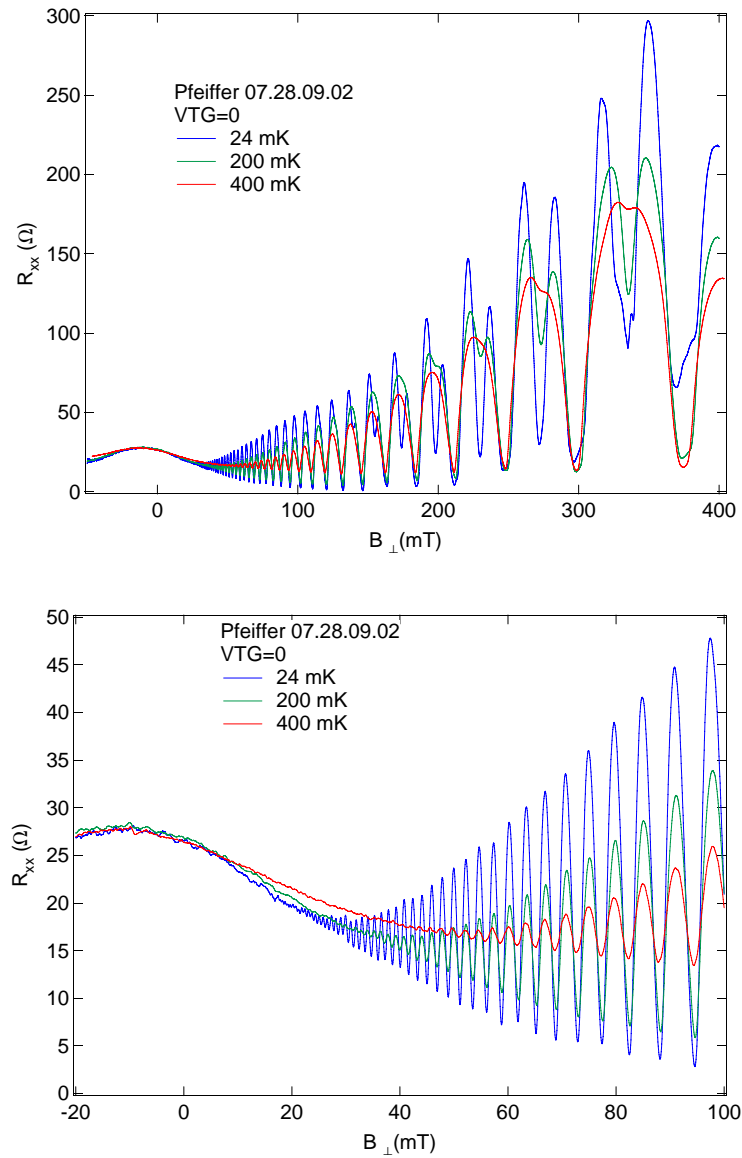


Figure 6.13: *Upper panel* Complete field trace for zero top gate voltage at different temperatures. *Right* Detailed view of left panel showing the SdH maxima at different temperatures. The magnet is swept down from high field to low field.

age. The top gate is changed from +100 mV to -350 mV with the interval of 50mV. The maximum density is $0.88 \times 10^{11}/cm^2$ and minimum is $0.17 \times 10^{11}/cm^2$ with corresponding change in mobility from $1.15 \times 10^7 cm^2/V.s$ to $2.2 \times 10^6 cm^2/V.s$ respectively. The density mobility variation with gate voltage is shown in table 6.2.

The change in density and mobility with respect to the gate voltage is consistent with the density and mobility values determined from individual Hall resistance within few %.

For τ_q measurement, the density for each gate voltage is determined using the corresponding Hall resistance since $R_H = \frac{1}{en}$. For base temperature measurement, the current used is 9.2 nA with 125 Hz, reference frequency of the lock-in, with time constant of 1s. Dingle curve is plotted using the amplitude of the R_{xx} oscillations and the inverse of magnetic field. The amplitude variation is considered in low magnetic field regime, classical regime. Fig. 7.3 shows the R_{xx} for different gate voltages.

To extract the amplitudes from the oscillations, a simple code is generated in IGOR, which takes into account the maximum and minimum points in each oscillation. This amplitude is the input for Dingle plot. From Eq. 7.3, and Eq. 7.4, logarithm of $\delta R/4R_0 X(T)$ is plotted against $1/B$. Here the R_0 is longitudinal resistance where the oscillations in the longitudinal resistance are onset.

For base temperatures, we have tried four different electron temperatures, 25 mK, 50 mK, 75 mK and 100 mK. Fig. 6.14 shows the Dingle plots for two different electron temperatures, 25 mK and 100 mK. These are set to be the lower and the upper limit of electron temperatures. The upper panel shows the Dingle plot for electron temperature 25 mK and the lower panel shows the Dingle plot for electron temperature of 100 mK. R_0 of 19Ω is determined from the onset of the SdH oscillations. The error bar on the individual Dingle plot is derived from the noise in R_{xx} . The magnetic field offset is corrected using the longitudinal resistance around zero field as shown in Fig. 6.9.

The upper bound of the temperature can be found from R_{xxmin} at the spin splitting valleys data which is used to determine the g^* in section 6.5. This upper limit of 100mK the electron temperature agrees with the upper limit of 100 mK, found in the same wafer, and same setup discussed in section 6.5.

But in this experiment, since we do not have enough data for spin splitting valleys,

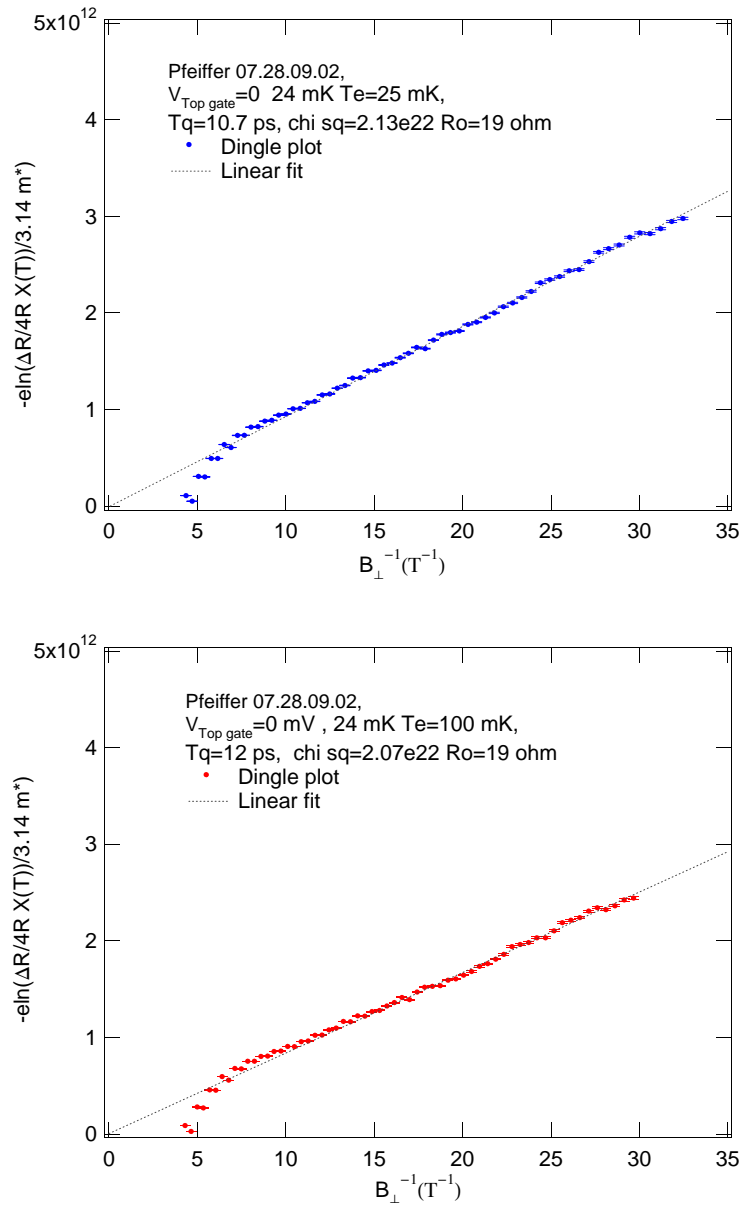


Figure 6.14: Dingle plot for base temperature, $V_{\text{TopGate}}=0$ mV assuming two different electron temperatures, 25mK (upper panel) and 100 mK(lower panel)

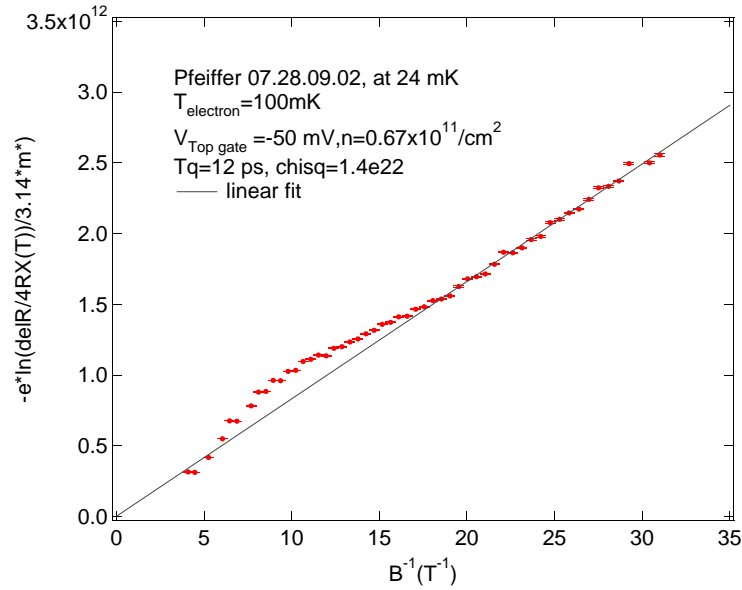


Figure 6.15: Dingle plot for base temperature, $V_{TopGate} = -50$ mV

we have used chi square (χ^2) error during the fit to define the upper limit of the electron temperature. χ^2 error is used to estimate goodness of fit of a statistical model or how well it fits a set of observations. It typically summarizes the discrepancy between observed values and the values expected under the model in question. It is a weighted sum of squared errors.

A typical Dingle plot at base temperature for -50 mV top gate voltage is shown in Fig. 7.4

The line fit passes through origin which is indication of a good Dingle plot. The noise in the measured R_{xx} data is indicated in the error bar. The fit range is determined from the oscillation in the low magnetic field regime. After a certain limit of magnetic field, the logarithmic term deviates from straight line. The individual amplitudes and $X/\sinh(X)$ term are straight lines but its the logarithm of these terms is saturating after a certain $1/B$. The reason could be onset of the quantum effect in the sample with increasing magnetic field. The effect is more prominent as the gate voltage is reduced i.e. the carrier density is lowered. This can be seen in Fig.6.16. The density at gate voltage +100 mV is $0.92 \times 10^{11} \text{ cm}^{-2}$ and for -200 mV is $0.42 \times 10^{11} \text{ cm}^{-2}$.

The slope of the straight line in the Dingle plot gives the quantum scattering time

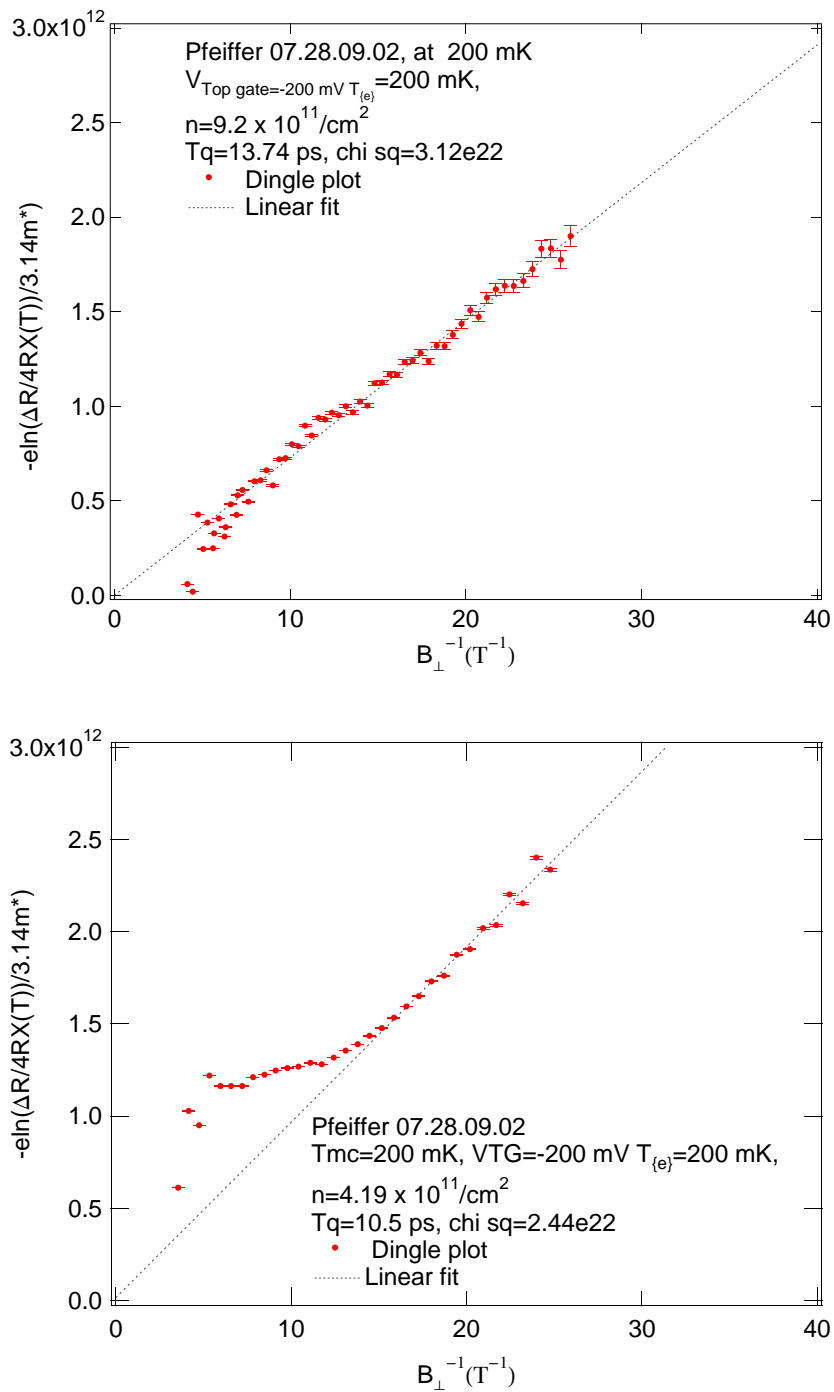


Figure 6.16: Dingle plot for 200mK, VTG=+100 mV (upper panel) and VTG=-200mV (lower panel)

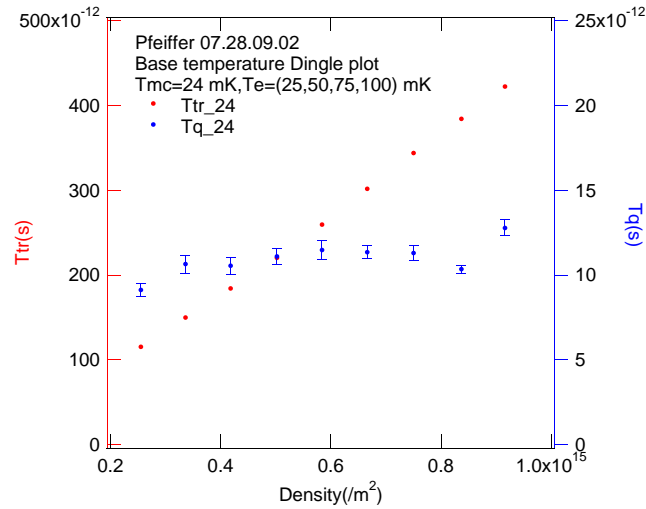


Figure 6.17: Transport time and quantum scattering time at base temperature as a function of carrier density at 24 mK

for the particular density. With the same procedure, τ_q is found for all the densities. Fig. 7.5 shows the variation of τ_q as a function of carrier density of the 2DEG.

The graph 7.5 shows the transport time with red dots on left axis and quantum scattering time with blue dots on right axis as a function of carrier density. Transport time τ_t increases with increasing carrier concentration. The variation of τ_q is almost constant as a function of carrier concentration. It seems that for our wafers, the quantum scattering time is almost independent of carrier density. Here we have assumed few different electron temperatures. With the average electron temperature, we get the result that the quantum scattering time is independent of carrier density. The error on the τ_q is derived from average of four different electron temperatures.

The quantum scattering time is plotted for different electron temperatures as a function of electron density at base temperature in Fig.6.18. The pink dots are for electron temperature of 25 mK, green dots indicate τ_q for electron temperature of 50 mK, brown and red dots are for 75 mK and 100 mK. All the electron temperature show no dependence on the density of the 2DEG. The average τ_q derived from τ_q with different electron temperature confirms that the quantum scattering time at 24 mK is independent of density of carriers.

We have done the same experiment with two different temperatures, 200 mK and

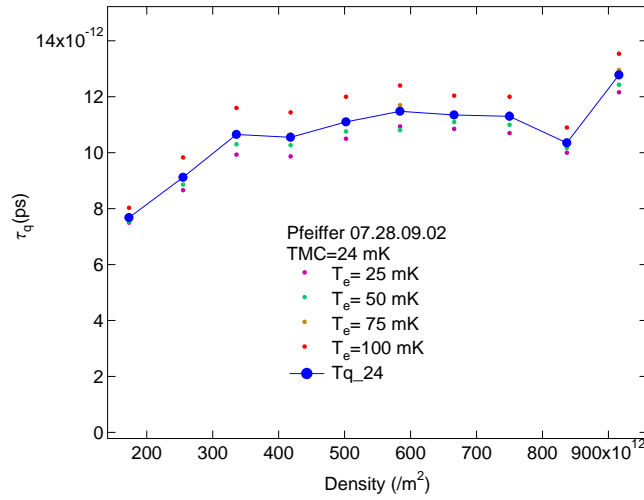


Figure 6.18: Quantum scattering time at base temperature as a function of carrier density for different electron temperatures and the average quantum scattering time.

400 mK. The current used for 200 mK experiment is 18.35 nA. The frequency and the time constant settings are same as for 24 mK, 1s . Fig 7.6 shows the variation of τ_q as a function of carrier density.

In Fig.7.6, transport time τ_t is shown by red dots on the left axis and quantum scattering time with blue dots on the right axis. The quantum scattering time for 200 mK shows decrease with decreasing carrier concentration. The τ_t variation at 200 mK shows the same behavior as for base temperature. The transport time also decreases with decreasing carrier concentration. according to the theory the quantum scattering time is independent of temperature ([41]), but our analysis shows that for higher temperature the quantum scattering time decreases with carrier density. The electron temperature used for analysis is 200 mK. The error on the linear fit of 200 mK data is very small and hence neglected here.

For 400 mK measurement, the current used is 46 nA, with time constant of 300 ms. The τ_q variation at 400 mK shows decrease with decrease in carrier concentration. The transport time also decreases with decrease in carrier concentration. In case of 400 mK, the amplitude of longitudinal resistance oscillations at lowest carrier density are not enough to plot a Dingle curve , so the lowest density point is neglected for 400 mK measurement data. Fig. 7.7 shows the graph for 400 mK, also includes the transport time for 400 mK. The error is not taken into account as the error from the line fit is small.

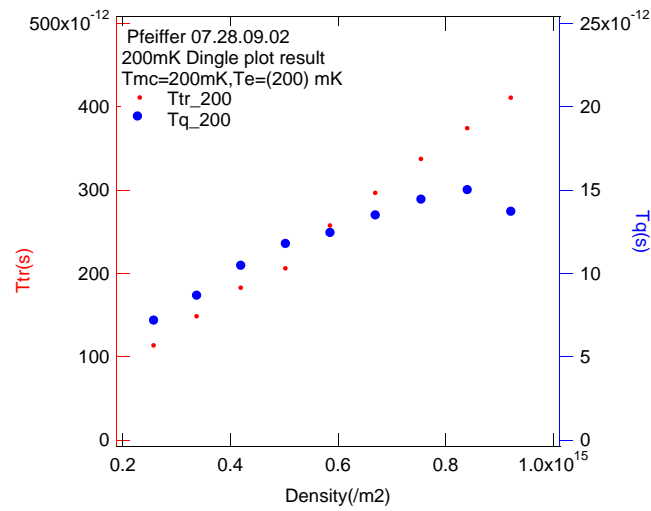


Figure 6.19: Transport time and quantum scattering time at 200 mK as a function of carrier density

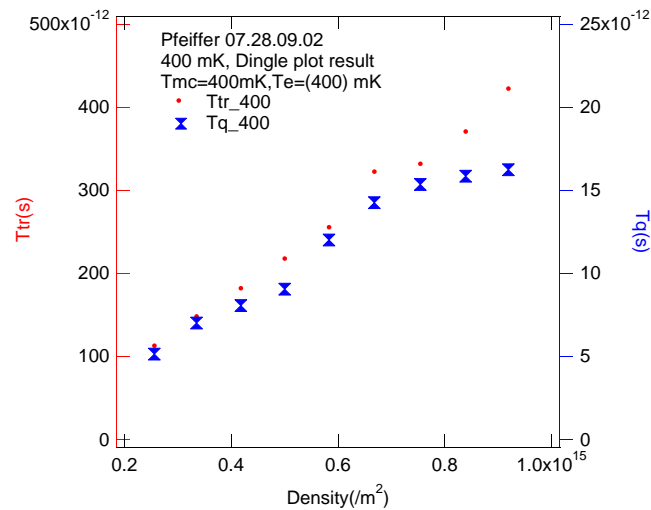


Figure 6.20: Transport time and quantum scattering time at 400 mK as a function of carrier density

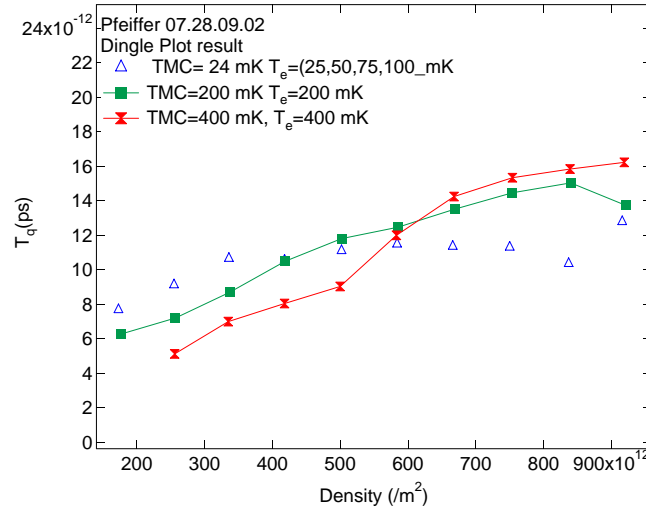


Figure 6.21: Quantum scattering time at different temperatures as a function of carrier density

In our experiments we have tried three different temperatures, base temperature, 200 and 400 mK. Our results for gated sample shows that at low temperature the τ_q is independent of carrier concentration while for higher temperatures, τ_q decreases with decreasing carrier density. Fig. 7.8

The ratio of transport time (τ_t) and quantum scattering time (τ_q) is shown for three different temperatures is shown in Fig. 7.10.

6.4.4 Conclusion

At 24 mK, the quantum scattering time is independent of density which suggests that the remote impurity scattering is dominant. The transport time for all temperatures shows decrease as a function of density, which means it is limited by background impurities.

For low temperatures the ratio of the two times decrease with decreasing with density. For high temperatures, the transport time seems to be dominant over quantum scattering time. Long range scattering events dominate over short range scattering. For other systems like FET [58] shows a similar behavior.

The ratio of the two lifetimes, τ_t/τ_q is higher than 10. For this ratio, we can conclude that the remote Coulomb centers play important role in the scattering events.

We showed a method to obtain quantum scattering time as a function of carrier

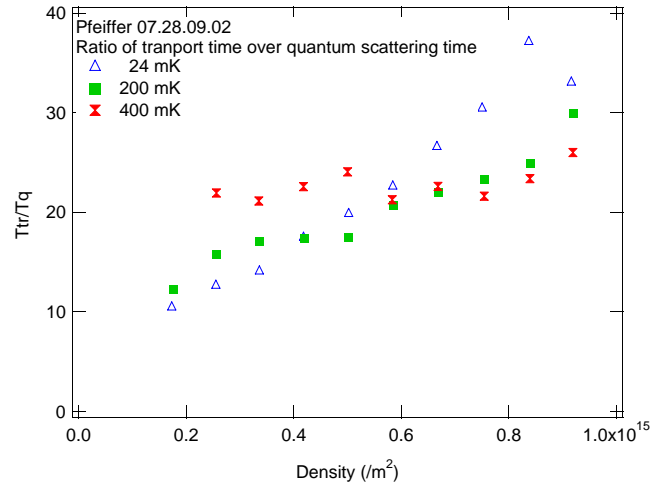


Figure 6.22: Ratio of transport time to quantum scattering time as a function of density for different remepratures.

concentration. More study is needed to be done for such a system at high temperatures.

6.5 Effective g^* factor

6.5.1 Introduction

The measurement of the electron g -factor helps in understanding of the interaction between the externally applied magnetic field and electronic states of the semiconductor heterostructure. Experimental measurements of g^* -factor provide an excellent tool to understand band-structure of electrons in low-dimensional semiconductor heterostructure.

The electron Landé g -factor is a proportionality constant between the magnetic moment and the total angular momentum of the electron.

In a magnetic field, the spin-up and spin down electrons form two sets of Landau levels. The spacing between them depends on perpendicular component of total magnetic field, $\hbar\omega_c = e\hbar B_{perp}/m^*$. However in presence of in plane magnetic field, the Landau level spacing are not influenced but increases the Zeemann energy is observed. Zeeman energy is given as $\Delta_z = g^*\mu_B B$, where g^* is the effective g -factor, μ_B is Bohr magneton, and B is the total magnetic field. Zeeman energy depends on total magnetic field. Presence of both perpendicular and in-plane magnetic field gives rise to a net spin-polarization with spin-subband densities n_{\downarrow}

and n_{\uparrow} . Each sub-density has a characteristic SdH frequency. Therefore, during an experiment with both fields present, the longitudinal resistivity is the sum of two frequencies depending on the spin polarization or total magnetic field.

The enhancement of the effective g-factor can be explained in terms of exchange interactions ([59]). Calculations of the exchange potential in a square quantum well confining potential have shown that the effective g-factor decreases when the 2D limit is approached [60]. An interacting two-dimensional electron system (2DES) makes a transition to a ferromagnetic state as the density is reduced below a certain threshold [[61],[62]]. Effective g-factor is associated with this transition.

6.5.2 Theory

At magnetic fields $B > 80mT$ (at base temperature, 24mK), the spin-splitting is visible in the SdH pattern. The Zeemann energy ($\Delta_Z = -g^* \mu_B B$) can be extracted from the exponential temperature dependence of spin-split minima $R_{min,xx}$ in the longitudinal resistance oscillations. (Fig. 6.23)

$$R_{min,xx} = exp\left(-\frac{\Delta_Z}{k_B T}\right) \quad (6.16)$$

Here $B = \sqrt{B_1^2 + B_2^2}$, is the total magnetic field. k_B is Boltzmann constant.

6.5.3 Results and discussion

First we will discuss experiment with Pfeiffer 09.12.05.2 sample. The current used is 9.4nA, at frequency of 176 Hz, with time constant of 300ms. The R_{xx} spin split minima depend on the temperature as shown in Fig.6.23. The temperature is varied from base temperature, 24 mK, to 300mK using AVS47 resistance bridge and picowatt temperature. The procedure is described in detail in section 6.3.

The $R_{xx,min}$ was extracted from the spin split minima for different temperatures at fixed magnetic field. The spin-split states were resolved without the resistance in the valley dropping to zero. This is due to the small energy gap between the spin states. With increase in temperature the SdH oscillations were suppressed and the resistance in the spin-split valleys increased. The logarithm of spin split minima $\ln(R_{xx,min})$ is plotted as function of $1/T$, here T is the temperature of the mixing chamber. This plot is called the Arrhenius plot. The g-factor is found from the slope of Arrhenius plot as shown in Fig. 6.24.

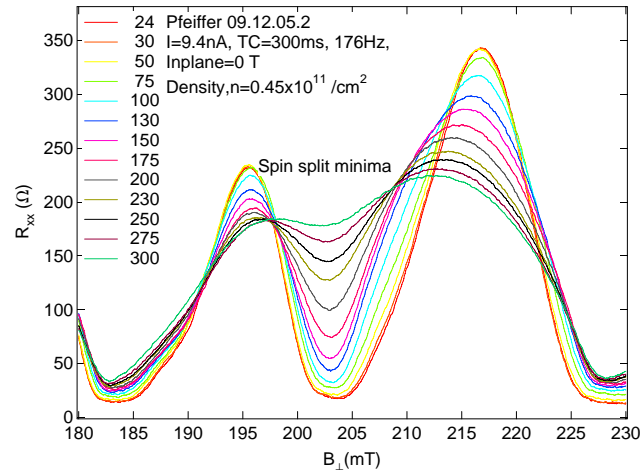


Figure 6.23: Temperature dependence of the spin-split minima with $B_{inplane} = 0$.

Fig.6.24 shows the Arrhenius plot for 166.5 mT in upper panel and for 261 mT in lower panel for Pfeiffer 09.12.05.2 sample. In both graphs, every point is the logarithm of $R_{xx,min}$ for different temperatures. The Arrhenius plot saturates at lower temperatures. The line is fitted in the range before the saturation of the Arrhenius plot. Slope of this plot gives us g^* . During this experiment, the total field is perpendicular field. No in-plane field is applied. The value of g^* shows dependence on the magnetic field.

The sample is then warmed and oriented in such a way that the solenoid magnet field is in plane and the split coil magnet field is perpendicular to the sample. The procedure to find the optimum current, sweep rates, time constant is repeated. The solenoid field is fixed at 1T and the SdH oscillations are probed using split coil magnet field. The g^* is extracted with the same described for sample in only perpendicular field. Fig.6.25 shows the extracted g^* for the same sample in absence and in presence of magnetic field. The error bar is determined from the fit range of g^* -factors.

In summary, g^* is extracted for two different cool-downs and two different total magnetic fields in Pfeiffer 09.12.05.2 sample with density $n = 0.47 \times 10^{11} \text{cm}^{-2}$

- (1) Absence of in-plane magnetic field
- (2) 1 Tesla in-plane field

Fig. 6.25 shows g^* normalized to the GaAs band g -factor $|g_b| = 0.44$ [63] for different total magnetic fields where a spin-split minima was visible.

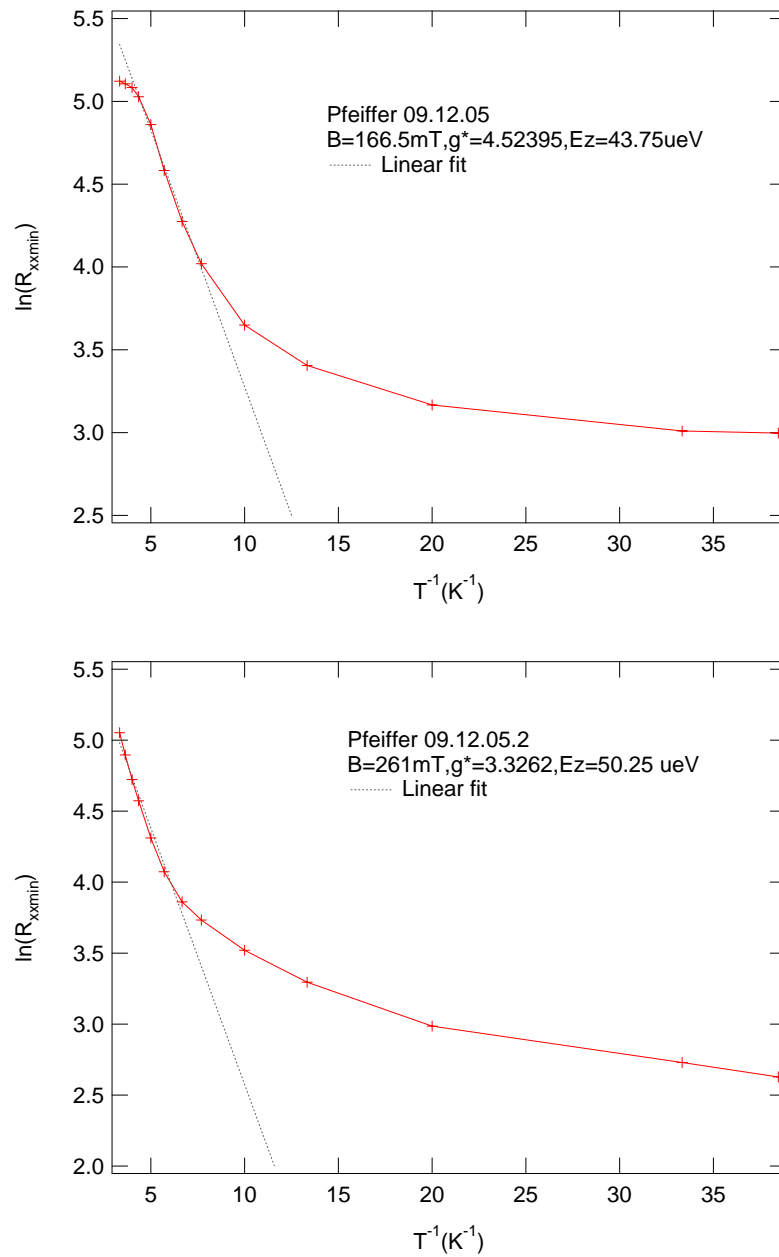


Figure 6.24: Arrhenius plots for two different magnetic fields, (in *upper panel*, for $B=166.5$ mT and in *lower panel*, for $B=261$ mT). g^* is extracted from a linear fit for temperatures where Eq. 6.16 is applicable in Pfeiffer 09.12.05.2 sample.

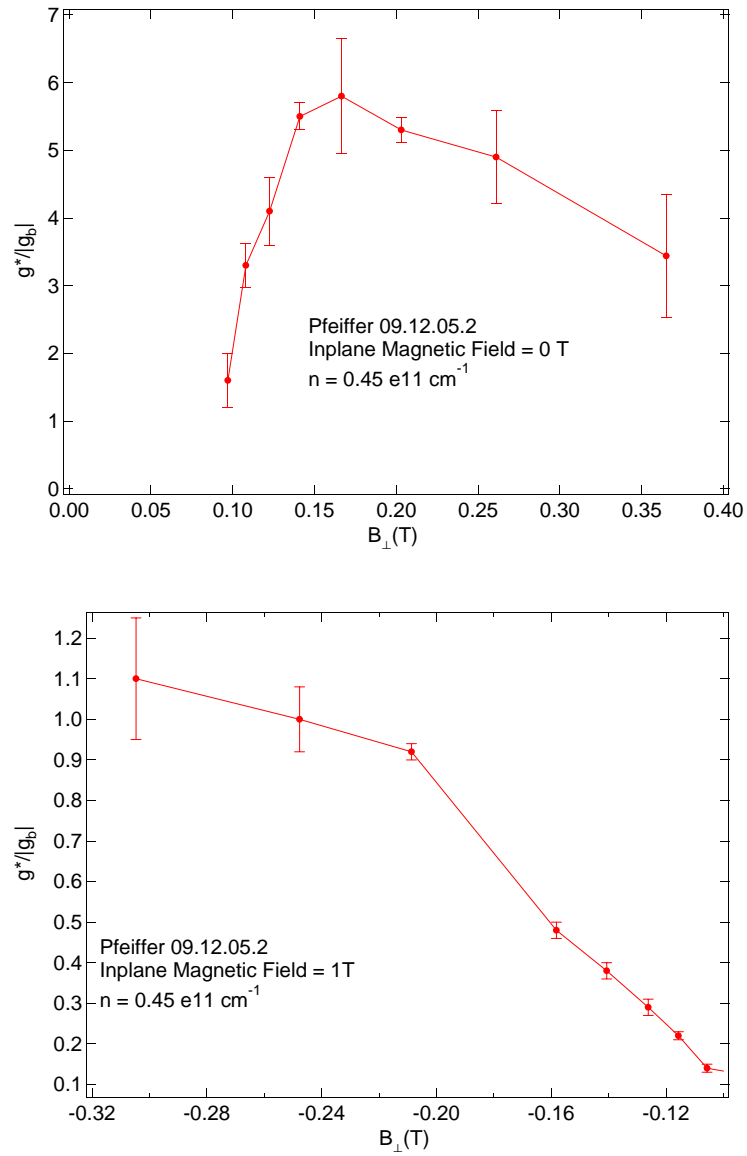


Figure 6.25: *Upper panel* g^* -factor with inplane magnetic field=0 T. *Lower panel* g^* -factor in the same sample in presence of inplane magnetic field of 1T in Pfeiffer 09.12.05.2 sample.

Similar experiment was done with Pfeiffer 7.28.08.2 sample. This sample is a Hall bar design with non gated and gated sections. The optimum current, magnet sweep rate, frequency of lock-in amplifier, time constant are determined first. The temperature is varied from base temperature, 24 mK to 600 mK. The $R_{xx,min}$ is obtained from spin split minima for every temperature at for a fixed magnetic field. $\ln(R_{xx,min})$ is plotted as a function of $1/T$. Fig.6.26 shows the Arrhenius plot for non gated section the Hall bar for two different magnetic field..

Fig.6.26 shows the Arrhenius plots for non gated section in Pfeiffer 7.28.08.2 sample in presence of only perpendicular magnetic field. Upper panel shows the Arrhenius plot for $B=285$ mT and lower panel for $B=346$ mT. The Arrhenius plot saturates at lower temperature. The linear fit is done in the range till the Arrhenius plot saturates. The slope of this plot gives g^* . The g^* for 285 mT is 3.6 ± 0.25 and that for 4.4 ± 0.25 . The error bar is determined from the fit error of the Arrhenius plot.

The same g^* extraction scheme is repeated for gated part of the Hall bar. Fig.6.27 shows the g^* factors for not gated and gated sections Hall bar. No in-plane magnetic field is used. The red trace is for non gated section which has density of $0.76 \times 10^{11}/cm^2$ and blue trace for gated section with density of $0.067 \times 10^{11}/cm^2$. The g^* factor in both sections depends on the magnetic field. The error bars are derived from different g^* -factor fit ranges.

In both wafers, Pfeiffer 09.12.05.2 and Pfeiffer 7.28.08.2, the effective g^* -factor is greater than its band value.

6.5.4 Conclusion

The measured g^* -factors show strong dependence on the perpendicular magnetic field and on the total magnetic field. In Fig. 6.25, upper panel in absence of in-plane field, for Pfeiffer 09.12.05.2 sample the maximum values are about 5.4 times higher ($\Delta_Z = 27.9\mu eV, B_{tot} = 0.203T$) than the GaAs band value. These high values were also measured by [64] for a similar system but are in contradiction with measurements done on GaAs/AlGaAs and Si-MOS systems in [65] and [42] where no large increase in g^* was seen for the same range of r_s . In presence of in-plane magnetic field, however, the g^* -factor values are high and the maximum value is almost 1.1 times larger than the band value. The presence of in-plane field changes the frequency of the SdH oscillations which reflects in the effective g^* .

For Pfeiffer 7.28.08.2 sample, the maximum value of the effective g^* -factor is 4.2 times higher than the band value in non gated section and 2.4 times higher in gated

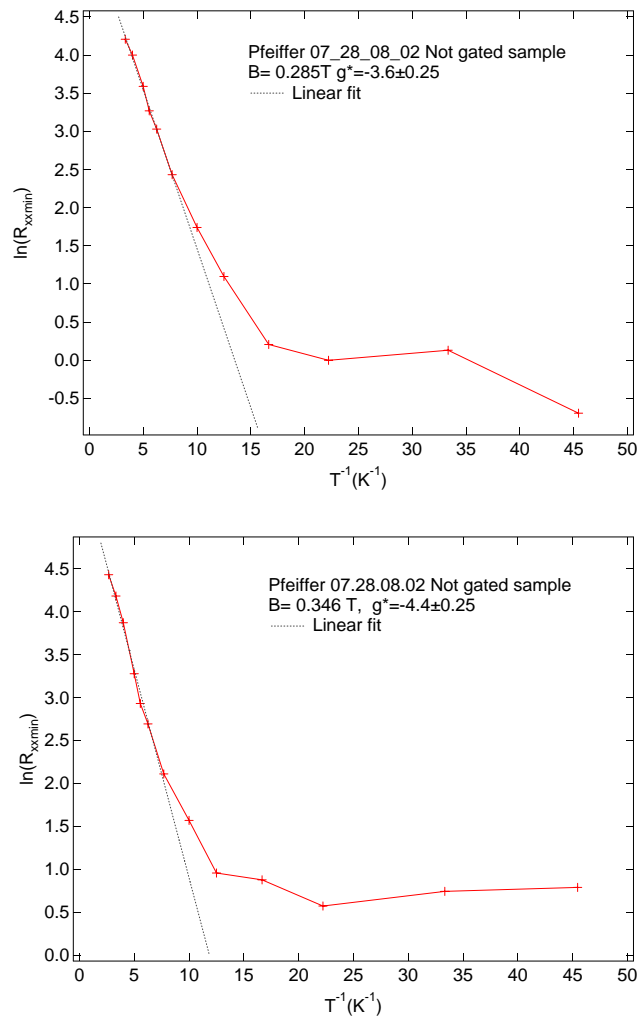


Figure 6.26: Arrhenius plots in non gated section for two different magnetic fields.. *Upper panel* shows Arrhenius plot in not-gated sample for $B=285$ mT and *Lower panel* g^* shows Arrhenius plot for $B=346$ mT in Pfeiffer 7.28.08.2 sample with $B_{in-plane} = 0$.

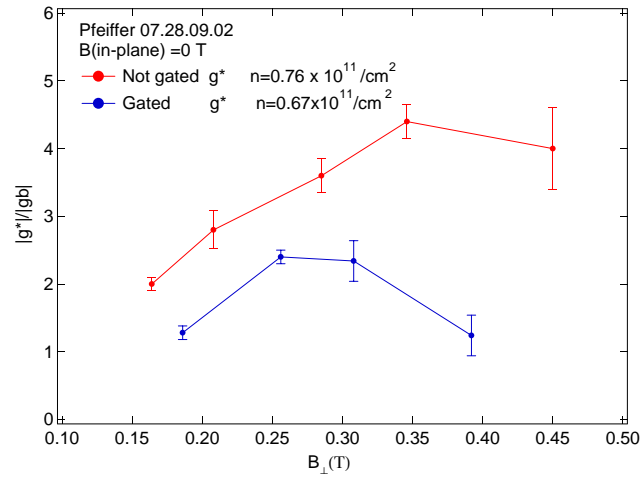


Figure 6.27: g^* -factor normalized to $|g_b|$ for not gated and gated sections of Pfeiffer 7.28.08.2 sample. $B_{in-plane} = 0$.

part of sample. This is the effect of different densities. In both sections, however, the qualitative behavior of effective g^* is similar.

6.5.5 Determination of electron temperature from Arrhenius plot

The slope of $\ln(R_{xxmin})$ vs $1/T$ is also used electron thermometry. The Arrhenius plot saturates after a certain temperature. It means, $\ln(R_{xxmin})$ is independent of inverse of temperature. The linear fit intercept on the inverse temperature axis gives the upper limit of electron temperature.

The linearity in the Arrhenius plot (Fig. 6.24, 6.26) of $\ln(R_{xx,min})$ as a function of $1/T$ with T being the mixing chamber, can be seen only if electron temperature T_e was equal to mixing chamber temperature. As soon as the temperature of the electrons and the helium mixture differed, the data points deviated from the linear behavior. This was used to estimate the electron temperature in the sample. The line fit intercepts at a certain point in $1/T$ axis. This temperature is taken as the upper limit of the electron temperature in the sample. However this is also limited by the disorder hence only gives upper boundary for the electron temperature.

From the Arrhenius plots for Pfeiffer 09.12.05.2 (Fig. 6.24) and Pfeiffer 7.28.08.2 (Fig. 6.26) samples, the upper limit of electron temperature was estimated to be around $90 \text{ mK} \pm 5 \text{ mK}$. For quantum scattering time, we assumed highest electron temperature to be 100 mK for base temperature measurement. This was confirmed in another experiment with lateral quantum dot where we found the

electron temperature to be around 85 mK. Though this electron temperature is high compared to other experimental set ups, it found to be sufficiently good for out further measurements.

7 Transport and Quantum Scattering times

7.1 Quantum Scattering Time

In the two-dimensional electron gas (2DEG) various lifetimes are introduced by a finite amount of disorder. Electron transport in semiconductors is generally characterized by a transport lifetime τ_t , which is defined by the relaxation-time approach to the Boltzmann equation and is related to the conductivity, through $\sigma = ne^2\tau_t/m^*$. However, there is a quantum lifetime (single-particle relaxation time) τ_q describing the decay time of one-particle excitations and characterizing the quantum-mechanical broadening of the single-particle electron state [[41] - [47]]. The quantum lifetime τ_q and the transport lifetime τ_t are given by [[43] - [44]]

$$\frac{1}{\tau_q} = \frac{m^*}{\pi\hbar^3} \int_{\pi}^0 d\theta |V(q)|^2 \quad (7.1)$$

$$\frac{1}{\tau_t} = \frac{m^*}{\pi\hbar^3} \int_{\pi}^0 d\theta |V(q)|^2 (1 - \cos\theta) \quad (7.2)$$

with $q = 2k_F \sin(\theta/2)$, and $k_F = \sqrt{2\pi n_s}$. $|V(q)|$ is the probability of scattering through an angle θ from a state \mathbf{k} to a state \mathbf{k}' on the Fermi circle. For a short-range scattering potential τ_t and τ_q are approximately equal [?]. But for modulation-doped GaAs/AlGaAs heterostructure, where the dominate scattering mechanism is the long-range potential associated with ionized donors which are far from the 2DEG and which produce predominantly small-angle scattering, τ_q will be much smaller than τ_t since the $(1 - \cos\theta)$ weighting factor diminishes at small angle θ .

Since all scattering events contribute with equal weight to τ_q , while τ_t is not sensitive to small-angle scattering, the two times are not identical. For short-range scattering potentials, like interface-roughness scattering in metal-oxide-semiconductor (MOS) structures, the two scattering times are the same [45]. However, in modulation doped heterostructure, where the dominant scattering mechanism is the long-range potential arising from remote ionized impurities, the two scattering times can differ significantly. The ratio of the two time τ_t/τ_q is expected to vary with carrier density.

The ratio of τ_t/τ_q for a 2DEG has been investigated theoretically and experimentally by a number of researchers. Das Sharma and Stern [45] have calculated τ_t and τ_q due to remote ionized impurity scattering and predicted that their dependence on spacer layer thickness as well as the carrier density. Gold [46] has investigated

the effects of interference-roughness scattering, alloy scattering, and remote ionized impurity scattering on the scattering times in the GaAs and $In_xGa_{1-x}As$ material systems. It is believed that in $GaAs/Al_xGa_{1-x}As$ modulation-doped heterostructure, at low temperatures, remote ionized impurity scattering is dominant scattering mechanism. Also, for remote ionized impurity scattering [2], $\tau_t/\tau_q = 1$ for $2k_F\alpha \ll 1$ and $\tau_t/\tau_q = (2k_F\alpha)^2$ for $2k_F\alpha \gg 1$, where α is the spacer layer width and k_F is the Fermi wave vector. In other words, for low carrier densities, the ratio of τ_t/τ_q is unity, while for higher densities, the ratio varies linearly with carrier density.

Experimentally, the ratio of transport and single particle scattering time or quantum scattering times has been investigated by Coleridge [47] for samples. The single particle scattering lifetime is related to the amplitude of the SDH oscillations and was calculated from Dingle plots [3]. The expressions given by Ando [55] and Ishihara and Smrcka [56] for the magnetoconductivity, valid for low fields, do not distinguish between long-range scattering and short range scattering. Coleridge, Stoner and Fletcher [57] offered a modified expression which made a distinction between the momentum relaxation time and single-particle scattering time. The amplitude ΔR of the SDH oscillations is given by

$$\delta R = 4R_0 X(T) \exp(-\pi/\omega_c \tau_q), \quad (7.3)$$

where R_0 is the zero-field resistance, ω_c is the cyclotron frequency and $X(T)$ a thermal damping factor, given by

$$X(T) = (2\pi^2 kT/\hbar\omega_c) / \sinh(2\pi^2 kT/\hbar\omega_c) \quad (7.4)$$

In a Dingle plot, the logarithm of $\delta R/4R_0 X(T)$ is plotted against $1/B$, which is a straight line with an intercept of zero. A good Dingle plot is linear and has an intercept of zero. The slope of this straight line gives $1/\tau_q$.

The experiments were carried out on a sample with electron density of $7.25 \times 10^{14}/m^2$ and mobility $9.55 \times 10^6 m^2/V.s$ at zero top gate voltage at base temperature (24mK) of the cryostat. The sample geometry is as described in

The experiment is done for three different mixing chamber temperatures, 24mK, 200 mK and 400 mK. The density in the 2DEG is tuned using top gate voltage. The top gate is changed from +100 mV to -350 mV with the interval of 50mV. The maximum density is $8.8 \times 10^{14}/m^2$ to $1.7 \times 10^{14}/m^2$ with corresponding change in mobility from $1.15 \times 10^3 m^2/V.s$ to $2.17 \times 10^2 m^2/V.s$. The variation of density and mobility as a function of top gate voltage can be seen in Fig.... The density mobility table is attached in Appendix A1.

7.1.1 Experimental Setup

The measurement setup for this experiment is current bias based Hall voltage measurement. The longitudinal voltage is measured to determine the τ_q across the top gate region in case of gated sample and also in non gated sample. The current for the measurement is determined by measuring the noise. The current is chosen such that the noise is low and the electrons are not heated by the current. This is determined from the longitudinal oscillation amplitudes as a function of magnetic field for different currents. The current is different for different temperatures. PAR 124A acts as current source. The time constant is determined by checking the test data for different time constants. Low noise BNC cables are used for entire measurement. The virtual ground to the sample is provided by Keithly IV convector. The sample is mounted perpendicular to the solenoid field. Keithley 2440 Source-Measure Unit acts as current source for solenoid field. The R_{xx} and R_{xy} are probed along the sample using two slave lock-in amplifiers. These lock-in amplifiers are synchronized with the master lock-in amplifier which is current source of the experiment.

The amplitude of the longitudinal oscillations are used to extract the quantum scattering time of the sample. The quantum scattering time is measured for different densities which are tuned by varying the gate voltage in case of a gated sample. For the non gated sample, τ_q is extracted for a fixed density. Both samples are fabricated from the same wafer. Non-gated and gated samples are used to determine the basic characteristics of the sample e.g. temperature dependence of density and mobility, m^* , g^* . Temperature variation of the wafer for both non-gated and gated sample can be seen in Fig. 7.1

The temperature is varied from 4K to base temperature of the cryostat, i.e. 20 mK. The density for not-gated and non gated samples is unaffected by the temperature variation. The variation of mobility as a function of temperature can be seen till around 500 mK. After that, for lower temperatures the mobility saturates. This can be seen for both gated and non gated samples, with or without perpendicular magnetic field. The mobility of the not-gated samples is higher than gated samples. The strain induced by the top gate layer on the GaAs lattice, increases scattering and hence the mobility is lower in gated sample. The variation of mobility agrees well with [32]. The variation of density and mobility as a function of gate voltage is shown in Fig. 7.2

The change in density and mobility with respect to the gate voltage is consistent with the density and mobility values determined from individual Hall resistance within few percent. As the density changes with gate voltage, the amplitude of

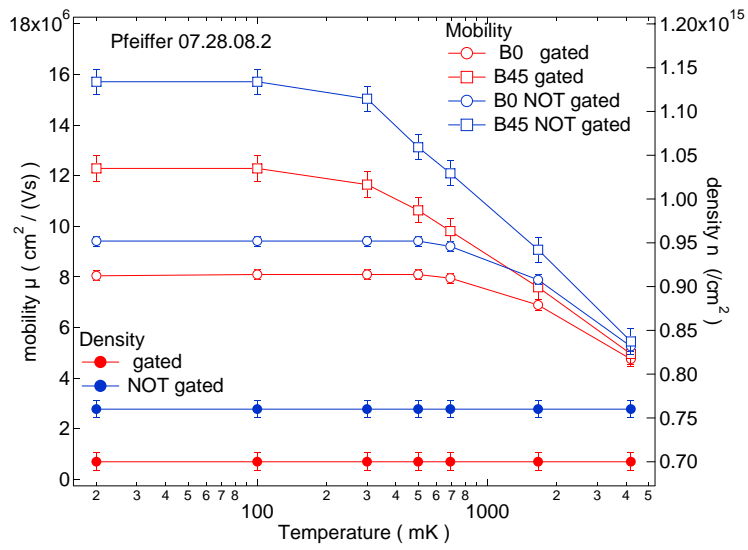


Figure 7.1: Variation of Density and mobility in a gated and non gated sample as a function of temperature

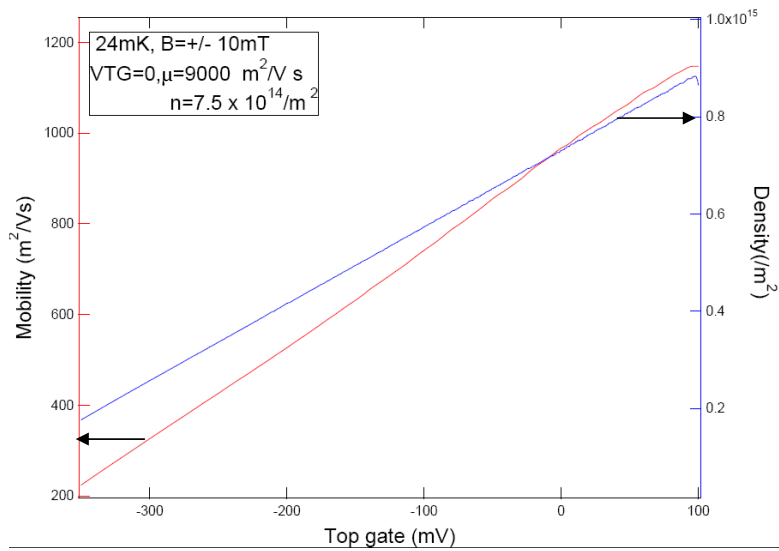


Figure 7.2: Density and mobility variation with gate voltage

the longitudinal resistance also changes.

For τ_q measurement, the density for each gate voltage is determined using the corresponding Hall resistance since $R_H = \frac{1}{en}$. The density and mobility along with mean free path, Fermi energy etc variation with gate voltage is shown in table For base temperature measurement, the current used is 9.22 nA with 125 Hz, reference frequency of the lock-in, time constant of 1s. Dingle curve is plotted using the amplitude of the R_{xx} oscillations and the inverse of magnetic field. The amplitude variation is considered in low magnetic field regime, classical regime. Fig. 7.3 shows the R_{xx} for different gate voltages.

To extract the amplitudes from the oscillations, a simple code is generated in IGOR, which takes into account the maximum and minimum points in each oscillation. This amplitude is the input for Dingle plot. From Eq. Equation 7.3, and Eq. Equation 7.4, logarithm of $\Delta R/4R_0X(T)$ is plotted against $1/B$. Here the R_0 is longitudinal resistance where the oscillations in the longitudinal resistance are onset. A typical Dingle plot at base temperature for -50mV gate voltage is shown in Fig. 7.4

The line fit passes through origin which is indication of a good Dingle plot. The noise in the measured R_{xx} data is indicated in the error bar. The fit range is determined from the oscillation in the low magnetic field regime. After a certain limit of magnetic field, the logarithmic term deviates from straight line. The individual amplitudes and $X/\sinh(X)$ term are straight lines but its the logarithm of these terms is saturating after a certain $1/B$. The reason could be onset of the quantum effect in the sample with increasing magnetic field. The effect is more prominent as the gate voltage is reduced i.e. the carrier density is lowered.

The slope of the straight line in the Dingle plot gives the quantum scattering time for the particular density. With the same procedure, τ_q is found for all the densities. Fig. 7.5 shows the variation of τ_q as a function of carrier density of the 2DEG.

The error on the τ_q is due to the different electron temperatures. For base temperatures, we have tried four different electron temperatures, 25 mK, 50 mK, 75 mK and 100 mK. The upper bound of the temperature can be found from R_{xxmin} at the spin splitting valleys data which is used to determine the g^* in section 6.5. But in this experiment, we do not have enough data for spin splitting valleys, we have used chi square error during the fit to define the upper limit of the electron temperature. This upper limit of the electron temperature agrees with the upper limit of 100 mK, found in the same wafer, and same setup discussed in chapter..

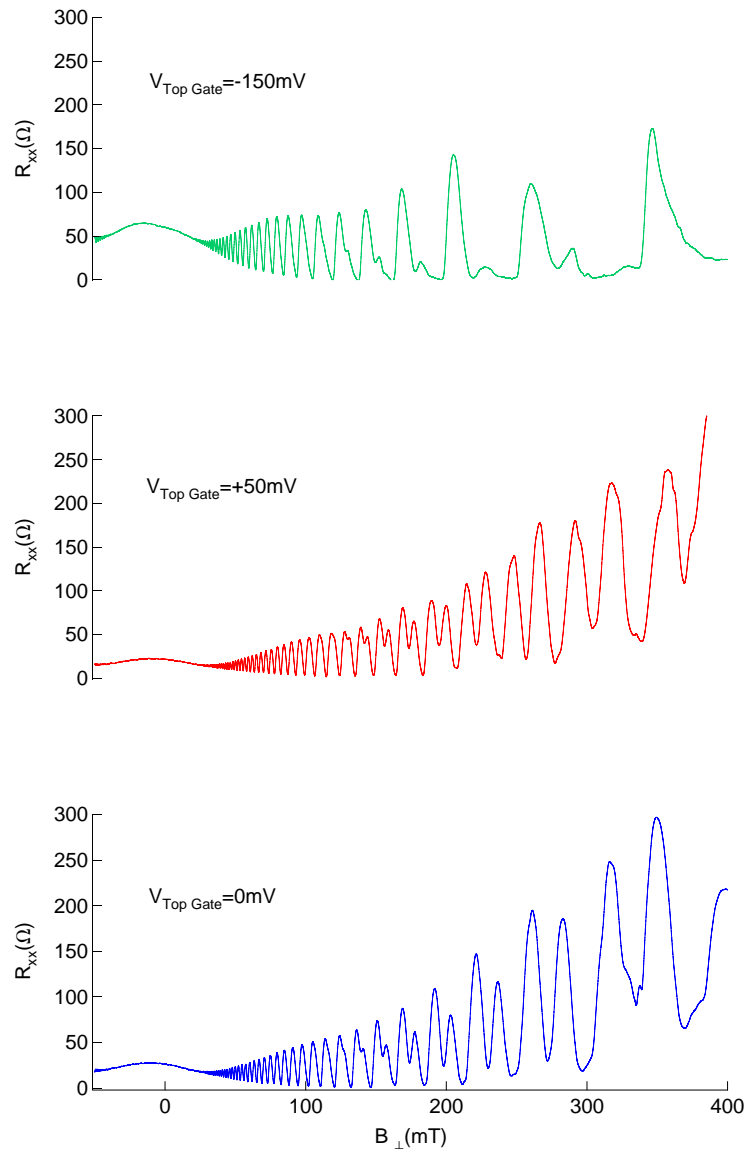


Figure 7.3: Longitudinal oscillations at three different gate voltages, +50,-50 and -100mV

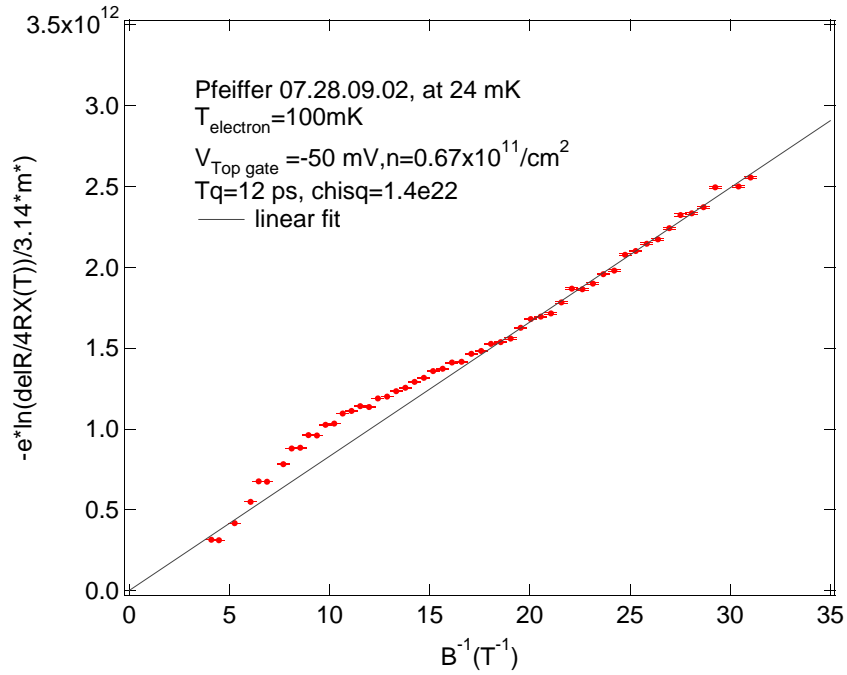


Figure 7.4: Dingle plot for base temperature, VTG=-50 mV

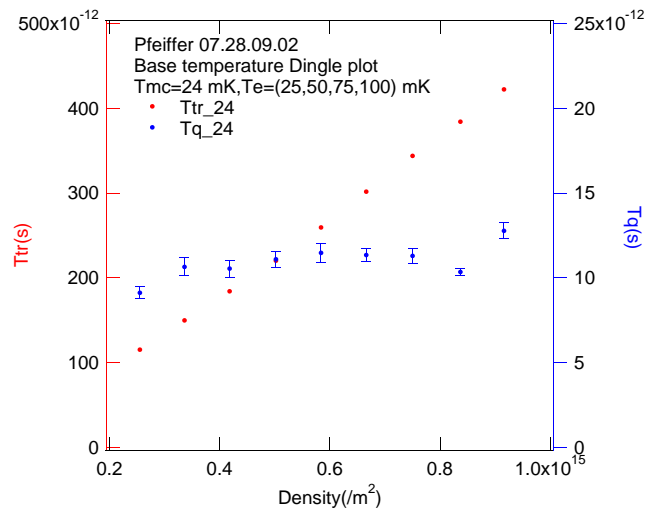


Figure 7.5: Transport time and quantum scattering time at base temperature as a function of carrier density

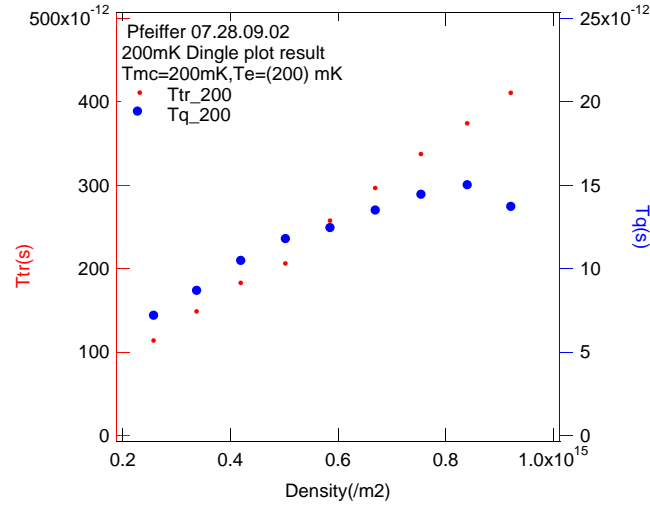


Figure 7.6: Transport time and quantum scattering time at 200 mK as a function of carrier density

The graph 7.5 also the variation of the measured values of transport time with the 2DEG density. Transport time τ_t increases with increasing carrier concentration. The variation of τ_q is almost constant as a function of carrier concentration. It seems that for our wafers, the quantum scattering time is almost independent of carrier concentration.

We have done the same experiment with two different temperatures, 200 mK and 400 mK. The current used for 200 mK experiment is 18.36 nA. The frequency and the time constant settings are same as for 24 mK. Fig 7.6 shows the variation of τ_q as a function of carrier density.

The quantum scattering time for 200 mK shows decrease with decreasing carrier concentration. The τ_t variation at 200 mK shows the same behavior as for base temperature. The transport time also decreases with decreasing carrier concentration. according to the theory the quantum scattering time is independent of temperature ([41]), but our analysis shows that for higher temperature the quantum scattering time decreases with carrier density. The electron temperature used for analysis is 200 mK

For 400 mK measurement, the current used is 46 nA. The τ_q variation at 400 mK shows decrease with decrease in carrier concentration. The transport time also decreases with decrease in carrier concentration. In case of 400 mK, the amplitude of longitudinal resistance oscillations at lowest carrier density are not enough to plot

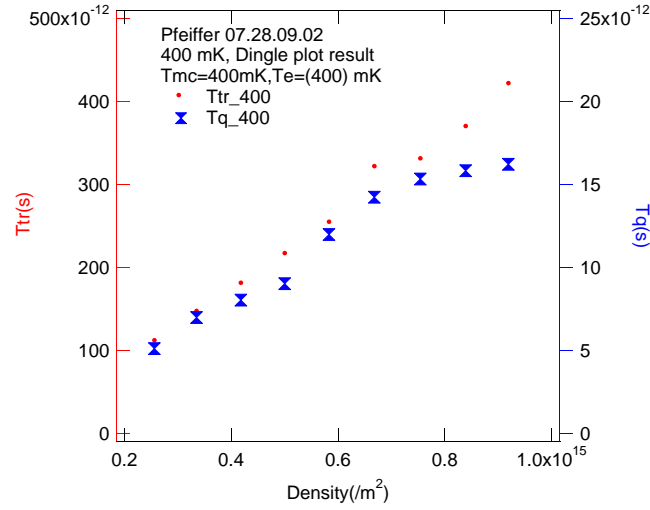


Figure 7.7: Transport time and quantum scattering time at 400 mK as a function of carrier density

a Dingle curve, so the lowest density point is neglected for 400 mK measurement data. Fig. 7.7 shows the graph for 400 mK, also includes the transport time for 400 mK

7.1.2 Results and Discussion

In earlier experiments, the single-particle lifetime τ_q in Si-MOSFET's was found [?] to be nearly equal to the transport lifetime τ_t while in AlGaAs/GaAs-heterostructure τ_t , turned out to be one or even two orders of magnitude larger than τ_q [[49], [50],[51]]. According to Das, subramaniam, [52], the τ_q is independent of carrier concentration. The τ_t is increasing with increasing the carrier concentration.

While the τ_q for wafer with thicker spacer layer decreases with decreasing the carrier concentration. In other sample, with InAs self assembled quantum dot, the quantum lifetime is almost independent of carrier concentration [53]. All these measurement are done at .. temperatures. In our experiments we have tried three different temperatures, base temperature, 200 and 400 mK. Our results for gated sample shows that at low temperature the τ_q is independent of carrier concentration while for higher temperatures, τ_q decreases with decreasing carrier density. Fig. 7.8

For non gated sample from the same wafer, at fixed density the value of τ_q agrees with the value of τ_q at zero gate voltage. Fig. 7.9.

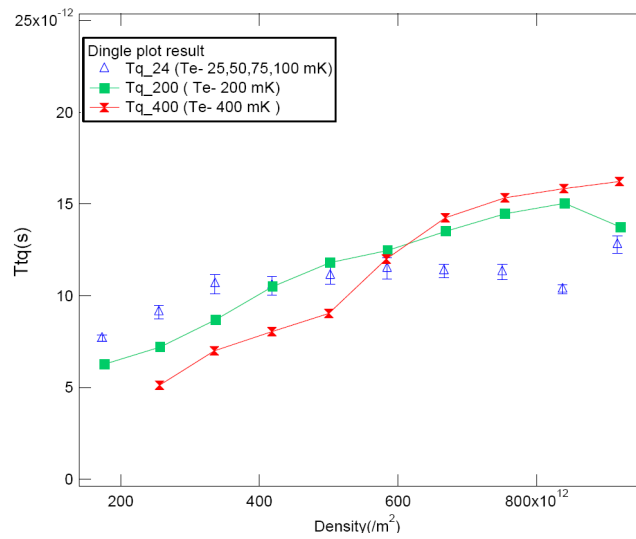


Figure 7.8: Quantum scattering time at different temperatures as a function of carrier density

The ratio of transport time (τ_t) and quantum scattering time (τ_q) is shown for three different temperatures is shown in Fig. 7.10.

For low temperatures the ratio of the two times decrease with decreasing with density. For high temperatures, the transport time seems to be dominant over quantum scattering time. Long range scattering events dominate over short range scattering. For other systems like FET [58] shows a similar behavior.

We showed a method to obtain quantum scattering time as a function of carrier concentration. More studz is need to be done for such a system at high temperatures.

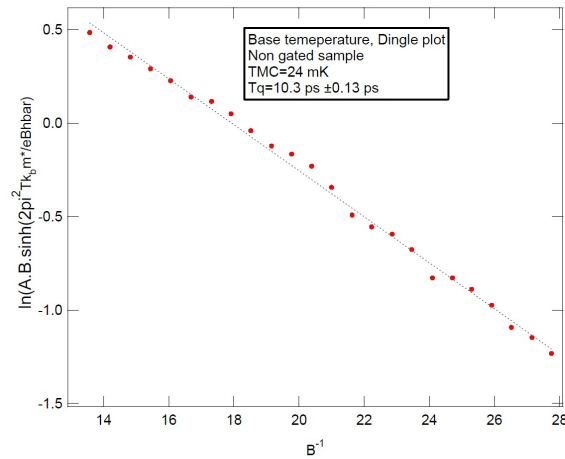


Figure 7.9: Quantum scattering time in a non gated sample

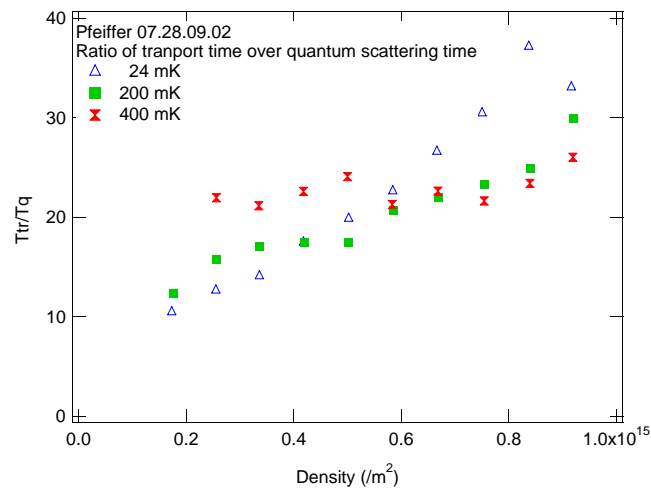


Figure 7.10: Ratio of transport time to quantum scattering time as a function of density for different remepratures.

8 Delocalization by disorder in layered system

8.1 Introduction

P.W. Anderson suggested the possibility of electron localization in a semiconductor [66]. An increase in degree of disorder will lower the conductivity. Thus the higher the disorder, lower the mean free path and possible absence of conductance. In recent years theoretical interest has been increased to break the Anderson localization [67]. This can be achieved by internal correlations in random sequence of scattering potentials.

8.2 Theory

Stronger disorder is induced in phase-incoherent regime. This leads to shorter scattering time. In phase-coherence regime, the stronger disorder leads to Anderson localization which reduces the conductivity. The theory by Maslov et al [68] proves this to be not applicable in all cases. They have proposed a model with two types of disorders, bulk disorder and planar disorder. Tuning one of these two disorders can break the Anderson localization and enhance conductivity in one direction. A simple model is proposed here with two types of disorder.

The planar barriers are located randomly and isotropic impurities are distributed randomly in between the barriers (Fig. 8.1). In the model, two types of disorders are introduced. Planar disorder is one dimensional and bulk disorder is three dimensional. According to Drude model, in a semiclassical case, conductivity is inversely proportional to the effective mass.

$$\sigma = \frac{ne^2\tau_t}{m^*} \quad (8.1)$$

However, in some cases, the observed ratio of the in-plane and out-of-plane conductivities exceeds the (inverse) ratio of the effective masses by few orders of magnitude. e.g. in graphite [69], where the graphene sheets are stacked, and also in NaCo2O4 [70], cuprates [71], etc. Large conductivities are observed in graphite due to stacking faults in graphene sheets. Electrons are localized in these arrays of sheets. Similar picture can be used to increase the conductivity in 2DEG where the "stacking faults" are artificially introduced.

$$\frac{\sigma_{\parallel}}{\sigma_{\perp}} \approx \left(\frac{m_{\parallel}^*}{m_{\perp}^*}\right)^{-1} \quad (8.2)$$

Assume $U(z)$ to be one dimensional potential and $V(x,y,z)$ to be the 3-dimensional potentials of isotropic impurities. In the absence of bulk disorder,

$$V(x, y, z) = 0 \quad (8.3)$$

The in–and–out of plane degrees of freedom separate

$$\epsilon(k_{\parallel}^{\rightarrow}, k_z) = \epsilon_{\parallel}(k_{\parallel}^{\rightarrow}) + \epsilon_z(k_z) \quad (8.4)$$

Accordingly, the electron wave function is factorized as

$$\psi(r_{\parallel}^{\rightarrow}, z) = \varphi(r_{\parallel}^{\rightarrow})\chi(z) \quad (8.5)$$

With effective 1D Schroedinger equation for χ

$$[\epsilon_z(-i\partial_z) + U(z)]\chi(z) = (E - \epsilon_{\parallel}(k_{\parallel}^{\rightarrow}))\chi(z) \quad (8.6)$$

where χ_{\parallel} is the (quasi) momentum along the planes. All the states are now localized along z -direction due to a small disorder. The dc conductivity across the planes, σ_{zz} , is zero while the in-plane conductivity, σ_{\parallel} , is infinite since barriers do not affect the electron motion along the planes.

If bulk disorder is added, in– and out– of plane degrees of freedom are mixed and there is no separation of variables. This destroys 1D localization in z -direction. σ_{zz} increases with bulk disorder. σ_{zz} is at peak when the two disorders are similar. σ_{zz} decreases upon further increase of bulk disorder. σ_{\parallel} decreases monotonously with bulk disorder. A sketch of expected dependences of σ_{zz} and σ_{\parallel} on 3D disorder is shown in Fig. 8.1(b)

In conclusion, a system with two types of disorder, randomly spaced planar barriers and bulk impurities exhibits quite unusual transport properties. In the absence of bulk disorder, it behaves as a 1D insulator in the out–of–plane direction and as an ideal metal in the in-plane direction. Bulk disorder renders both conductivities finite; conductivity in z -direction increases with bulk disorder until two disorders become comparable.

Such a system can be realized in a 2D electron gas with an array of randomly spaced stripe-like gates.

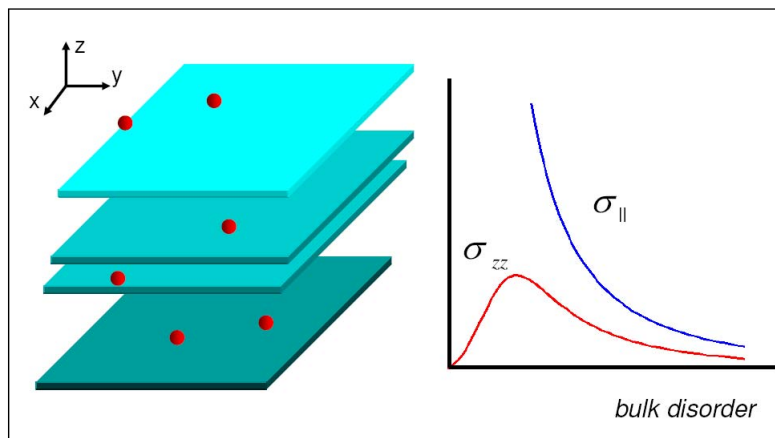


Figure 8.1: (a) A system of randomly spaced parallel potential barriers and randomly distributed isotropic impurities. (b) expected dependences of the in- and out-of-plane conductivities on bulk disorder. [68]

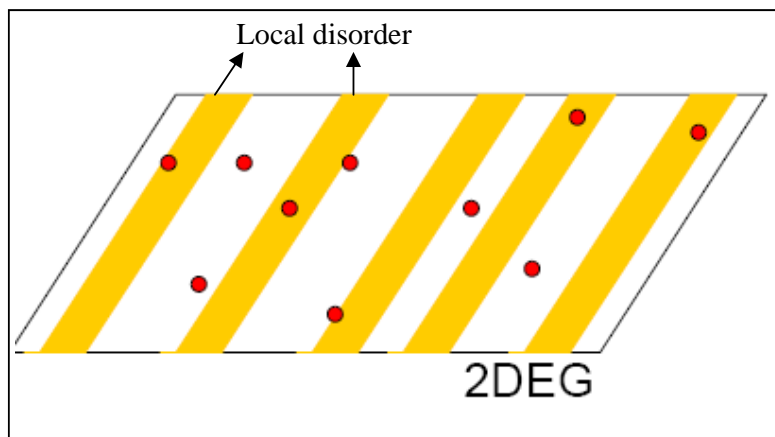


Figure 8.2: an array of randomly spaced stripe-like gates as a local disorder

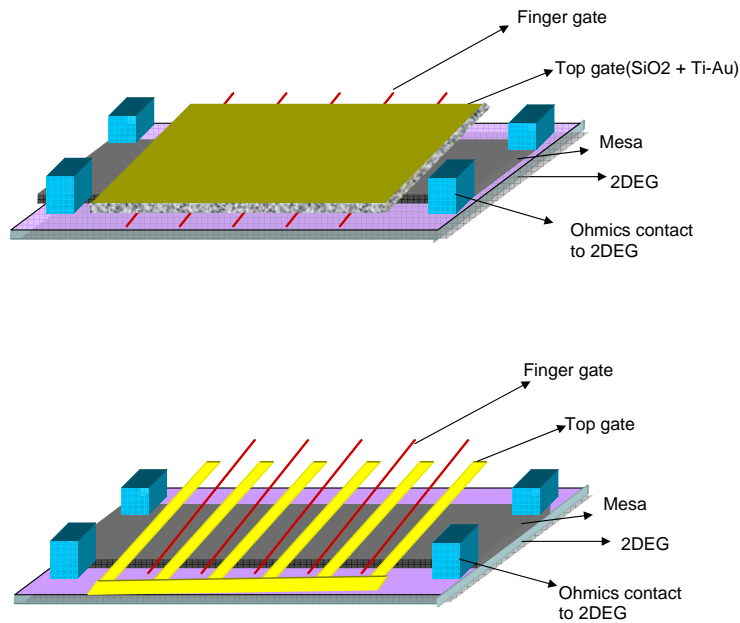


Figure 8.3: Device designs used in the experiment. (a) Device with SiO_2 (b) Device with intercalated finger and top gates

The realization of such a system can be shown as in Fig.8.2¹. Yellow strips are the local disorder and the red filled circles are randomly distributed impurities.

8.3 Experiments

The samples designed for this experiment are discussed in 5.2. There are two types of designs used in this experiments. We will discuss both types in detail in following sections. The local disorder is created using finger gates. Applying some voltage on these gates creates potential barrier which acts as local disorder. The bulk disorder is created with top gates. This top gate is fabricated in two different ways. In one type the continuous top gate is overlapping the finger gates, and these two types of gates are separated by insulating layer of SiO_2 . In the second type, the top gate is not overlapping the finger gates, instead they are intercalated. There is a gap of $1.4\mu m$ between the part of top gate and the finger gate on each side. Fig. 8.3 shows the design for both the samples.

¹Prof. D.M.Zumbuhl's presentation in journal club

8.3.1 Experiments with finger gates sample with SiO_2

The sample is fabricated using Pfeiffer 8.29.09.01. The growth profile is shown in Fig.5.3(b) The sample is Hall bar with dimension of $1595\mu \times 1445\mu m$. The dimensions of Hall bar are $1560\mu m \times 100\mu m$. The mesa is etched below the the donor level i.e. around 100 nm. tests done on the wafer for etching shows that 100 nm is sufficient to separate the devices. The mesa height was first simulated in Matlab. Mesa is defined using optical photolithograph and wet etching technique The details are described in section 5.7.1.

After mesa photolithography, ohmics pattern is fabricated. Before material deposition, the sample is dry etched for 55 sec. with oxygen plasma. This removes the resist residue and improves ohmic contact functionality. The sample is then dipped in 37% hydrochloric acid (HCl) and rinsed with water and immediately mounted in the evaporator. Ohmics are defined by optical photolithography. Ohmics materials are deposited in ebeam evaporator. We have deposited $Ni : Ge : Au : NI : Au :: 5 : 125 : 250 : 20 : 50$. The first Ni layer is acts as wetting layer and Ge is for doping the ohmics contact. Annealing is done at $480^\circ C$ Details are described in 5.7.2. The average ohmic resistance in this sample at 4.2K is $200\ \Omega$ in dark. The 2DEG resistance is $20\ \Omega/\square$ at 4.2K, in dark.

After ohmic contacts, the finger gates are fabricated using electron beam lithography. In the design, the width of finger gates is 150 nm. The average lithographic width of finger gates is 200 nm. The spacing between the finger gates is $23\mu m \pm 5\%$. This is determined from the mean free path at different gate voltages of the wafer. The details of wafer characteristics are shown in tabel 6.3. EHT of 20kV was used for PMMA (450 nm after spinning at 6000 rpm) exposure. The sample is developed in solution of 1:3 of methyl-isobutyl-ketone (MIBK) mixed with 1:3% methyl ethyl ketone (MEK) by volume of the total solution. In the finger gate fabrication, it is important that the finger gates are continuous. In order to achieve the continuity, we need to remove the resist residue from the sample surface. After developing the sample, it was dry etched in presence of oxygen plasma. The rate of etching is maintained to be 1 nm/min. The sample is dry etched for 40 seconds. This removes the resist residue after developing.

Mesa height is around 100 nm. To deposit the finger gate material, we have to make sure that the gates steps the mesa. Also in our case, we had to think about not to deposit excess finger gate materials as we have two more layers to deposit in this sample with SiO_2 . We did experiments with few test samples to find out the minimum amount of material deposition to step up the mesa. Mesa is wet etched and it is isotropic. We used this property and estimated a relation between

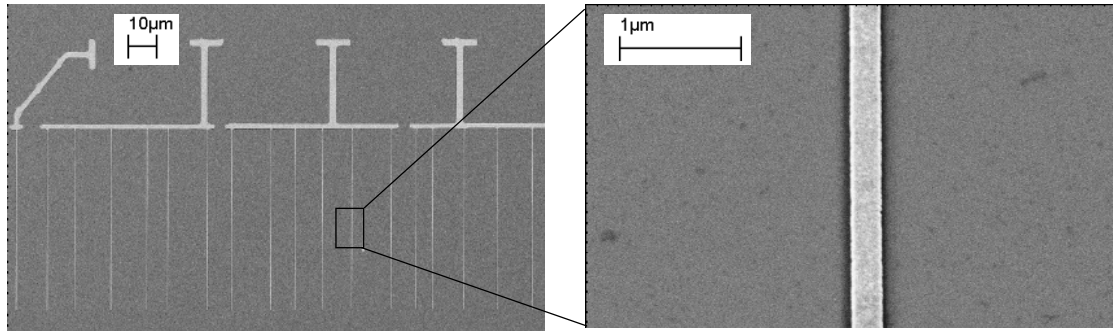


Figure 8.4: SEM image of finger gates, from test sample

the mesa height and the deposited material. To step up the mesa, it is sufficient to deposit the material with thickness of 80% of the mesa height. In our sample where the mesa height is 100 nm, we deposited around 80 nm of Ti-Au for finger gates, with 5 nm of Ti as wetting layer for 75 nm of Au. The SEM micrograph of finger gates is shown in Fig.8.4.

Lift off is done in acetone and sample is rinsed in IPA. The next step was to deposit insulating layer to separate the finger gates and top gates. In some test samples we tried to deposit Al_2O_3 in atomic layer deposition (ALD). This insures the continuous film deposition even at the edges. This process is usually done at high temperatures like 350°C. But we were using negative photoresist so ALD process temperature is limited upto 180°C. Above this temperature, the photoresist undergoes glass transition which is hard to lift off. Deposition of 10 nm of Al_2O_3 takes around 7-8 hours. But this turned out be not sufficient to insulate the two gates. So SiO_2 was used to insulate the finger gates and the top gate. 150 nm of SiO_2 and followed by 150 nm of Ti-Au covering the Hall bar was deposited.

The last fabrication step was for large gates which connects the gates to the bonding pads. For this step, 170 nm of Ti-Au was deposited. The sample is glued on chip carrier with PMMA glue and bonded with gold wire. Completed sample shown in Fig. 8.5. For convenience, the sample is labeled in three different sections of dimensions $300\mu m \times 100\mu m$ i.e. between two adjacent ohmics contacts on the Hall bar. The section which has just the top gate and no finger gates is labeled as 'top gate region', then 'finger gate region I' and 'finger gate region II' as shown in Fig. 8.5.

The first task was to characterize the sample at base temperature. The ohmic contact resistance, 2DEG resistance and the gate leakage current were measured

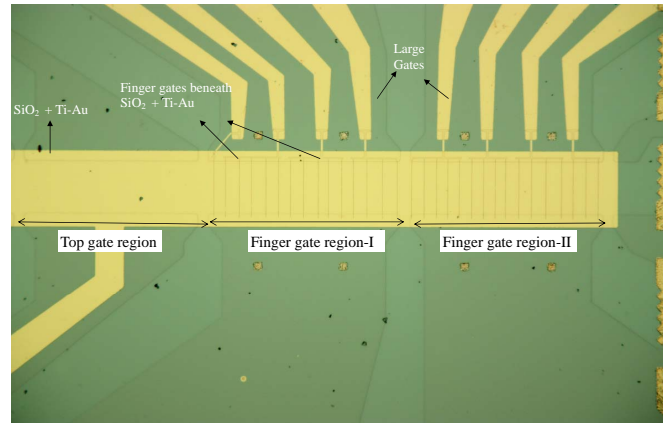


Figure 8.5: Optical image of a finger gate sample with SiO_2 . Three sections of each $300\mu m \times 100\mu m$ dimensiona are labeled as top gate region, finger gate region I and finger gate region II from left to right.

in dark. The average ohmic contact resistance was 150Ω and the 2DEG resistance was $8\Omega/\square$. The leakage current is 4 picoamps(pA) on the background of 9 nanoamps(nA). The density and mobility of the sample was determined as a function of gate voltage. Fig.6.4 shows density and mobility behaviors in this sample as a function of top gate voltage. The black line in the graph shows the density and the blue line shows the variation of mobility. The trace is taken at $\pm 20mT$. The details are described in section 6.2. The density and mobility at zero top gate voltage are $0.699 \times 10^{11}/cm^2$ and $11.14 \times 10^{11}cm^2/Vs$ respectively. The other relevant parameters like mean free path, Fermi wavelength, interaction strength are shown in table 6.3. The minimum density is 0.2×10^{11} and maximum density is $0.9 \times 10^{11}/cm^2$. The mean free path as a function of top gate voltage varied from $10.18\mu m$ to $71.35 \mu m$. As described earlier, the finger gate spacing depends on the mean free path of the wafer. In this sample, the average spacing between the finger gates is $23\mu m$ with a variation of $\pm 5\%$. In this sample, the mean free path of $23\mu m$ is achieved around $-350 mV$ of top gate. This is the region of gate voltage where we were expecting to see the increase in conductance.

In the first experiment set, the sample was current biased. PAR 124 lock in amplifier is used as master source and voltage is measured across the different regions of the sample. Fig.8.6 shows the characteristics of different regions in the sample as a function of top gate voltage at zero magnetic field.

In Fig.8.6, panels (a,b,c) show the voltages across different sections of Hall bar at zero magnetic field as a function of top gate voltage, at current of 9 nA, at

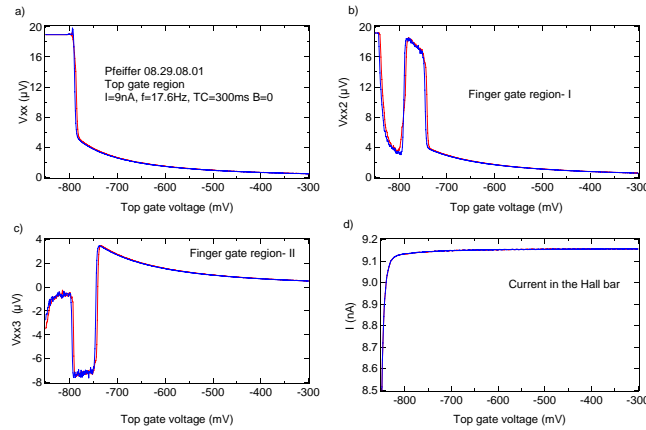


Figure 8.6: Characteristics of different regions of Hall bar as a function of top gate voltage at $B=0$ and zero finger gate voltage, with sweep down and sweep up directions at base temperature, 24 mK. (a) in top gate region (b) in finger gate region-I, (c) in finger gate region-II, (d) current across the Hall bar.

lock in frequency of 17.6 Hz and time constant of 300 ms. The red trace is for sweep down direction and blue trace is for sweep up direction. Panel (d) shows the current across the Hall bar. The 2DEG starts to deplete around -810 and current starts to decrease.

In panel 8.6(b), it was observed that the voltage peaks up at -735 mV and drops around -795 mV. The reverse can be seen in panel (c) around the same voltages. The in-phase and out-of phase components of lock in measurements were specially checked in these regions. Both the components are the same as for top gate region. This could be due to the presence of finger gates. The finger gate voltage is zero. The hysteresis in sweep up and down directions of top gate noticeable but still very small.

For a more sensitive measurement, the sample was then voltage biased. The lock in amplifier was used as the voltage source. The AC voltage was divided by 5000000, using a AC-DC bias box (self made). The current was probed across the whole sample to see the variation in the resistance across the whole sample. The voltage across the sample is $40 \mu V$. This measurement was done without and with magnetic field and also changing the finger gate voltage. Fig.8.7 shows the voltage biased and current supplied across the sample at 24 mK, and in the absence of magnetic field.

In Fig.8.7, the solid lines are for voltage sweep down direction and dashed lines

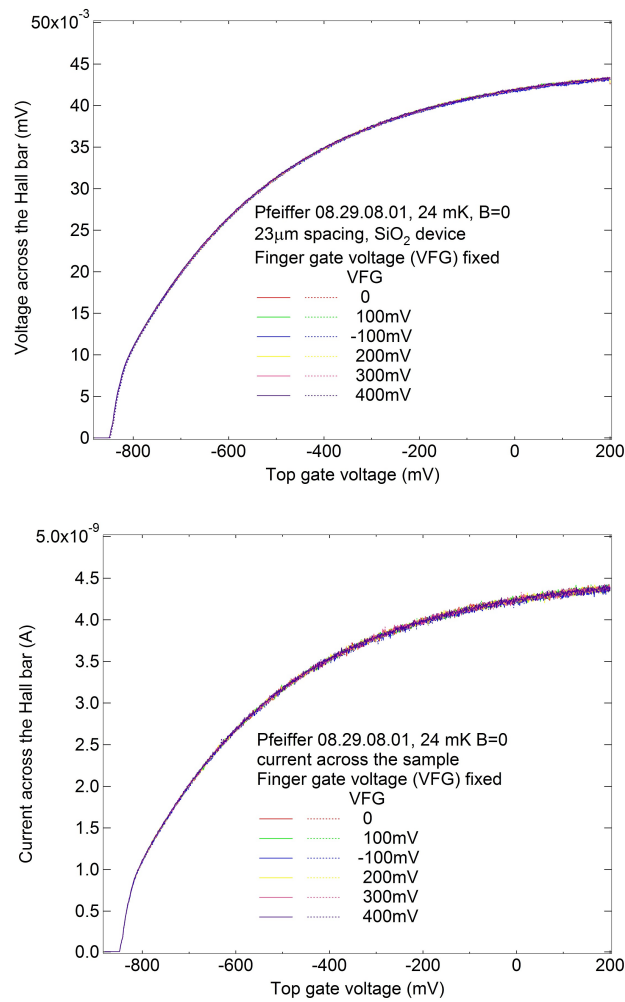


Figure 8.7: Voltage biased measurement at base temperature at $B=0$. The solid lines are for voltage down sweep and dashed lines are for voltage up sweep. The upper panel shows the voltage sourced and the lower panel shows the current probed. The finger gates regions are tuned to tunneling regime.

are for voltage up sweep. The finger gate voltage is tuned such that the 2DEG experiences scattering potential. The system is tuned in tunneling regime and the top gate voltage is swept. But the current across the sample shown in lower panel of the Fig. 8.7 shows no effect of tunneling regime.

In the same set up, a small perpendicular magnetic field was introduced. Fig.8.8 shows the voltage and current across the sample in presence of magnetic field of 10 mT. The solid lines are for voltage sweep down direction and dashed lines are for voltage up sweep.

In both experiments, the hysteresis in the top gate voltage is very small. Unlike the graphs for $B=0$, current traces taken in presence for magnetic field do show some difference for different finger gate voltages. But it still does not show the effect on resistance due to the local disorder of the finger gates.

The reason for not to observe the delocalization, could be the sweeping of top gate whose dimension is huge compared with the individual finger gate and this top gate voltage is also influencing the density of states beneath it and with respect to this change the local barrier created by the finger gates is negligible. To overcome this problem, we decided to find a compensation between the two gates.

To determine the compensation, we did a 2D sweep for top gate voltage and finger gate voltage in current bias mode. In both finger gate regions, we have single gates. This single gate is used to characterize the behavior of individual finger gates. We used finger gate in region I to find the compensation. The single finger gate voltage and top gate voltage are swept simultaneously. Fig.8.9 wave shows the wave found for compensation.

In Fig.8.9, the bottom axis is for finger gate voltage and left axis is for top gate voltage. The blue line in the 2D graph is the threshold wave for current 8.5 nA when the current sourced is 9 nA. This limit is chosen so that at this point the 2DEG is not depleted but can deplete beyond. So 8.5nA is chosen as a boundary for both the gate voltages. The color scale shows the current variation in the sample. The compensation wave is interpolated and used for further experiments. Using this compensation wave, we set the finger gate voltage according to the top gate voltage. How does the compensation work?. The top gate voltage is at certain voltage e.g. 0mV. At that point the finger gate voltage is set to -657.15 mV. For the next point on the top gate voltage, the finger gate voltage is set to the voltage accordingly. Thus it maintains some effective potential on the finger gate as the top gate is swept.

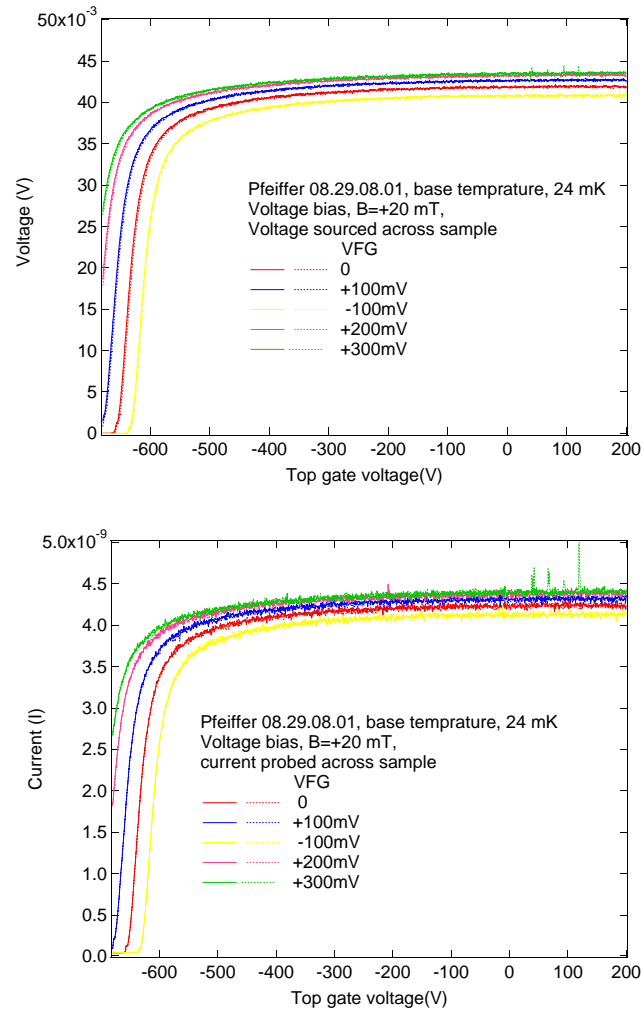


Figure 8.8: Voltage biased measurement at base temperature at $B=0$. The solid lines are for voltage down sweep and dashed lines are for voltage up sweep. The upper panel shows the voltage sourced and the lower panel shows the current probed. The finger gates regions are tuned to tunneling regime.

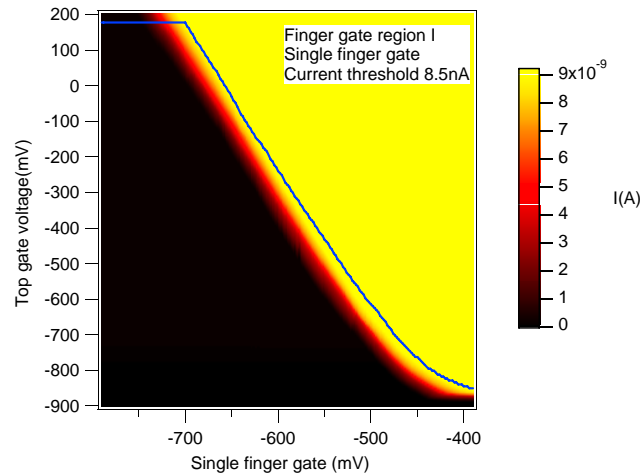


Figure 8.9: 2D diagram for current, sweeping single finger gate and top gate together, at base temperature, $B=0$

The sample is current biased. We did the further test with single gate. With the single gate, we should not see any localization. Finger gate region I is then tuned to see the localization. Fig.8.10 shows the resistance and current across the FG-I region using compensation to single gate and all finger gates in the region.

In Fig.8.10, the resistance across the finger gate I region is shown as a function of top gate voltage in the upper panel. The lower panel shows the current across the Hall bar. The blue line shows the resistance/current when single gate is compensated and the Red traces show the resistance/current when all the finger gate region is compensated with top gate voltage. The solid lines show the down sweep of top gate voltage while the dashed line is for up voltage sweep. From the graph, it can be clearly seen that the single gate is not showing any influence on the resistance. While in the case when all the finger gates in the FG-I region are compensated, the resistance does show some influence on the resistance in the FG-I region.

To determine the % of compensation, The region I of finger gates is now set to some weak tunneling regime of $136k\Omega$ by applying -660 mV on all the finger gates in region I. This tunnelling regime is maintained using the compensation wave. We compensated with no compensation and 95%,105% of the total compensation. This will edpalin us if the compensation is needed, and what should be the limit of compensation.

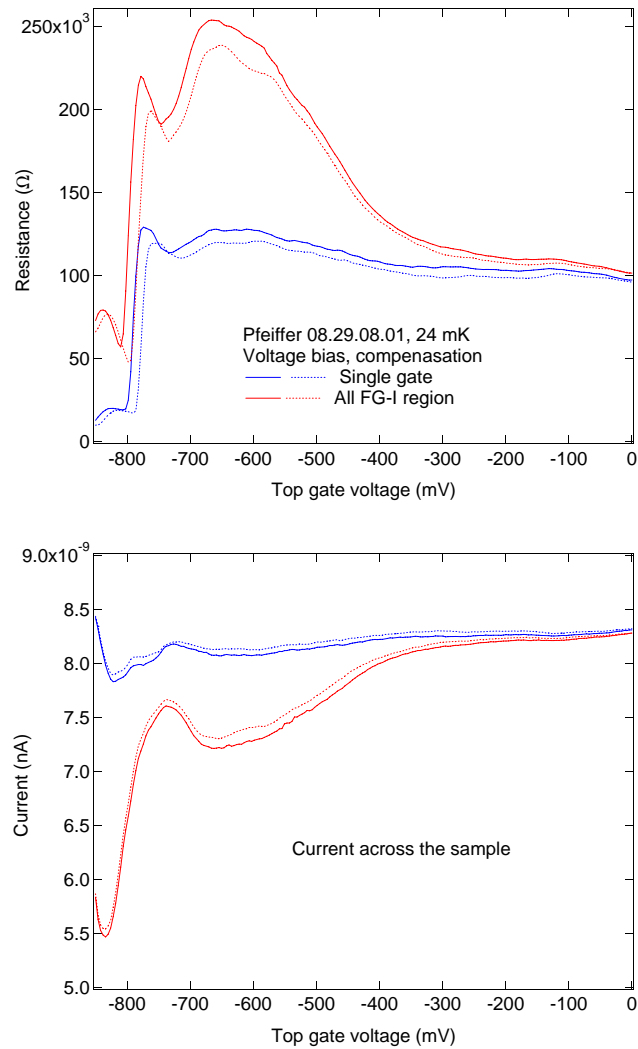


Figure 8.10: Resistance across FG-I region (*upper panel*) and current across the sample (*lower panel*) when the single finger gate and all finger gates in region I are compensated for top gate voltage. Solid lines- voltage down sweep, dashed lines-voltage up sweep

It is quite clear from Fig.8.11 that the compensation is needed to see the effect of finger gate potential. Green traces are for 95%, brown for 100% and blue for 105%. The solid and dashed lines are for voltage sweep down and sweep up directions respectively. For 95% compensation the change in resistance and current is larger than other compensation %. The decrease in resistance or increase in conductance/current can be seen more or less for all the %. But for 95% it is more prominent than other two %. So in the next few experiments 95% compensation was used between the finger gates and the top gate voltages. The change in current and resistance is however very close to the depletion voltage of the 2DEG. So there are limitations for the experiment. Now the tunneling barrier is changed using different finger gate voltages. We have used 42.1 k Ω , 100 k Ω and 450 k Ω . The resistance and current variations can be seen in 8.12 at zero magnetic field.

In Fig.8.12, the pink traces show resistance and current for 42.1 k Ω , the red trace is for 100k Ω and the blue trace is for 450k Ω . The solid and dashed lines are for sweep up and sweep down directions of the top gate voltage. For this experiment, the FG I region is tuned to a fixed tunneling regime and the top gate voltage is swept while probing the resistance across FG I region and current across Hall bar. From these graphs, we can conclude that the resistance and current variations depend on the tunneling regime set by the local disorder which agrees with the theory.

The same experiment is done for finger gate region II. This region also has a single gate which we used to find the compensation for the finger gates in region II and top gate. Fig. 8.13 shows the compensation wave determined from sweeping the single finger gate voltage and top gate voltage in a 2D.

The 2D trace for top gate voltage (bottom axis) and single finger gate voltage (left axis) was used to determine the compensation wave with a threshold current of 8.5nA. The blue line follows the current threshold. Here also we have set the compensation to 95%. The finger gate region II is set to some tunneling regimes, 54 k Ω , 110k Ω , 240k Ω and 494k Ω . In Fig.8.14 the resistance and current are shown for these different regimes. Blue traces are for 54 k Ω , red traces for 110k Ω , 240k Ω is shown by green line and the black line is for 494k Ω . The solid and dashed lines are for sweep down and up directions of the top gate voltage. The voltage in finger gate region I is zero during this experiment and magnetic field is zero.

The variation in resistance is dependent on the top gate voltage and also on the tunneling regime in the finger gate region II. As the top gate voltage is lowered, the resistance in the region goes up and after a certain gate voltage the resistance

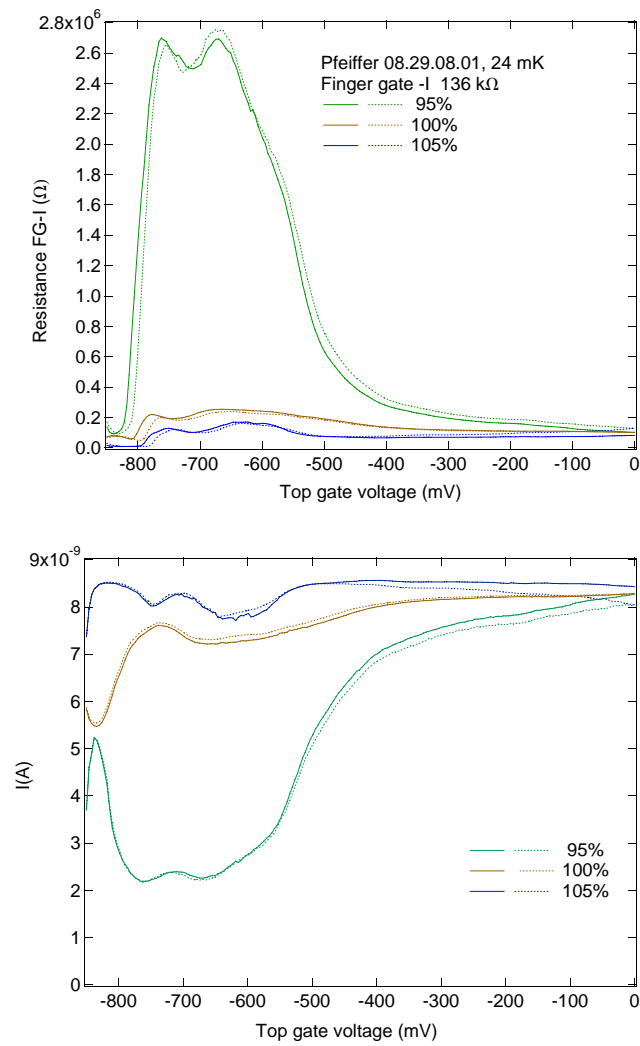


Figure 8.11: Resistance across FG-I region (*upper panel*) and current across the sample (*lower panel*) when the % is varied as 0%, 95%, 100% and 105%. Solid lines- voltage down sweep, dashed lines- voltage up sweep

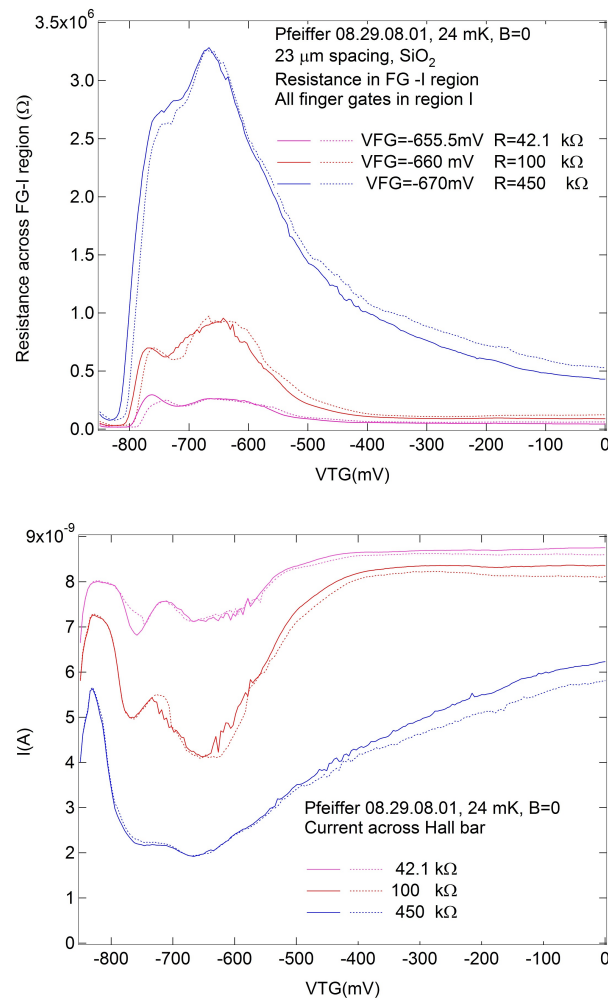


Figure 8.12: Resistance across FG-I region (*upper panel*) and current across the sample (*lower panel*) when the tunneling regime in the FG I region is varied at $B=0$. Solid lines- voltage down sweep, dashed lines- voltage up sweep

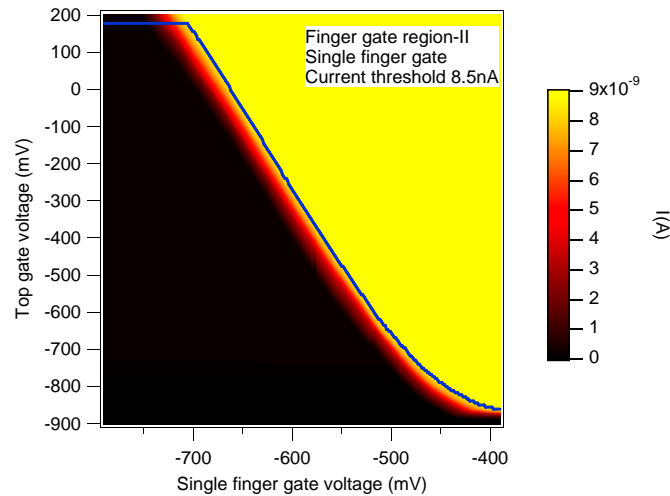


Figure 8.13: 2D diagram for current, sweeping single finger gate and top gate together in finger gate region II, at base temperature, $B=0$

goes down. We also saw increase in current at this voltage. This indicates the enhancement of the conductance for a certain amount of disorder. This proves the theory to some extent. As the bulk disorder is increased, the planar conductance rises and this increase also proportional to the local disorder created by the finger gate voltage.

After the scans in finger gate II region, we wanted to get some more data from finger gate I region. So the experiment was set for probing the current while sourcing the voltage. But the result was not same as in Fig.8.12. We tuned the FG I region in two different tunneling regimes, $50\text{k}\Omega$ and $10\text{k}\Omega$. The resistance increases and decreases at some point but then we see a sharp increase in the resistance. First we tested the single gate to see if it shows any localization. The resistance for single gate shows no effect of single finger gate potential. Then the FG region was tuned to different tunneling regimes. Fig.8.15 shows the traces for single gate, $50\text{k}\Omega$ and $100\text{k}\Omega$, in comparison with old traces for $50\text{k}\Omega$.

The red trace shows the resistance/current. The resistance is linear as in previous experiment. So there is not localization. The green and the blue traces are for $50\text{k}\Omega$ and $100\text{k}\Omega$ respectively. If we compare these new traces with old trace (brown lines), resistance change is peculiar. The current in the new traces goes to zero, it shows a very small increase around top gate voltage around -650 mV , but after that the 2DEG depletes. This peak in current is very small compared with the increase in current from the old trace (brown traces). Similar behavior is observed in FG-II region.

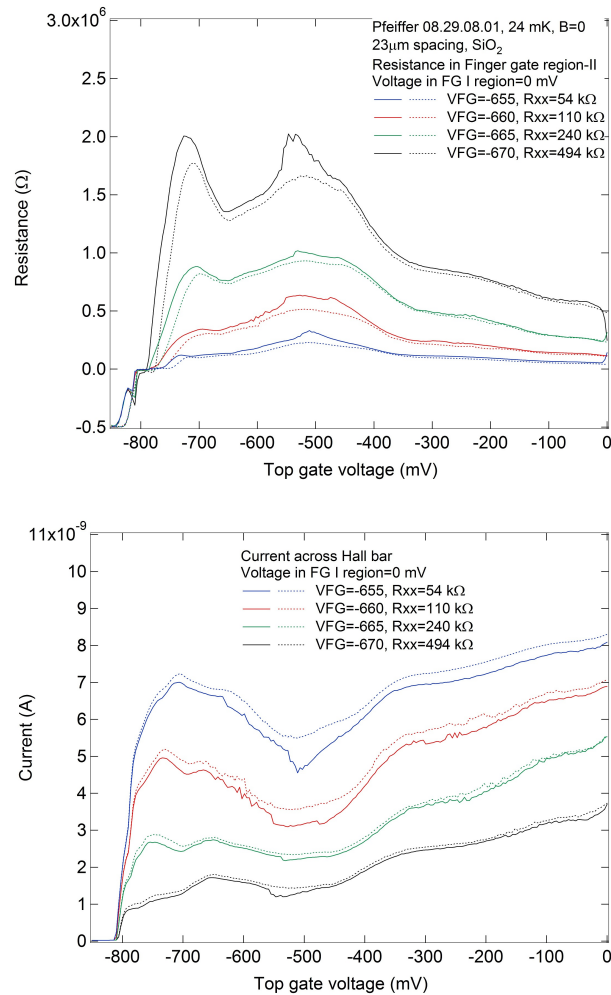


Figure 8.14: Resistance across FG-II region (*upper panel*) and current across the sample (*lower panel*) when the tunneling regime in the FG II region is varied, at B=0. Solid lines- voltage down sweep, dashed lines-voltage up sweep

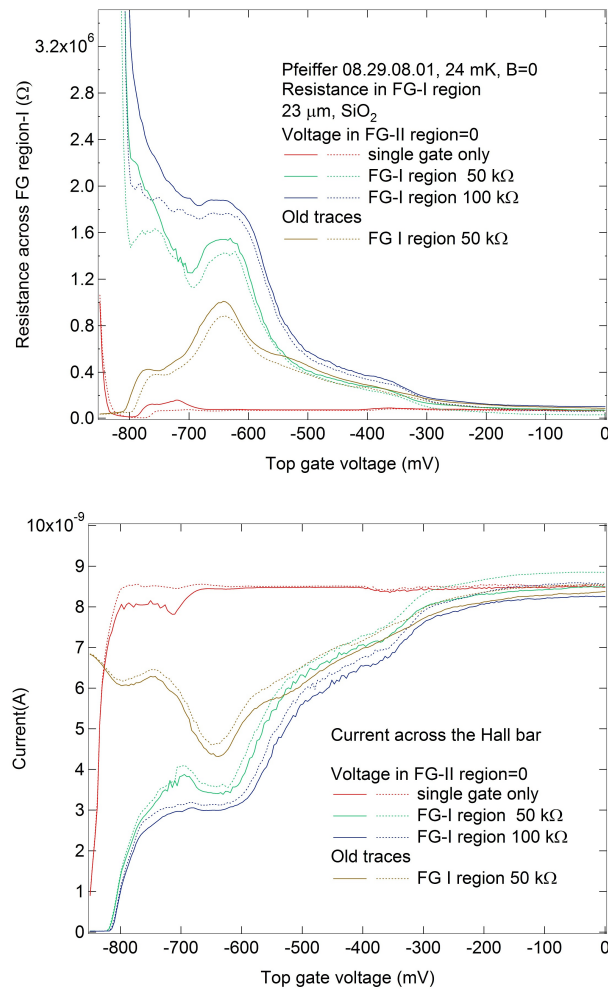


Figure 8.15: Resistance across FG-I region (*upper panel*) and current across the sample (*lower panel*) for single gate potential, 50k Ω and 100 Ω , at B=0. Solid lines- voltage down sweep, dashed lines- voltage up sweep

The reason could be the charge trapped in the SiO_2 layer due to changing the top gate frequently upto the depletion layer. To avoid this we had designed and fabricated finger gate device where we tried to avoid the insulating layer and replaced it with intercalated gates.

8.3.2 Experiments with intercalated finger gate samples

The main purpose of intercalated sample design is to avoid use of oxide to separate the top gate and the finger gate. The design of such a sample is discussed in section 5.7. For this sample we used wafer Pfeiffer 7.28.08.02 since Pfeiffer 8.29.09.01 has issues of breaks in the 2DEG which are not easily visible. The sample properties are discussed in section 6.2 and the gate dependence properties are shown in table 6.2.

The mesa and ohmics are fabricated in the same way as for sample with SiO_2 . The next step is to fabricate the top gate and finger gates. This is done in one ebeam step. Different write fields are used to expose the different designs. The Hall bar is divided in there different regions. Only top gate region, FG-I and FG-II regions, same as for sample with SiO_2 . First the finger gates are exposed followed by intercalated top gate portion and the top gate in one section of the Hall bar. After ebeam lithograph, the sample is developed and plasma cleaning step is carried. The Ti-Au evaporation is done in the ebeam evaporator with 5 nm of Ti as sticking layer and 85 nm of gold. We have fabricated two different samples, one with average spacing between the finger gates with $23\mu m \pm 5\%$ and other sample with average spacing between the finger gates $12\mu m \pm \%$. In this material mean free path of $23\mu m$ is achieved around top gate voltage of -150mV and mean free path of $12\mu m$ is achieved around -250mV. Table 6.2.

Fig. 8.16 shows the SEM micrograph for a sample with average spacing of $23\mu m$.

The different sections of th Hall bar are called top gate region, finger gate I region (FG-I region) and finger gate II region (FG-II region) from left to right as in sample 8.5.

The ohmics, 2DEG resistance and all the gates are first tested to determine the depletion properties of 2DEG, especially for top gate and the leakage current at 4.2K. All the measurements are done in dark. The density of the sample is $7.7 \times 10^{11}/cm^2$ and mobility is $4.9 \times 10^6 cm^2/Vs$. The 2DEG resistance is $16.6\Omega/\square$. The 2DEG depletes around -370mV of top gate voltage. The leakage current is few pA in the background of nA. The density and mobility are measured at base temperature,

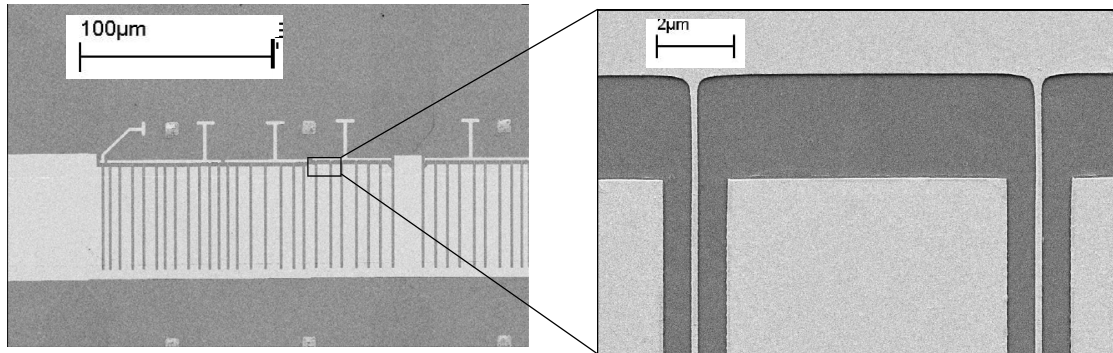


Figure 8.16: SEM micrograph of intercalated finger gate sample with average spacing between the finger gates of $23\mu m$.

24 mK. The density and mobility are $7 \times 10^{11}/cm^2$ and 9.5×10^6 respectively. The 2DEg resistance is $12k\Omega$.

In the first experiment, the FG I region is set to different tunneling regimes, $56 k\Omega$, $101 k\Omega$, $201 k\Omega$ applying different negative voltages on the finger gates in region I. Voltage on finger gates in FG II region are zero. The measurement is current biased, with current of $9.4 nA$, frequency of $176 Hz$ and time constant of $300 ms$. Fig.8.17 shows the resistance across the FG I region and the current across the Hall bar. The resistance is shown on a logarithmic scale.

In Fig.8.17, the red lines show the resistance/current for tunneling regime $56 k\Omega$, the blue trace for $101 k\Omega$ and brown traces show the resistance/current for $201 k\Omega$ at base temperature, $24 mK$ and zero magnetic field. The solid and dashed lines are for down and up sweep of the top gate voltage. The hysteresis due to voltage sweep directions is very small. The resistance is increasing monotonously without any decrease as we seen in the case of sample with SiO_2 when the region is tuned to tunneling regime. Then we tested only the single gate to see the effect of a single gate potential. Fig.8.18 shows the resistance and current when only the single gate is used to drive the FG I region in tunneling regime.

There is no effect of single gate potential as can be seen in Fig. 8.18. The resistance in the FG I region is set to different values, $20k\Omega$ (red trace), $60k\Omega$ (green trace) and 200Ω (pink trace) and 600Ω (blue lines). The solid lines are for top gate voltage down direction and dashed lines are for top gate voltage sweep up direction. The resistance is increasing monotonously and the current is decreasing and 2DEG depletes around $-380 mV$. The absence of delocalization is expected due to single gate potential. Then the finger gates are added one by one and resistance and current are probed in similar way, keeping the the FG I region in the same tunneling

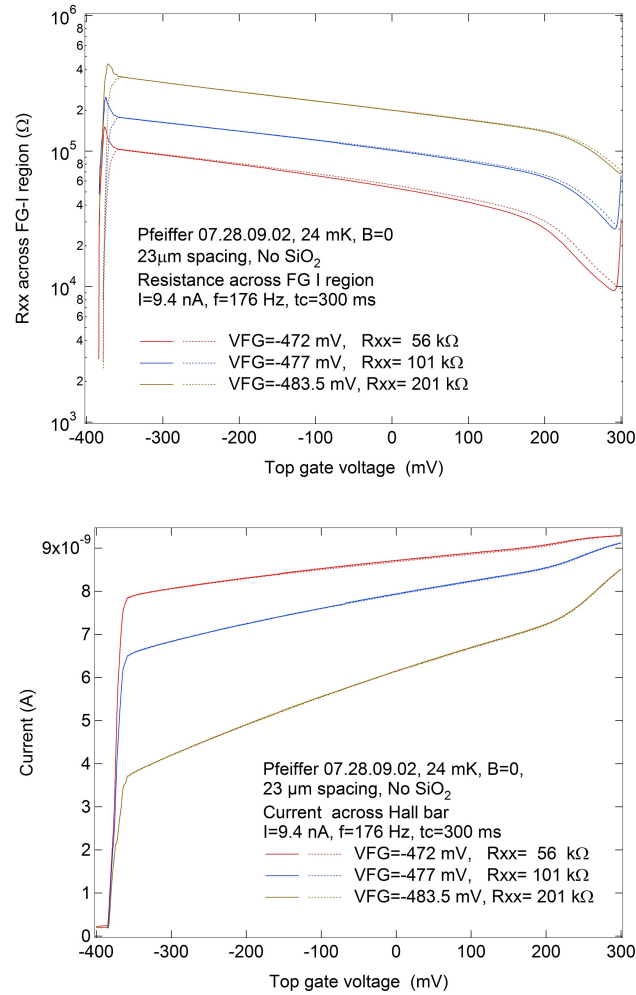


Figure 8.17: Resistance across FG-I region (*upper panel*) and current across the Hall bar (*lower panel*) for different tunneling regimes, 56k Ω and 101 Ω and 201 Ω , at $B=0$. Solid lines- voltage down sweep, dashed lines-voltage up sweep

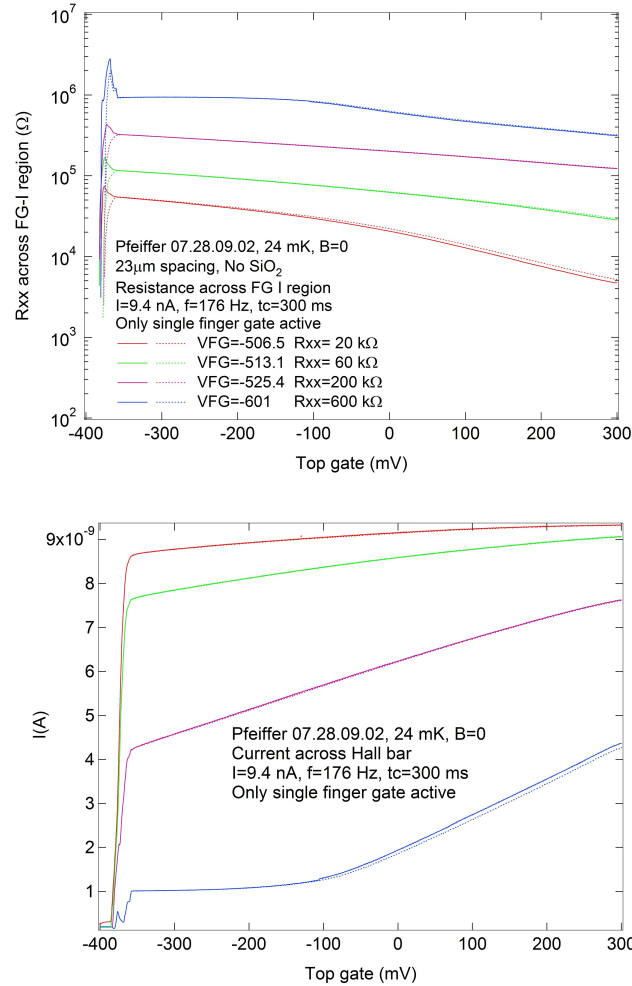


Figure 8.18: Effect of single gate potential. Resistance across FG-I region (*upper panel*) and current across the sample (*lower panel*) for different tunneling regimes, 20k Ω , 60k Ω and 200 Ω and 600 Ω , at B=0. Solid lines- voltage down sweep, dashed lines-voltage up sweep

regime $20\text{k}\Omega$, $60\text{k}\Omega$ and 200Ω and 600Ω .

Fig.8.19 shows the effect of single gate and all FG I region on the resistance and current. The newly added lines for FG I region are shown in the legends. Comparing the effect of single gate and all FG I region potentials, the change in resistance and current are almost. Qualitatively and quantitatively, the effect of single gate and all finger gates in region I is negligible. It is quite clear that in this sample, there is not delocalization by local disorder created due to local finger gate potentials. On the positive gate voltage side, the resistance and current for FGI region slightly deviates from the single gate potential behavior. similar behavior was seen in FG II region. We thought that this could be the effect of mean free path and the spacing between the finger gates ($23\mu\text{m}$) which is slightly high to see the delocalization. So we decided to change the sample and instead of $23\mu\text{m}$, we used the sample with $12\mu\text{m}$ spacing.

The $12\mu\text{m}$ sample is fabricated along with the sample with $23\mu\text{m}$ sample (intercalated sample), on the same wafer (Pfeiffer 07.28.09.02). The Hall bar had three sections, only top gate region, finger gate region (FG-I), finger gate region II (FG-II). We did the tests for optimum current, frequency, time constant, sweep speed etc. The current of 46.7 nA was determined to be giving less noise and not heating the elections, with frequency of 176 Hz , and time constant of 300 ms . All the finger gates were tested to find the depletion limit for each single finger gate or bunch of finger gates on the gate pad. We found that all the gates except the single gate on FG II region is not working, the current is constant, not depleting beneath this particular gate. The gate seems to be broken.

To start with, we measured the resistance across the FG I region and current across the Hall bar as a function of top gate voltage in few different tunneling regimes tuned due to single finger gate in a current bias mode of measurement. Then the individual gates in FG I region were added and then the FG II region. Fig.8.20, Fig.8.21 and Fig.8.22 show the resistance and current for different tunneling regions $20\text{k}\Omega$, 60Ω and $100\text{k}\Omega$.

From Fig.8.23, the resistance increases monotonously and the current decreases and then the 2DEG depletes. The corresponding color schemes are for single gate (SG), finger gates in FG I region (FG I) and all gates in FG I and FG II region. The tunneling regimes are adjusted to at $20\text{k}\Omega$, $60\text{k}\Omega$ and 100Ω . It is clear that the potentials from all the gates does not create any disorder and electrons do not delocalize. To see the effect of top gate voltage and the finger gate voltage on the current when both the gates are swept simultaneously, a 2D scan was done at zero magnetic field at base temperature.

Fig. 8.24 shows the 2D plot for current across FG I region when the single gate

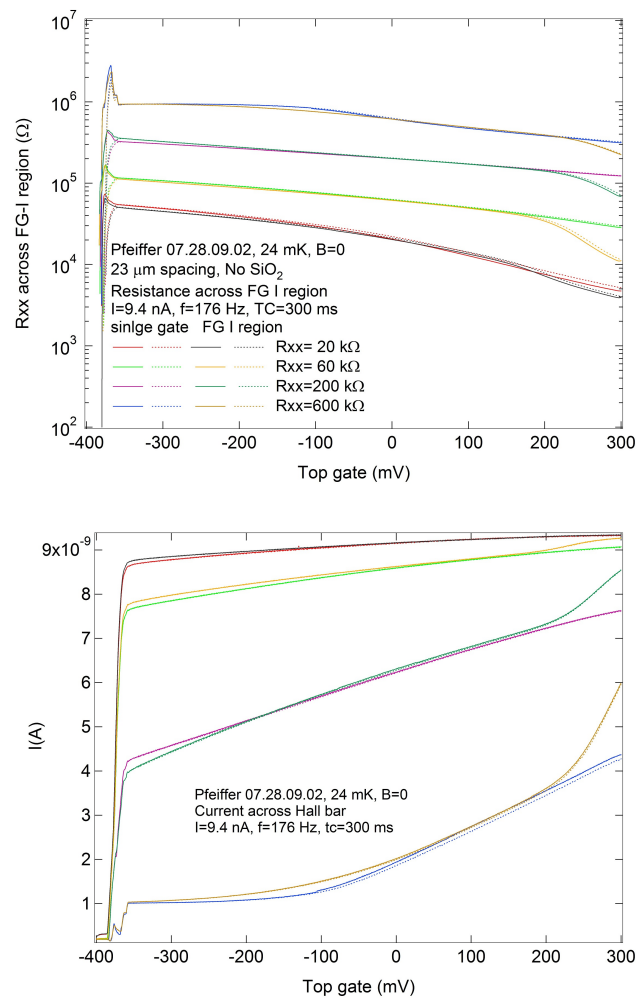


Figure 8.19: Comparison of single gate and FG I region potentials. Resistance across FG-I region (*upper panel*) and current across the sample (*lower panel*) for different tunneling regimes, 20k Ω , 60k Ω , 200 Ω and 600 Ω , at B=0. Solid lines- voltage down sweep, dashed lines-voltage up sweep

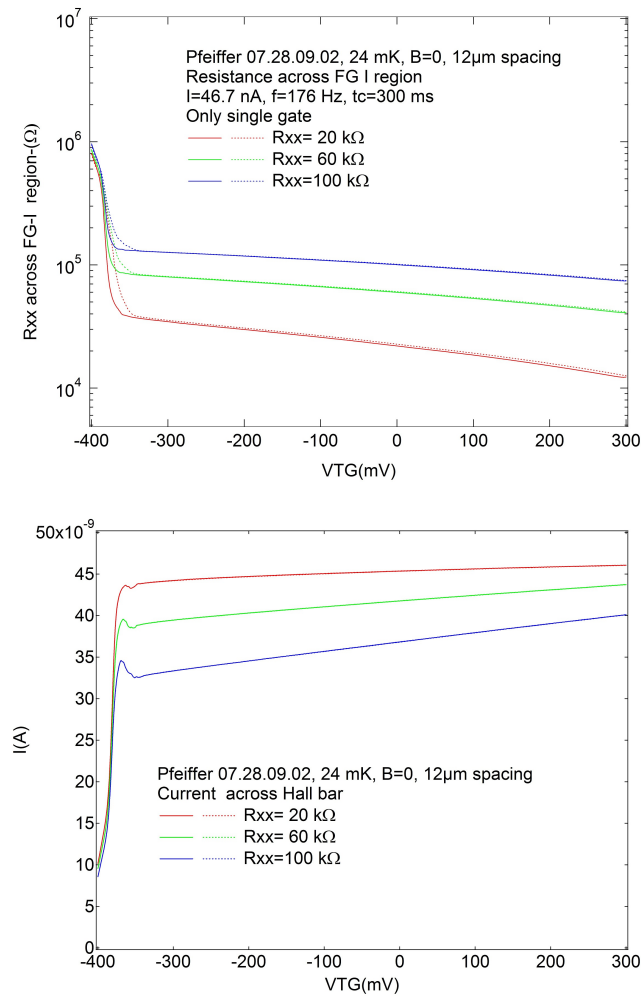


Figure 8.20: Effect of single gate potential. Resistance across FG-I region (*upper panel*) and current across the sample (*lower panel*) for different tunneling regimes, 20k Ω , 60k Ω and 100 Ω , at B=0. Solid lines- voltage down sweep, dashed lines- voltage up sweep

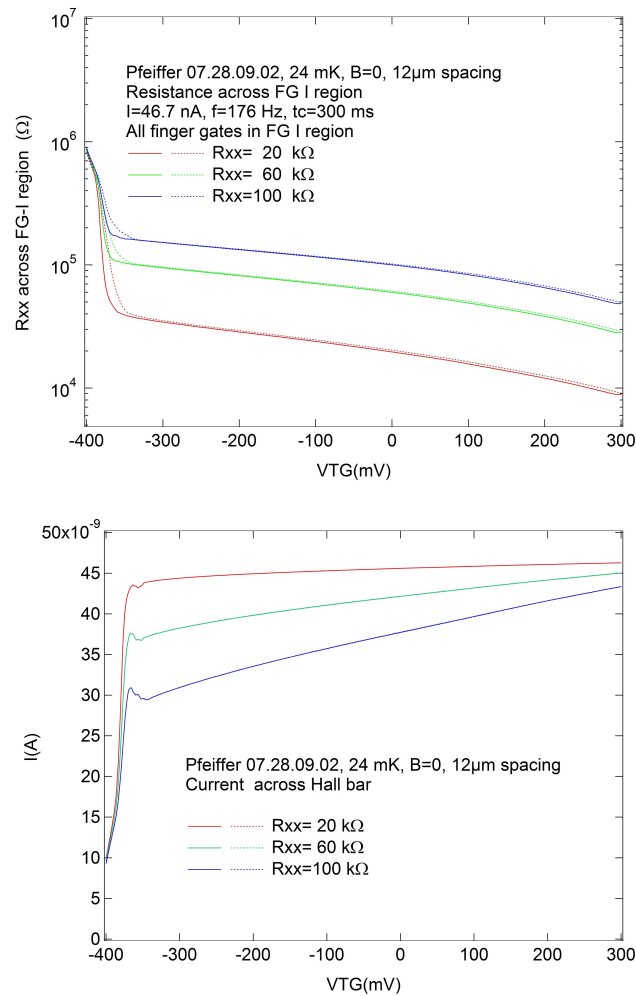


Figure 8.21: Effect of all gates in FG I region. Resistance across FG-I region (*upper panel*) and current across the sample (*lower panel*) for different tunneling regimes, 20k Ω , 60k Ω and 100 Ω , at B=0. Solid lines- voltage down sweep, dashed lines-voltage up sweep

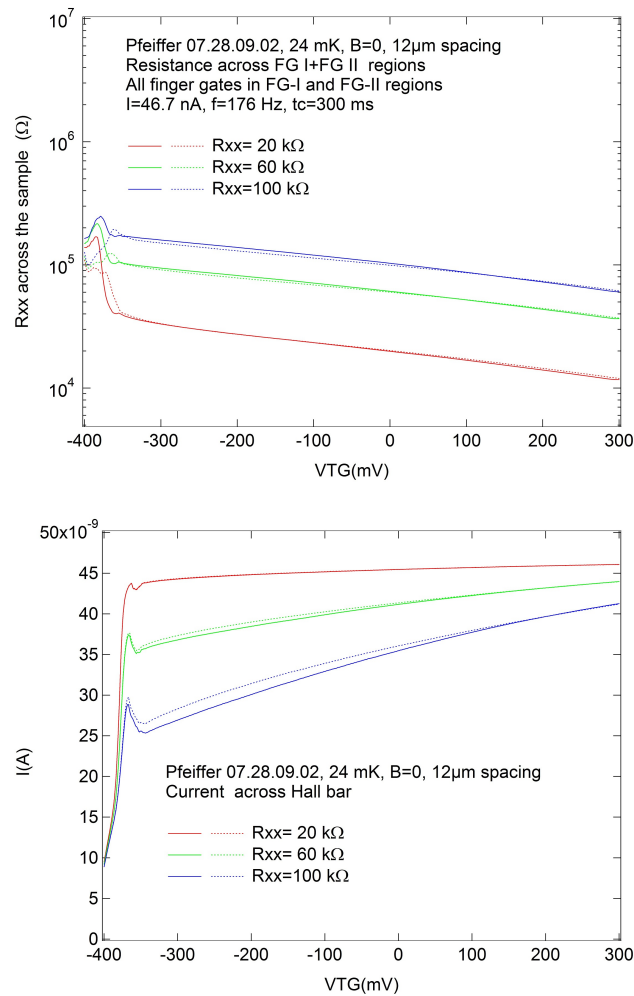


Figure 8.22: Effect of FG I region and FG II gate potentials. Resistance across FG-I and FG-II region (*upper panel*) and current across the sample (*lower panel*) for different tunneling regimes, 20k Ω , 60k Ω and 100 Ω , at B=0. Solid lines- voltage down sweep, dashed lines-voltage up sweep

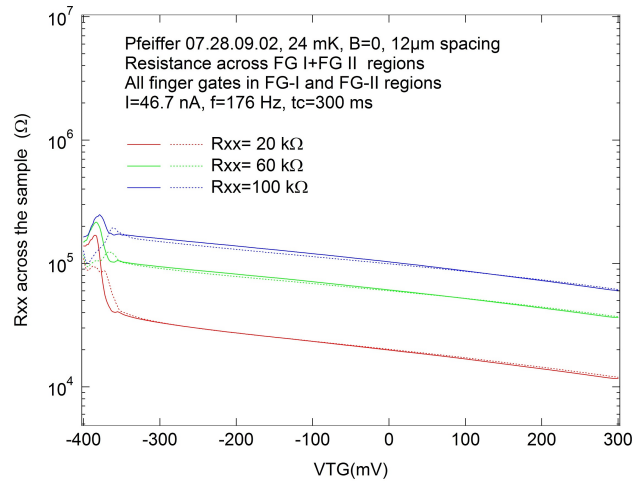


Figure 8.23: Comparison of single gate, FG I and FG II region potentials. Resistance across FG-I due to single gate (SG) and gates in FG I region (FG I) and FG-II (FG II) regions due to all gates potential for different tunneling regimes, 20k Ω , 60k Ω and 100 Ω , at B=0. Solid lines- voltage down sweep, dashed lines-voltage up sweep

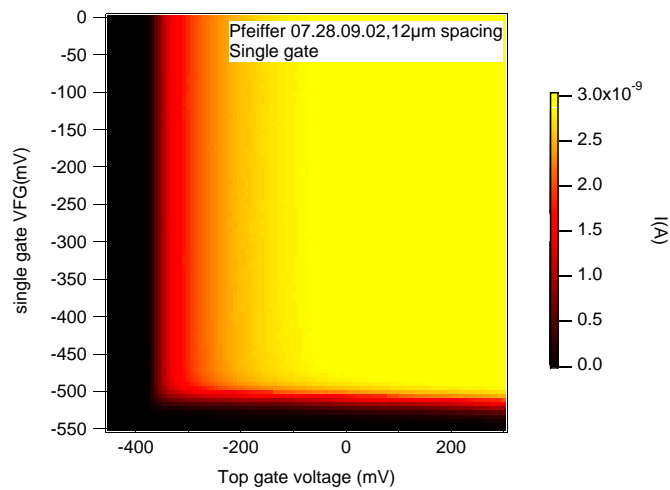


Figure 8.24: 2D plot showing current across the FG I region when the single gate and top gate voltages are swept together.

and top gate voltages are swept together. The color scale indicates the current on the scale of nA. From the plot, it can be seen that the effect of top gate voltage and single gate voltage is independent of each other. We could not find a compensation for each other as we did in the case of sample with SiO_2 . The local scattering potential and the bulk disorder are independent of each other as in the case of sample with $23\mu m$ spacing. To know the reason, we did some ohmic resistance tests on the sample.

As we know that the resistances in series are added:

$$R_{Total} = R_1 + R_2 + R_3 + \dots \quad (8.7)$$

where R_{Total} is the sum of resistance in series $R_1, R_2, R_3 \dots$. We used this to see the effect of single gate and the effect of group of finger gates. -500 mV is the voltage on the single gate gave rise to a resistance of 1.1 k Ω in the FG I region. With the same voltage, the gate which is group of 11 finger gates gave resistance of 6.9 k Ω and gate which has 7 finger gates gave resistance more than 40 Ω , while that for other gate with 7 gates is 1.32 k Ω . The resistance due to a single gate does not add ohmically for group of finger gates and all the gates are different from each other.

To verify this, all the gates were swept separately. Fig.8.25 shows the log of resistance in the sample as function of finger gate voltages.

Fig. 8.25 shows the log of resistance plotted in log scale as a function of finger gate voltage. The different gate sweeps are indicated in different colors. The solid lines are for voltage down sweep, dashed lines shows voltage up sweep. The number of gates are written at corresponding color. As can be seen in the graph, different gates behave in different way irrespective of number of gates. Two gates with 7 finger gates each have different characteristics (pink and black traces). similarly the gates with 11 finger gates each are close to each other but still the characteristics are different. In the sample, every gate acts differently. The reason is not known but this limits the experimental realization of delocalization by local disorder.

To see if there is any delocalization exists in the sample, we did experiment of cooling the sample from 1.5K to base temperature. Fig.8.26 shows the resistance in the FG I region in tunneling regimes.

Fig. 8.26 shows the resistance as a function of mixing chamber temperature in a log-log scale in different tunneling regimes 10k Ω , 100k Ω and 1M Ω , with three different gates, single gates (SG), group of 7 finger gates and group of 10 gates. The jump in the resistance around 850 mK is due to the cooling effect while

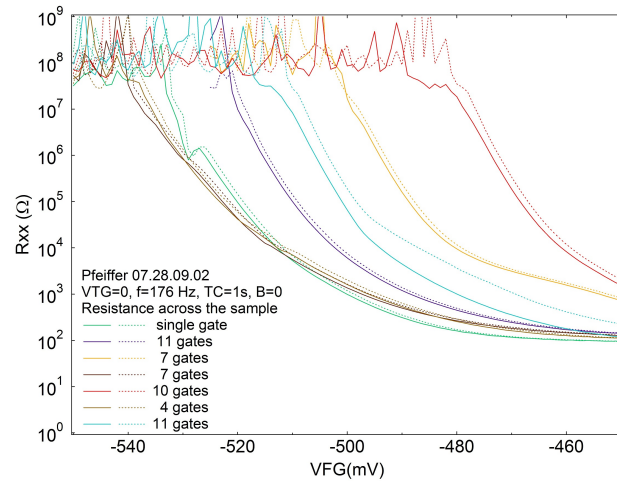


Figure 8.25: Resistance log in the sample as a function of finger gates in the log scale, at base temperature, 24 mK and $B=0$. The solid and dashed lines are voltage sweep down and sweep up directions. Solid lines- voltage down sweep, dashed lines-voltage up sweep

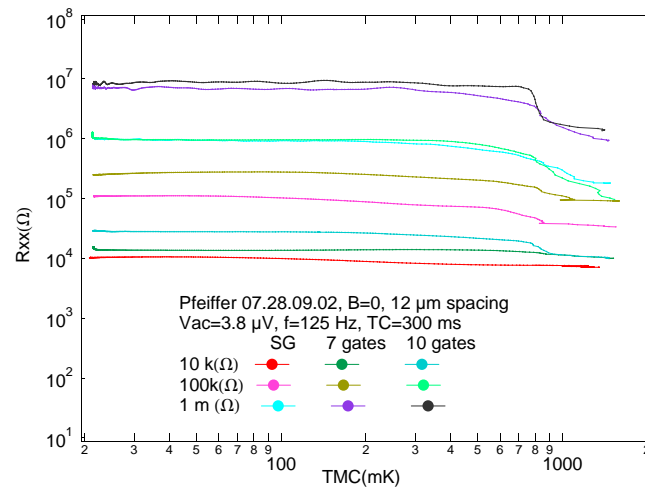


Figure 8.26: Resistance in the sample as a function of mixing chamber temperature, in different tunneling regimes 10k Ω , 100k Ω and 1M Ω with three different gates, single gates (SG), group of 7 finger gates and group of 10 gates.

condensing the mixture in the cryostat. The measurement is done in voltage bias mode with voltage of $3.8\mu\text{m}$ and frequency of 176 Hz, and time constant of 300 ms. The resistance shows no effect of group of 7 gates or 10 gates. Qualitatively the resistance behavior is same as for single gate.

8.4 Conclusion and outlook

To experimentally realize the breakdown of Anderson localization and enhance the conductivity, we had fabricated the samples in such a way to create delocalization by disorder according to theory of D.L. Maslov [68]. We fabricated two different types of samples, the first where the finger gates and top gates are separated by SiO_2 and in the other type the top gate and finger gates are intercalated. In the intercalated samples we fabricated samples with two different finger gate spacings, $12\mu\text{m} \pm 5\%$ and $23\mu\text{m} \pm \%$. Both types of samples are fabricated on high mobility GaAs/AlGaAs heterostructures ($\mu \geq 9.5 \times 10^6 \text{ cm}^2/\text{Vs}$).

We measured the resistance as a function of top gate voltage at zero magnetic field at 24 mK in sample with SiO_2 . After determining the right compensation between the top gate and finger gates, we could see the decrease in resistance in tunneling regime. This effect was seen in both finger gate regions. But due to possible charge trap in the oxide layer, the effect was not repeated.

In the intercalated sample with average spacing of $23\mu\text{m}$ between the finger gates, the effect was not seen and the resistance in the sample was increasing monotonously in the tunneling regime as a function of top gate voltage. The measurements were done at base temperature and zero magnetic fields.

In the intercalated sample with average spacing of $12\mu\text{m}$, the resistance in the sample was measured as a function of top gate voltage. The result was similar to that of $23\mu\text{m}$ sample. The ohmic behavior was studied to see the characteristics of the finger gates in different groups. Each group of finger gates behaves separately, which makes difficult to get overall effect of local disorder. All these measurements were done at base temperature. To see whether this delocalization exists at all, we did experiment with cooling the system from 1.5 K to base temperature, 24 mK. In this case also the resistance shows no sign of delocalisation.

One need to realize the effect in a system, where the bulk disorder and local disorder are separable and tunable with respect to each other. We wish to proceed the experiment with the sample where the mean free path is smaller at the base temperature and zero gate voltage. This can be achieved in a sample with a low mobility.

9 Electron Temperature measurement in a Quantum Dot

9.1 Introduction

Using quantum mechanical superposition states and entanglement in a quantum computer would allow solving complicated mathematical and physical problems much faster than with classical computers[72]. But the realization of such a computer is a challenge because it requires precise control of fragile quantum states. Nevertheless, the state of the electron spin has been identified early as an attractive realization of a quantum bit [73]. As a host for the electron spin, semiconductor quantum dots seem to be a promising approach. In the last years, many of the elements necessary for quantum computation have been experimentally realized in semiconductor quantum dots, showing the advances for such a host system. Nowadays, a single electron can be isolated [74] and the spin can be initialized in the ground state [75]. Spin-states are long lived, i.e. spins have long relaxation times [76]. Decoherence times of up to one second have been measured recently [77]. A single-shot read-out of one single spin state is possible[76] as well as inducing coherent spin rotations of a single electron spin[78]. Our goal with this experiment is to determine the electron temperature in a quantum dot. This gives an upper bound of the electron temperature, which helped to improve further the measurement set up. Work is done on the electrical setup of dilution refrigerator. A simple bias-circuit was built for the application of the AC and DC voltages to the sample ¹. The fridge was also completely electrically isolated from the ground and then grounded at one single point to avoid ground loops and to reduce electrical noise from the surrounding. Furthermore, a cooldown of the system was performed successfully and a few-electron quantum dot could be formed. The electron temperature of the system then was estimated.

9.2 Charge Tunneling in a quantum dot

To observe tunneling of single charge carriers into and out of a quantum dot, the thermal energy $k_B T$ must be smaller than the change in the Coulomb energy on the dot, which is given in terms of capacitance C_{dot} of the dot $E_c = e^2/C_{dot}$ [5]. The first condition to see single tunnel events is

$$e^2/C_{dot} \gg k_B T \quad (9.1)$$

¹Sandro Erni assisted during this project

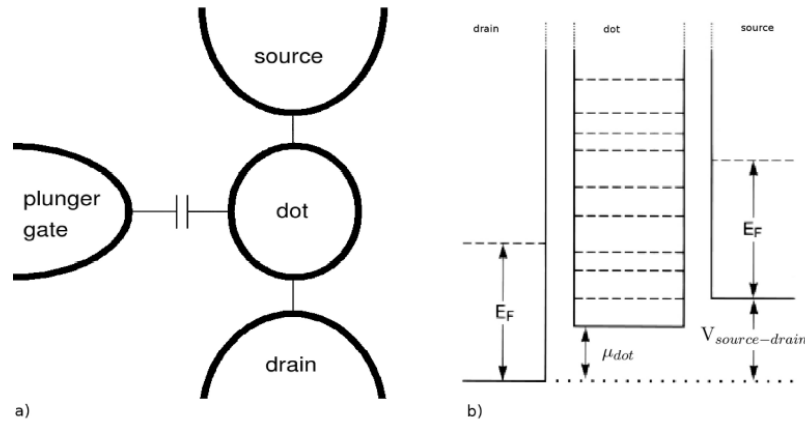


Figure 9.1: (a) Schematic picture of a quantum dot that couples capacitively to the plunger gate and by tunnel junction to the source and drain reservoirs. (b) By applying a source-drain bias V_{dc} one can tune the difference in electrochemical potential of source and drain and with the voltage on the plunger gate the potential of the dot. [80]

The second condition is a high tunnel barrier. This assures that the electrons are well located either in the source or drain reservoirs, or on the dot [79]. Therefore the tunnel conductance G_t must be much smaller than the conductance quantum e^2/h

$$G_t \ll e^2/h \quad (9.2)$$

Consider quantum dot where temperature is zero. Charge tunneling can occur if states on the dot are available which are lying between the electrochemical potential of the source and drain. This energy window can be tuned by applying a source–drain voltage $V_{sd} = (\mu_s - \mu_d)/e$. The electrochemical potential of the dot μ_{dot} can be tuned by a gate electrode (Fig. 9.1).

9.3 Different Temperature regimes

In a lateral single quantum dot, three temperature regimes can be distinguished by comparing thermal energy $k_B T$ to charging energy e^2/C , average energy level spacing Δ and tunneling rate Γ . [81],[82]

$\Delta, e^2/C, \ll k_B T$: In this high temperature regime there are no charging effects and no Coulomb blockade. Therefore the discreteness of charge can not be

discerned.

$\Gamma, \Delta \ll k_B T \ll e^2/C$: The regime of the classical Coulomb blockade is thermally broadened. Transport takes place through several quantum dot energy levels. The peak conductance is independent of T and its full width at half maximum (FWHM) is proportional to $k_B T$ ($4.35k_B T$). Fig. 9.2

In the quantum Coulomb blockade regime, a temperature broadened and a lifetime broadened regime can be distinguished. In both cases only one dot level is involved in transport through the dot.

$k_B T \ll \Gamma, \Delta \ll e^2/C$: In the lifetime broadened regime, the peak conductance is independent of T . The peak has a Lorentzian line shape and its FWHM is proportional to Γ .

$\Gamma \ll k_B T \ll \Delta \ll e^2/C$: The peak conductance in the temperature broadened regime is proportional to $1/T$. The peak's line shape is different from the lifetime broadened regime, its tails are exponentially decaying. The FWHM is approximately $3.5k_B T$. Fig. 9.2 Because of the small tunneling rates the broadening of the energy levels is mainly due to the thermal energy. Tuning the dot into this regime, the electron temperature can be estimated by measuring the FWHM.

9.4 Materials and methods

9.4.1 Quantum dot sample

The quantum dot sample used for this experiment is fabricated using standard fabrication processes. These are described in section 5.3. The sample is fabricated from Gossard wafer. For this GaAs/AlGaAs heterostructure, the 2DEG is around 100 nm deep and the sample is etched till 110 nm to remove the donors and separate the devices. The gates formed using electron beam lithography are approximately 35 nm wide and metalized using Ti–Au. They are designed to form a double quantum dot, including two quantum point contacts (QPC) for read–out of the charge state on each dot. To determine the electron temperature, a single quantum dot has been formed by using the three plunger gates in the middle as one gate. The QPCs were not used; the conductance through the dot has been measured by using ohmic contacts S and D as source and drain as shown in Fig.9.3

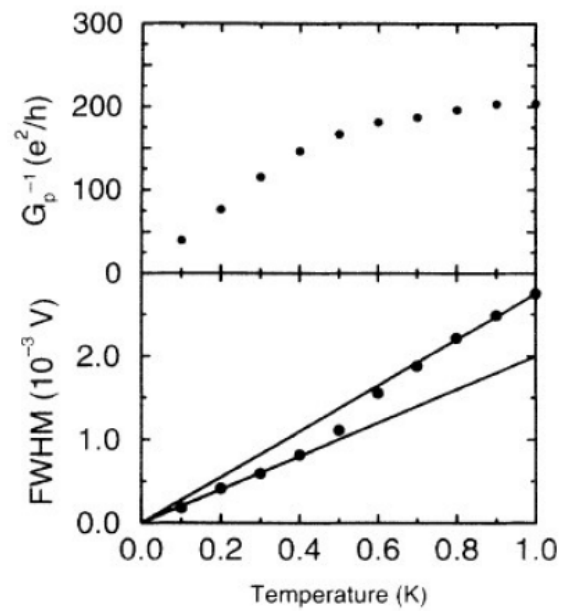


Figure 9.2: In the upper panel the inverse of the maximal differential conductance is printed, in the lower panel FWHM as a function of temperature. Two slopes are visible, $\text{FWHM} = 4.35k_B T$ for the classical regime and $\text{FWHM} = 3.5k_B T$ for the quantum regime. [82]

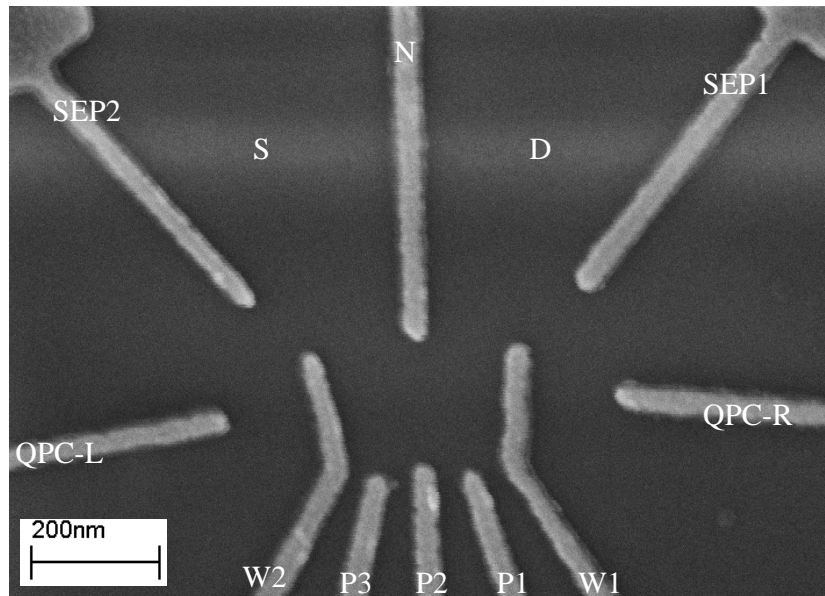


Figure 9.3: SEM micrograph of the measured sample. N=nose,w1=right wall, w2=left wall, p1,p2,p3=plunger gates,SEP=separators, QPC=quantum point contact, S=source ohmics, D=drain ohmics

9.4.2 Measurement set up

The voltages that are applied to the sample are controlled on the computer with the software Igor Pro (WaveMetrics, Lake Oswego, USA). The signal is transmitted over GPIB and optical fibers (National Instruments, Austin, USA) to the Digital to Analog Converter (DAC). A self-built AC/DC bias box (Fig. 9.4) is used to apply an AC modified DC signal to the source of the sample. The AC signal is generated and read out by a Lock-In Amplifier (EG&G Instruments Corporation, Princeton, USA). The DC input for the bias box and the signals for the gates are coming from the DAC. All the electrical signals are then transmitted to the insert via one of two breakout boxes. The current that is measured on the sample is amplified by a current amplifier and filtered with the Lock-In Amplifier. The signal is then transmitted back to the computer via optical fibers to be analyzed in Igor Pro.

The whole system with the fridge and the control instruments has been electrically isolated from the ground by using optical fibers for signal transmission and using transformers for power supply. Noise due to ground loops could be reduced significantly by grounding the whole set up at one point, i.e. response to other electrical systems (e.g. a crane) was eliminated. But 50 Hz noise from the power supply system was barely reduced, despite using transformers for all power supplies to

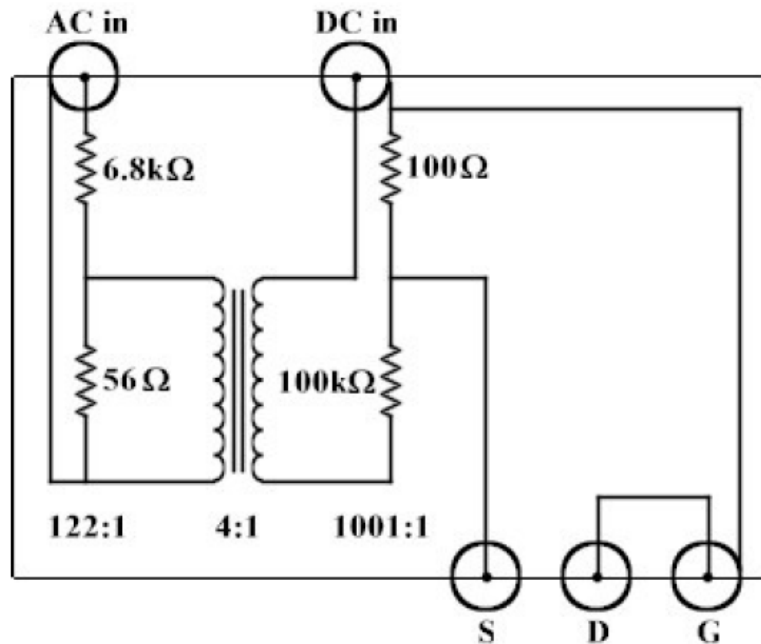


Figure 9.4: Electrical circuit of the AC/DC bias box, which divides the applied voltages by approximately 1 : 500000 (AC) and 1 : 1000 (DC) respectively.

the system.

9.5 Electron Temperature measurement

9.5.1 Single dot characterization

To check if a quantum dot can be formed on the sample and to get an idea of the scope of the voltages that have to be applied therefore, wall-wall measurements have been performed. The plunger gate and the nose are kept constant and the left and right walls are scanned over a range of voltages while measuring the conductance from source to drain through an eventually formed quantum dot. These measurements then have been carried out at different values for the plunger and nose (Fig.9.5).

The results show that a quantum dot can be formed, but quite high voltages are needed therefore. The risk of electrons striking through from the gates is getting bigger at such high voltages. Nevertheless, the few-electron regime probably can be reached. Some isolated conductance peaks at the highest wall gates voltages

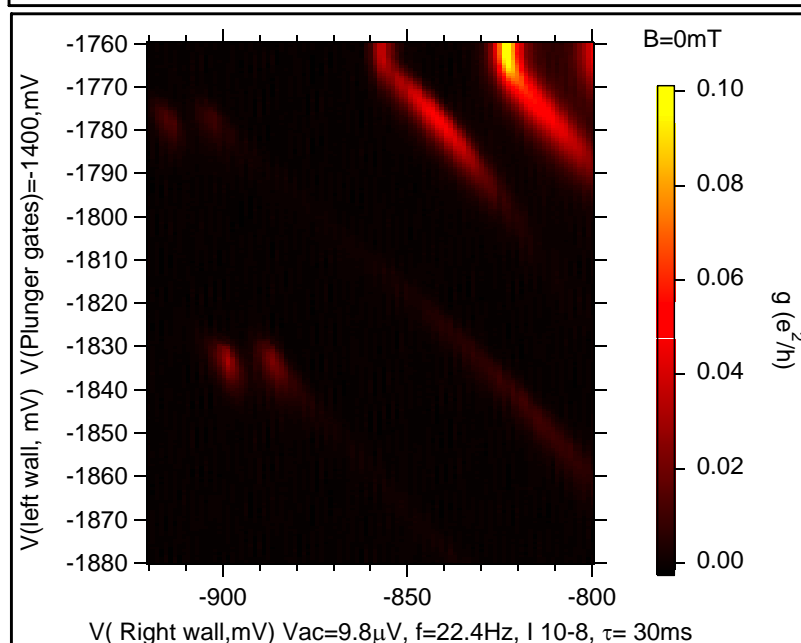
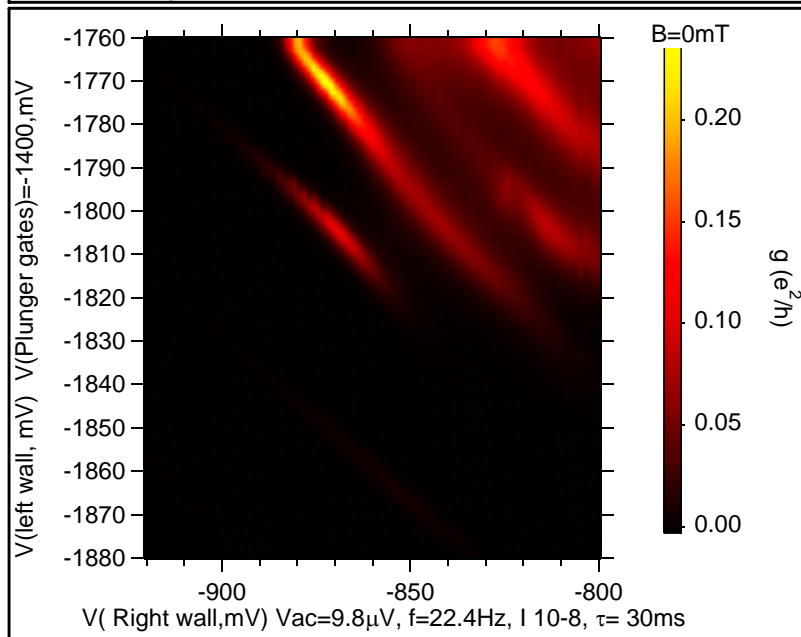
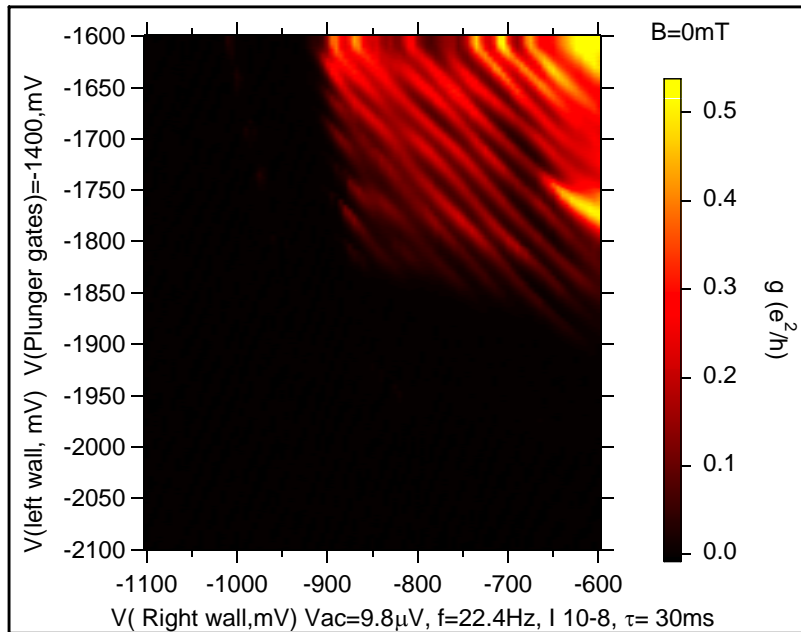
represent this few electron regime most presumably.

In the experiments, a single quantum dot is formed. But since the sample actually is a double quantum dot device, a partial double dot character can be seen in some plots as a slight honeycomb pattern in the conductance peaks. A region of an isolated conductance peak of amplitude of approximately $0.1e^2/h$ in the few electron regime was selected in order to perform a Coulomb diamond measurement (Fig. 9.6). The nose and wall gates are held constant while a 2D scan is performed over the voltage of the plunger gate and the source-drain DC voltage. The source–drain voltage splits a conductance peak into two peaks giving the plot a diamond-like pattern. This plot also suggests that the measurements take place in the few electron regime, since going to higher plunger gate voltages reveals no further conductance peaks.

The plots still reveal a quite high noise level whereof most of it is 50Hz noise. For a first characterization of the device this noise level is not that troublesome, but for further experiments it should be clearly reduced to get reliable results. The wave function of a electron on the dot is very sensible to the fine tuning of all the gates and other local changes of the electronic potential. This measurement is used to find the regime of the dot where the tunnel barriers are very opaque that the electrons are well located either in or outside the dot.

9.5.2 Temperature measurement

To estimate the electron temperature on the quantum dot, the device is tuned into the temperature broadened regime. Conductance through the dot is then measured while varying the plunger gate voltage. One single isolated peak of height $\approx 0.1e^2/h$ is selected. The selected conductance peak is clearly exponentially decaying, as can be seen in the logarithmic plot, which is proof that we are in temperature broadened regime. A curve is fitted to the peak to calculate the FWHM ($\tilde{1}.18$ mV). This number in mV is converted to an energy with $1mV = 95\mu eV$. This factor is calculated from the amount of peak splitting due to a certain DC voltage that is applied. The energy corresponding to the FWHM is then equal to $3.5k_B T$, so that the temperature can be calculated. An electron temperature of $372mK$ was estimated in this way. This value seems to be quite high but the range of 350 to 400 mK has been confirmed in further measurements.



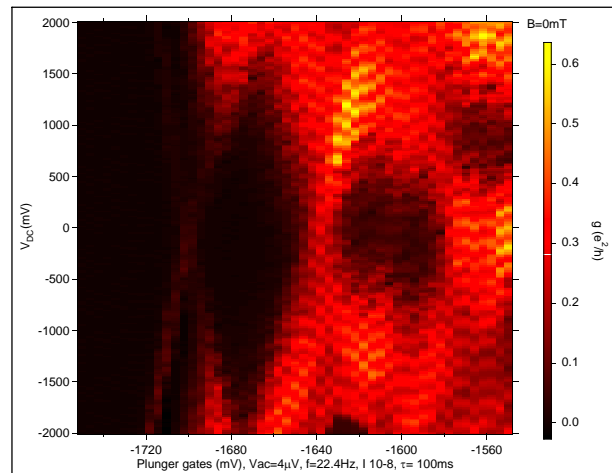


Figure 9.6: Coulomb diamond: measuring conductance through the dot while scanning over the applied DC voltage and the plunger gate voltage.

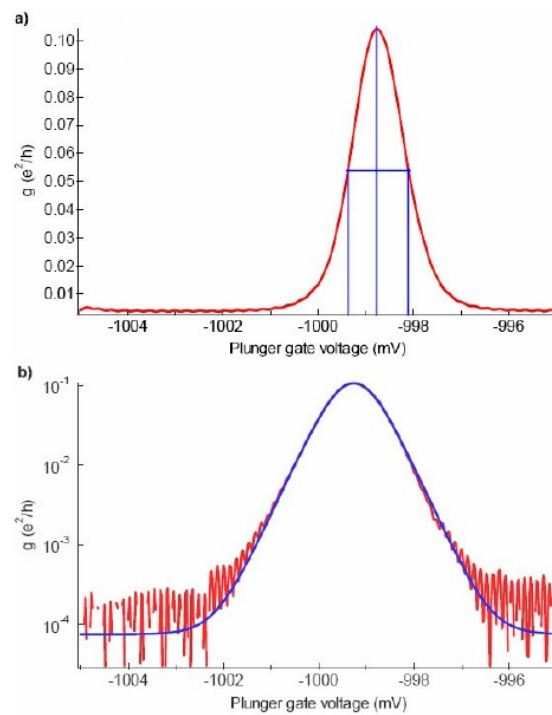


Figure 9.7: Conductance peak in a linear (a) and logarithmic (b) scale. The FWHM can be used to determine the electron temperature. (peak position=-999.26mV, peak height= $0.1076 e^2/h$, FWHM=1.1788 mV)

9.5.3 Improvements in the set up and the device

The electron temperature was very high and needed definitely to be improved. This needed improvement in thermal conductivity from mixing chamber and the sample. The first step was to change the solder joints between the sample and the mixing chamber plug. The solder joints at the socket were changed and now more stable 7 mil copper wire was used instead of 5 mil wire, both manufactured by California Fine wires. The pi-D-sub filters, manufactured by Spectrum control, are used at the break out boxes. Additional filters are used between the mixing chamber and sample. These two pole filters are designed by Prof. Dominik Zumhul and fabricated by Mr. Michael Steinacher at Electronics workshop in Dept. of Physics, Univ. of Basel. The insert with the filters mounted on is shown in 9.8. Each filter in the line is a RC filter with total resistance of 2.02k Ω and capacitance of 26.7 nF.

According to Eq. 9.1, the size of the quantum dot also plays a role. so for the next experiment to determine the electron temperature, we have used a smaller dot. The SEM micrograph of this sample is shown in Fig.9.9. This sample is produced with the same fabrication process as for Fig.9.3

9.6 Electron temperature measurement in small sized quantum dot

9.6.1 Wall-wall measurements

The wall wall measurements are done with defining a quantum dot. No DC voltage is applied to the device. The voltage is applied only to the right and left wall and plunger gates. The procedure is same as for big dot.

9.6.2 Determination of the Electron Temperature

The procedure to determine the electron temperature is the same as for the big dot. A lever arm is found $\alpha = \frac{C_g}{C_{dot}}$ to know how much the energy of the dot is shifted when the plunger voltage is changed. To find α_g we need to know the energy splitting for a certain applied bias voltage. From the Coulomb diamond diagram, a split of 8.1 mV at $-360\mu V$ applied voltage ($-400\mu V$ minus offset of $-40\mu V$) giving a lever arm of 0.044. In the quantum regime where conduction is provided through one single energy level of the dot, the FWHM of the Coulomb peak is linear in temperature: $FWHM = 3.5k_B T$. We get a FWHM of $0.5965mV \cdot 0.044 = 0.026246mV$. This corresponds to an electron temperature of $T \approx 88$ mK. ¹

¹Gregor Fessler assisted during the experiment.

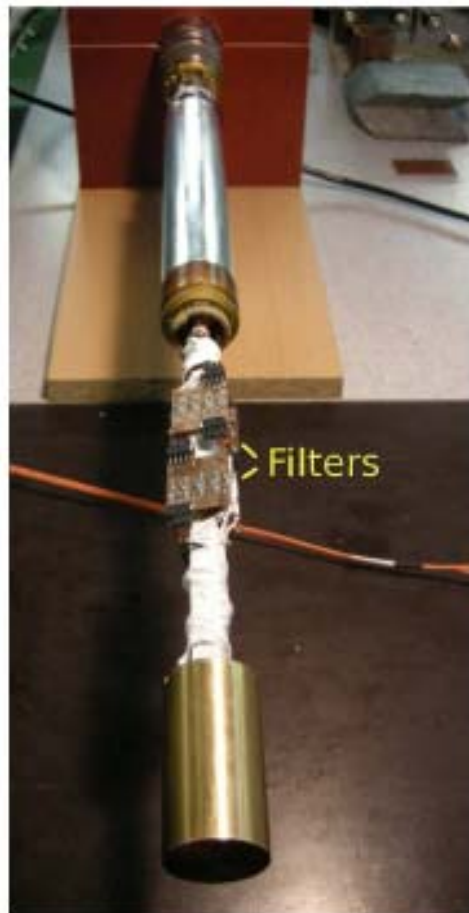


Figure 9.8: Insert of the dilution refrigerator MCK50-100 TOF with the filters mounted on the cold finger

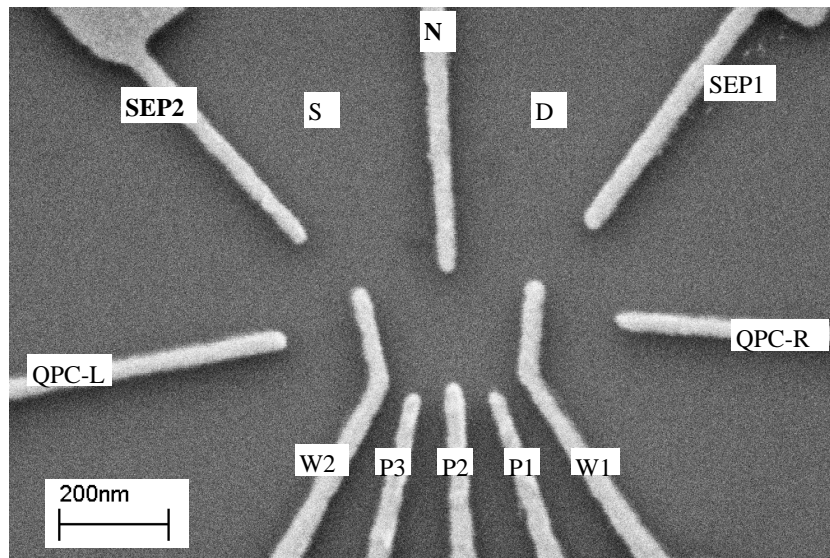


Figure 9.9: SEM micrograph of the small quantum dot sample. N=nose, w1=right wall, w2=left wall, p1,p2,p3=plunger gates, SEP=separators, QPC=quantum point contact, S=source ohmics, D=drain ohmics

The temperature in the cool-down with the big dot was more than 300 mK. So the filters and the new solder joints improved and helped us to reach a lower electron temperature. In further cooldowns, (not with the dot), it was realized that the capacitors in the two terminal filters was creating a problem and adding in to the capacitance of the device. So in the further cool downs these filters are removed. Even after removing the two pole filters, the electron temperature is below 100 mK. This is proved in the g -factor measurement with the upper bound of the temperature.

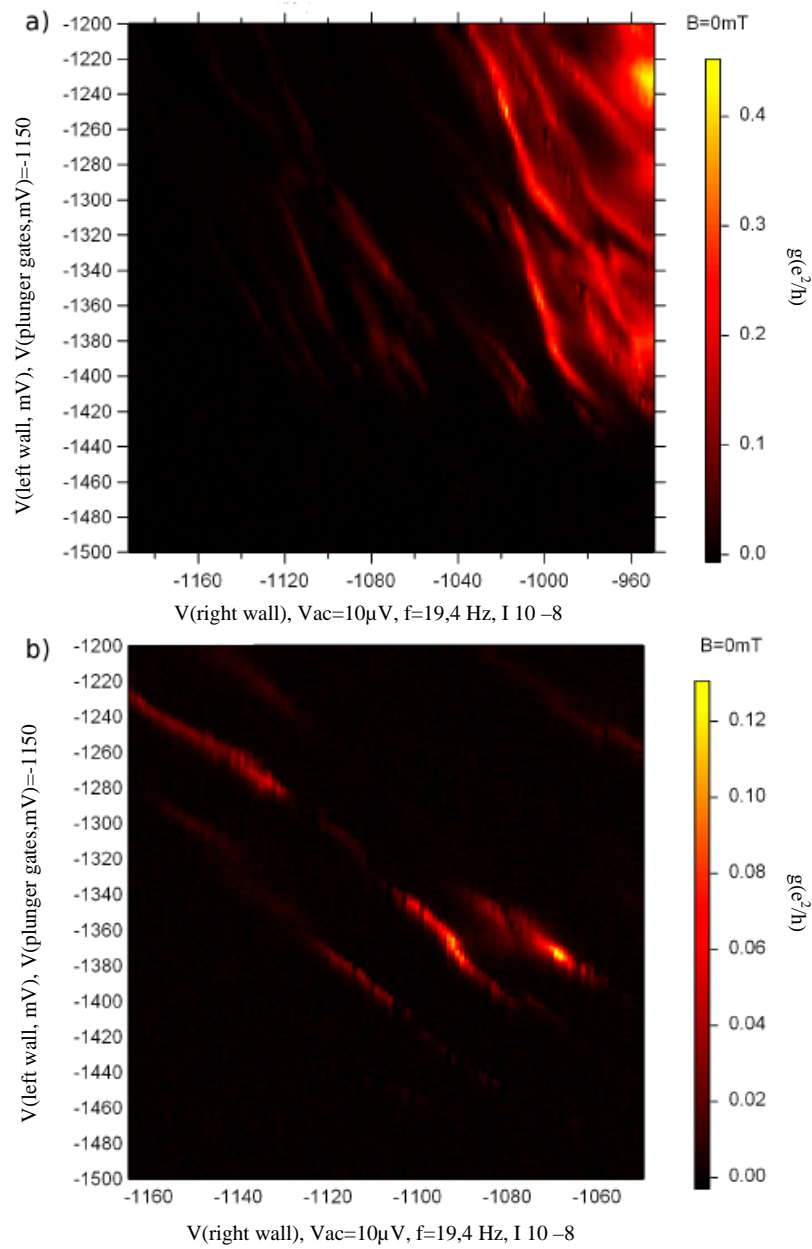


Figure 9.10: Wall–wall conductance plots for different voltages on plunger and nose gates in small dot.

10 Conductance Quantization in Quantum Wires

10.1 Introduction

In this section, we will discuss an experiment carried out on a surface gate defined quantum wire. Here we tried to see the conductance quantization as a function of applied gate voltages in a high mobility GaAs/AlGaAs heterostructure. This was done as a step to test the quantum wire at 24 mK before cooling it down to 5mK since cooling and testing with MCK-50 is fast and time efficient before cooling it down in a system where the cooling cycle is time consuming.

This project is first initiated by A. Yacoby et al. [83]

One of the fingerprints of a noninteracting 1D conductor is its quantized conductance in multiples of the universal value $G_0 = 2e^2/h$ [84]. This quantization results from a compensation of the increasing electron velocity and the decreasing density of states as the number of carriers increases. Therefore, as subsequent 1D electronic subbands are filled with electrons, the conductance appears as a series of plateaus or steps with values equal to G_Q multiplied by the number of partly occupied wire modes (N).

10.2 Quantum Wire device

The wafer used for fabrication of quantum wire is device from wafer Pfeiffer 8.29.08.01. The density and mobility table for this sample is given in table 6.3. The sample fabrication steps are described in section 5.3. In a single device, we have one quantum point contact, and wires of four different lengths, $2\mu m$, $5\mu m$, $10\mu m$ and $20\mu m$. The gates are deposited on the mesa of the Hall bar. The Hall bar has three sections, each of dimension $100\mu m \times 300\mu m$, one section is non-gated section and other two sections have the quantum wire gated. The quantum wire gates design on one section of the Hall are shown in Fig. 10.1.

The width of the quantum wires is $1.2\mu m$ in the design and the lithographic width is $1\mu m$. The roughness of the wire is $\pm 10nm$ which is reasonably good. The SEM micrograph of such a gate is shown in 10.2.

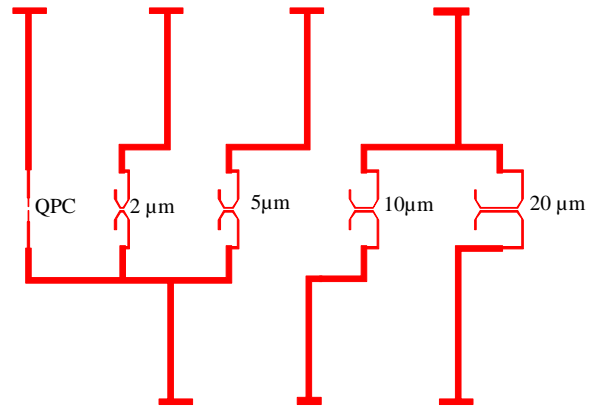


Figure 10.1: Design of a quantum wire device in one section of the Hall bar. The qpc length is $500\ \text{nm}$, and qws of different lengths $2\ \mu\text{m}$, $5\ \mu\text{m}$, $10\ \mu\text{m}$ and $20\ \mu\text{m}$.

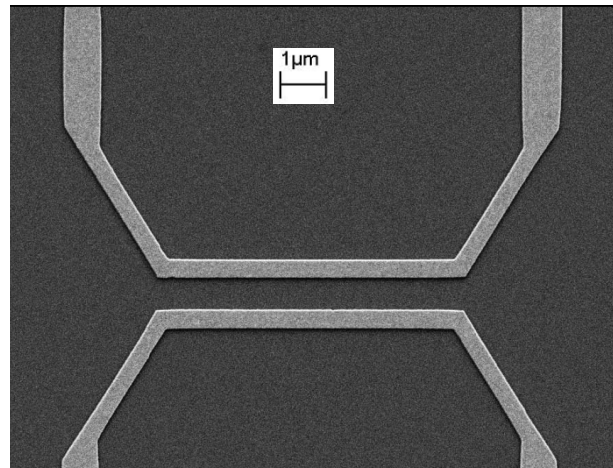


Figure 10.2: Scanning electron microscope (SEM) micrograph of a $5\ \mu\text{m}$ quantum wire gates

10.3 Measurement set up

The voltages that are applied to the sample are controlled on the computer with the software Igor Pro (WaveMetrics, Lake Oswego, USA). The signal is transmitted over GPIB and optical fibers (National Instruments, Austin, USA) to the Digital to Analog Converter (DAC). A self-built AC/DC bias box (Fig. 9.4) is used to apply an AC modified DC signal to the source of the sample. The AC signal is generated and read out by a Lock-In Amplifier (EG&G Instruments Corporation, Princeton, USA). The DC input for the bias box and the signals for the gates are coming from the DAC. All the electrical signals are then transmitted to the insert via one of two breakout boxes. The current that is measured on the sample is amplified by a current amplifier and filtered with the Lock-In Amplifier. The signal is then transmitted back to the computer via optical fibers to be analyzed in Igor Pro. Thanks to my colleague Christian Scheller for the experimental set up. The conductance is measured with applying negative voltages to the upper and lower gates and current in the Hall bar is probed.

Fig.10.3 shows the conductances in QPC and different wires of length $5\mu m$, $10\mu m$ and $20\mu m$ in one section of Hall bar. The color scale shows the conductance quantization with e^2/h . The conductance plateaus as a function can be seen in the right panel. The QPC has well resolved conductance except for 1 and 2 e^2/h plateaus. Bu as the length of the wire is increased the plateaus can be seen clearly but they are not well resolved as for qpc.

So in this test, we have seen the conductance plateaus in the wires of same width but different lengths. all the tests are done at base temperature of the mixing chamber. The data looks reasonably good. The device is then cooled in another system with base temperature of 5mK for further tests.

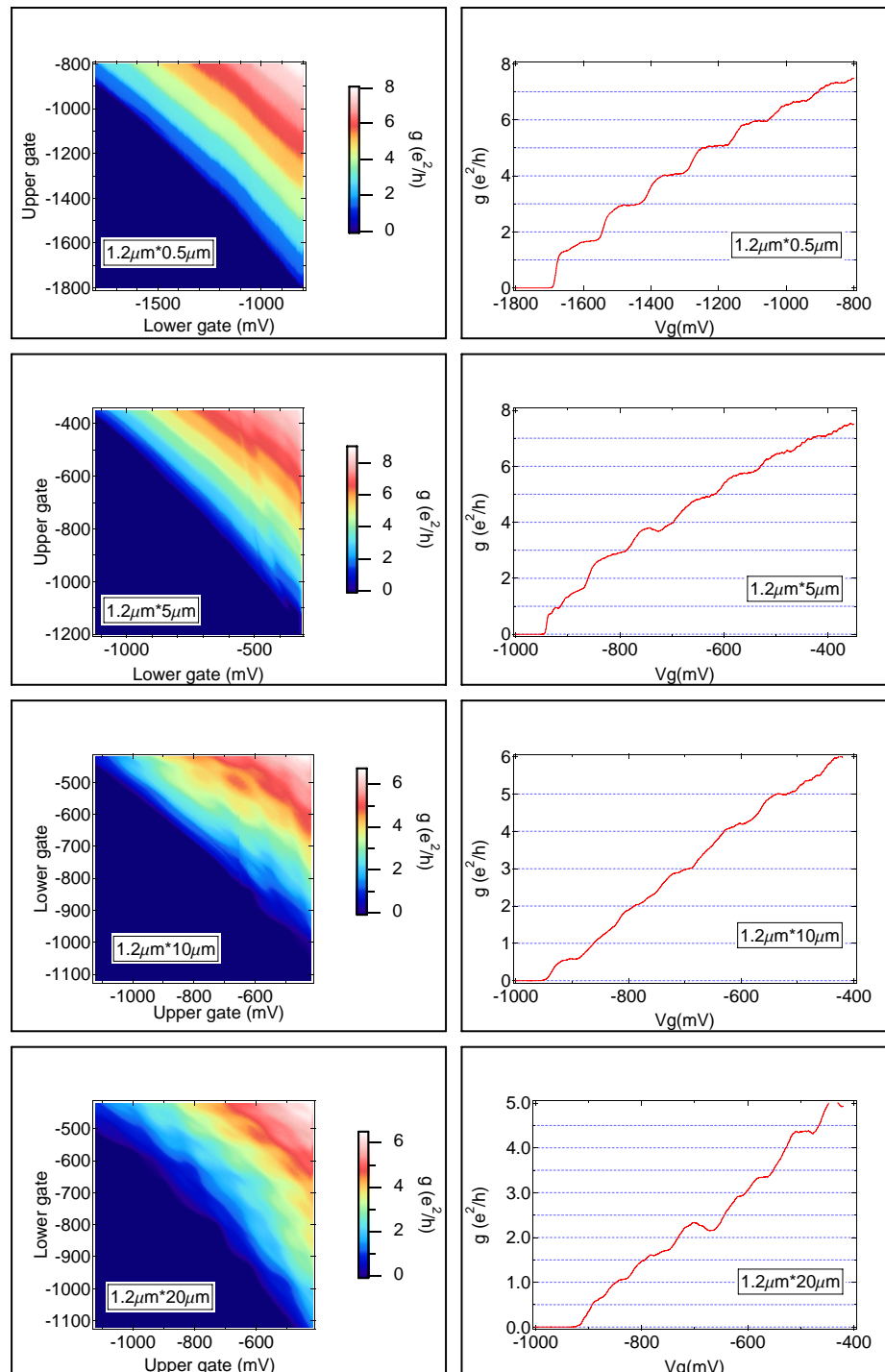


Figure 10.3: Conductance in QPC, and wires of length $5\mu\text{m}$, $10\mu\text{m}$ and $20\mu\text{m}$ showing quantization with e^2/h

1 Appendix

1.1 Fabrication processes

1.2 Mesa Photolithography

1. Cleave a piece from wafer
2. Three solvent clean: TCE, acetone, methanol, 5 min. each, sonication at high power.
3. Blow dry with N_2 gas.
4. Prebake $120^\circ C$, 3min., cool for 2-3 min.
5. Spin resist, ma-N 415 at 4000 rpm, 40 sec.
6. Bake the resist for at $90^\circ C$ for 90 sec.
7. Exposure for 14 sec, CH1, soft contact
8. Develop in ma-D377 for ≈ 100 sec.
9. Rinse with DI water.
10. Blow dry with N_2 gas.

1.3 Mesa Etching

1. Mix $H_2SO_4 : H_2O_2 : H_2O :: 2:16:480$ ml.
2. Check the temperature.
3. Etch ≈ 40 s, rinse in DI water.
4. Check height with profile meter and etch further if needed.
5. Remove the resist with warm (50°) NMP (N-Methyl pyrrolidone)
6. Rinse with DI water.

1.4 Ohmic Photolithography

1. Three solvent clean: TCE, acetone, methanol, 5 min. each, sonication at high power.
2. Blow dry with N_2 gas.
3. Prebake $120^\circ C$, 3min., cool for 2-3 min.
4. Spin resist, ma-N 415 at 6000 rpm, 40 sec.
5. Bake the resist for at $90^\circ C$ for 90 sec.
6. Exposure for 14 sec, CH1, soft contact
7. Develop in ma-D377 for ≈ 100 sec.
8. Rinse with DI water.
9. Blow dry with N_2 gas.

1.5 Ohmics Evaporation

1. Oxygen plasma clean at pressure=250 mbar, DC bias ≈ 90 V, power=30 w, time=55 s, etch rate ≈ 1.7 nm/s.
2. Dip in 37% HCl, rinse with DI water, glue on the sample holder with PMMA glue.
3. Immediately mount the sample in the evaporator.
4. Cool sample holder with liquid N_2 externally till $0^\circ C$.
5. Wait till pressure in the chamber $\leq 5 \times 10^{-6}$ mbar.
6. Evaporate Ni:Ge: Au:Ni: Au::50:1250:2500:200:50 A \circ
7. Lift off in warm (50°) NMP.
8. Rinse with DI water.

1.6 Ohmic Annealing

1. Three solvent clean: TCE, acetone, methanol, 5 min. each, sonication at high power.
2. Load the sample at the center of the ceramic bridge in the oven.
3. Annealing recipe

Step	Temperature($^{\circ}C$)	Time (s)	Type	Comment
1	100	60	1	Dehydration
2	100	60	3	Chamber cleaning
3	100	60	1	Sample heating
4	370	120	2	Eutectic formation
5	480	60	2	Diffusion
6	100	60	3	Cooling

1.7 Electron beam lithography

1. Three solvent clean: TCE, acetone, methanol, 5 min. each, sonication at high power.
2. Blow dry with N_2 gas.
3. Prebake $180^{\circ}C$, 3min., cool for 2-3 min.
4. Spin resist, 4.5 % PMMA 6000 rpm, 40 sec, PMMA thickness ≈ 450 nm.
5. Bake the resist for at $180^{\circ}C$ for 120 sec.
6. Load the sample in Leo chamber.
7. Connect Leo computer and pattern generator computer.
8. Origin correction.
9. Angle correction.
10. Focus correction.
11. Write-field alignment.
12. Exposure with $10\mu m$ aperture, ≈ 40 pA for small features and $120\mu m$ aperture, few nA for big features.

13. Develop for ≈ 75 sec. in MIBK:IPK:MEK mixture.
14. Rinse with IPA.
15. Blow dry with N_2 gas.

1.8 Small Gates Evaporation

1. Oxygen plasma clean at pressure=250 mbar, DC bias ≈ 90 V, power=30 w, time=10 s, etch rate ≈ 1.7 nm/s.
2. Rinse with IPA, glue on the sample holder with PMMA glue.
3. Immediately mount the sample in the evaporator.
4. Cool sample holder with liquid N_2 externally.
5. Wait till pressure in the chamber $\leq 5 \times 10^{-6}$ mbar.
6. Evaporate Ti:AU::50:750 \AA
7. Lift off in warm (50 $^\circ$) acetone.
8. Rinse with DI water.

1.9 Large Gates Photolithography

1. Three solvent clean: TCE, acetone, methanol, 5 min. each, sonication at low power.
2. Blow dry with N_2 gas.
3. Prebake 120 $^\circ$ C, 3min., cool for 2-3 min.
4. Spin resist, ma-N 415 at 6000 rpm, 40 sec.
5. Bake the resist for at 90 $^\circ$ C for 90 sec.
6. Exposure for 14 sec, CH1, soft contact
7. Develop in ma-D377 for ≈ 100 sec.
8. Rinse with DI water.
9. Blow dry with N_2 gas.

1.10 Large Gates Evaporation

1. Mount in the evaporator.
2. Cool sample holder with liquid N_2 externally.
3. Wait till pressure in the chamber $\leq 5 \times 10^{-6}$ mbar.
4. Evaporate Ti:AU::50:1650 A_0
5. Lift off in warm (50°) acetone.
6. Rinse with DI water.

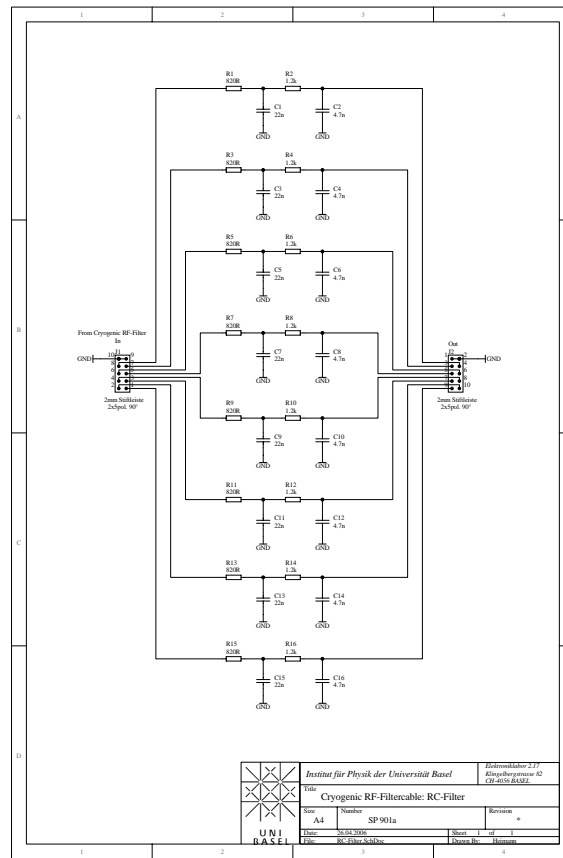


Figure 1.1: Low noise filter design, designed and fabricated at Department of Physics, University of Basel

1.11 Low noise filters

List of Figures

2.1	2-dimensional electron gas is formed at the interface between intrinsic GaAs and n-doped AlGaAs. Silicon atoms act as a electron–dopant. After giving away an electron, the Si-atoms are positively charged.[5]	5
2.2	Illustration of the diffusive and ballistic transport regime.[8]	11
2.3	Density of states of a 2DEG with only one subband occupied ($E_F < E_2$). Inset: Energy levels in the 2DEG. [9]	12
2.4	(a) Density of states of a 2DEG without external magnetic field. (b) Landau level quantization starts at low magnetic fields. (c) At high magnetic fields, the spacing is larger than the level broadening ($\hbar\omega_c c > \Gamma$) and the density of states is zero between the Landau levels. [10]	14
2.5	The Landau quantization without potential fluctuations in the bulk contains only extended states. When disorder potentials are present due to impurities, scattering in the bulk broadens the Landau levels and creates localized states. The extended states carry the current via edge states and the localized states stabilize the Fermi energy between the Landau levels.[11]	15
2.6	Landau level bending at the boundaries of a confined 2DEG. The resulting edge states at the Fermi energy transport the current spatially separated, giving rise to zero longitudinal resistance. [10]	17
2.7	(a) Edge states near the sample boundaries and localized states in the bulk. (b) Regarding the Fermi velocity $v_F = 1/\hbar \delta E_n(k = k_F)/\delta k$ at the disorder potentials (black points and crosses), the cyclotron orbits circle along equipotential contours and are therefore localized. Localized states are the result of scattering on impurities due to local equipotentials. The scattering dependent broadening of the Landau levels stabilizes the Fermi energy between the Landau levels. [9]	17
3.1	Phase diagram of ^4He . [16]	20
3.2	Phase diagram of ^3He . [16]	21
3.3	Left:Phase diagram of $^3\text{He}/^4\text{He}$ mixture vs. ^3He concentration x and temperature Θ . The tricritical point is at $x=0.67$ and $\Theta = 860\text{mK}$. At lower temperatures, the mixture segregates into a ^3He –rich concentrated (C) phase and ^3He – poor dilute (D) phase. Right: Sketch of the chemical potential of the two phases at $\Theta = 0$ [15]	22
3.4	MCK 50 set up with dewar and gas handling system	24
3.5	Mixing chamber plug, cold finger and cold finger extension	27
3.6	Cold finger, socket and sample holder	28

4.1	(a) the disassembled cage with the upper flange, the cage, the lower flange and the four spools. (b),(c),(d) assembled cage and mounted into the solenoid. yellow: IVC, green/red: solenoid. [23]	31
4.2	Hall resistance measurement on a dot mesa as a function of solenoid field. The same sample and calibration is used to determine the split pair fields.	32
4.3	Transverse resistance as a function of current through split pair 3–4. The Hall slope from the linear fit is $51.59 \Omega/A$	33
4.4	Maximum fields reached by split pairs 1–2 and 3–4 with solenoid field. The solenoid field is kept constant (positive) and the split pairs are ramped till the quenching points of the split pairs.	34
5.1	Growth profile and bandstructure of typical GaAs heterostructures.[28]	36
5.2	Complete growth-profile of the wafer Pfeiffer 9.12.05.2 used in this work. A spacing layer of 80nm separates the Si-atoms from the 2DEG plane. GaAs was used as a cap layer to protect the layers containing Al from fast oxidation.	37
5.3	Complete growth-profile of the wafer (a) Pfeiffer 7.28.08.02 and (b) Pfeiffer 8.29.08.1 used in this thesis work. A spacing layer of 100 nm separates the Si-atoms from the 2DEG plane. GaAs was used as a cap layer to protect the layers containing Al from fast oxidation.	38
5.4	Complete growth-profile of the wafer Gossard 060926B used in this work.	39
5.5	Hallbar design. The 2DEG is located at the white regions. The hallbar has a dimension of $1240 \times 100 \mu m^2$. The spacing between to adjacent ohmic contacts is $300 \mu m$. The width of Hall bar is $100 \mu m^2$. The measured ρ_{xx} between this two nearby contacts has to be divided by three to get ρ_{\square}	40
5.6	Quantum dot design. (a) Complete mesa dimension of $1520 \times 1140 \mu m^2$. The 2DEG is located at the white regions. (b) The yellow squares denote the source and drain. Quantum dot is formed by applying voltages to the fine gates.	41
5.7	Quantum wire design. The Hall bar has a dimension of $1210 \times 100 \mu m^2$. (a) shows the complete device.The 2DEG is located at the white regions. (b) shows the $10 \mu m$ wide quantum wire gate.	42
5.8	Finger gate design without top gate. The Hall bar has a dimension of $1210 \times 100 \mu m^2$. The average spacing between two adjacent finger gate $23 \mu m$.(a) shows the complete device.The 2DEG is located at the white regions. (b) shows detailed view of the finger gates.	43
5.9	Optical Photolithography steps.	46
5.10	Reactive Ion Etching setup showing the RIE chamber [30]	47

5.11	Sample fabrication steps. (a) Mesa:- After photolithography and etching, (b) Ohmic contact pads on the mesa, (c) Ebeam lithography step for finger gates, (d) Detailed view of finger gates after ebeam, (e) Ebeam exposure for top gate (f) Detailed view of top gate and finger gate, (g) Finished device with large gates	49
5.12	Ohmic contact (a)before annealing , (b) after annealing	51
5.13	SEM micrograph (a) quantum dot gates (b) quantum wire gates	52
5.14	Finger gate with top gate + SiO_2 . + SiO_2 acts as a insulator between the finger gates and top gate	53
5.15	Finger gates sample design with intercalated top gate and finger gates.The distance between finger gate and portion of top gate is $1.3\mu m$	53
5.16	SEM micrograph of a finger gate sample	54
5.17	Finger Gate sample	55
6.1	Hall bar geometry	57
6.2	Low field magnetoresistance data used to determine the density (<i>left axis</i>) and mobility (<i>right axis</i>) of sample Pfeiffer 7.28.08.2. The Hall slope is $8.2385 \pm 0.0028k\Omega/T$	58
6.3	Variation of density (<i>right axis</i>) and mobility (<i>left axis</i>) in a gated and non gated sample as a function of temperature in Pfeiffer 7.28.08.2.	59
6.4	Variation of density (n) and mobility (μ) with gate voltage in sample from Pfeiffer 8.29.08.01. (a) shows the Hall voltage for both positive and negative fields. (b) show the longitudinal voltage and (c) shows current for bot positive and negative fields. From (d) we get the density and mobility at zero gate voltage. The data is taken at $B=\pm 20$ mT and base temperature 24 mK	62
6.5	Variation of density (n) and mobility (μ) with gate voltage in Pfeiffer 7.28.09.02. The data is taken at $B=\pm 10$ mT and base temperature $T=24$ mK	63
6.6	Low field magneto-resistance data for different currents in sample Pfeiffer 07.28.09.02 at base temperature $T=24$ mK	68
6.7	<i>Upper panel</i> Magnet sweep up and down direction before shifting the traces. <i>Lower panel</i> The up direction trace is shifted to coincide with the magnet down sweep. The field shift is around -20 mT. The data is taken with 1mT/s and at base temperature $T=24$ mK	70
6.8	<i>Upper panel</i> Shubnikov de-Haas oscillations at different temperatures, complete field trace. <i>Lower panel</i> shows low field zoom in. These traces are for Pfeiffer 09.12.05.2	72
6.9	Polynomial fit around virtual zero magnetic field used to obtain the B_{offset} and $\rho_{xx}(0)$	73

6.10	<i>Upper panel</i> Shows a low-field SdH oscillation which was used to extract the amplitude. <i>Lower panel</i> The effective mass m^* was obtained by fitting the linear regions in $\ln(\Delta R_{xx})$ vs T for Pfeiffer 09.12.05.2. The Dashed lines show the line fits.	74
6.11	<i>Upper panel</i> shows $\ln(\Delta R_{xx})$ in the nongated region of the Hall bar. <i>Lower panel</i> shows $\ln(\Delta R_{xx})$ in gated region of the Hall bar. The effective mass m^* was obtained by fitting the linear regions in $\ln(\Delta R_{xx})$ vs T for Pfeiffer 07.28.09.02. The dashed lines show the line fits.	75
6.12	Longitudinal oscillations at three different top gate voltages, +50,0 and -150mV at base temperature 24 mK	80
6.13	<i>Upper panel</i> Complete field trace for zero top gate voltage at different temperatures. <i>Right</i> Detailed view of left panel showing the SdH maxima at different temperatures. The magnet is wept down from high field to low field.	81
6.14	Dingle plot for base temperature, $V_{TopGate}=0$ mV assuming two different electron temperatures, 25mK (upper panel) and 100 mK(lower panel)	83
6.15	Dingle plot for base temperature, $V_{TopGate}=-50$ mV	84
6.16	Dingle plot for 200mK, VTG=+100 mV (upper panel) and VTG=-200mV (lower panel)	85
6.17	Transport time and quantum scattering time at base temperature as a function of carrier density at 24 mK	86
6.18	Quantum scattering time at base temperature as a function of carrier density for different electron temperatures and the average quantum scattering time.	87
6.19	Transport time and quantum scattering time at 200 mK as a function of carrier density	88
6.20	Transport time and quantum scattering time at 400 mK as a function of carrier density	88
6.21	Quantum scattering time at different temperatures as a function of carrier density	89
6.22	Ratio of transport time to quantum scattering time as a function of density for different remepratures.	90
6.23	Temperature dependence of the spin-split minima with $B_{inplane} = 0$	92
6.24	Arrhenius plots for two different magnetic fields, (in <i>upper panel</i> , for B=166.5 mT and in <i>lower panel</i> , for B=261 mT). g^* is extracted from a linear fit for temperatures where Eq. 6.16 is applicable in Pfeiffer 09.12.05.2 sanple.	93

6.25	<i>Upper panel</i> g^* -factor with inplane magnetic field=0 T. <i>Lower panel</i> g^* -factor in the same sample in presence of inplane magnetic field of 1T in Pfeiffer 09.12.05.2 sample.	94
6.26	Arrhenius plots in non gated section for two different magnetic fields.. <i>Upper panel</i> shows Arrhenius plot in not-gated sample for B=285 mT and <i>Lower panel</i> g^* shows Arrhenius plot for B=346 mT in Pfeiffer 7.28.08.2 sample with $B_{in-plane} = 0$	96
6.27	g^* -factor normalized to $ g_b $ for not gated and gated sections of Pfeiffer 7.28.08.2 sample. $B_{in-plane} = 0$	97
7.1	Variation of Density and mobility in a gated and non gated sample as a function of temperature	102
7.2	Density and mobility variation with gate voltage	102
7.3	Longitudinal oscillations at three different gate voltages, +50,-50 and -100mV	104
7.4	Dingle plot for base temperature, VTG=-50 mV	105
7.5	Transport time and quantum scattering time at base temperature as a function of carrier density	105
7.6	Transport time and quantum scattering time at 200 mK as a function of carrier density	106
7.7	Transport time and quantum scattering time at 400 mK as a function of carrier density	107
7.8	Quantum scattering time at different temperatures as a function of carrier density	108
7.9	Quantum scattering time in a non gated sample	109
7.10	Ratio of transport time to quantum scattering time as a function of density for different remepratures.	109
8.1	(a) A system of randomly spaced parallel potential barriers and randomly distributed isotropic impurities.(b) expected dependences of the in- and out-of-plane conductivities on bulk disorder.[68]	112
8.2	an array of randomly spaced stripe-like gates as a local disorder	112
8.3	Device designs used in the experiment. (a) Device with SiO_2 (b) Device with intercalated finger and top gates	113
8.4	SEM image of finger gates, from test sample	115
8.5	Optical image of a finger gate sample with SiO_2 . Three sections of each $300\mu m \times 100\mu m$ dimensiona are labeled as top gate region, finger gate region I and finger gate region II from left to right.	116

8.6	Characteristics of different regions of Hall bar as a function of top gate voltage at $B=0$ and zero finger gate voltage, with sweep down and sweep up directions at base temperature, 24 mK. (a) in top gate region (b) in finger gate region-I, (c) in finger gate region-II, (d) current across the Hall bar.	117
8.7	Voltage biased measurement at base temperature at $B=0$. The solid lines are for voltage down sweep and dashed lines are for voltage up sweep. The upper panel shows the voltage sourced and the lower panel shows the current probed. The finger gates regions are tuned to tunneling regime.	118
8.8	Voltage biased measurement at base temperature at $B=0$. The solid lines are for voltage down sweep and dashed lines are for voltage up sweep. The upper panel shows the voltage sourced and the lower panel shows the current probed. The finger gates regions are tuned to tunneling regime.	120
8.9	2D diagram for current, sweeping single finger gate and top gate together, at base temperature, $B=0$	121
8.10	Resistance across FG-I region (<i>upper panel</i>) and current across the sample(<i>lower panel</i>) when the single finger gate and all finger gates in region I are compensated for top gate voltage. Solid lines- voltage down sweep, dashed lines-voltage up sweep	122
8.11	Resistance across FG-I region (<i>upper panel</i>) and current across the sample(<i>lower panel</i>) when the % is varied as 0%,95%,100% and 105% Solid lines- voltage down sweep, dashed lines-voltage up sweep	124
8.12	Resistance across FG-I region (<i>upper panel</i>) and current across the sample(<i>lower panel</i>) when the tunneling regime in the FG I region is varied at $B=0$. Solid lines- voltage down sweep, dashed lines-voltage up sweep	125
8.13	2D diagram for current, sweeping single finger gate and top gate together in finger gate region II, at base temperature, $B=0$	126
8.14	Resistance across FG-II region (<i>upper panel</i>) and current across the sample(<i>lower panel</i>) when the tunneling regime in the FG II region is varied, at $B=0$. Solid lines- voltage down sweep, dashed lines-voltage up sweep	127
8.15	Resistance across FG-I region (<i>upper panel</i>) and current across the sample(<i>lower panel</i>) for single gate potential, $50k\Omega$ and 100Ω , at $B=0$. Solid lines- voltage down sweep, dashed lines-voltage up sweep	128
8.16	SEM micrograph of intercalated finger gate sample with average spacing between the finger gates of $23\mu m$	130

8.17	Resistance across FG-I region (<i>upper panel</i>) and current across the Hall bar(<i>lower panel</i>) for different tunneling regimes, 56k Ω and 101 Ω and 201 Ω , at B=0. Solid lines- voltage down sweep, dashed lines-voltage up sweep	131
8.18	Effect of single gate potential. Resistance across FG-I region (<i>upper panel</i>) and current across the sample(<i>lower panel</i>) for different tunneling regimes, 20k Ω , 60k Ω and 200 Ω and 600 Ω , at B=0. Solid lines- voltage down sweep, dashed lines-voltage up sweep	132
8.19	Comparison of single gate and FG I region potentials. Resistance across FG-I region (<i>upper panel</i>) and current across the sample(<i>lower panel</i>) for different tunneling regimes, 20k Ω , 60k Ω , 200 Ω and 600 Ω , at B=0. Solid lines- voltage down sweep, dashed lines-voltage up sweep	134
8.20	Effect of single gate potential. Resistance across FG-I region (<i>upper panel</i>) and current across the sample(<i>lower panel</i>) for different tunneling regimes, 20k Ω , 60k Ω and 100 Ω , at B=0. Solid lines- voltage down sweep, dashed lines-voltage up sweep	135
8.21	Effect of all gates in FG I region. Resistance across FG-I region (<i>upper panel</i>) and current across the sample(<i>lower panel</i>) for different tunneling regimes, 20k Ω , 60k Ω and 100 Ω , at B=0. Solid lines-voltage down sweep, dashed lines-voltage up sweep	136
8.22	Effect of FG I region and FG II gate potentials. Resistance across FG-I and FG-II region (<i>upper panel</i>) and current across the sample(<i>lower panel</i>) for different tunneling regimes, 20k Ω , 60k Ω and 100 Ω , at B=0. Solid lines- voltage down sweep, dashed lines-voltage up sweep	137
8.23	Comparison of single gate, FG I and FG II region potentials. Resistance across FG-I due to single gate (SG) and gates in FG I region (FG I) and FG-II (FG II) regions due to all gates potential for different tunneling regimes, 20k Ω , 60k Ω and 100 Ω , at B=0. Solid lines-voltage down sweep, dashed lines-voltage up sweep	138
8.24	2D plot showing current across the FG I region when the single gate and top gate voltages are swept together.	138
8.25	Resistance log in the sample as a function of finger gates in the log scale, at base temperature, 24 mK and B=0. The solid and dashed lines are voltage sweep down and sweep up directions. Solid lines-voltage down sweep, dashed lines-voltage up sweep	140
8.26	Resistance in the sample as a function of mixing chamber temperature, in different tunneling regimes 10k Ω , 100k Ω and 1M Ω with three different gates, single gates (SG), group of 7 finger gates and group of 10 gates.	140

9.1	(a) Schematic picture of a quantum dot that couples capacitively to the plunger gate and by tunnel junction to the source and drain reservoirs. (b) By applying a source-drain bias V_{dc} one can tune the difference in electrochemical potential of source and drain and with the voltage on the plunger gate the potential of the dot. [80]	144
9.2	In the upper panel the inverse of the maximal differential conductance is printed, in the lower panel FWHM as a function of temperature. Two slopes are visible, $FWHM = 4.35k_B T$ for the classical regime and $FWHM = 3.5k_B T$ for the quantum regime. [82]	146
9.3	SEM micrograph of the measured sample. N=nose,w1=right wall, w2=left wall, p1,p2,p3=plunger gates,SEP=separators, QPC=quantum point contact, S=source ohmics, D=drain ohmics	147
9.4	Electrical circuit of the AC/DC bias box, which divides the applied voltages by approximately 1 : 500000 (AC) and 1 : 1000 (DC) respectively.	148
9.5	Wall-wall conductance plots for different voltages on plunger and nose gates.	150
9.6	Coulomb diamond: measuring conductance through the dot while scanning over the applied DC voltage and the plunger gate voltage.	151
9.7	Conductance peak in a linear (a) and logarithmic (b) scale. The FWHM can be used to determine the electron temperature. (peak position=-999.26mV, peak height=0.1076 e^2/h , FWHM=1.1788 mV)	151
9.8	Insert of the dilution refrigerator MCK50-100 TOF with the filters mounted on the cold finger	153
9.9	SEM micrograph of the small quantum dot sample. N=nose,w1=right wall, w2=left wall, p1,p2,p3=plunger gates,SEP=separators, QPC=quantum point contact, S=source ohmics, D=drain ohmics	154
9.10	Wall-wall conductance plots for different voltages on plunger and nose gates in small dot.	155
10.1	Design of a quantum wire device in one section of the Hall bar. The qpc length is 500 nm, and qws of different lengths $2\mu m$, $5\mu m$, $10\mu m$ and $20\mu m$.	157
10.2	Scanning electron microscope (SEM) micrograph of a $5\mu m$ quantum wire gates	157
10.3	Conductance in QPC, and wires of length $5\mu m$, $10\mu m$ and $20\mu m$ showing quantization with e^2/h	159
1.1	Low noise filter design, designed and fabricated at Department of Physics, University of Basel	vi

List of Tables

4.1	A short summary of the number of windings, resistance and inductance. [23]	31
4.2	Short summary of the maximum fields of the split pair magnet in negative and positive directions at fixed solenoid field	34
6.1	Density, mobility derived from Hall resistance R_H for samples Pfeiffer 9.12.05.2 (after LED illumination, details in the text), Pfeiffer 7.28.08.2 and Pfeiffer 08.29.08.1 at 24 mK.	60
6.2	Density, mobility and other parameters derived from gate voltage variation of density and mobility for sample Pfeiffer 07.28.09.02 at base temperature $T=24$ mK.	64
6.3	Density, mobility and other parameters derived from gate voltage variation of density and mobility for sample Pfeiffer 08.29.08.01 at base temperature $T=24$ mK.	65

References

- [1] K. von Klitzing, G. Dorda, and M. Pepper, *Phys. Rev. Lett.*, **45**,494 (1980).
- [2] D. C. Tsui, H. L. Stormer, and A. C. Gossard, *Phys. Rev. Lett.*, **48**,1559 (1982).
- [3] H.Lüth. *Surfaces and Interfaces of Solid Materials*. Springer–Verlag, Berlin (1996).
- [4] C. T. Foxon, J. J. Harris, D. Hilton, J. Hewitt, and C. Roberts *Semicond. Sci. Technol.*, **4**,582 (1989).
- [5] Supriyo Dutta *Electronic transport in Mesoscopic system*
- [6] Zumbuhl, D. M. *Lecture Notes: Introduction to Mesoscopic Physics and Quantum Dots*. University of Basel, (2006)
- [7] Drude, Paul *Zur Elektronentheorie der metalle*. *Annalen der Physik* **306**, 566, (1990).
- [8] Thomas Schaeppers, *Article: Transport in Nanostructures*
- [9] C. W. J. Beenakker and H. van Houten, *Solid State Physics*, **44**, 1-228 (1991)
- [10] C. Mitzkus, PhD thesis, University Regensburg (2005)
- [11] B. Jeckelmann and B. Jeanneret, *Rep. Prog. Phys.* **64**,160 (2001)
- [12] H. Kamerlingh Onnes, *The Superconductivity of Mercury*, *Comm. Phys. Lab. Univ. Leiden*, (1911)
- [13] H. London, *Proceedings of the International Conference on Low-Temperature Physics*, Oxford University Press (1951)
- [14] G. Frossati, *Experimental Techniques: Methods for Cooling Below 300 mK*, *J. Low Temp. Phys.*, **87**, 595 (1992)
- [15] Thomas Heinzel *Mesoscopic Electronics in Solid State Nanostructures*, 116–127, 2nd Edition, Willey-Vch Verlag GmbH & CoKGaA
- [16] Frank Pobell, *Matter and Methods at Low Temperatures*, second edition, Springer (1996)
- [17] F. London, *Nature*,**141**,163 (1938)

-
- [18] Frank Pobell, *Matter and Methods at Low Temperatures*, second edition, Springer (1996)
- [19] G. Frossati, *Experimental Techniques: Methods for Cooling Below 300 mK*, *J. Low Temp. Phys.*, **87**, 595 (1992)
- [20] Cryogenic Ltd, Superconducting magnet system, Job No. 2582, Manual
- [21] Leiden Cryogenics BV, Model Microkelvin 50-100/200 TOF, Dilution Refrigerator, Instruction Manual
- [22] <http://www.locknest.com/newsite/products/lcc/index.htm>
- [23] Petar Jurcevic 3-Axis Vector Magnet: Construction and Characterization of Split Coils at RT
Semester Project report, Quantum Coherence lab, 2010
- [24] Fowler, Michael Historical Beginnings of Theories of Electricity and Magnetism, http://galileoandstein.physics.virginia.edu/more_stuff/E&M_Hist.html,
- [25] Clarke, R., Clarke, R. Magnetic properties of materials, <http://info.ee.surrey.ac.uk/Workshop/advice/coils/mu/>
- [26] Ekin, J.W., 2007, *Experimental techniques for low-temperature measurements*, Oxford, p. 601–602.
- [27] Ekin, J.W., 2007, *Experimental techniques for low-temperature measurements*, Oxford, p. 504–505.
- [28] Michael Switkes, Ph.D. thesis, *Decoherence and adiabatic transport in semiconductor quantum dots*, November (1999).
- [29] PMMA resist data sheet www.microchem.com/products
- [30] <http://www.memsnet.org/mems/processes/etch.html>
- [31] *Solid State Physics* by Ashcroft, Mermin *Solid State Physics*
- [32] Nobel lecture *Rev. Mod. Phys.* **71**, 875 (1999).
- [33] M.A. Paalanen, D.C. Tsui, J.C.M. Hwang, *Phys. Rev. Lett.*, **51**, 2226 (1983).
- [34] A. Houghton, J.R. Senna, and S.C. Ying, *Phys. Rev. B* **25**, 6468 (1982).
- [35] S.M. Girvin, M. Jonson, and P.A. Lee, *Phys. Rev. B* **26**, 1651 (1982).

-
- [36] F.F. Fang, A.B. Fowler and A. Hartstein, *Phys. Rev.B* **16**,4446 (1977)
- [37] D.V. Galchenkov, I.M. Grodnenskii, O.R. Matov, T.N.Pinsker and K.V. Starostin, *JETP Lett.* **40**, 1228 (1984)
- [38] F.A.P. Blom, P.F. Fontein, J.H. Wolter, F.M. Peeters, X. Wu *, F. Geerinckx and J.T. Devreese, *Surface Science*, **229**,70 (1990).
- [39] T. Ando. Theory of quantum transport in a two-dimensional electron system under magnetic fields. *J. Phys. Soc. Jpn*, **36**,959 (1974).
- [40] P.T. Coleridge, R. Stoner, and R. Fletcher, *Phys. Rev. B* **39**,1120 (1989).
- [41] T.Ando, *J. Phys. Soc. Japan* **51** ,3900 (1982)
- [42] Tan, Y. W., Zhu, J., Stormer, H. L., Pfeiffer, L. N., Baldwin, K. W., and West, K. W., *Phys. Rev. Lett. B* **73** , 045334 (2006).
- [43] T.Ando, A. Fowler, *F. Stern Rev. Mod. Phys.* **54** 437, (1982).
- [44] G. Bastard *Wave Mechanics Applied to Semiconductor Heterostructures*, Les Editions de Physique, Les Ulis, France (1988)
- [45] S.Das Sarma and F. Stern, *Phys. Rev. B* **32** , 8442 (1985).
- [46] A. Gold, *Phys. Rev. B* **38**, 10798 (1988).
- [47] P.T. Coleridge, *Phys. Rev. B* **44**, 3793 (1991).
- [48] U.Bockelmann, G.Abstreiter, G. Weimann, W. Schalpp *Phys. Rev. B* **41**, 7864 (1990).
- [49] M. Grabowski and A. Madhukar, *Surf. Sci. I* **13**, 273 (1982).
- [50] J.P. Harrang, R.J. Higgins, R.K. Goodall, P.R. Jay, M.Laviron and P. Delescluse, *Phys. Rev. B* **32**, 8126 (1985).
- [51] M.A. Paalanen, DC. Tsui and J.C.M. Hwang, *Phys. Rev. Lett.* **51**, 2226 (1983).
- [52] B.Das, S. Subramaniam, M.R. Melloch and D.C. Miller, *Phys. Rev. B* **47**, 9650 (1993).
- [53] Tse-Ming Chen, C.-T. Liang, M.Y. Simmons, Gil-Ho Kim, D.A. Ritchie, *Physica E* **22**, 312 (2004).

-
- [54] J. Nuebler, V. Umansky, R. Morf, M. Heiblum, K. von Klitzing, and J. Smet Phys. Rev. B **81**, 035316 (2010)
- [55] T. Ando, J. Phys. Soc. Japan **37**, 1233 (1974).
- [56] A. Isihara and L. Smrčka, J. Phys. C **19**, 6777 (1986).
- [57] P.T. Coleridge, R. Stoner, and R. Fletcher, Phys. Rev. B **39**, 1120 (1989).
- [58] M. Sakowicz, J. Lusakowski, K. Karpierz, M. Grynberg, B. Maikusiak Applied Physics Letters **90**, 172104 (2007).
- [59] I. Pallecchi et al., Phys. Rev. B **65**, 125303 (2002).
- [60] A. Majumdar, J. Appl. Phys. **83**, 297 (1998).
- [61] F. Bloch, Z. Phys. **57** 545 (1929).
- [62] E.C. Stoner, Proc. R. Soc. Lond. A **165**, 372 (1938).
- [63] Weisbuch, C. and Hermann, C., Phys. Rev. Lett. **15**, 816 (1977).
- [64] Tutuc, E., Melinte, S., and Shayegan, M., Phys. Rev. Lett. **88**, 036805 (2002).
- [65] Pudalov, V. M., Gershenson, M. E., Kojima, H., Butch, N., Dizhur, E. M., Brunthaler, G., Prinz, A., and Bauer, G., Phys. Rev. Lett. **88**, 196404 (2002).
- [66] P.W. Anderson, Phys. Rev. **109**, 1491 (1958).
- [67] M. Hilke and J. C. Flores, Phys. Rev. B. **55**, 10625 (1997).
- [68] Dmitrii L. Maslov, Vladimir I. Yudson, Andres M. Somoza, and Miguel Ortuno^c Phys. Rev. Lett. **102**, 216601 (2009).
- [69] N. B. Brandt, S. M. Chudinov, and Ya. G. Ponomarev, Semimetals: I. Graphite and its Compounds (North-Holland, Amsterdam, 1988)
- [70] D. J. Singh, Phys. Rev. B **61**, 13397 (2000)
- [71] W. E. Pickett, Rev. Mod. Phys. **61**, 433 (1989)
- [72] Shor, P. W. Proc. 35nd Annual Symposium on Foundations of Computer Science (Shafi Goldwasser, ed.) IEEE Computer Society Press (1994)
- [73] Loss, D., DiVincenzo, D.P., Phys. Rev. A **57**, 120 (1998).
- [74] Elzerman, J. M. et al. Phys. Rev. B **67**, 161308 (2003).

-
- [75] Atature, M. et al. *Science* **312**, 551 (2006).
- [76] Elzerman, J. M. et al. *Nature* **430**, 431 (2004).
- [77] Amasha et al. , *Phys. Rev. Lett.* **100** ,046803 (2008).
- [78] Koppens, F. H. L. et al. *Nature* **442**, 766 (2006).
- [79] P. L. McEuen S. Tarucha R. M. Westervelt N. S. Wingreen L. P. Kouwenhoven, C. M. Marcus. *Electron Transport in Quantum Dots.* (1997).
- [80] Van Houten et al., Coulomb blockade oscillations in semiconductor Nanostructures *Surface Science* **263** (1992).
- [81] Kouwenhoven, L. P. et al. *Proceedings of the Advanced Study Institute on Mesoscopic Electron Transport, Review Article* (1997)
- [82] Foxman et al. *Phys. Rev. B* **50**, 14193 (1994).
- [83] A. Yacoby, et al . *Phys. Rev. Lett.* **77**, 4612 (1996).
- [84] C. W. J. Beenakker and H. von Houten, in *Solid State Physics, Semiconductor Heterostructures and Nanostructures*, edited by H. Ehrenreich and D. Turnbull (Academic Press, New York, 1991).

Curriculum vitae

Charulata Yashwantrao Barge
Friedrich Lau strasse 21
40474, Dusseldorf
Germany

Personal Information

Name:- Charulata Yashwantrao Barge
Nationality:- Indian
Date of Birth:- 10 July 1978
Email address:- charulata.barge@unibas.ch, charulatabarge@yahoo.com
Phone no.:- +49 211 97717423

Academic carrier

Year	Degree	University
May 2003	M.Tech. (Atmospheric Physics)	Pune University, Pune, India
May 2001	M.Sc. (Physics)	Shivaji Univerisy, Kolhapur, India
May 1999	B.Sc. (Physics)	Shivaji Univerisy, Kolhapur, India

Career History

2005-2006 Project Assistant at Institute of Semiconductor Technology, Technical University, Braunschweig, Germany
2004-2005 Project Assistant at Deutsches Zentrum für Lüft-und Raumfahrt (DLR), Wessling, Germany
2003-2004 Researcher at high performance computing center, IIT Delhi, INDIA